EFFECTIVENESS OF FOUNDATION REINFORCEMENT ON SEISMIC PERFORMANCE OF RETAINING WALLS

by

Muhammed Taha Demirel

B.S., Civil Engineering, Istanbul Bilgi University, 2018

Submitted to the Institute for Graduate Studies in Science and Engineering in partial fulfilment of the requirements for the degree of Master of Science

Graduate Program in Earthquake Engineering Department

Boğaziçi University

2023

EFFECTIVENESS OF FOUNDATION REINFORCEMENT ON SEISMIC PERFORMANCE OF RETAINING WALLS

DATE OF APPROVAL: 29.03.2022

To my mother

ACKNOWLEDGEMENTS

I would like to thank my thesis supervisor Prof. Ayşe Edinçliler who has always supported me during my studies. I appreciate her continuous guidance, patience and research experience.

I would like to thank my committee members Prof. Ali Pınar and Prof. Musaffa Ayşen Lav for their contributions. I would like to thank experts, Oktay Çırağ and Ekrem Ulusoy, who helped me during my experiments in KOERI Shaking Table Laboratory, and doctoral candidates Gözde Sezgin Tunçay and Yasin Sait Toksoy for their contributions and for sharing their experiences to guide.

In the realization of this thesis, the exoerinfrastructure supported by the Boğaziçi University Research Fund (Project No. BU-BAP8084) and Geotechnical Earthquake Engineering Research Center (Project No. 2012K120500) was used. I thank BÜ-BAP for making this thesis possible.

I would like to thank İstanbul Teknik for supporting the study by supplying geogrid materials used during the experiments. I also would like to thank Destech Müşavirlik Mühendislik ve Proje AŞ for being a sponsor for building the retaining wall model used during the experiments.

Lastly, I would like to express my deepest gratitude to my mother for her everlasting love and compassion, my family for their support, and my beloved Elif Hümeyra for her encouragement during my studies. I will always cherish their unwavering love and support, and I could not have made it this far without them. I am grateful to have them beside me, and I hope to make them proud in all my future endeavours.

ABSTRACT

EFFECTIVENESS OF FOUNDATION REINFORCEMENT ON SEISMIC PERFORMANCE OF RETAINING WALLS

Soil reinforcement is a widely studied improvement method to improve the strength and stiffness of the soil. The primary goals of soil reinforcement are to increase the bearing capacity and decrease the settlement of the soil along with improving the strength of the soil. Geosynthetic soil reinforcement is founded on the idea of taking advantage of the characteristics of geosynthetic materials like the tensile strength of geosynthetic materials, the pressure distribution potential of geosynthetic materials, and the interlocking mechanism between soil and geosynthetic materials. Many studies in the literature focus on using geosynthetic materials in slopes, embankments, or soil foundations below footings. However, there is not any study focusing on the use of geosynthetic reinforcement under retaining walls. This study aims to investigate the effectiveness of geogrid-reinforcement on the seismic performance of the retaining walls under different earthquake motions by shaking table tests. The effects of the length of reinforcement (L) and the number of reinforcement layers (N) on the seismic performance of the retaining walls constructed on geogrid reinforced sand under the different earthquake motions were investigated.

ÖZET

TEMEL DONATISININ İSTİNAT DUVARLARININ SİSMİK PERFORMANSI ÜZERİNDEKİ ETKİNLİĞİ

Temel donatısı, zeminin mukavemetini ve rijitliğini arttırmak için yaygın olarak kullanılan bir iyileştirme yöntemidir. Temel donatısının amacı, zeminin taşıma gücünü arttırarak ve/veya oturma potansiyelini azaltarak zemini iyileştirmektir. Geosentetik temel donatısı fikri; geosentetik malzemelerin çekme dayanımı, basınç dağıtma potansiyeli ve zemin ile geosentetik malzemeler arasındaki kilitleme mekanizması gibi özelliklerinden yararlanılarak zeminin iyileştirilmesini amaçlar. Literatürde geosentetik malzemelerin şevlerde, yol dolgularında veya temellerin altında temel donatısı olarak kullanımına odaklanan birçok çalışma bulunmaktadır. Ancak, istinat duvarlarının altında geosentetik temel donatısı kullanımına yönelik herhangi bir çalışma bulunmamaktadır. Bu çalışmada, temel donatısının istinat duvarlarının çeşitli deprem hareketleri altındaki sismik performansına etkinliğinin sarsma masası deneyleri ile araştırılması amaçlanmaktadır. Geogrid donatılı kum üzerine inşa edilen istinat duvarlarının farklı deprem hareketleri altındaki sismik performansına donatı boyu (L) ve donatı katmanları sayısının (N) etkileri incelenmiştir.

TABLE OF CONTENTS

EFFECTIVENESS OF FOUNDATION REINFORCEMENT ON SEISMIC PERFORMANCE OF RETAINING WALLS i

ACKNOWLEDGEMENTS iv

ABSTRACT v

ÖZET vi

TABLE OF CONTENTS vii

LIST OF FIGURES x

LIST OF TABLES xxxv

LIST OF SYMBOLS AND ABBREVIATIONS xxxvii

1. INTRODUCTION 1

1.1. General 1

1.2. Problem Statement and Objective of Thesis 2

2. RETAINING STRUCTURES 3

2.1. Introduction 3

2.2. Analyses of Retaining Walls for Static Conditions 5

2.3. Retaining Wall Analyses for Earthquake Conditions 9

2.4. Failure of Retaining Structures 12

3. IMPROVEMENT METHODS FOR RETAINING STRUCTURES TO MITIGATE EARTHQUAKE EFFECTS 17

4. GEOGRID-REINFORCED SOIL FOUNDATIONS 39

4.1. Introduction 39

4.2. Geosynthetics 39

4.3. Geogrid-Reinforced Soil Foundations 41

5. EXPERIMENTAL STUDY 58

5.1. General 58

5.2. Materials and Methods 58

5.2.1. Shaking Table 58
5.2.2. Laminar Box 59
5.2.3. Measuring Instruments and Instrumentation 61
5.2.4. Soil Material 62
5.2.5. Geogrid 62
5.2.6. Retaining Wall Model 63
5.2.7. Seismic Motions 64
5.3. Shaking Table Experiments 67
5.3.1. Case 01 69
5.3.2. Case 02 72
5.3.3. Case 03 74
5.3.4. Case 04 77
5.3.5. Case 05 80
5.3.6. Case 06 84
5.3.7. Case 07 86
5.3.8. Case 08 89
5.3.9. Case 09 92
5.4. Results of Shaking Table Experiments 96
5.4.1. Performance of The Retaining Wall Model Under The 1940 Imperial Valley Earthquake Motion – El Centro Station 96
5.4.2. Performance Of The Retaining Wall Model Under The 1999 Kocaeli Earthquake Motion - Iznik Station 114
5.4.3. Performance Of The Retaining Wall Model Under The 1999 Kocaeli Earthquake Motion - Izmit Station 131
5.4.4. Performance Of The Retaining Wall Model Under The 2014 North Aegean Sea Earthquake Motion - Gokceada Station 149
6. DISCUSSION 167

6.1. Effects Of The Geogrid-Reinforcement On Top Of The Retaining Wall Model Under The 1940 Imperial Valley Earthquake Motion – El Centro Station.....167

6.1.1. Effects Of The Number Of Reinforcement Layers Under The 1940 Imperial Valley Earthquake Motion - El Centro Station. 171

6.1.2. Effects Of The Reinforcement Length Under The 1940 Imperial Valley Earthquake Motion - El Centro Station. 172

6.2. Effects Of The Geogrid-Reinforcement On Top Of The Retaining Wall Model Under The 1999 Kocaeli Earthquake Motion – Iznik Station.....174

6.2.1. Effects Of The Number Of Reinforcement Layers Under The 1999 Kocaeli Earthquake Motion – Iznik Station.....177

6.2.2. Effects Of The Reinforcement Length Under The 1999 Kocaeli Earthquake Motion – Iznik Station. 178

6.3. Effects Of The Geogrid-Reinforcement On Top Of The Retaining Wall Model Under The 1999 Kocaeli Earthquake Motion - Izmit Station 179

6.3.1. Effects of The Number of Reinforcement Layers Under The 1999 Kocaeli Earthquake Motion – Izmit Station. 182

6.3.2. Effects of The Reinforcement Length Under The 1999 Kocaeli Earthquake Motion – Izmit Station.....183

6.4. Effects of The Geogrid-Reinforcement On Top Of The Retaining Wall Model Under The 2014 North Aegean Sea Earthquake Motion – Gokceada Station 184

6.4.1. Effects of The Number Of Reinforcement Layers Under The 2014 North Aegean Sea Earthquake Motion – Gokceada Station 187

6.4.2. Effects of The Reinforcement Length Under The 2014 North Aegean Sea Earthquake Motion – Gokceada Station 188

7. CONCLUSIONS 189

8. REFERENCES 191

LIST OF FIGURES

Figure 2.1. Common Types Of Earth Retaining Structures (Kramer, 1996). 3

Figure 2.2. Principal Types Of Rigid Retaining Walls (Murthy, 2002). 4

Figure 2.3. Typical Failure Mechanisms For A Gravity Retaining Wall: (a) Translational Failure, (b) Rotational Failure, And (c) Gross Instability Failure (Kramer, 1996). 5

Figure 2.4. Wall Movement For The Development Of (a) Active And (b) Passive Earth Pressures (Murthy, 2002). 7

Figure 2.5. (a) Soil Pressures, (b) Bending Moments, And (c) Flexural Failure Mechanism For Cantilever Retaining Wall (Kramer, 1996). 8

Figure 2.6. Derivation Of Mononobe-Okabe Equation (Das & Ramana, 2011). 11

Figure 2.7. Passive Earthquake Force on a Retaining Wall By Mononobe-Okabe Equation (Das & Ramana, 2011). 11

Figure 2.8. Vertical and Horizontal Displacement of Retaining Wall Due To Surface Fault Rupture (Day, 2012). 12

Figure 2.9. Lateral Retaining Wall Movement Due To Liquefaction During the 1995 Kobe Earthquake (Day, 2012). 13

Figure 2.10. Liquefaction Caused Lateral Displacement of the Retaining Wall by the 1995 Kobe Earthquake (Day, 2012). 14

Figure 3.1. Overview Of Geosynthetic Categories (Koerner, 2012). 18

Figure 3.2. Cross-section View Of The Test Setup And Instrumentation (Bathurst et al., 2007). 20

Figure 3.3. The Maximum Horizontal Force (kN) Recorded On The Wall Per Peak Input Base Acceleration (g) During The Experiments (Bathurst et al., 2007). 20

Figure 3.4. Logarithmic Geofoam-Thickness-To-Wall-Height Ratio: (a) Reduction In The Lateral Pressure And (b) Reduction Factor For The Lateral Earth Pressure Coefficient (AbdelSalam & Azzam, 2016).....22

Figure 3.5. Diagrams Illustrating (a) The Retaining Wall, (b) Dimensions Of The Toe And Heel For Granular Soil Backfill, And (c) The Dimensions Of The Toe And Heel For Shredded Tire Backfill (Shrestha et al., 2016).....23

Figure 3.6. Comparison Of The Calculated Peak Shear Force (kN/m) And Bending Moment(kN.m/m) (Shrestha et al., 2016).....23

Figure 3.7. Effect Of Input Motion Parameters (a) The Horizontal Deflection (cm) Of The Wall Tip, (b) The Distribution Of Shear Force (kN/m) Along The Stem, And (c) The Distribution Of Bending Moment (kN.m/m) Along The Stem (Shrestha et al., 2016). 24

Figure 3.8. Cantilever Retaining Wall Model (Edinçliler & Toksoy, 2017). 25

Figure 3.9. A Finite Element Model Of Proposed System (Edinçliler & Toksoy, 2019)....26

Figure 3.10. Set-Up Of Rigid Retaining Wall Model (Gade & Dasaka, 2022).....27

Figure 3.11. Reinforced Model Wall Configurations: (a) Walls 1 And 3, (b) Walls 8, 9, and 13 (El-Emam & Bathurst, 2007).....29

Figure 3.12. Influence Of Reinforcement Properties On The Measured Displacement On Top Of The Wall-Facing Panel Versus The Maximum Acceleration Amplitude At The Base (El-Emam & Bathurst, 2007). 30

Figure 3.13. Horizontal Displacements For Accelerations Of 0.4 g And 0.8 g (Guler et al., 2012). 31

Figure 3.14. Maximum Geogrid Tensile Loads Along Wall Height (Guler et al., 2012). ..31

Figure 3.15. Distribution Of Lateral Earth Pressure At The End Of And Post Construction (Yang et al., 2012). 32

Figure 3.16. Maximum Tensile Strains Measured In The Reinforcements Under 200% Izmit, Sakarya, And El Centro Earthquake Inputs (Başbuğ et al., 2021). 34

Figure 3.17. Distribution Of Settlement (Scale Factor:1/4): (a) Wolong Station Of The 2008 Wenchuan Earthquake (WL) And (b) El Centro Station Of The 1940 Imperial Valley Earthquake (EL) (Cai et al., 2021).....35

Figure 3.18. Distribution Of Settlement (Scale Factor:1/2): (a) Wolong Station Of The 2008 Wenchuan Earthquake (WL) And (b) El Centro Station Of The 1940 Imperial Valley Earthquake (EL) (Cai et al., 2021).....35

Figure 3.19. Distribution Of The Recorded Peak Strain (Scale Factor:1/4): (a) Wolong Station Of The 2008 Wenchuan Earthquake (WL) And (b) El Centro Station Of The 1940 Imperial Valley Earthquake (EL) (Cai et al., 2021). 36

Figure 3.20. Distributions Of The Recorded Peak Strain (Scale Factor:1/2): (a) Wolong Station Of The 2008 Wenchuan Earthquake (WL) And (b) El Centro Station Of The 1940 Imperial Valley Earthquake (EL) (Cai et al., 2021). 36

Figure 3.21. Peak Relative Displacement Along The Wall Height; (a) Setup 1, (b) Setup 2, (c) Setup 3, And (d) Setup 4 (Kilic et al., 2021).....38

Figure 4.1. Overview Of Geosynthetic Categories (Koerner, 2012). 40

Figure 4.2. 3D View Of Geocells (D8269-21: Standard Guide For The Use Of Geocells In Geotechnical And Roadway Projects 1, 2021). 41

Figure 4.3. Square And Strip Foundations Supported By Sand Reinforced With Layers Of Geogrid. ***q***, load per unit area (Omar et al., 1993). 43

Figure 4.4. Strip Foundation On Geogrid-Reinforced Clay (Shin et al., 1993).....44

Figure 4.5. Changing Of BCR with d/B (Das et al., 1994).....46

Figure 4.6. Variation Of Bearing Capacity Ratio With Foundation Width B (Das & Omar, 1994). 47

Figure 4.7. Variation Of Bearing Capacity Ratio With Relative Density (Das & Omar, 1994). 47

Figure 4.8. Strip Foundation On Sand Reinforced With Geogrid (Shin & Das, 2000). 48

Figure 4.9. Ultimate Bearing Capacity Versus D_f/B (Shin & Das, 2000). 48

Figure 4.10. Ultimate Bearing Capacity Versus d_f/B (Series A) (Patra et al., 2005). 50

Figure 4.11. Reinforced Ultimate Bearing Capacity Versus d/B For Surface Foundation (Series B) (Patra et al., 2005). 51

Figure 4.12. Reinforced Ultimate Bearing Capacity Versus d_f/B For d/B=1.1 For Surface Foundation (Series C) (Patra et al., 2005). 51

Figure 4.13. Assumed Failure Mode Under An Eccentrically Loaded Strip Foundation On Geogrid-Reinforced Sand (Patra et al., 2006). 52

Figure 4.14. Comparison Of BCR With Number Of Reinforcement Layers (N) For Geogrid Reinforced Sand For The Selected Studies (Sharma et al., 2009). 53

Figure 4.15. Geometric Parameters In The Laboratory Model Tests (Sawwaf, 2009)..... 54

Figure 4.16. Variation Of BCR With e_G/B Ratio (Sawwaf, 2009). 55

Figure 4.17. Variation Of BCR With e/B Ratio (Sawwaf, 2009). 55

Figure 4.18. A Diagram Showing (a) A Model Strip Footing And (b) The Layout Of The Test Setup. (Not To Scale) (Nasr & Azzam, 2017). 56

Figure 5.1. Side View Of Laminar Box On Shaking Table. 60

Figure 5.2. Laminar Box On Shaking Table. 60

Figure 5.3. Instrumentation Of Test Model. 62

Figure 5.4. ForTex GG 40/40 P By Istanbul Teknik. 63

Figure 5.5. Scaled Motion Of The 1940 Imperial Valley Earthquake – El Centro Station. 65

Figure 5.6. Scaled Motion Of The 1999 Kocaeli Earthquake – Iznik Station. 66

Figure 5.7. Scaled Motion Of The 1999 Kocaeli Earthquake – Izmit Station. 66

Figure 5.8. Scaled Motion Of The 2014 North Aegean Sea Earthquake – Gokceada Station. 67

Figure 5.9. Model Geometry of Case 01. 70

Figure 5.10. Constructed Experimental Setup of Case 01. 70

Figure 5.11. Constructed Experimental Setup of Case 01. 71

Figure 5.12. Constructed Experimental Setup of Case 01. 71

Figure 5.13. Model Geometry of Case 02. 72

Figure 5.14. Placing Of Geogrid Material for Case 02. 73

Figure 5.15. Placing of Retaining Wall Model. 73

Figure 5.16. Constructed Experimental Setup of Case 02. 74

Figure 5.17. Model Geometry Of Case 03. 75

Figure 5.18. The Placing Of The Second Layer. 75

Figure 5.19. The Placing Of The First Layer. 76

Figure 5.20. Placing of Retaining Wall Model and Backfill For Case 03. 76

Figure 5.21. Completed Experimental Setup of Case 03. 77

Figure 5.22. Model Geometry of Case 04. 78

Figure 5.23. Placing Third Layer Of Reinforcement Of Case 04. 78

Figure 5.24. Placing Second Reinforcement Layer of Case 04. 79

Figure 5.25. Placing First Layer Reinforcement of Case 04. 79

Figure 5.26. Completed Experimental Setup for Case 04. 80

Figure 5.27. Model Geometry of Case 05. 81

Figure 5.28. Placing Fourth Layer Of Reinforcement Of Case 05. 81

Figure 5.29. Placing Third Reinforcement Layer of Case 05. 82

Figure 5.30. Placing Second Reinforcement Layer of Case 05. 82

Figure 5.31. Placing First Layer Of Reinforcement Of Case 05. 83

Figure 5.32. Placing Retaining Wall Model and Backfill for Case 05. 83

Figure 5.33. Completed Experimental Setup for Case 05. 84

Figure 5.34. Model Geometry of Case 06. 85

Figure 5.35. Placing Reinforcement Layer of Case 06. 85

Figure 5.36. Placing of Retaining Wall Model and Backfill for Case 06. 86

Figure 5.37. Completed Experimental Setup for Case 06. 86

Figure 5.38. Model Geometry of Case 07. 87

Figure 5.39. Placing Second Reinforcement Layer of Case 07. 87

Figure 5.40. Placing First Reinforcement Layer and Accelerometer A27 For Case 07. 88

Figure 5.41. Placing Model Retaining Wall and Backfill For Case 07. 88

Figure 5.42. Completed Experimental Setup for Case 07. 89

Figure 5.43. Model Geometry of Case 08. 90

Figure 5.44. Placing Third Reinforcement Layer For Case 08. 90

Figure 5.45. Placing Second Reinforcement Layer For Case 08. 91

Figure 5.46. Placing First Reinforcement Layer and Accelerometer A27 For Case 08. 91

Figure 5.47. Placing Retaining Wall Model and Backfill For Case 08. 92

Figure 5.48. Completed Experimental Setup for Case 08. 92

Figure 5.49. Model Geometry of Case 09. 93

Figure 5.50. Placing Fourth Reinforcement Layer for Case 09. 93

Figure 5.51. Placing Third Reinforcement Layer for Case 09. 94

Figure 5.52. Placing Second Reinforcement Layer For Case 09. 94

Figure 5.53. Placing First Reinforcement Layer and Accelerometer A27 For Case 09. 95

Figure 5.54. Completed Experimental Setup for Case 09. 95

Figure 5.55. Comparison Of Acceleration, Fourier Amplitude, And Spectral Acceleration Values On Top Of The Retaining Wall Model Of Case 01 With Case 02 Under The 1940 Imperial Valley Earthquake Motion – El Centro Station. 98

Figure 5.56. Comparison Of Acceleration, Fourier Amplitude, With Spectral Acceleration Values On Top Of The Retaining Wall Model Of Case 01 With Case 03 Under The 1940 Imperial Valley Earthquake Motion – El Centro Station. 98

Figure 5.57 Comparison Of Acceleration, Fourier Amplitude, And Spectral Acceleration Values On Top Of The Retaining Wall Model Of Case 01 With Case 04 Under The 1940 Imperial Valley Earthquake Motion – El Centro Station. 99

Figure 5.58. Comparison Of Acceleration, Fourier Amplitude, And Spectral Acceleration Values On Top Of The Retaining Wall Model Of Case 01 With Case 05 Under The 1940 Imperial Valley Earthquake Motion – El Centro Station. 99

Figure 5.59. Comparison Of Acceleration, Fourier Amplitude, And Spectral Acceleration Values On Top Of The Retaining Wall Model Of Case 01 With Case 06 Under The 1940 Imperial Valley Earthquake Motion – El Centro Station. 100

Figure 5.60. Comparison Of Acceleration, Fourier Amplitude, And Spectral Acceleration Values On Top Of The Retaining Wall Model Of Case 01 With Case 07 Under The 1940 Imperial Valley Earthquake Motion – El Centro Station. 100

Figure 5.61. Comparison Of Acceleration, Fourier Amplitude, And Spectral Acceleration Values On Top Of The Retaining Wall Model Of Case 01 With Case 08 Under The 1940 Imperial Valley Earthquake Motion – El Centro Station. 101

Figure 5.62. Comparison Of Acceleration, Fourier Amplitude, And Spectral Acceleration Values On Top Of The Retaining Wall Model Of Case 01 With Case 09 Under The 1940 Imperial Valley Earthquake Motion – El Centro Station. 101

Figure 5.63. Comparison Of Displacement, Fourier Amplitude, And Spectral Displacement Values On Top Of The Retaining Wall Model Of Case 01 With Case 02 For Sensor D19 Under The 1940 Imperial Valley Earthquake Motion – El Centro Station. 102

Figure 5.64. Comparison Of Displacement, Fourier Amplitude, And Spectral Displacement Values On Top Of The Retaining Wall Model Of Case 01 With Case 03 For Sensor D19 Under The 1940 Imperial Valley Earthquake Motion – El Centro Station. 102

Figure 5.65. Comparison Of Displacement, Fourier Amplitude, And Spectral Displacement Values On Top Of The Retaining Wall Model Of Case 01 With Case 04 For Sensor D19 Under The 1940 Imperial Valley Earthquake Motion – El Centro Station. 103

Figure 5.66. Comparison Of Displacement, Fourier Amplitude, And Spectral Displacement Values On Top Of The Retaining Wall Model Of Case 01 With Case 05 For Sensor D19 Under The 1940 Imperial Valley Earthquake Motion – El Centro Station. 103

Figure 5.67. Comparison Of Displacement, Fourier Amplitude, And Spectral Displacement Values On Top Of The Retaining Wall Model Of Case 01 With Case 06 For Sensor D19 Under The 1940 Imperial Valley Earthquake Motion – El Centro Station. 104

Figure 5.68. Comparison Of Displacement, Fourier Amplitude, And Spectral Displacement Values On Top Of The Retaining Wall Model Of Case 01 With Case 07 For Sensor D19 Under The 1940 Imperial Valley Earthquake Motion – El Centro Station. 104

Figure 5.69. Comparison Of Displacement, Fourier Amplitude, And Spectral Displacement Values On Top Of The Retaining Wall Model Of Case 01 With Case 08 For Sensor D19 Under The 1940 Imperial Valley Earthquake Motion – El Centro Station. 105

Figure 5.70. Comparison Of Displacement, Fourier Amplitude, And Spectral Displacement Values On Top Of The Retaining Wall Model Of Case 01 With Case 09 For Sensor D19 Under The 1940 Imperial Valley Earthquake Motion – El Centro Station. 105

Figure 5.71. Comparison Of Acceleration, Fourier Amplitude, And Spectral Acceleration Values Below The Reinforced Soil Foundation Of The Retaining Wall Model Of Case 01 With Case 02 For Accelerometer A10 Under The 1940 Imperial Valley Earthquake Motion – El Centro Station.....106

Figure 5.72. Comparison Of Acceleration, Fourier Amplitude, And Spectral Acceleration Values Below The Reinforced Soil Foundation Of The Retaining Wall Model Of Case 01 With Case 03 For Accelerometer A10 Under The 1940 Imperial Valley Earthquake Motion – El Centro Station.....106

Figure 5.73. Comparison Of Acceleration, Fourier Amplitude, And Spectral Acceleration Values Below The Reinforced Soil Foundation Of The Retaining Wall Model Of Case 01 With Case 04 For Accelerometer A10 Under The 1940 Imperial Valley Earthquake Motion – El Centro Station.....107

Figure 5.74. Comparison Of Acceleration, Fourier Amplitude, And Spectral Acceleration Values Below The Reinforced Soil Foundation Of The Retaining Wall Model Of Case 01 With Case 05 For Accelerometer A10 Under The 1940 Imperial Valley Earthquake Motion – El Centro Station.....107

Figure 5.75. Comparison Of Acceleration, Fourier Amplitude, And Spectral Acceleration Values Below The Reinforced Soil Foundation Of The Retaining Wall Model Of Case 01 With Case 06 For Accelerometer A10 Under The 1940 Imperial Valley Earthquake Motion – El Centro Station.....108

Figure 5.76. Comparison Of Acceleration, Fourier Amplitude, And Spectral Acceleration Values Below The Reinforced Soil Foundation Of The Retaining Wall Model Of Case 01 With Case 07 For Accelerometer A10 Under The 1940 Imperial Valley Earthquake Motion – El Centro Station.....108

Figure 5.77. Comparison Of Acceleration, Fourier Amplitude, And Spectral Acceleration Values Below The Reinforced Soil Foundation Of The Retaining Wall Model Of Case 01

With Case 08 For Accelerometer A10 Under The 1940 Imperial Valley Earthquake Motion – El Centro Station.....109

Figure 5.78. Comparison Of Acceleration, Fourier Amplitude, And Spectral Acceleration Values Below The Reinforced Soil Foundation Of The Retaining Wall Model Of Case 01 With Case 09 For Accelerometer A10 Under The 1940 Imperial Valley Earthquake Motion – El Centro Station.....109

Figure 5.79. Comparison Of Acceleration, Fourier Amplitude, And Spectral Acceleration Values In The Backfill Of The Retaining Wall Model Of Case 01 With Case 02 For Accelerometer A16 Under The 1940 Imperial Valley Earthquake Motion – El Centro Station. 110

Figure 5.80. Comparison Of Acceleration, Fourier Amplitude, And Spectral Acceleration Values In The Backfill Of The Retaining Wall Model Of Case 01 With Case 03 For Accelerometer A16 Under The 1940 Imperial Valley Earthquake Motion – El Centro Station. 110

Figure 5.81. Comparison Of Acceleration, Fourier Amplitude, And Spectral Acceleration Values In The Backfill Of The Retaining Wall Model Of Case 01 With Case 04 For Accelerometer A16 Under The 1940 Imperial Valley Earthquake Motion – El Centro Station. 111

Figure 5.82. Comparison Of Acceleration, Fourier Amplitude, And Spectral Acceleration Values In The Backfill Of The Retaining Wall Model Of Case 01 With Case 05 For Accelerometer A16 Under The 1940 Imperial Valley Earthquake Motion – El Centro Station. 111

Figure 5.83. Comparison Of Acceleration, Fourier Amplitude, And Spectral Acceleration Values In The Backfill Of The Retaining Wall Model Of Case 01 With Case 06 For Accelerometer A16 Under The 1940 Imperial Valley Earthquake Motion – El Centro Station. 112

Figure 5.84. Comparison Of Acceleration, Fourier Amplitude, And Spectral Acceleration Values In The Backfill Of The Retaining Wall Model Of Case 01 With Case 07 For

Accelerometer A16 Under The 1940 Imperial Valley Earthquake Motion – El Centro Station. 112

Figure 5.85. Comparison Of Acceleration, Fourier Amplitude, And Spectral Acceleration Values In The Backfill Of The Retaining Wall Model Of Case 01 With Case 08 For Accelerometer A16 Under The 1940 Imperial Valley Earthquake Motion – El Centro Station. 113

Figure 5.86. Comparison Of Acceleration, Fourier Amplitude, And Spectral Acceleration Values In The Backfill Of The Retaining Wall Model Of Case 01 With Case 08 For Accelerometer A16 Under The 1940 Imperial Valley Earthquake Motion – El Centro Station. 113

Figure 5.87. Comparison Of Acceleration, Fourier Amplitude, And Spectral Acceleration Values On Top Of The Retaining Wall Model Of Case 01 With Case 02 For Accelerometer A07 Under The 1999 Kocaeli Earthquake Motion - Iznik Station. 116

Figure 5.88. Comparison Of Acceleration, Fourier Amplitude, And Spectral Acceleration Values On Top Of The Retaining Wall Model Of Case 01 With Case 03 For Accelerometer A07 Under The 1999 Kocaeli Earthquake Motion - Iznik Station. 116

Figure 5.89. Comparison Of Acceleration, Fourier Amplitude, And Spectral Acceleration Values On Top Of The Retaining Wall Model Of Case 01 With Case 04 For Accelerometer A07 Under The 1999 Kocaeli Earthquake Motion - Iznik Station. 117

Figure 5.90. Comparison Of Acceleration, Fourier Amplitude, And Spectral Acceleration Values On Top Of The Retaining Wall Model Of Case 01 With Case 05 For Accelerometer A07 Under The 1999 Kocaeli Earthquake Motion - Iznik Station. 117

Figure 5.91. Comparison Of Acceleration, Fourier Amplitude, and Spectral Acceleration Values On Top Of The Retaining Wall Model Of Case 01 With Case 06 For Accelerometer A07 Under The 1999 Kocaeli Earthquake Motion - Iznik Station. 118

Figure 5.92. Comparison Of Acceleration, Fourier Amplitude, And Spectral Acceleration Values On Top Of The Retaining Wall Model Of Case 01 With Case 07 For Accelerometer A07 Under The 1999 Kocaeli Earthquake Motion - Iznik Station. 118

Figure 5.93. Comparison Of Acceleration, Fourier Amplitude, And Spectral Acceleration Values On Top Of The Retaining Wall Model Of Case 01 With Case 08 For Accelerometer A07 Under The 1999 Kocaeli Earthquake Motion - Iznik Station. 119

Figure 5.94. Comparison Of Acceleration, Fourier Amplitude, And Spectral Acceleration Values On Top Of The Retaining Wall Model Of Case 01 With Case 09 For Accelerometer A07 Under The 1999 Kocaeli Earthquake Motion - Iznik Station. 119

Figure 5.95. Comparison Of Displacement, Fourier Amplitude, And Spectral Displacement Values On Top Of The Retaining Wall Model Of Case 01 With Case 02 For Sensor D19 Under The 1999 Kocaeli Earthquake Motion - Iznik Station. 120

Figure 5.96. Comparison Of Displacement, Fourier Amplitude, And Spectral Displacement Values On Top Of The Retaining Wall Model Of Case 01 With Case 03 For Sensor D19 Under The 1999 Kocaeli Earthquake Motion - Iznik Station. 120

Figure 5.97. Comparison Of Displacement, Fourier Amplitude, And Spectral Displacement Values On Top Of The Retaining Wall Model Of Case 01 With Case 04 For Sensor D19 Under The 1999 Kocaeli Earthquake Motion - Iznik Station. 121

Figure 5.98. Comparison Of Displacement, Fourier Amplitude, And Spectral Displacement Values On Top Of The Retaining Wall Model Of Case 01 With Case 05 For Sensor D19 Under The 1999 Kocaeli Earthquake Motion - Iznik Station. 121

Figure 5.99. Comparison Of Displacement, Fourier Amplitude, And Spectral Displacement Values On Top Of The Retaining Wall Model Of Case 01 With Case 06 For Sensor D19 Under The 1999 Kocaeli Earthquake Motion - Iznik Station. 122

Figure 5.100. Comparison Of Displacement, Fourier Amplitude, And Spectral Displacement Values On Top Of The Retaining Wall Model Of Case 01 With Case 07 For Sensor D19 Under The 1999 Kocaeli Earthquake Motion - Iznik Station. 122

Figure 5.101. Comparison Of Displacement, Fourier Amplitude, And Spectral Displacement Values On Top Of The Retaining Wall Model Of Case 01 With Case 08 For Sensor D19 Under The 1999 Kocaeli Earthquake Motion - Iznik Station. 123

Figure 5.102. Comparison Of Displacement, Fourier Amplitude, And Spectral Displacement Values On Top Of The Retaining Wall Model Of Case 01 With Case 09 For Sensor D19 Under The 1999 Kocaeli Earthquake Motion - Iznik Station. 123

Figure 5.103. Comparison Of Acceleration, Fourier Amplitude, And Spectral Acceleration Values Below The Reinforced Soil Foundation Of The Retaining Wall Model Of Case 01 With Case 02 For Accelerometer A10 Under The 1999 Kocaeli Earthquake Motion - Iznik Station. 124

Figure 5.104. Comparison Of Acceleration, Fourier Amplitude, And Spectral Acceleration Values Below The Reinforced Soil Foundation Of The Retaining Wall Model Of Case 01 With Case 03 For Accelerometer A10 Under The 1999 Kocaeli Earthquake Motion - Iznik Station. 124

Figure 5.105. Comparison Of Acceleration, Fourier Amplitude, And Spectral Acceleration Values Below The Reinforced Soil Foundation Of The Retaining Wall Model Of Case 01 With Case 04 For Accelerometer A10 Under The 1999 Kocaeli Earthquake Motion - Iznik Station. 125

Figure 5.106. Comparison Of Acceleration, Fourier Amplitude, And Spectral Acceleration Values Below The Reinforced Soil Foundation Of The Retaining Wall Model Of Case 01 With Case 05 For Accelerometer A10 Under The 1999 Kocaeli Earthquake Motion - Iznik Station. 125

Figure 5.107. Comparison Of Acceleration, Fourier Amplitude, And Spectral Acceleration Values Below The Reinforced Soil Foundation Of The Retaining Wall Model Of Case 01 With Case 06 For Accelerometer A10 Under The 1999 Kocaeli Earthquake Motion - Iznik Station. 126

Figure 5.108. Comparison Of Acceleration, Fourier Amplitude, And Spectral Acceleration Values Below The Reinforced Soil Foundation Of The Retaining Wall Model Of Case 01 With Case 07 For Accelerometer A10 Under The 1999 Kocaeli Earthquake Motion - Iznik Station. 126

Figure 5.109. Comparison Of Acceleration, Fourier Amplitude, And Spectral Acceleration Values Below The Reinforced Soil Foundation Of The Retaining Wall Model Of Case 01

With Case 08 For Accelerometer A10 Under The 1999 Kocaeli Earthquake Motion - Iznik Station. 127

Figure 5.110. Comparison Of Acceleration, Fourier Amplitude, And Spectral Acceleration Values Below The Reinforced Soil Foundation Of The Retaining Wall Model Of Case 01 With Case 09 For Accelerometer A10 Under The 1999 Kocaeli Earthquake Motion - Iznik Station. 127

Figure 5.111. Comparison Of Acceleration, Fourier Amplitude, And Spectral Acceleration Values In The Backfill Of The Retaining Wall Model Of Case 01 With Case 02 For Accelerometer A16 Under The 1999 Kocaeli Earthquake Motion - Iznik Station. 128

Figure 5.112. Comparison Of Acceleration, Fourier Amplitude, And Spectral Acceleration Values In The Backfill Of The Retaining Wall Model Of Case 01 With Case 03 For Accelerometer A16 Under The 1999 Kocaeli Earthquake Motion - Iznik Station. 128

Figure 5.113. Comparison Of Acceleration, Fourier Amplitude, And Spectral Acceleration Values In The Backfill Of The Retaining Wall Model Of Case 01 With Case 04 For Accelerometer A16 Under The 1999 Kocaeli Earthquake Motion - Iznik Station. 129

Figure 5.114. Comparison Of Acceleration, Fourier Amplitude, And Spectral Acceleration Values In The Backfill Of The Retaining Wall Model Of Case 01 With Case 05 For Accelerometer A16 Under The 1999 Kocaeli Earthquake Motion - Iznik Station. 129

Figure 5.115. Comparison Of Acceleration, Fourier Amplitude, And Spectral Acceleration Values In The Backfill Of The Retaining Wall Model Of Case 01 With Case 06 For Accelerometer A16 Under The 1999 Kocaeli Earthquake Motion - Iznik Station. 130

Figure 5.116. Comparison Of Acceleration, Fourier Amplitude, And Spectral Acceleration Values In The Backfill Of The Retaining Wall Model Of Case 01 With Case 07 For Accelerometer A16 Under The 1999 Kocaeli Earthquake Motion - Iznik Station. 130

Figure 5.117. Comparison Of Acceleration, Fourier Amplitude, And Spectral Acceleration Values In The Backfill Of The Retaining Wall Model Of Case 01 With Case 08 For Accelerometer A16 Under The 1999 Kocaeli Earthquake Motion - Iznik Station. 131

Figure 5.118. Comparison Of Acceleration, Fourier Amplitude, and Spectral Acceleration Values In The Backfill Of The Retaining Wall Model Of Case 01 With Case 09 For Accelerometer A16 Under The 1999 Kocaeli Earthquake Motion - Iznik Station. 131

Figure 5.119. Comparison Of Acceleration, Fourier Amplitude, And Spectral Acceleration Values On Top Of The Retaining Wall Model Of Case 01 With Case 02 For Accelerometer A07 Under The 1999 Kocaeli Earthquake Motion - Izmit Station. 133

Figure 5.120. Comparison Of Acceleration, Fourier Amplitude, And Spectral Acceleration Values On Top Of The Retaining Wall Model Of Case 01 With Case 03 For Accelerometer A07 Under The 1999 Kocaeli Earthquake Motion - Izmit Station. 134

Figure 5.121. Comparison Of Acceleration, Fourier Amplitude, And Spectral Acceleration Values On Top Of The Retaining Wall Model Of Case 01 With Case 04 For Accelerometer A07 Under The 1999 Kocaeli Earthquake Motion - Izmit Station. 134

Figure 5.122. Comparison Of Acceleration, Fourier Amplitude, And Spectral Acceleration Values On Top Of The Retaining Wall Model Of Case 01 With Case 05 For Accelerometer A07 Under The 1999 Kocaeli Earthquake Motion - Izmit Station. 135

Figure 5.123. Comparison Of Acceleration, Fourier Amplitude, And Spectral Acceleration Values On Top Of The Retaining Wall Model Of Case 01 With Case 06 For Accelerometer A07 Under The 1999 Kocaeli Earthquake Motion - Izmit Station. 135

Figure 5.124. Comparison Of Acceleration, Fourier Amplitude, And Spectral Acceleration Values On Top Of The Retaining Wall Model Of Case 01 With Case 07 For Accelerometer A07 Under The 1999 Kocaeli Earthquake Motion - Izmit Station. 136

Figure 5.125. Comparison Of Acceleration, Fourier Amplitude, And Spectral Acceleration Values On Top Of The Retaining Wall Model Of Case 01 With Case 08 For Accelerometer A07 Under The 1999 Kocaeli Earthquake Motion - Izmit Station. 136

Figure 5.126. Comparison Of Acceleration, Fourier Amplitude, And Spectral Acceleration Values On Top Of The Retaining Wall Model Of Case 01 And Case 09 For Accelerometer A07 Under The 1999 Kocaeli Earthquake Motion - Izmit Station. 137

Figure 5.127. Comparison Of Displacement, Fourier Amplitude, And Spectral Displacement Values On Top Of The Retaining Wall Model Of Case 01 With Case 02 For Sensor D19 Under The 1999 Kocaeli Earthquake Motion - Izmit Station. 137

Figure 5.128. Comparison Of Displacement, Fourier Amplitude, And Spectral Displacement Values On Top Of The Retaining Wall Model Of Case 01 With Case 03 For Sensor D19 Under The 1999 Kocaeli Earthquake Motion - Izmit Station. 138

Figure 5.129. Comparison Of Displacement, Fourier Amplitude, And Spectral Displacement Values On Top Of The Retaining Wall Model Of Case 01 With Case 04 For Sensor D19 Under The 1999 Kocaeli Earthquake Motion - Izmit Station. 138

Figure 5.130. Comparison Of Displacement, Fourier Amplitude, And Spectral Displacement Values On Top Of The Retaining Wall Model Of Case 01 With Case 05 For Sensor D19 Under The 1999 Kocaeli Earthquake Motion - Izmit Station. 139

Figure 5.131. Comparison Of Displacement, Fourier Amplitude, And Spectral Displacement Values On Top Of The Retaining Wall Model Of Case 01 With Case 06 For Sensor D19 Under The 1999 Kocaeli Earthquake Motion - Izmit Station. 139

Figure 5.132. Comparison Of Displacement, Fourier Amplitude, And Spectral Displacement Values On Top Of The Retaining Wall Model Of Case 01 With Case 07 For Sensor D19 Under The 1999 Kocaeli Earthquake Motion - Izmit Station. 140

Figure 5.133. Comparison Of Displacement, Fourier Amplitude, And Spectral Displacement Values On Top Of The Retaining Wall Model Of Case 01 With Case 08 For Sensor D19 Under The 1999 Kocaeli Earthquake Motion - Izmit Station. 140

Figure 5.134. Comparison Of Displacement, Fourier Amplitude, And Spectral Displacement Values On Top Of The Retaining Wall Model Of Case 01 With Case 09 For Sensor D19 Under The 1999 Kocaeli Earthquake Motion - Izmit Station. 141

Figure 5.135. Comparison Of Acceleration, Fourier Amplitude, And Spectral Acceleration Values Below The Reinforced Soil Foundation Of The Retaining Wall Model Of Case 01 With Case 02 For Accelerometer A10 Under The 1999 Kocaeli Earthquake Motion - Izmit Station. 141

Figure 5.136. Comparison Of Acceleration, Fourier Amplitude, And Spectral Acceleration Values Below The Reinforced Soil Foundation Of The Retaining Wall Model Of Case 01 With Case 03 For Accelerometer A10 Under The 1999 Kocaeli Earthquake Motion - Izmit Station. 142

Figure 5.137. Comparison Of Acceleration, Fourier Amplitude, And Spectral Acceleration Values Below The Reinforced Soil Foundation Of The Retaining Wall Model Of Case 01 With Case 04 For Accelerometer A10 Under The 1999 Kocaeli Earthquake Motion - Izmit Station. 142

Figure 5.138. Comparison Of Acceleration, Fourier Amplitude, And Spectral Acceleration Values Below The Reinforced Soil Foundation Of The Retaining Wall Model Of Case 01 With Case 05 For Accelerometer A10 Under The 1999 Kocaeli Earthquake Motion - Izmit Station. 143

Figure 5.139. Comparison Of Acceleration, Fourier Amplitude, And Spectral Acceleration Values Below The Reinforced Soil Foundation Of The Retaining Wall Model Of Case 01 With Case 06 For Accelerometer A10 Under The 1999 Kocaeli Earthquake Motion - Izmit Station. 143

Figure 5.140. Comparison Of Acceleration, Fourier Amplitude, And Spectral Acceleration Values Below The Reinforced Soil Foundation Of The Retaining Wall Model Of Case 01 With Case 07 For Accelerometer A10 Under The 1999 Kocaeli Earthquake Motion - Izmit Station. 144

Figure 5.141. Comparison Of Acceleration, Fourier Amplitude, And Spectral Acceleration Values Below The Reinforced Soil Foundation Of The Retaining Wall Model Of Case 01 With Case 08 For Accelerometer A10 Under The 1999 Kocaeli Earthquake Motion - Izmit Station. 144

Figure 5.142. Comparison Of Acceleration, Fourier Amplitude, And Spectral Acceleration Values Below The Reinforced Soil Foundation Of The Retaining Wall Model Of Case 01 With Case 09 For Accelerometer A10 Under The 1999 Kocaeli Earthquake Motion - Izmit Station. 145

Figure 5.143. Comparison Of Acceleration, Fourier Amplitude, And Spectral Acceleration Values In The Backfill Of The Retaining Wall Model Of Case 01 With Case 02 For Accelerometer A16 Under The 1999 Kocaeli Earthquake Motion - Izmit Station. 145

Figure 5.144. Comparison Of Acceleration, Fourier Amplitude, And Spectral Acceleration Values In The Backfill Of The Retaining Wall Model Of Case 01 With Case 03 For Accelerometer A16 Under The 1999 Kocaeli Earthquake Motion - Izmit Station. 146

Figure 5.145. Comparison Of Acceleration, Fourier Amplitude, And Spectral Acceleration Values In The Backfill Of The Retaining Wall Model Of Case 01 With Case 04 For Accelerometer A16 Under The 1999 Kocaeli Earthquake Motion - Izmit Station. 146

Figure 5.146. Comparison Of Acceleration, Fourier Amplitude, And Spectral Acceleration Values In The Backfill Of The Retaining Wall Model Of Case 01 With Case 05 For Accelerometer A16 Under The 1999 Kocaeli Earthquake Motion - Izmit Station. 147

Figure 5.147 Comparison Of Acceleration, Fourier Amplitude, And Spectral Acceleration Values In The Backfill Of The Retaining Wall Model Of Case 01 With Case 06 For Accelerometer A16 Under The 1999 Kocaeli Earthquake Motion - Izmit Station. 147

Figure 5.148. Comparison Of Acceleration, Fourier Amplitude, And Spectral Acceleration Values In The Backfill Of The Retaining Wall Model Of Case 01 With Case 07 For Accelerometer A16 Under The 1999 Kocaeli Earthquake Motion - Izmit Station. 148

Figure 5.149. Comparison Of Acceleration, Fourier Amplitude, And Spectral Acceleration Values In The Backfill Of The Retaining Wall Model Of Case 01 With Case 08 For Accelerometer A16 Under The 1999 Kocaeli Earthquake Motion - Izmit Station. 148

Figure 5.150. Comparison Of Acceleration, Fourier Amplitude, And Spectral Acceleration Values In The Backfill Of The Retaining Wall Model Of Case 01 With Case 09 For Accelerometer A16 Under The 1999 Kocaeli Earthquake Motion - Izmit Station. 149

Figure 5.151. Comparison Of Acceleration, Fourier Amplitude, And Spectral Acceleration Values On Top Of The Retaining Wall Model Of Case 01 With Case 02 For Accelerometer A07 Under The 2014 North Aegean Sea Earthquake Motion - Gokceada Station. 151

Figure 5.152. Comparison Of Acceleration, Fourier Amplitude, And Spectral Acceleration Values On Top Of The Retaining Wall Model Of Case 01 With Case 03 For Accelerometer A07 Under The 2014 North Aegean Sea Earthquake Motion - Gokceada Station. 151

Figure 5.153. Comparison Of Acceleration, Fourier Amplitude, And Spectral Acceleration Values On Top Of The Retaining Wall Model Of Case 01 With Case 04 For Accelerometer A07 Under The 2014 North Aegean Sea Earthquake Motion - Gokceada Station. 152

Figure 5.154. Comparison Of Acceleration, Fourier Amplitude, And Spectral Acceleration Values On Top Of The Retaining Wall Model Of Case 01 With Case 05 For Accelerometer A07 Under The 2014 North Aegean Sea Earthquake Motion - Gokceada Station. 152

Figure 5.155. Comparison Of Acceleration, Fourier Amplitude, And Spectral Acceleration Values On Top Of The Retaining Wall Model Of Case 01 With Case 06 For Accelerometer A07 Under The 2014 North Aegean Sea Earthquake Motion - Gokceada Station. 153

Figure 5.156. Comparison Of Acceleration, Fourier Amplitude, And Spectral Acceleration Values On Top Of The Retaining Wall Model Of Case 01 With Case 07 For Accelerometer A07 Under The 2014 North Aegean Sea Earthquake Motion - Gokceada Station. 153

Figure 5.157. Comparison Of Acceleration, Fourier Amplitude, And Spectral Acceleration Values On Top Of The Retaining Wall Model Of Case 01 With Case 08 For Accelerometer A07 Under The 2014 North Aegean Sea Earthquake Motion - Gokceada Station. 154

Figure 5.158. Comparison Of Acceleration, Fourier Amplitude, And Spectral Acceleration Values On Top Of The Retaining Wall Model Of Case 01 With Case 09 For Accelerometer A07 Under The 2014 North Aegean Sea Earthquake Motion - Gokceada Station. 154

Figure 5.159. Comparison Of Displacement, Fourier Amplitude, And Spectral Displacement Values On Top Of The Retaining Wall Model Of Case 01 With Case 02 For Sensor D19 Under The 2014 North Aegean Sea Earthquake Motion - Gokceada Station. 155

Figure 5.160. Comparison Of Displacement, Fourier Amplitude, And Spectral Displacement Values On Top Of The Retaining Wall Model Of Case 01 With Case 03 For Sensor D19 Under The 2014 North Aegean Sea Earthquake Motion - Gokceada Station. 155

Figure 5.161. Comparison Of Displacement, Fourier Amplitude, And Spectral Displacement Values On Top Of The Retaining Wall Model Of Case 01 With Case 04 For Sensor D19 Under The 2014 North Aegean Sea Earthquake Motion - Gokceada Station. 156

Figure 5.162. Comparison Of Displacement, Fourier Amplitude, And Spectral Displacement Values On Top Of The Retaining Wall Model Of Case 01 With Case 05 For Sensor D19 Under The 2014 North Aegean Sea Earthquake Motion - Gokceada Station. 156

Figure 5.163. Comparison Of Displacement, Fourier Amplitude, And Spectral Displacement Values On Top Of The Retaining Wall Model Of Case 01 With Case 06 For Sensor D19 Under The 2014 North Aegean Sea Earthquake Motion - Gokceada Station. 157

Figure 5.164. Comparison Of Displacement, Fourier Amplitude, And Spectral Displacement Values On Top Of The Retaining Wall Model Of Case 01 With Case 07 For Sensor D19 Under The 2014 North Aegean Sea Earthquake Motion - Gokceada Station. 157

Figure 5.165. Comparison Of Displacement, Fourier Amplitude, And Spectral Displacement Values On Top Of The Retaining Wall Model Of Case 01 With Case 08 For Sensor D19 Under The 2014 North Aegean Sea Earthquake Motion - Gokceada Station. 158

Figure 5.166. Comparison Of Displacement, Fourier Amplitude, And Spectral Displacement Values On Top Of The Retaining Wall Model Of Case 01 With Case 09 For Sensor D19 Under The 2014 North Aegean Sea Earthquake Motion - Gokceada Station. 158

Figure 5.167. Comparison Of Acceleration, Fourier Amplitude, And Spectral Acceleration Values Below The Reinforced Soil Foundation Of The Retaining Wall Model Of Case 01 With Case 02 For Accelerometer A10 Under The 2014 North Aegean Sea Earthquake Motion - Gokceada Station. 159

Figure 5.168. Comparison Of Acceleration, Fourier Amplitude, And Spectral Acceleration Values Below The Reinforced Soil Foundation Of The Retaining Wall Model Of Case 01 With Case 03 For Accelerometer A10 Under The 2014 North Aegean Sea Earthquake Motion - Gokceada Station. 159

Figure 5.169. Comparison Of Acceleration, Fourier Amplitude, And Spectral Acceleration Values Below The Reinforced Soil Foundation Of The Retaining Wall Model Of Case 01 With Case 04 For Accelerometer A10 Under The 2014 North Aegean Sea Earthquake Motion - Gokceada Station. 160

Figure 5.170. Comparison Of Acceleration, Fourier Amplitude, And Spectral Acceleration Values Below The Reinforced Soil Foundation Of The Retaining Wall Model Of Case 01 With Case 05 For Accelerometer A10 Under The 2014 North Aegean Sea Earthquake Motion - Gokceada Station. 160

Figure 5.171. Comparison Of Acceleration, Fourier Amplitude, And Spectral Acceleration Values Below The Reinforced Soil Foundation Of The Retaining Wall Model Of Case 01 With Case 06 For Accelerometer A10 Under The 2014 North Aegean Sea Earthquake Motion - Gokceada Station. 161

Figure 5.172. Comparison Of Acceleration, Fourier Amplitude, And Spectral Acceleration Values Below The Reinforced Soil Foundation Of The Retaining Wall Model Of Case 01 With Case 07 For Accelerometer A10 Under The 2014 North Aegean Sea Earthquake Motion - Gokceada Station. 161

Figure 5.173. Comparison Of Acceleration, Fourier Amplitude, And Spectral Acceleration Values Below The Reinforced Soil Foundation Of The Retaining Wall Model Of Case 01 With Case 08 For Accelerometer A10 Under The 2014 North Aegean Sea Earthquake Motion - Gokceada Station. 162

Figure 5.174. Comparison Of Acceleration, Fourier Amplitude, And Spectral Acceleration Values Below The Reinforced Soil Foundation Of The Retaining Wall Model Of Case 01 With Case 09 For Accelerometer A10 Under The 2014 North Aegean Sea Earthquake Motion - Gokceada Station. 162

Figure 5.175. Comparison Of Acceleration, Fourier Amplitude, And Spectral Acceleration Values In The Backfil Of The Retaining Wall Model Of Case 01 With Case 02 For Accelerometer A16 Under The 2014 North Aegean Sea Earthquake Motion - Gokceada Station. 163

Figure 5.176. Comparison Of Acceleration, Fourier Amplitude, And Spectral Acceleration Values In The Backfil Of The Retaining Wall Model Of Case 01 With Case 03 For Accelerometer A16 Under The 2014 North Aegean Sea Earthquake Motion - Gokceada Station. 163

Figure 5.177. Comparison Of Acceleration, Fourier Amplitude, And Spectral Acceleration Values In The Backfil Of The Retaining Wall Model Of Case 01 With Case 04 For Accelerometer A16 Under The 2014 North Aegean Sea Earthquake Motion - Gokceada Station. 164

Figure 5.178. Comparison Of Acceleration, Fourier Amplitude, And Spectral Acceleration Values In The Backfil Of The Retaining Wall Model Of Case 01 With Case 05 For Accelerometer A16 Under The 2014 North Aegean Sea Earthquake Motion - Gokceada Station. 164

Figure 5.179. Comparison Of Acceleration, Fourier Amplitude, And Spectral Acceleration Values In The Backfil Of The Retaining Wall Model Of Case 01 With Case 06 For Accelerometer A16 Under The 2014 North Aegean Sea Earthquake Motion - Gokceada Station. 165

Figure 5.180. Comparison Of Acceleration, Fourier Amplitude, And Spectral Acceleration Values In The Backfil Of The Retaining Wall Model Of Case 01 With Case 07 For Accelerometer A16 Under The 2014 North Aegean Sea Earthquake Motion - Gokceada Station. 165

Figure 5.181. Comparison Of Acceleration, Fourier Amplitude, And Spectral Acceleration Values In The Backfil Of The Retaining Wall Model Of Case 01 With Case 08 For Accelerometer A16 Under The 2014 North Aegean Sea Earthquake Motion - Gokceada Station. 166

Figure 5.182. Comparison Of Acceleration, Fourier Amplitude, And Spectral Acceleration Values In The Backfil Of The Retaining Wall Model Of Case 01 With Case 09 For Accelerometer A16 Under The 2014 North Aegean Sea Earthquake Motion - Gokceada Station. 166

Figure 6.1. Comparison Of Acceleration, Fourier Amplitude, And Spectral Acceleration Values On Top Of The Retaining Wall Model For (a) Cases 02 To 05 And (b) Cases 06 To 09 Under The 1940 Imperial Valley Earthquake Motion - El Centro Station. 169

Figure 6.2. Comparison Of Displacement, Fourier Amplitude, And Spectral Displacement Values On Top Of The Retaining Wall Model For (a) Cases 02 To 05 And (b) Cases 06 To 09 Under The 1940 Imperial Valley Earthquake Motion - El Centro Station. 170

Figure 6.3. Improvement Percentages And Peak Accelerations On Top Of The Retaining Wall Model Of (a) Cases 02 To 05 And (b) Cases 06 To 09 For Accelerometer A07 Under The 1940 Imperial Valley Earthquake Motion - El Centro Station. 172

Figure 6.4. Comparisons Of Improvement Percentages And Peak Accelerations On Top Of The Retaining Wall Model Of (a) Case 02 And Case 06, (b) Case 03 And Case 07, (c) Case 04 And Case 08, And (d) Case 05 And Case 09 To Understand The Effect Of Reinforcement Length Under The 1940 Imperial Valley Earthquake Motion - El Centro Station. 173

Figure 6.5. Comparison Of Acceleration, Fourier Amplitude, And Spectral Acceleration Values On Top Of The Retaining Wall Model For (a) Cases 02 To 05 And (b) Cases 06 To 09 Under The 1999 Kocaeli Earthquake Motion – Iznik Station. 175

Figure 6.6. Comparison Of Displacement, Fourier Amplitude, And Spectral Displacement Values On Top Of The Retaining Wall Model For (a) Cases 02 To 05 And (b) Cases 06 To 09 Under The 1999 Kocaeli Earthquake Motion – Iznik Station. 176

Figure 6.7. Improvement Percentages And Peak Accelerations On Top Of The Retaining Wall Model Of (a) Cases 02 To 05 And (b) Cases 06 To 09 Under The 1999 Kocaeli Earthquake Motion – Iznik Station. 177

Figure 6.8. Comparisons Of Improvement Percentages And Peak Accelerations On Top Of The Retaining Wall Model For (a) Case 02 And Case 06, (b) Case 03 And Case 07, (c) Case 04 And Case 08, And (d) Case 05 And Case 09 To Understand The Effect Of Reinforcement Length Under The 1999 Kocaeli Earthquake Motion – Iznik Station. 178

Figure 6.9. Comparison Of Acceleration, Fourier Amplitude, And Spectral Acceleration Values On Top Of The Retaining Wall Model For (a) Cases 02 To 05 And (b) Cases 06 To 09 Under The 1999 Kocaeli Earthquake Motion – Izmit Station. 180

Figure 6.10. Comparison Of Displacement, Fourier Amplitude, And Spectral Displacement Values On Top Of The Retaining Wall Model For (a) Cases 02 To 05 And (b) Cases 06 To 09 Under The 1999 Kocaeli Earthquake Motion – Izmit Station. 181

Figure 6.11. Improvement Percentages And Peak Accelerations On Top Of The Retaining Wall Model Of (a) Cases 02 To 05 And (b) Cases 06 To 09 Under The 1999 Kocaeli Earthquake Motion – Izmit Station. 182

Figure 6.12. Comparisons Of Improvement Percentages And Peak Accelerations On Top Of The Retaining Wall Model For (a) Case 02 And Case 06, (b) Case 03 And Case 07, (c) Case 04 And Case 08, And (d) Case 05 And Case 09 To Understand The Effect Of Reinforcement Length Under The 1999 Kocaeli Earthquake Motion – Izmit Station. 183

Figure 6.13. Comparison Of Acceleration, Fourier Amplitude, And Spectral Acceleration Values On Top Of The Retaining Wall Model For (a) Cases 02 To 05 And (b) Cases 06 To 09 Under The 2014 North Aegean Sea Earthquake Motion – Gokceada Station.....185

Figure 6.14. Comparison Of Displacement, Fourier Amplitude, And Spectral Displacement Values On Top Of The Retaining Wall Model For (a) Cases 02 To 05 And (b) Cases 06 To 09 Under The 2014 North Aegean Sea Earthquake Motion – Gokceada Station.....186

Figure 6.15. Improvement Percentages And Peak Accelerations On Top Of The Retaining Wall Model Of (a) Cases 02 To 05 And (b) Cases 06 To 09 Under The 2014 North Aegean Sea Earthquake Motion – Gokceada Station 187

Figure 6.16. Comparisons Of Improvement Percentages And Peak Accelerations On Top Of The Retaining Wall Model For (a) Case 02 And Case 06, (b) Case 03 And Case 07, (c) Case 04 And Case 08, And (d) Case 05 And Case 09 To Understand The Effect Of Reinforcement Length Under The 2014 North Aegean Sea Earthquake Motion – Gokceada Station 188

LIST OF TABLES

Table 2.1. Displacements And Failures Of Quay Walls (Day, 2012). 14

Table 3.1. Numerical Results From FEM Analyses (Edinçliler & Toksoy, 2011)..... 21

Table 3.2. Summary Of The Numerical Results (Edinçliler & Toksoy, 2017). 25

Table 3.3. Results Of Finite Element Analysis Under Earthquake Motions (Edinçliler & Toksoy, 2019). 26

Table 3.4. Configurations and Parameters for the Scaled Model (El-Emam & Bathurst, 2007). 29

Table 3.5. Properties Of Wall Model For The Shaking Table Tests (Kilic et al., 2021)..... 37

Table 4.1. Details of Laboratory-Model Test (Das et al., 1994)..... 45

Table 4.2. Dynamic Bearing Capacity Ratio (Santhakumar et al., 2001)..... 49

Table 4.3. Details Of Model Tests (Patra et al., 2005). 50

Table 4.4. Test Results Of Model Footings On Sand Reinforced With Geogrid (Series II) (Nasr & Azzam, 2017). 57

Table 5.1. Details Of Instrumentation 61

Table 5.2. Material Properties Of ForTex GG 40/40 P By Istanbul Teknik..... 63

Table 5.3. Scaling Factors For Geotechnical Studies (Wood, 2004)..... 64

Table 5.4. Earthquake Motions Used In The Experiments..... 65

Table 5.5. Scaling Factors (Iai, 1989). 68

Table 5.6. Dimensions Of Model And Prototype Retaining Walls. 68

Table 5.7. Experimental Program (The Case Numbers of the Models) 68

Table 5.8. Peak Acceleration And Displacement Values For (a) Cases With A Reinforcement Length Of 2B And (b) Cases With A Reinforcement Length Of 4B Under The 1940 Imperial Valley Earthquake Motion – El Centro Station. 97

Table 5.9. Peak Acceleration And Displacement Values For (a) Cases With A Reinforcement Length Of 2B And (b) Cases With A Reinforcement Length Of 4B Under The 1999 Kocaeli Earthquake Motion - Iznik Station.....114

Table 5.10. Peak Acceleration And Displacement Values For (a) Cases With A Reinforcement Length Of 2B And (b) Cases With A Reinforcement Length Of 4B Under The 1999 Kocaeli Earthquake Motion - Izmit Station.....132

Table 5.11. Peak Acceleration And Displacement Values For (a) Cases With A Reinforcement Length Of 2B And (b) Cases With A Reinforcement Length Of 4B Under The 2014 North Aegean Sea Earthquake Motion - Gokceada Station 150

LIST OF SYMBOLS AND ABBREVIATIONS

a_{max}	Maximum horizontal acceleration at the ground surface
ASTM	American Standard Test Method
B	Width of the base/foundation
BCR	Bearing capacity ratio
C_c	Coefficient of curvature
C_u	Coefficient of uniformity
d	Depth of the reinforcement zone
DBCR	Dynamic bearing capacity ratio
D_f	Depth of foundation
D_r	Relative density
e	Eccentricity
E	Young's modulus
e_G	Reinforcement eccentricity
e_L	Load eccentricity
e_{max}	Maximum void ratio
e_{min}	Minimum void ratio
EPS	Expanded polystyrene foam
FEM	Finite element model
FS	Factor of safety
g	Acceleration of gravity
GCL	Geosynthetic clay liners
G_s	Specific gravity
H	Height
h	Distance between layers
i	The angle of the backfill concerning horizontal
J_m	Reinforcement stiffness
k_A	Active earth pressure coefficient
K_{AE}	Active earth pressure coefficient under earthquake effect (Mononobe-Okabe equation)

k_h	Horizontal seismic coefficient
kN	Kilonewton
kN/m	Kilonewton per meters
k_P	Passive earth pressure coefficient
K_{PE}	Passive earth pressure coefficient under earthquake effect (Mononobe-Okabe equation)
k_v	Vertical seismic coefficient
L	Length
M	Magnitude
N	Number of reinforcement layers
n	Scaling ratio
P_A	Active earth pressure resultant force
P_{AE}	Active pseudo-static force by Mononobe and Okabe solution
P_E	Pseudo-static horizontal force
P_p	Passive earth pressure resultant force
P_{PE}	Passive pseudo-static force by Mononobe and Okabe solution
Q	Footing load
q'	Largest bearing pressure
q''	Lowest bearing pressure
q_u	Ultimate bearing capacity
R_{inter}	Boundary reduction factor
S	Section modulus
SP	Poorly graded sand
S_v	Vertical spacing
t	Thickness
u	Distance between the base and first reinforcement layers
W	Total weight of the active wedge
β	The angle of the back of the wall concerning vertical
γ_t	Total unit weight of the soil
Δ	Horizontal translation of the wall
δ	The angle of friction between the wall and the soil

λ	Scaling ratio
φ	Internal friction angle of the soil

1. INTRODUCTION

1.1. General

Advances in related fields such as material, machinery etc. allow engineers to provide innovative solutions to one of the main quests of engineering which is the mitigation of earthquake effects.

New technologies for preventing building damage from major earthquakes have been created as a result of new engineering techniques. Building safety is provided by the innovative idea of shielding structures from harmful influences. New techniques were used to manage the internal forces and displacement to make sure of this. The best way to defend a structure is to lower seismic energy by using structural components. The way a structure absorbs the seismic energy input is directly related to the degree of structural system damage. Through the ductility of the material, it has provided in conventional. This approach does not ensure the necessary damage control, hence alternative approaches have begun to be chosen.

Over the years, various methods have been established by engineers focusing on the seismic performance of structures regarding geotechnics. In recent decades, newer approaches focusing on benefitting from the material properties of geosynthetics have been used and investigated. So far, there are two main approaches to using geosynthetics to mitigate earthquake effects. The first one is geotechnical seismic isolation in which geosynthetic materials are used to absorb seismic energy induced by the earthquake. The second approach is using geosynthetics to advance the seismic performance of soils by reinforcing the soils beneath the structures (Tsang, 2009).

The practice of geosynthetic reinforcement can enhance the bearing capacity and tensile strength of the soil, reduce settlement, construction and maintenance costs, and offer benefits in terms of drainage and stability. Geosynthetic reinforcement has gained widespread use in civil engineering projects due to the numerous research and studies conducted to assess its effectiveness under various conditions. This thesis aims to investigate the effects of geosynthetic-reinforced soil foundations on the performance of cantilever retaining walls under different earthquake motions by a series of shaking table tests.

1.2. Problem Statement and Objective of Thesis

Before this experimental study, lots of experimental and mathematical studies have been conducted to inspect the performance of retaining walls with geosynthetic reinforcement and the performance of foundation soils altered by geosynthetic materials under dynamic and static conditions. However, there are not any studies focusing on the effect of using foundation soil improved with geosynthetic materials beneath a retaining wall under dynamic loadings.

The study aims to evaluate and determine the effectiveness of geosynthetic-reinforced soil foundations beneath retaining walls under earthquake loadings. It is important to provide an efficient review of existing studies on geosynthetic-reinforcement and performance of the retaining walls under cyclic loadings to understand the need for the presented improvement method and the outcomes of the experimental study.

2. RETAINING STRUCTURES

2.1. Introduction

Retaining structures, also known as retaining walls, are structures designed to hold vertical or nearly vertical earth banks or other materials to improve site conditions. These structures primarily provide lateral support, but can also provide vertical support in some cases. There are various types of retaining structures, including cantilever walls, gravity walls, counterfort walls, semi-gravity walls, sheet pile walls, quay walls, and bridge abutments as presented in Figures 2.1 and 2.2 (Murthy, 2002).

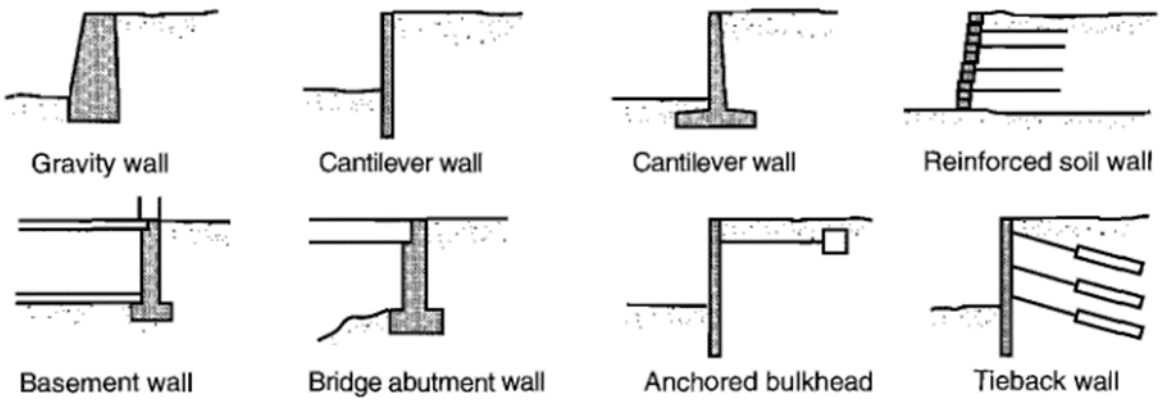

Figure 2.1. Common Types Of Earth Retaining Structures (Kramer, 1996).

Many historical earthquakes caused damage to the retaining structures which can be considered key elements of transportation systems such as harbours, bridges, railways etc. resulting in catastrophic physical and economic losses (Kramer, 1996).

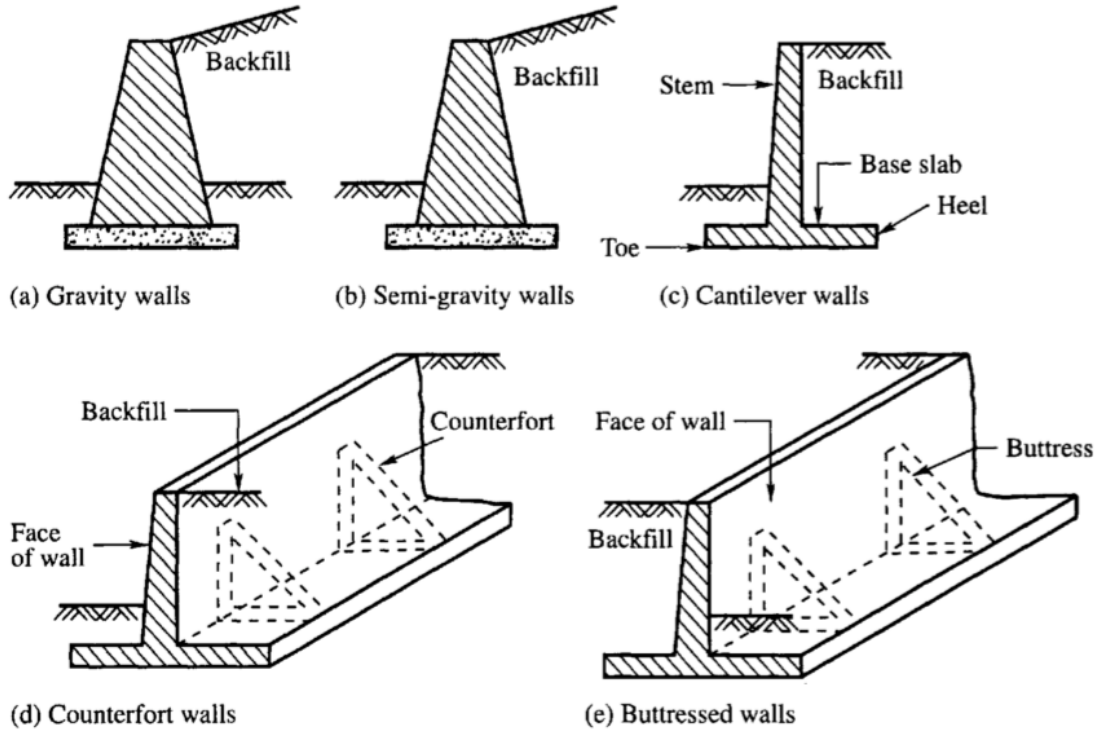

Figure 2.2. Principal Types Of Rigid Retaining Walls (Murthy, 2002).

The retaining wall design aims to achieve a balance between forces acting upon the wall without inducing any shear stresses that would come close to the shear strength of the soil. These forces can be listed as the mass of the wall, earth pressures, and external forces acting on the wall. An earthquake may lead to additional forces acting upon the wall and changes in soil strength behind or beneath the wall resulting in excessive deformation of the wall. These deformations can be observed as sliding, tilting, bending, or some other mechanisms (Day, 2012; Kramer, 1996).

Sliding of the wall can occur when lateral earth pressures acting on the wall exceed the sliding resistance at the foundation, disrupting the horizontal force equilibrium. Similarly, overturning of the wall can result from disruption of the moment equilibrium. Another potential failure mechanism is gross instability, involving both the soils behind and beneath the structure. These failure mechanisms can be observed in Figure 2.3 (Kramer, 1996).

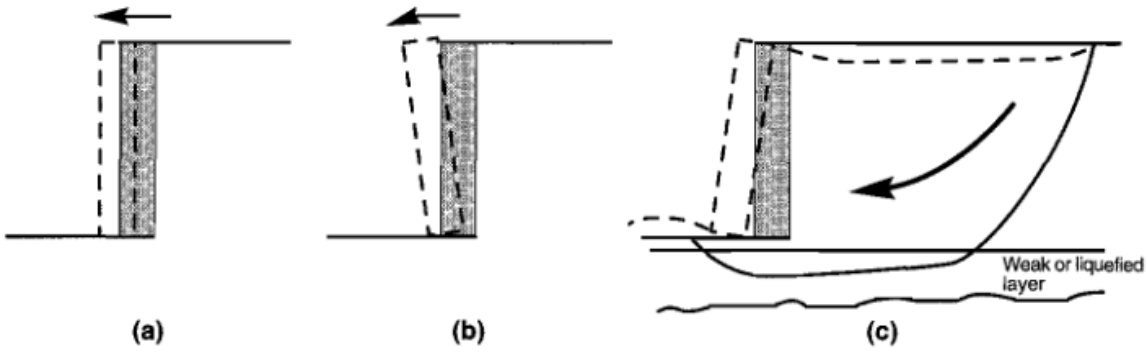

Figure 2.3. Typical Failure Mechanisms For A Gravity Retaining Wall: (a) Translational Failure, (b) Rotational Failure, And (c) Gross Instability Failure (Kramer, 1996).

To understand the failure mechanisms of the retaining walls under dynamic excitation and/or static conditions, the forces behind these failures should be investigated considering earthquakes firstly because all retaining structures are to resist these forces to be stable.

2.2. Analyses of Retaining Walls for Static Conditions

The first type of lateral earth pressure acting upon retaining walls is the active earth pressure resultant force, $\boldsymbol{P_A}$ (kN/m per meter)

$$\boldsymbol{P_A = {}^{1}\!/_{2}\, k_A \gamma_t H^2} \qquad (2.1)$$

caused by the active wedge. This force is dependent on the total unit weight of the backfill soil (γ_t), the active earth pressure coefficient ($\boldsymbol{k_A}$)

$$\boldsymbol{k_A = tan^2\left(45^\circ - {}^{1}\!/_{2}\, \varphi\right)} \qquad (2.2)$$

the internal friction angle of the soil ($\boldsymbol{\varphi}$), and the height of the wall ($\boldsymbol{H}$) (Day, 2012).

Another type of lateral earth pressure acting upon the retaining wall is passive earth pressure resultant force, $\boldsymbol{P_p}$ (kN/m per meter),

$$\boldsymbol{P_P = {}^{1}/_{2}\, k_P \gamma_t H^2} \tag{2.3}$$

caused by the passive wedge. The passive earth pressure resultant force under static conditions is dependent on the total unit weight of the backfill soil (γ_t), the passive earth pressure coefficient ($\boldsymbol{k_P}$),

$$\boldsymbol{k_P = tan^2\left(45^\circ + {}^{1}/_{2}\, \varphi\right)} \tag{2.4}$$

the internal friction angle of the soil ($\boldsymbol{\varphi}$), and the height of the wall ($\boldsymbol{H}$) (Day, 2012).

Besides the geometry of the structure and soil properties, both of the earth pressures need a sufficient movement of the respective wedge towards the wall to be developed as seen in Figure 2.4. An empirical relationship to estimate the needed horizontal translation of the wall ($\boldsymbol{\Delta}$)

$$\Delta = \boldsymbol{H(7 - 0.13\varphi)10^{-4}} \tag{2.5}$$

for the active state is developed by Sherif et al (1982) (Day, 2012; Kramer, 1996).

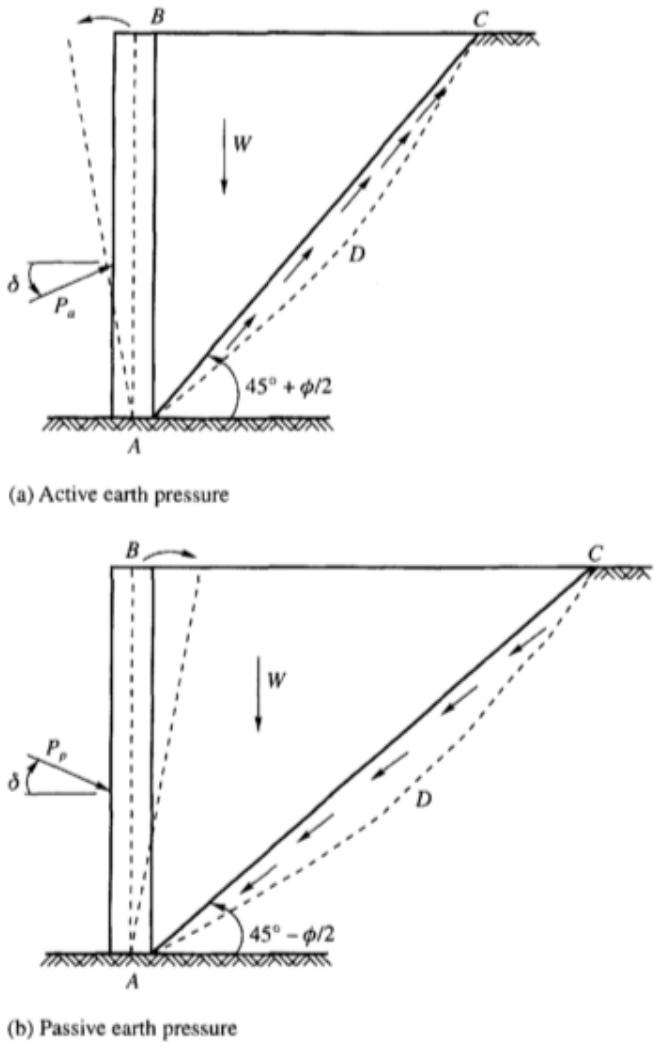

Figure 2.4. Wall Movement For The Development Of (a) Active And (b) Passive Earth Pressures (Murthy, 2002).

The last pressure type acting on the retaining wall is called footing bearing pressure. Besides, the vertical loading acting on the footing such as the wall and footing weights, dynamic and static loadings may also exist. A general approach is to resist such horizontal loads by using the soil pressure and frictional resistance and keeping the loads symmetric. However; symmetricity is generally not a case for the retaining structures due to their general geometry. This situation leads to eccentrical loading where eccentricity is defined as the distance between the impact point of the resultant vertical force and the gravitational centre of the footing. Eccentrically loaded footings experience a different amount of bearing pressure on the reverse sides of the footing. This requires the use of section modulus (***S***)

$$S = {}^{1}/_{6}\, B^2 \tag{2.6}$$

to estimate the highest (q')

$$q' = \frac{(Q(B+6e))}{B^2} \tag{2.7}$$

and the lowest (q'')

$$q'' = \frac{(Q(B-6e))}{B^2} \tag{2.8}$$

bearing pressures due to footing load (Q) where B is the width of the foundation and e is the eccentricity (Day, 2012).

Diagrams of soil pressures and bending moments acting upon a retaining wall and the occurrence of flexural failure mechanism are shown in Figure 2.5.

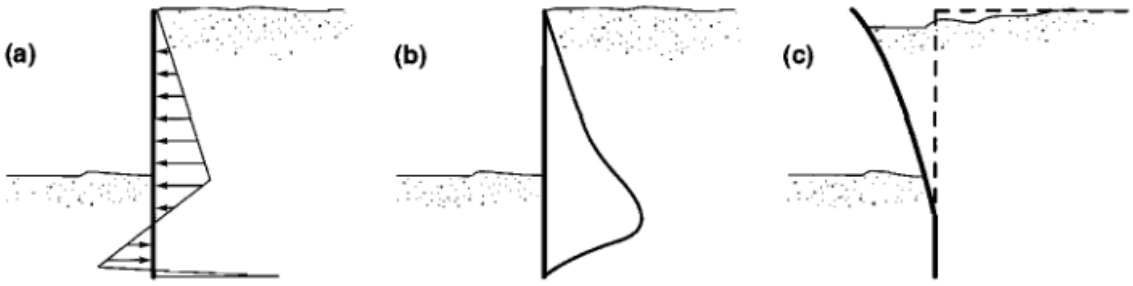

Figure 2.5. (a) Soil Pressures, (b) Bending Moments, And (c) Flexural Failure Mechanism For Cantilever Retaining Wall (Kramer, 1996).

2.3. Retaining Wall Analyses for Earthquake Conditions

There are several methods used to account for the outcome of earthquake excitation on the design of the retaining walls. Amongst them, the pseudo-static method considering earthquake loading as an additional static load is the most commonly used one. In this approach, earthquake load is taken into account as a force acting through the centroid of the active wedge which is located at ***2/3H*** from the bottom of the retaining wall. Since the effect of the vertical component of the earthquake load is much less than its horizontal component, the vertical component and its effect on the retaining wall are generally ignored. Pseudo-static horizontal force, $\boldsymbol{P_E}$, can be calculated by

$$\mathbf{W} = \frac{\mathbf{1}}{\mathbf{2}}\sqrt{\mathbf{k_A}}\mathbf{H^2}\boldsymbol{\gamma_t} \tag{2.9}$$

$$\mathbf{P_E} = \mathbf{k_h W} = \frac{\mathbf{1}}{\mathbf{2}}\sqrt{\mathbf{k_A}}\left(\frac{\mathbf{a_{max}}}{\mathbf{g}}\right)\mathbf{H^2}\boldsymbol{\gamma_t} \tag{2.10}$$

where $\boldsymbol{P_E}$ is pseudo-static horizontal force (kN), $\boldsymbol{W}$ is the total weight of the active wedge (***kN***), $\boldsymbol{k_h}$ is the horizontal seismic coefficient ($\boldsymbol{a_{max}/g}$), $\boldsymbol{k_A}$ is the active earth pressure coefficient, and $\boldsymbol{a_{max}}$ is the maximum horizontal acceleration at the ground surface induced by the earthquake ($\boldsymbol{m/s^2}$) (Day, 2012).

An alternative method used to calculate the pseudo-static force by considering

$$\frac{\mathbf{1}}{\mathbf{2}}\sqrt{\boldsymbol{k_A}} = \frac{\mathbf{3}}{\mathbf{8}} \tag{2.11}$$

$$\boldsymbol{P_E} = \frac{\mathbf{3}}{\mathbf{8}}\frac{\boldsymbol{a_{max}}}{\boldsymbol{g}}\boldsymbol{H^2\gamma_t} \tag{2.12}$$

is called the method by Seed and Whitman. In this method, the pseudo-static horizontal force is supposed to be exerted at ***0.6H*** from the bottom of the wall (Day, 2012).

Another method to obtain pseudo-static horizontal force is derived by modification of Coulomb's active force equation by bearing in mind the seismic coefficients ($\boldsymbol{k_h}$ and $\boldsymbol{k_v}$) of accelerations induced by the ground motion. It is referred to as the method by Mononobe and Okabe and assumes that the force is applied at a distance of ***1/3H*** from the bottom of the

wall. In this method, the pseudo-static force is estimated by using the horizontal seismic coefficient (k_h),

$$k_h = \frac{horizontal\ component\ of\ acceleration}{g} \tag{2.13}$$

and the vertical seismic coefficient (k_v),

$$k_v = \frac{vertical\ component\ of\ acceleration}{g} \tag{2.14}$$

$$P_{AE} = \frac{1}{2}\gamma_t H^2 (1 - k_v) K_{AE} \tag{2.15}$$

$$K_{AE} = \frac{cos^2(\varphi - \theta - \beta)}{(cos\theta)(cos^2\beta)(cos(\delta + \beta + \theta))\left[1 + \sqrt{\frac{sin(\varphi + \delta)sin(\varphi - \theta - i)}{cos(\delta + \beta + \theta)cos(i - \beta)}}\right]^2} \tag{2.16}$$

$$\theta = tan^{-1}\left(\frac{k_h}{1 - k_v}\right) \tag{2.17}$$

$$P_{PE} = \frac{1}{2}\gamma_t H^2 (1 - k_v) K_{PE} \tag{2.18}$$

$$K_{PE} = \frac{cos^2(\varphi + \beta - \theta)}{(cos\theta)(cos^2\beta)(cos(\delta - \beta + \theta))\left[1 - \sqrt{\frac{sin(\varphi + \delta)sin(\varphi - \theta + i)}{cos(\delta - \beta + \theta)cos(i - \beta)}}\right]^2} \tag{2.19}$$

where P_{AE} is the active pseudo-static force by Mononobe and Okabe solution, K_{AE} is the active earth pressure coefficient under earthquake effect, P_{PE} is the passive pseudo-static force by Mononobe and Okabe solution, K_{PE} is the passive earth pressure coefficient under earthquake effect, i is the angle of the backfill concerning horizontal, φ is the internal friction angle of the soil, β is the angle of the back of the wall concerning vertical, and δ is the angle of friction between the wall and the soil. Figures 2.6 and 2.7 presents the derivation of active and passive earthquake forces by the Mononobe-Okabe solution (Das & Ramana, 2011).

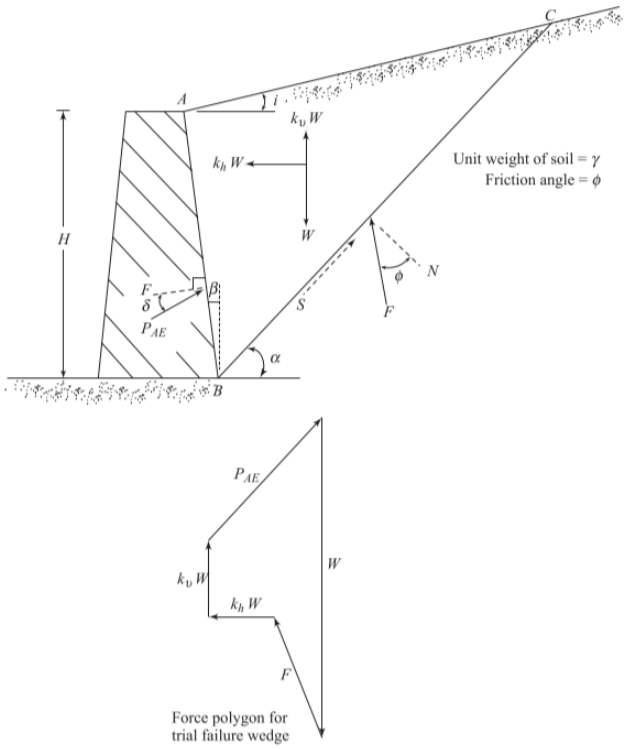

Figure 2.6. Derivation Of Mononobe-Okabe Equation (Das & Ramana, 2011).

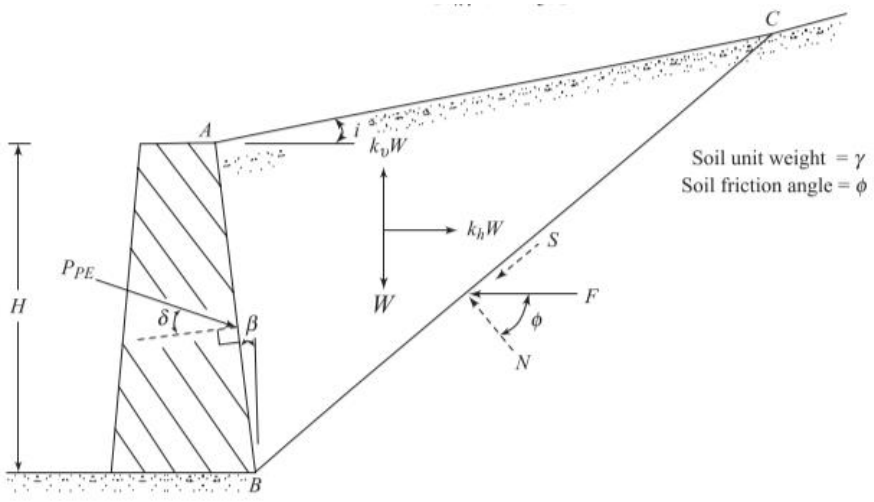

Figure 2.7. Passive Earthquake Force on a Retaining Wall By Mononobe-Okabe Equation (Das & Ramana, 2011).

2.4. Failure of Retaining Structures

As mentioned earlier, the retaining walls can experience different failures if the forces explained above are not balanced during the planning and construction of the retaining walls. However, earthquake effects and damage experienced by the site can also cause structural damage or permanent deformation of the retaining walls. The first of such effects is damage by surface rupture. Surface fault rupture caused by an earthquake may cause permanent displacement of a retaining wall at the affected site as seen in Figure 2.8.



Figure 2.8. Vertical and Horizontal Displacement of Retaining Wall Due To Surface Fault Rupture (Day, 2012).

Another earthquake effect that may lead to the failure of the retaining walls is liquefaction. Since the retaining walls are important parts of facilities such as ports which are generally built on liquefaction susceptible sites, there are many examples of failures of such structures in the literature. Depending on the location of the earthquake-induced liquefaction, there are three types of liquefaction. The first one is passive wedge liquefaction

in which a decrease in the passive force in front of the wall leading to sliding and/or overturning of the wall is observed. Another one is active wedge liquefaction in which an increase in the active pressure is detected due to the failure of shear strength in the soil behind the wall. These two cases can take place individually or together resulting in the overturning of the wall, translation of the wall, or structural failure of the wall by exceeding its strength of the wall. The last one is liquefaction below the base of the wall which causes the failure of shear strength in the soil beneath resulting in a bearing capacity failure. It generally leads to the excessive settlement of the retaining wall or lateral spreading of the retaining wall. In Figures 2.9 and 2.10, examples of damaged retaining walls due to earthquake-induced liquefaction during the 1995 Kobe Earthquake are presented. Also, observed failures of quay walls in terms of displacement caused by earthquakes are given in Table 2.1.



Figure 2.9. Lateral Retaining Wall Movement Due To Liquefaction During the 1995 Kobe Earthquake (Day, 2012).



Figure 2.10. Liquefaction Caused Lateral Displacement of the Retaining Wall by the 1995 Kobe Earthquake (Day, 2012).

Table 2.1. Displacements And Failures Of Quay Walls (Day, 2012).

Earthquake	**Date**	**M[e]**	**Harbour**	**Distance from Epicentre**	**Damage**	**Approximated Movement**
Kitaizu	25 November 1930	7.1	Shimizu	48 km	The collapse of gravity walls[b]	7.93 m
Shizuoka	11 July 1935	-	Shimizu	-	Retaining wall collapse[b]	4.88 m
Tonankai	7 December 1944	8.2	Shimizu	175 km	Sliding of retaining wall[b]	-
			Nagoya	128 km	Outward movement of bulkhead with relieving platform[b]	3.05 – 3.96 m

Table 2.1. Displacements And Failures Of Quay Walls (Day, 2012) (cont.).

Earthquake	Date	M[e]	Harbour	Distance from Epicentre	Damage	Approximated Movement
			Yokkaichi	144 km	Outward movement of pile-supported deck[b]	3.66 m
Nankai	21 December 1946	8.1	Nagoya	200 – 304 km	Outward movement of bulkhead with relieving platform[b]	3.96 m
			Osaka	200 – 304 km	The collapse of the retaining wall above relieving platform[b]	4.27 m
			Yokkaichi	200 – 304 km	Outward movement of pile-supported deck[b]	3.66 m
			Uno	-	Outward movement of gravity wall[b]	0.61 m
Tokachioki	4 March 1952	7.8	Kushiro	144 km	Outward movement of gravity wall[b]	5.49 m
Chile	22 May 1960	8.4	Puerto Montt	112 km	The complete overturning of gravity walls[c]	>4.57 m
					Outward movement of anchored bulkheads[c]	0.6 – 0.9 m
Niigata	16 June 1964	7.5	Niigata	51.2 km	Tilting of gravity wall[d]	3.05 m

Table 2.1. Displacements And Failures Of Quay Walls (Day, 2012) (cont.).

Earthquake	Date	M[e]	Harbour	Distance from Epicentre	Damage	Approximated Movement
Niigata	16 June 1964	7.5	Niigata	51.2 km	Outward movement of anchored bulkheads[d]	0.3 – 2.1 m

[a] After Seed and Whitman (1970)
[b] Reported by Amano, Azuma, and Ishii (1956)
[c] Reported by Duke and Leeds (1963)
[d] Reported by Hayashi, Kubo, and Nakase (1966)
[e] Magnitude

Another earthquake effect leading to the failure of the retaining walls is the reduction in the soil resistance due to the weakening of the soil. The soil located under the retaining wall or in front of the wall may experience weakening due to earthquake excitation. Since this soil is the bearing soil for the retaining wall, its weakening may lead to excessive settlement of the wall, sliding failure, overturning failure, and/or bearing capacity failure (Day, 2012).

3. IMPROVEMENT METHODS FOR RETAINING STRUCTURES TO MITIGATE EARTHQUAKE EFFECTS

In general, the main approaches of improvement in any case for mitigation of earthquake effects are avoiding susceptible sites, prevention, and engineered design. The latter two approaches are also valid for retaining structures to mitigate earthquake effects. The earthquakes may disturb the equilibrium of forces acting on the retaining structures, or weaken soil around the retaining structures. To prevent these, improvement methods have been altered concerning advances in materials and the need for engineering and financial efficiency. So far, the general improvement methods focus on lightening the backfill or altering the soil parameters of the backfill by reinforcement.

A traditional mitigation method used to prevent liquefaction in the backfill is to replace the backfill with granular material to increase drainage and reduce liquefaction potential by removing the liquefaction-susceptible soil. This approach can be considered an improvement method based on the prevention approach.

With the advances in material production and understanding of the reinforcement concept following the 70s, geosynthetics have been used in improvements. A geosynthetic is a two-dimensional product composed of polymeric material that is utilized in combination with other geotechnical engineering supplies as an integrated fragment of a system. The main reasons for using geosynthetic materials in soils are separation, purification, reinforcement, drainage, and control along with advantages like improving the performance of soil, reducing initial cost, providing longer service time and low-cost maintenance (D4439 - 20: Standard Terminology For Geosynthetics, 2020; Koerner, 2012).

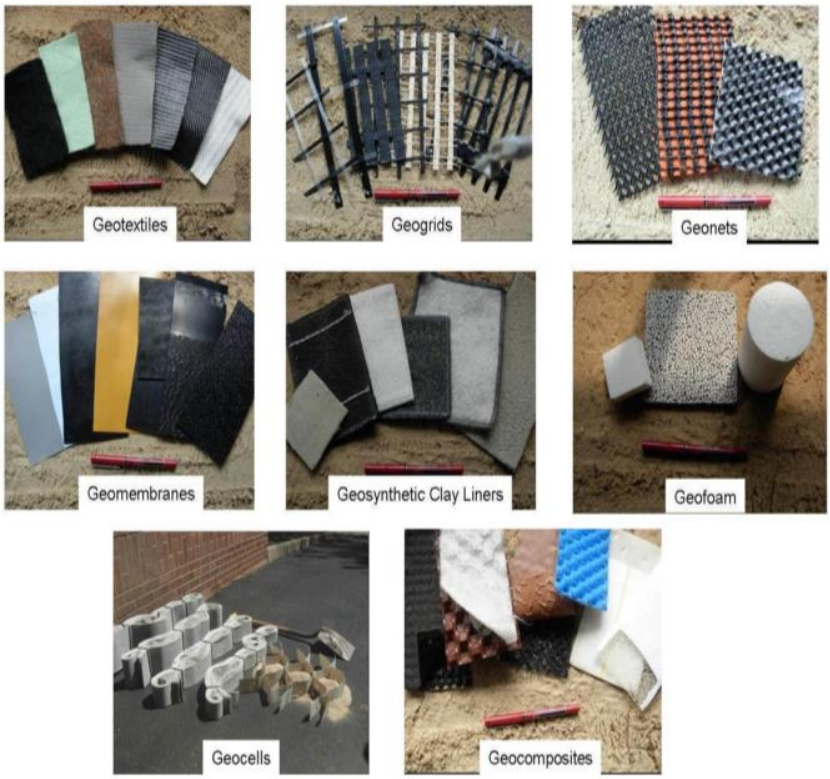

Figure 3.1. Overview Of Geosynthetic Categories (Koerner, 2012).

As shown in Figure 3.1, there are eight types of geosynthetics used according to the aim of soil improvement. Geotextiles are porous fabrics consisting of synthetic fibres and they are primarily used for drainage, purification, reinforcement, and separation. Geogrids are geosynthetics made up of a uniform grid of integrally connected components with openings large enough to allow meshing with other materials and they are mainly used for reinforcement. Geonets are geosynthetics composed of matching sets of integrally connected ribs covering similar sets at varied angles enabling planar drainage of gases or liquids. Geomembranes are impervious polymeric sheets that are typically utilized for the covers and linings of liquid or solid-storage facilities. Their application in geotechnical and transportation fields is expanding, as is their application in environmental fields. Geosynthetic clay liners (GCLs) are rolls of pre-fabricated tinny sheets of bentonite clay. GCLs are utilized in environmental and containment applications, as well as transportation and geotechnical development, as a composite element beneath a geomembrane or on their own. Geofoam is a polymeric expansion process product that is typically in the shape of big, yet light, blocks that provide lightweight fill in a variety of applications. Geocells are

produced in the form of a network of connected strips that, when opened, form a network of open cells. Geocomposites are composed of a combination of geosynthetic elements in a factory-fabricated unit, and they accomplish all of the functions previously described for geosynthetics (D4439 - 20: Standard Terminology For Geosynthetics, 2020; D8269-21: Standard Guide For The Use Of Geocells In Geotechnical And Roadway Projects 1, 2021; Koerner, 2012).

One of the improvement methods is using compressible inclusions in the backfill to reduce the impact of dynamic and static forces acting on the retaining structure. Inclusions can be done by creating a layer of geosynthetic material between the structure and the backfill as well as mixing geosynthetic material with soil. There are plenty of studies investigating the effectiveness of the improvement based on various parameters under static and dynamic situations.

Bathurst et al. (2007) conducted reduce-scaled shaking table tests as shown in Figure 3.2 to understand the use of seismic buffers made of EPS geofoam between rigid retaining walls and backfill under dynamic loading. Three different types of geofoam materials are used in the tests. The results state that the efficiency of the seismic buffer in terms of load exerted on the retaining wall and peak ground acceleration increases with decreasing density of geofoams as seen in Figure 3.3 (Bathurst et al., 2007).

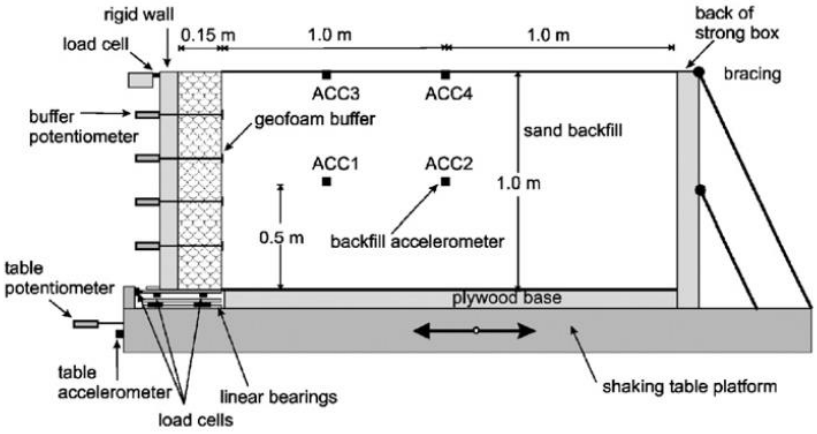

Figure 3.2. Cross-section View Of The Test Setup And Instrumentation (Bathurst et al., 2007).

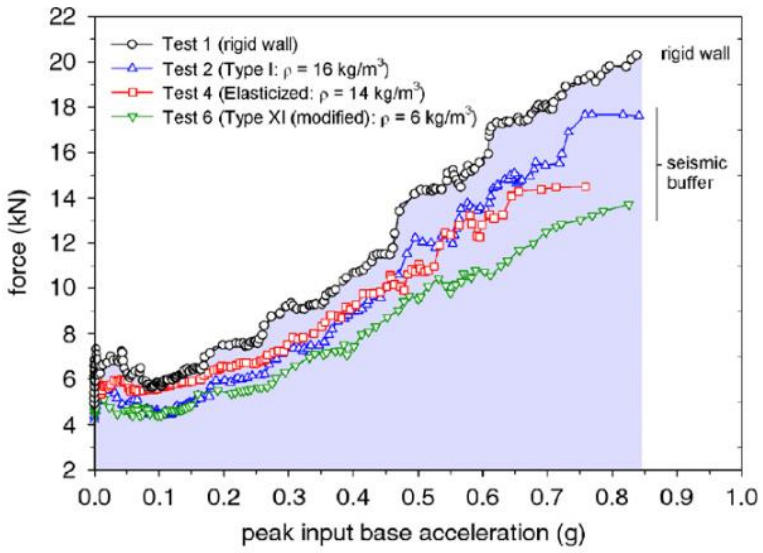

Figure 3.3. The Maximum Horizontal Force (kN) Recorded On The Wall Per Peak Input Base Acceleration (g) During The Experiments (Bathurst et al., 2007).

Edinçliler and Toksoy (2011) propose a mixture of tire crumb and sand to be considered as a seismic buffer behind the retaining wall. A series of numerical analyses are done to determine the optimum value of seismic buffer thickness concerning the height. The findings of the study are presented in Table 3.1, and demonstrated that the performance of such structures under cyclic loadings may be successfully and efficiently increased by using

the seismic cushion concerning the retaining wall models. Dynamic performance evaluations of retaining wall models reveal that using a (***t/H***) ratio of 0.3 rather than 0.4 significantly improves the stability of retaining structures (Edinçliler & Toksoy, 2011).

Table 3.1. Numerical Results From FEM Analyses (Edinçliler & Toksoy, 2011).

	Model 1 (t/H=0.4)	Model 2 (t/H=0.3)	Model 3 (t/H=0.4)	Model 4 (t/H=0.3)
Wall Height (m)	5	5	7	7
Total Displacements (cm)	33.9	34.9	78.0	67.9
Rotations (°)	2.1	2.2	3.4	2.8
Axial Force (kN/m)	138.7	139.2	192.3	201.6
Shear Force (kN/m)	155.2	159.6	266.6	281.3
Bending Moment (kNm/m)	131.9	147.8	342.6	427.7
Peak Transmitted Acceleration (g)	4.10	3.51	3.70	3.57
Acceleration at Top of the Wall (g)	1.21	0.74	2.72	0.56
Factor of Safety (FS)	1.62	1.72	1.72	1.75

Abdel Salam and Azzam (2016) studies the properties of local geofoams to provide a standard numerical approach for the design of retaining walls reinforced with seismic buffers. The discoveries of the study which are given in Figure 3.4, show that the application of seismic buffers with a thickness-to-wall-height ratio (***t/H***) of 0.01 for flexible and rigid walls decreased the lateral pressures exerted on the retaining wall by 10% and 6%, respectively. The reduction of the lateral pressures reaches 65% when ***t/H***=0.5. Also, it is noted that the boundary reduction factor (R_{inter}) increases with increasing interaction pressure (AbdelSalam & Azzam, 2016).

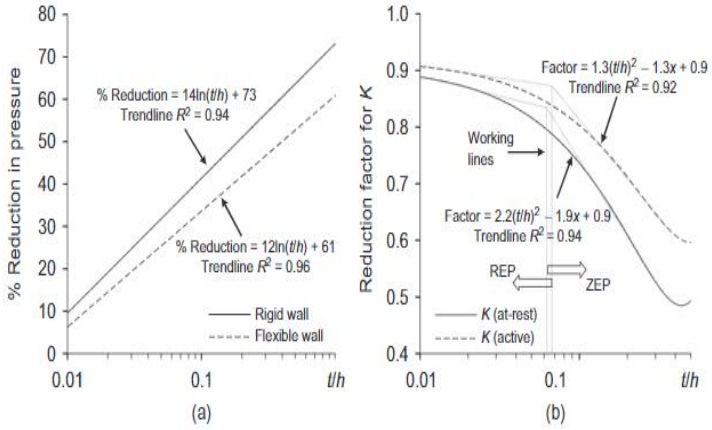

Figure 3.4. Logarithmic Geofoam-Thickness-To-Wall-Height Ratio: (a) Reduction In The Lateral Pressure And (b) Reduction Factor For The Lateral Earth Pressure Coefficient (AbdelSalam & Azzam, 2016).

Shrestha et al. (2016) run a study to investigate the applicability of shredded tires as backfill soil for retaining walls in terms of economical, geotechnical, and structural considerations. Also, the efficiency of the reinforcement method under earthquake loading is investigated by finite element analysis. The results of the simulation showed that there was not any failure under the earthquake effect. It was detected that the use of torn tire backfill reduces the volume of concrete and excavation, the amount of structural reinforcement required for structural stability, and the volume of backfill materials as seen in Figure 3.5. According to Figures 3.6 and 3.7, the finite element analyses also revealed that bending moments, shear force, and the wall tip deflection experienced by the retaining wall were much smaller for shredded tire backfills compared to granular backfills (Shrestha et al., 2016).

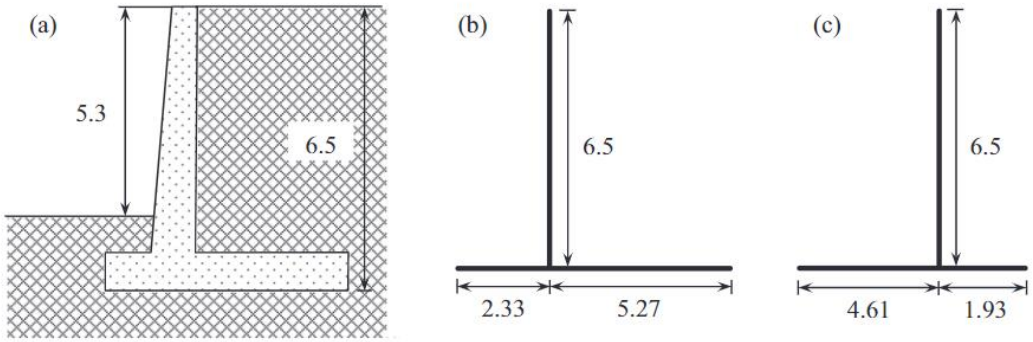

Figure 3.5. Diagrams Illustrating (a) The Retaining Wall, (b) Dimensions Of The Toe And Heel For Granular Soil Backfill, And (c) The Dimensions Of The Toe And Heel For Shredded Tire Backfill (Shrestha et al., 2016).

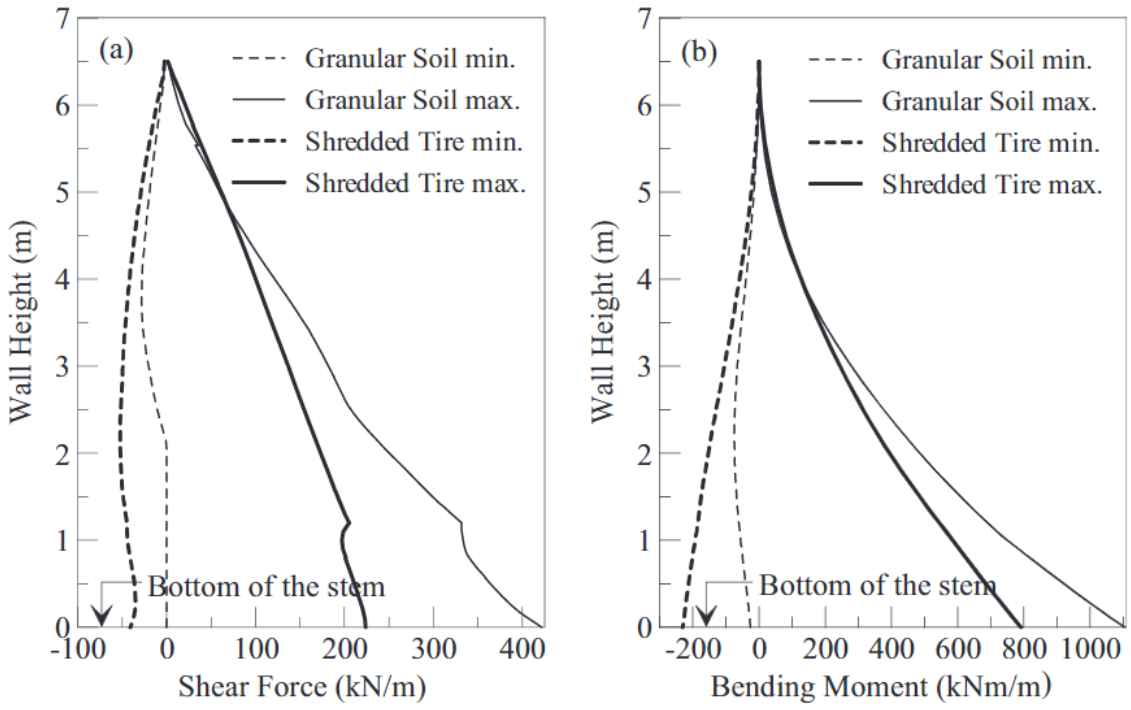

Figure 3.6. Comparison Of The Calculated Peak Shear Force (kN/m) And Bending Moment(kN.m/m) (Shrestha et al., 2016).

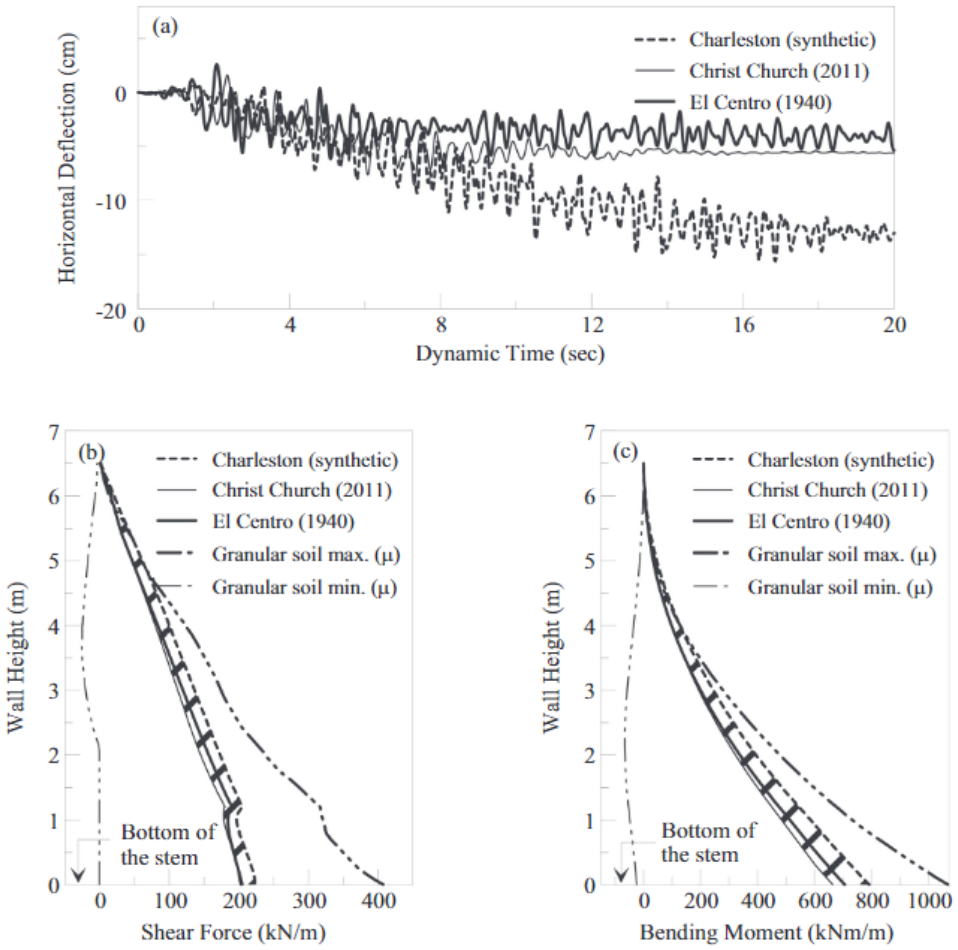

Figure 3.7. Effect Of Input Motion Parameters (a) The Horizontal Deflection (cm) Of The Wall Tip, (b) The Distribution Of Shear Force (kN/m) Along The Stem, And (c) The Distribution Of Bending Moment (kN.m/m) Along The Stem (Shrestha et al., 2016).

Edinçliler and Toksoy (2017) investigated the use of a cushion made of tire waste-sand mixture between the retaining wall and backfill under static loading and earthquake excitations based on a retaining wall model shown in Figure 3.8. Since tire waste is a lightweight material with high energy absorption properties, the application of the cushion proved to be efficient in terms of mitigating earthquake effects. Table 3.2 presents the results indicating that the method can reduce the axial stresses and shear stresses by about 21% and 17% respectively. Also, a reduction in lateral stresses under dynamic and static conditions is observed (Edinçliler & Toksoy, 2017).

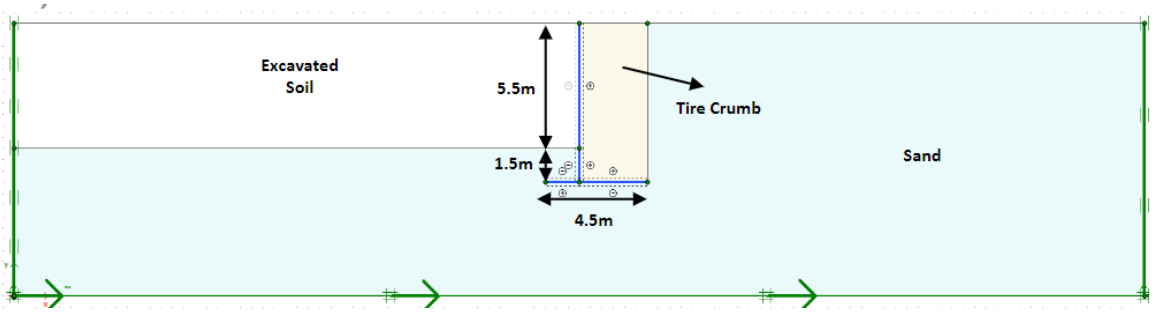

Figure 3.8. Cantilever Retaining Wall Model (Edinçliler & Toksoy, 2017).

Table 3.2. Summary Of The Numerical Results (Edinçliler & Toksoy, 2017).

	Static Case		El Centro Eqe.		Kobe Eqe.	
	Model 1	Model 2	Model 1	Model 2	Model 1	Model 2
Total Displacements (cm)	3.2	2.6	24.9	23.8	78.1	72.9
Rotation (°)	0.2	0.1	1.1	1.1	3.4	3.0
Axial Stress (kN/m)	167.2	158.8	200.8	189.1	242.4	192.3
Shear Stress (kN/m)	199.7	174.0	259.3	251.1	319.0	266.6
Bending Moment (kNm/m)	289.8	231.5	420.2	377.4	333.4	342.6

Edinçliler and Toksoy (2019) conducted a series of numerical analyses to understand the impact of the thickness of the geofoam cushion on the seismic performance of quay walls based on a quay wall model shown in Figure 3.9. Since such structures are at risk of earthquake-induced damages based on previous earthquakes, it is important to understand the impacts of improvement on the seismic resistance of these structures. The results summarized in Table 3.3 clearly state that the dynamic forces due to earthquake excitation acting on the rigid quay wall model were reduced by applying a geofoam cushion. Also, the transmitted peak accelerations were decreased up to a ratio of 84%. Another finding was that the thickness of the cushion had a positive effect on the reduction of the dynamic forces (Edinçliler & Toksoy, 2019).

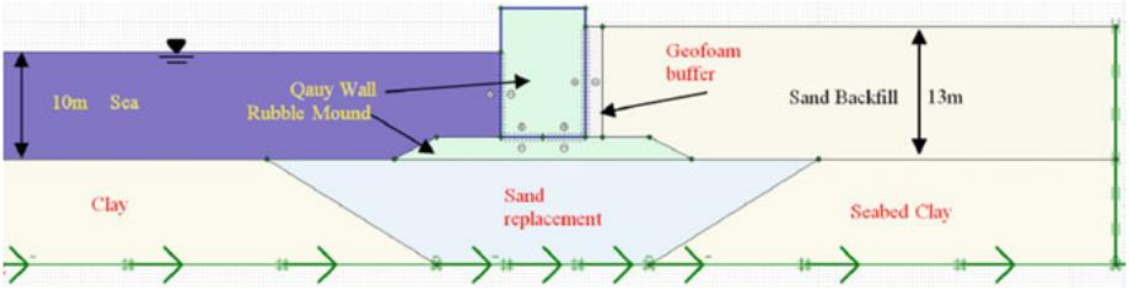

Figure 3.9. A Finite Element Model Of Proposed System (Edinçliler & Toksoy, 2019).

Table 3.3. Results Of Finite Element Analysis Under Earthquake Motions (Edinçliler & Toksoy, 2019).

	Kocaeli earthquake (0.23 g)			El Centro earthquake (0.36 g)		
	Model 1	Model 2	Model 3	Model 1	Model 2	Model 3
Total displacements (m)	0.90	1.12	1.10	0.89	0.97	0.96
Rotation (°)	1.34	2.14	2.22	1.35	1.76	1.90
Axial stress (kN/m)	470.8	457.1	462.8	493.5	494.9	495.9
Shear stress (kN/m)	433.9	423.3	423.0	453.7	443.4	440.8
Bending moment (kN/m)	1232	1204	1107	1171	1092	1078
Peak transmitted acceleration PGA (g)	2.35	0.82	0.38	1.06	0.91	0.43

Gade and Dasaka (2022) investigated the long- and short-term performance of geofoam reinforcement in decreasing lateral earth pressures on stiff retaining walls. Figure 3.10 shows the testing model used in the laboratory. Varying density and thickness values of geofoam material are used to understand these properties' effects on the behaviour of the cushion. Lateral earth pressures are decreased by geofoam cushion under repeating loading without regarding the density of the geofoam. The ratio of decrease in lateral earth pressure varies from 55.1% to 78.6% and the reduction is higher in long-term tests than in short-term tests (Gade & Dasaka, 2022).

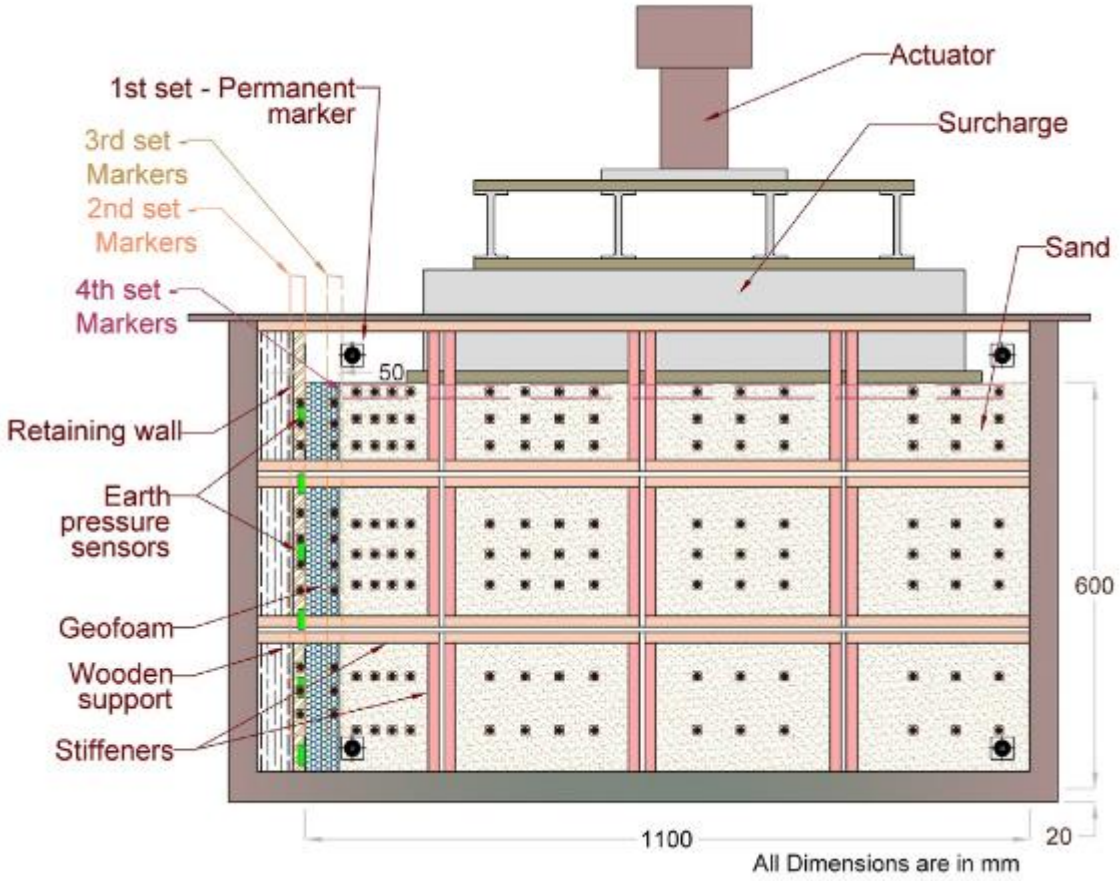

Figure 3.10. Set-Up Of Rigid Retaining Wall Model (Gade & Dasaka, 2022).

Another improvement method for retaining structures to mitigate earthquake effects is reinforcing the backfill with geosynthetics such as geotextile and geogrid. The inclusion of geosynthetics, especially geogrids, improves the assets of backfill soil. There are many studies in the literature focusing on various aspects of this improvement method.

Matsuo et al. (1998) did some laboratory tests on shaking table to examine the behaviour and the reinforcement mechanism of model retaining walls reinforced with geosynthetics. The height of the wall, the length of reinforcement, the wall-facing type, the wall slope, and ground motion acceleration were the variables considered in the study. The results showed that the improvement method brings safety in contradiction of failure for retaining structures. Based on the results of the study;

1. Wall deformation decreases with increasing ratio of the length of reinforcement to wall weight,
2. Earthquake-induced dislocations are governed by the main frequency of the input wave,
3. The sliding block method can potentially provide the permanent dislocation of geosynthetic-reinforced soil retaining walls (Matsuo et al., 1998).

El-Emam and Bathurst (2007) studied the effects of parameters of reinforcement such as length, stiffness, and vertical spacing for reinforced retaining walls using configurations and parameters shown in Table 3.4 and Figure 3.11. Outcomes of the shaking table tests given in Figure 3.12 showed that the size of lateral dislocation of the retaining structure under earthquake effects decreases with the increasing length of reinforcement, the stiffness of the reinforcement, and the number of reinforcement layers. The placement and kind of reinforcement had an impact on the size of the total earth force. Through increasing reinforcement length, the amplitude of acceleration amplification factors reduced, but it rose with increasing reinforcement vertical spacing. When the amplitude of the input base acceleration surpassed the critical acceleration value of each wall, the degree of amplification factors considerably increased (El-Emam & Bathurst, 2007).

Table 3.4. Configurations and Parameters for the Scaled Model (El-Emam & Bathurst, 2007).

Model number	Reinforcement			Facing thickness (mm)
	L/H	Stiffness J_m (kN/m)	Vertical spacing S_V (mm)	
1	1.0	90[a]	185	76
3	0.6	90[a]	185	76
8	0.6	90[a]	225	76
9	0.6	90[a]	225	38
13	0.6	1250[b]	225	38

Notes: L = reinforcement length; H = wall height = 1 m; J_m = reinforcement stiffness taken at 2% strain from wide-width strip tensile test (El-Emam and Bathurst, 2004).

[a]Type 1.

[b]Type 2.

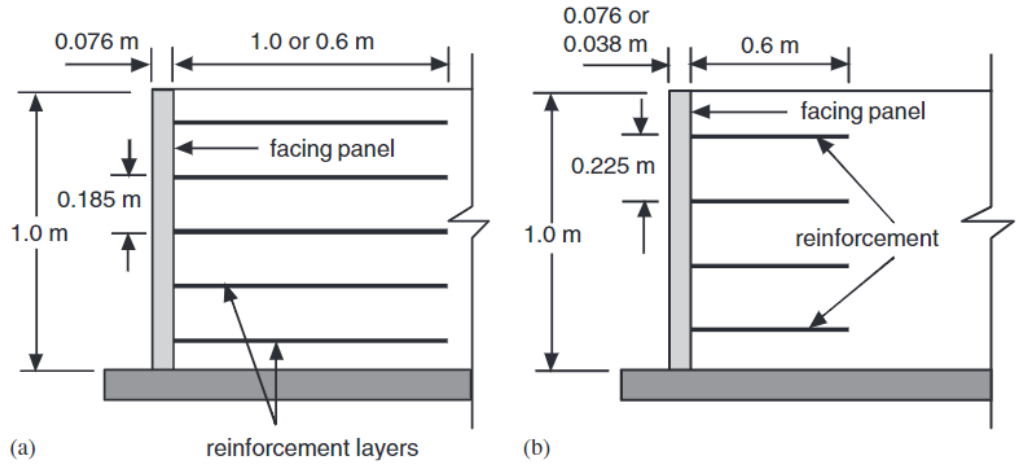

Figure 3.11. Reinforced Model Wall Configurations: (a) Walls 1 And 3, (b) Walls 8, 9, and 13 (El-Emam & Bathurst, 2007).

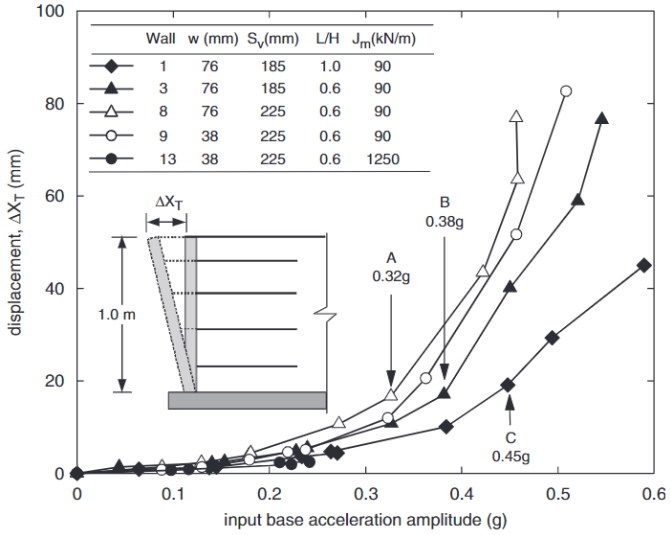

Figure 3.12. Influence Of Reinforcement Properties On The Measured Displacement On Top Of The Wall-Facing Panel Versus The Maximum Acceleration Amplitude At The Base (El-Emam & Bathurst, 2007).

Güler et al. (2012) investigated the impacts of several parameters such as type of facing, type of backfill, reinforcement stiffness, and peak ground acceleration on the seismic performance of reinforced soil retaining walls. The outcomes of the study are summarized in Figures 3.13 and 3.14. It was observed that deformation and reinforcement tensile loads increased during the cyclic loading. It was also noted that deformation induced by cyclic loading is associated with these parameters. The wall's movement was limited by the use of stronger reinforcement. But using stronger reinforcement enlarged the tensile stresses on the reinforcement. The dynamic performance of the walls was significantly influenced by the peak acceleration of the ground. The horizontal wall movements were more than twice when the peak ground acceleration was doubled. This shows that the movements of an earthquake-resistant reinforced soil wall are not linearly connected to the earthquake's peak acceleration (Guler et al., 2012).

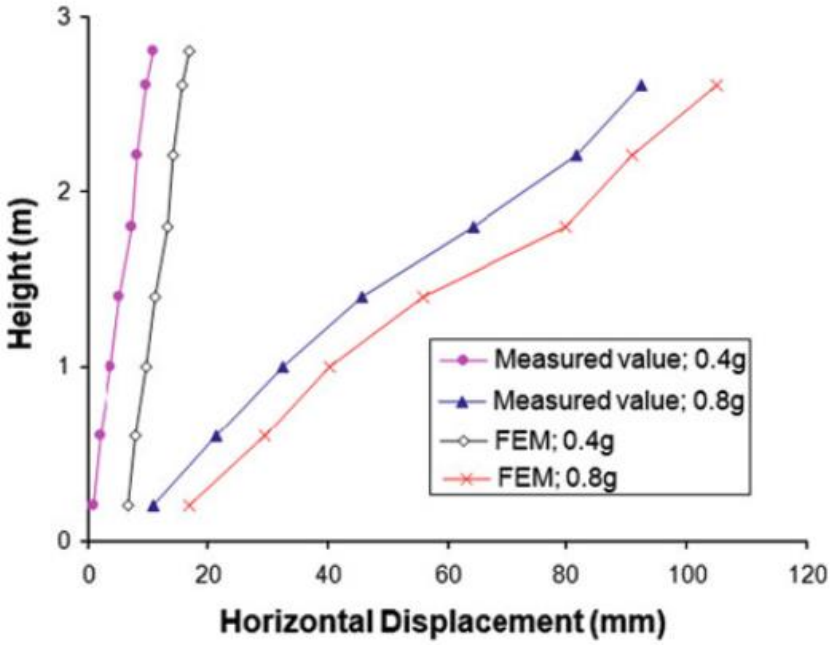

Figure 3.13. Horizontal Displacements For Accelerations Of 0.4 g And 0.8 g (Guler et al., 2012).

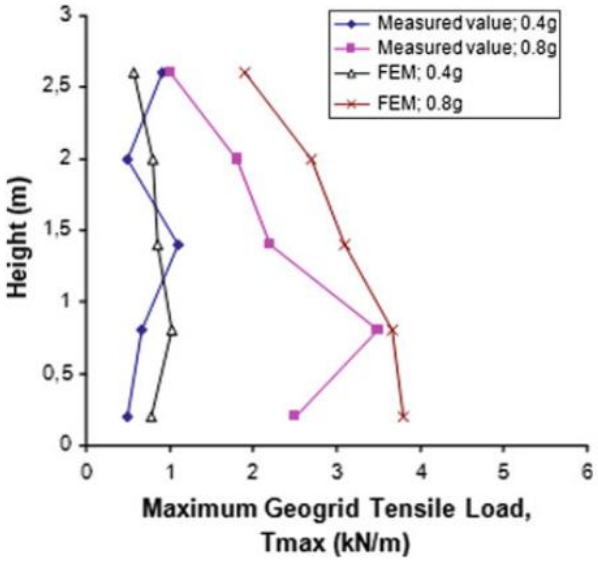

Figure 3.14. Maximum Geogrid Tensile Loads Along Wall Height (Guler et al., 2012).

Yang et al. (2012) monitored a retaining wall reinforced with geogrids having lime-treated cohesive soil as backfill to understand the behaviour of the reinforcement method concerning the time as seen in Figure 3.15. Based on their observations;

1. Under working stress conditions, lime-treated backfill soil regulated the wall's response, and backfill distortion was largely flexible; geogrid reinforcements played a secondary role under gravity loading,
2. The reinforcing impact was demonstrated to be minimal under gravity loading, but it may be greater under severe stress, such as earthquakes (Yang et al., 2012).

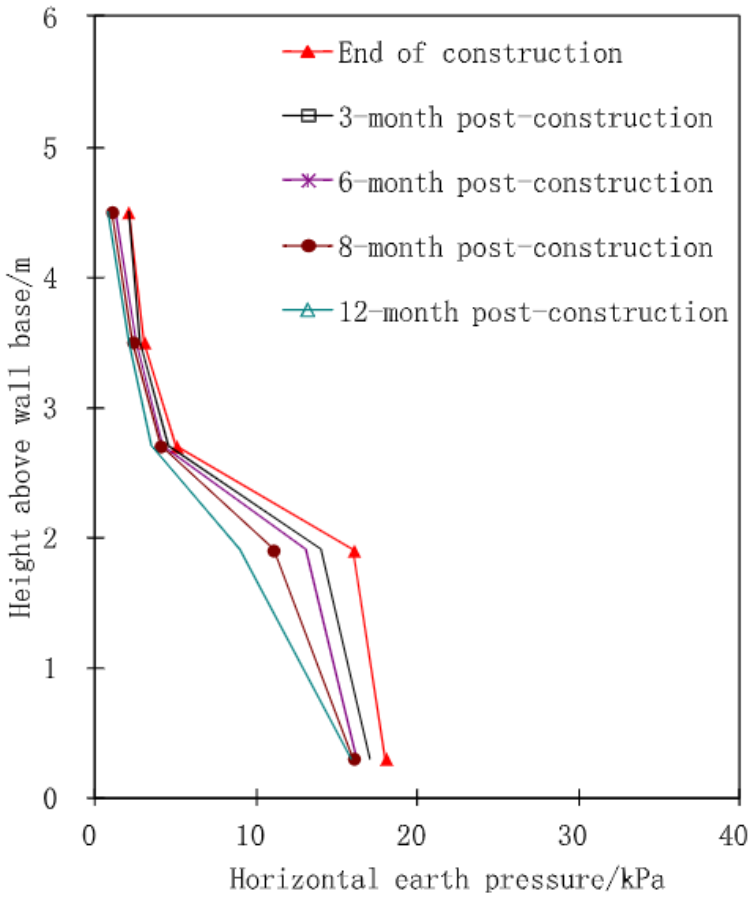

Figure 3.15. Distribution Of Lateral Earth Pressure At The End Of And Post Construction (Yang et al., 2012).

In 2015, Wang and colleagues conducted an experiment to investigate how geogrid-reinforced stiff retaining walls with saturated backfill respond to seismic activity. They used a large laminar shear container that allowed them to test both reinforced and unreinforced models simultaneously by shaking them on a table. Their findings showed that seismic waves from the far field had a greater effect on the seismic performance of the reinforced retaining wall compared to those from the near field. The use of geogrid reinforcement prevented the occurrence of liquefaction and increased the wall's resistance to deformation caused by seismic activity (Wang et al., 2015).

Başbuğ et al. (2021) studied the effects of several limitations such as reinforcement arrangements and backfill material using large-scale geosynthetic reinforced retaining walls under seismic loading. The results summarized in Figure 3.16 showed that the stiffness of the reinforcement is the key element in controlling the reduction of reinforcement strain under seismic loading conditions. The reinforcement's length had little impact on reducing the strain requirement on the reinforcement. Also, it is noted that for input movements with magnitudes greater than the critical acceleration, there was a more noticeable increase in soil amplification. Soil amplification in this investigation was amplitude dependent. Additionally, the reinforced soil segment's soil amplification values were lower than those of the unreinforced backfill part (Başbuğ et al., 2021).

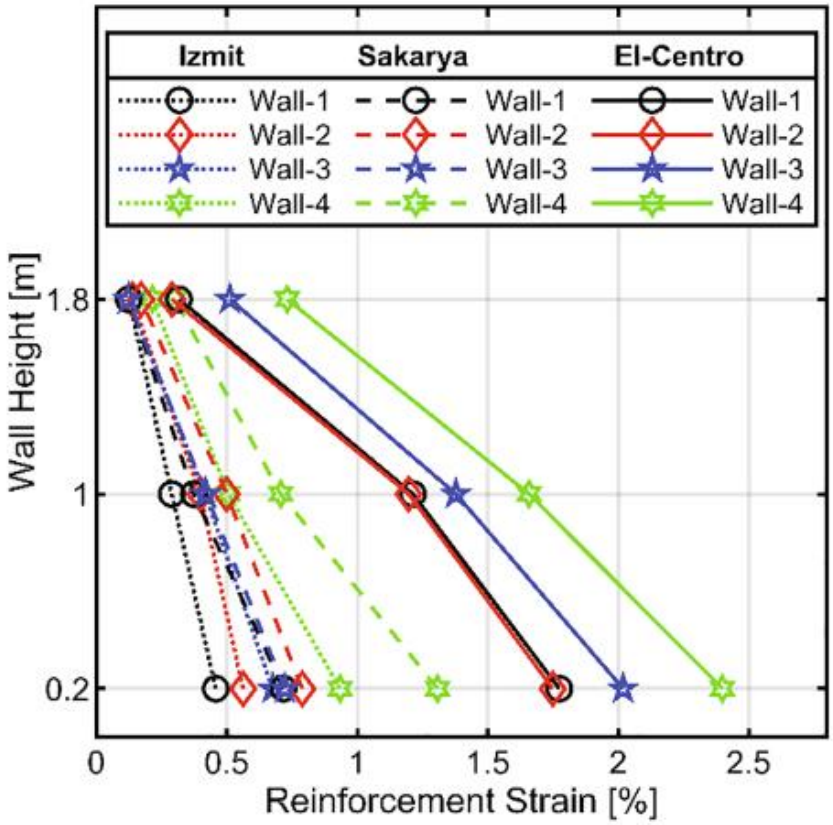

Figure 3.16. Maximum Tensile Strains Measured In The Reinforcements Under 200% Izmit, Sakarya, And El Centro Earthquake Inputs (Başbuğ et al., 2021).

Cai et al. (2021) used a reduced-scale geogrid-reinforced retaining wall to conduct a series of shaking table tests. The objective of the research was to examine how acceleration amplification, backfill surface settlement, fundamental frequency, and reinforcement strain respond to changes in peak accelerations and durations in terms of seismic performance. The results showed that the settlement of the backfill was negligibly small under base excitations smaller than 0.4 g. The findings demonstrate that when peak acceleration increases in magnitude across all reinforcing layers, incremental peak stresses also rise. Due to the core layers being subjected to greater peak forces during the earthquake waves, the central layers suffered greater incremental peak strains than the others. Figures 3.17 and 3.18 show the distribution of settlement values obtained during the study while Figures 3.19 and 3.20 show the distribution of obtained peak strains (Cai et al., 2021).

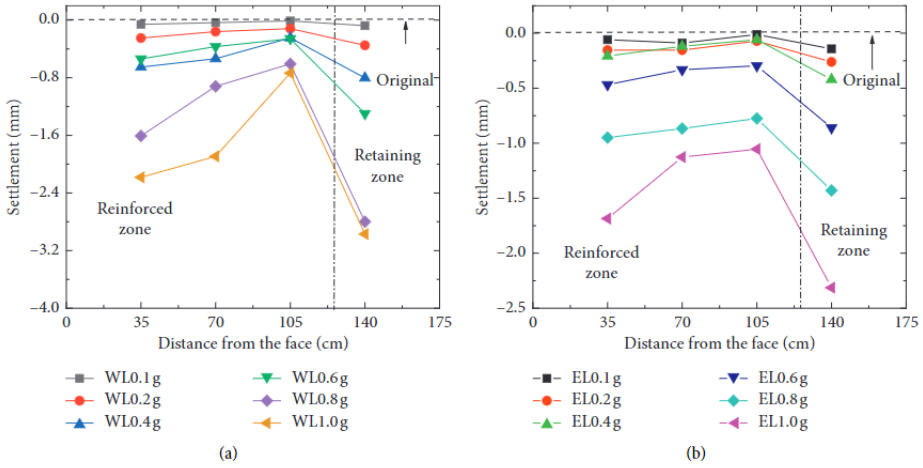

Figure 3.17. Distribution Of Settlement (Scale Factor:1/4): (a) Wolong Station Of The 2008 Wenchuan Earthquake (WL) And (b) El Centro Station Of The 1940 Imperial Valley Earthquake (EL) (Cai et al., 2021).

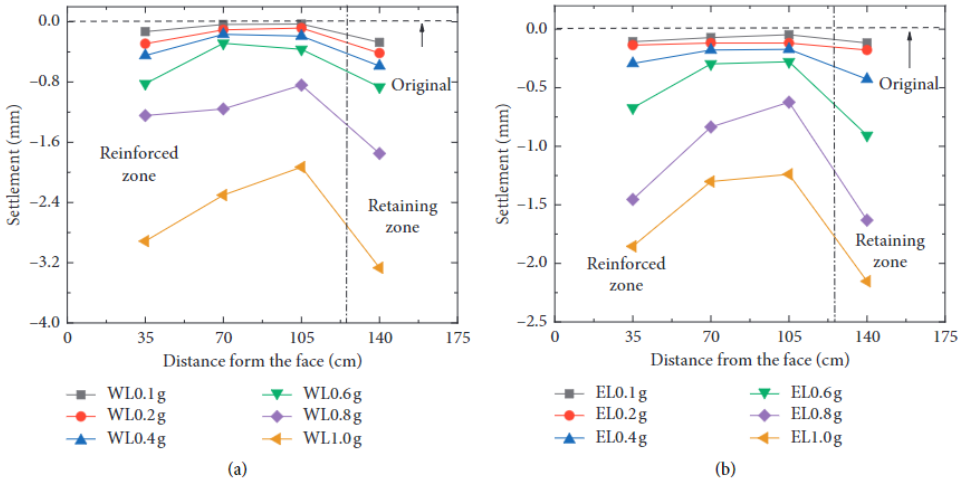

Figure 3.18. Distribution Of Settlement (Scale Factor:1/2): (a) Wolong Station Of The 2008 Wenchuan Earthquake (WL) And (b) El Centro Station Of The 1940 Imperial Valley Earthquake (EL) (Cai et al., 2021).

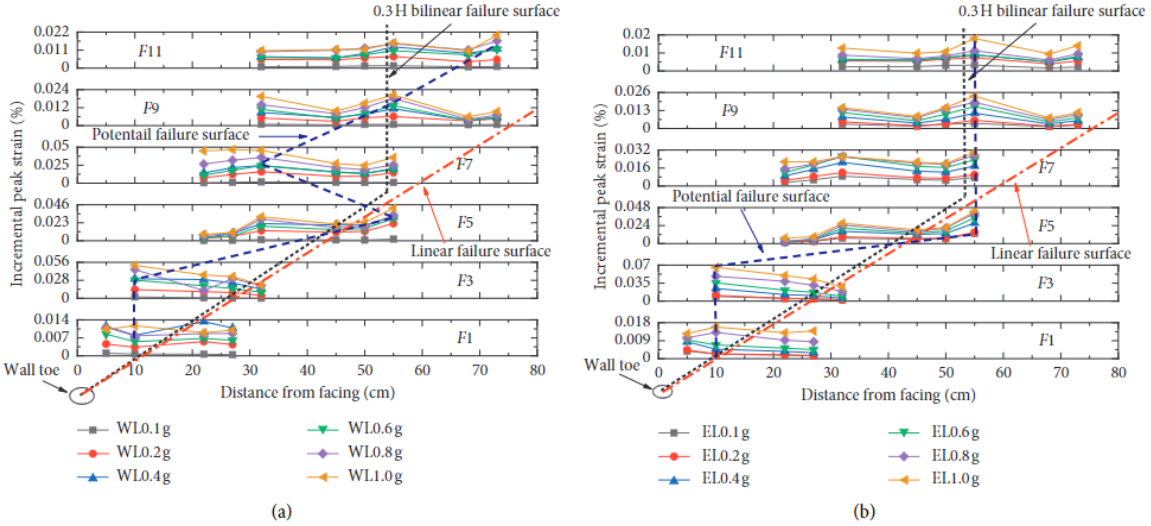

Figure 3.19. Distribution Of The Recorded Peak Strain (Scale Factor:1/4): (a) Wolong Station Of The 2008 Wenchuan Earthquake (WL) And (b) El Centro Station Of The 1940 Imperial Valley Earthquake (EL) (Cai et al., 2021).

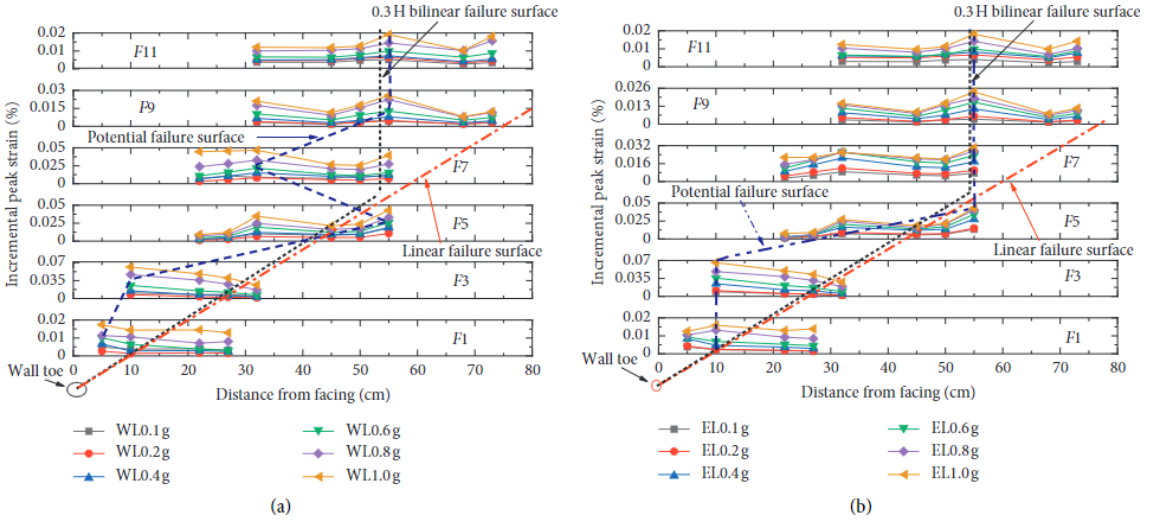

Figure 3.20. Distributions Of The Recorded Peak Strain (Scale Factor:1/2): (a) Wolong Station Of The 2008 Wenchuan Earthquake (WL) And (b) El Centro Station Of The 1940 Imperial Valley Earthquake (EL) (Cai et al., 2021).

Kılıç et al. (2021) investigated the effects of the type of backfill, length of reinforcement, and stiffness of reinforcement using two different scale factors of ½ and ¼. Details of model walls used in the study are summarized in Table 3.5. The model walls were put through a lot of shaking, yet they showed no symptoms of instability or approaching failure. The cohesive backfill models showed peak distortions that were less than half of the distortions observed in the sand model. Despite the similarity in load transmissions between the geogrid and cohesive soil and the sand and soil, the same length of reinforcement was necessary. When compared to their granular backfilled counterparts, the cohesive backfilled model walls performed within acceptable bounds under seismic stress circumstances. The relative displacements along the wall height under dynamic excitations are given in Figure 3.21 (Kilic et al., 2021).

Table 3.5. Properties Of Wall Model For The Shaking Table Tests (Kilic et al., 2021).

Setup #	Scale Ratio	Dimensions			Backfill Type	L/H	S_v (cm)
		Height (cm)	Width (cm)	Depth (cm)			
Setup 1	½	190	50	280	Sand	0.8	20
Setup 2	½	190	50	280	K30S70	0.8	20
Setup 3	½	190	50	280	K30S70	0.6	20
Setup 4	¼	95	50	140	K30S70	0.8	10

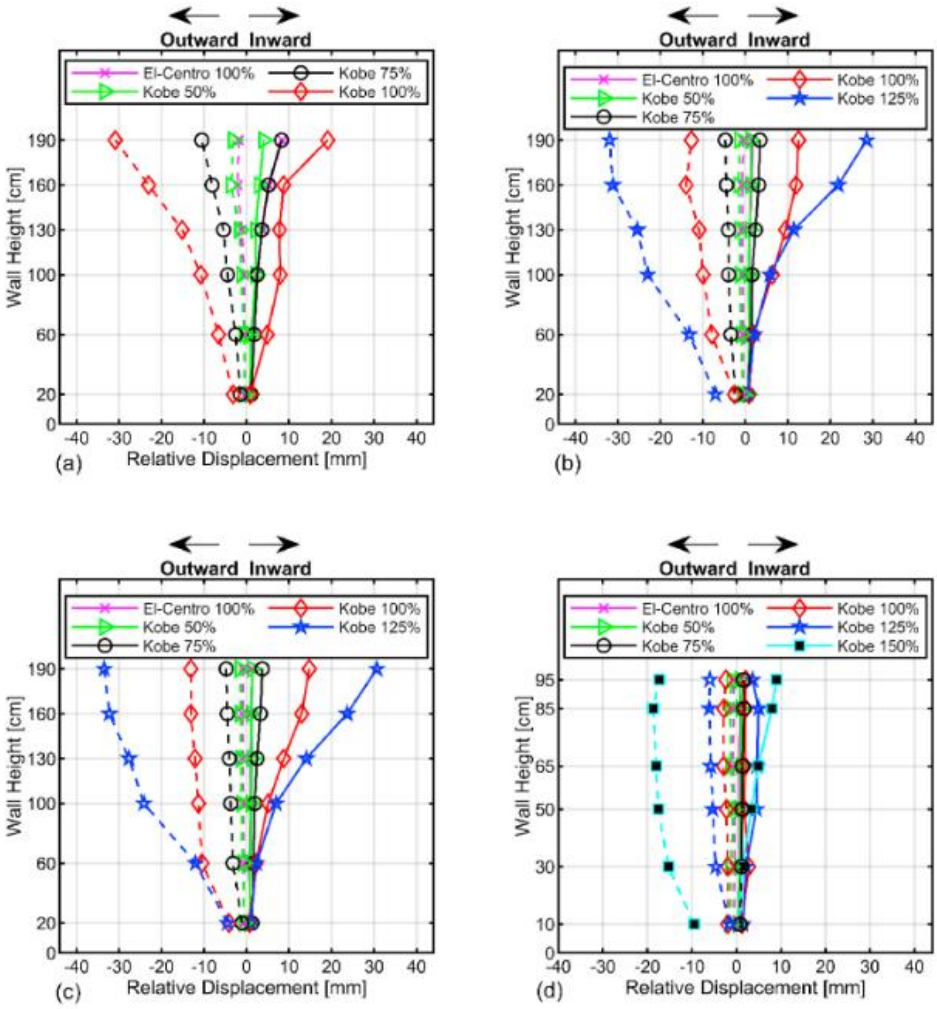

Figure 3.21. Peak Relative Displacement Along The Wall Height; (a) Setup 1, (b) Setup 2, (c) Setup 3, And (d) Setup 4 (Kilic et al., 2021).

4. GEOGRID-REINFORCED SOIL FOUNDATIONS

4.1. Introduction

Construction on soft soils which are susceptible to earthquake hazards has been an obstacle for engineers to overcome. When challenging site conditions are encountered, the main approaches to deal with the situation are: avoiding the site if possible, designing the structure accordingly, replacing the unsuitable soil if possible, and modifying the soil. Since the earlier approaches get more and more challenging in terms of technical applicability and financial sustainability due to increased urban and industrial development, therefore; alternative improvement methods for soils to mitigate earthquake effects have been developed for years. These modification techniques can be classified as mechanical alteration, hydraulic alteration, physical and chemical alteration, and alteration by inclusions and confinement. One of the latest approaches in modification by inclusions and confinement is using geosynthetics to improve various properties of soil in a range from drainage to tensile strength (Hausmann, 1989).

4.2. Geosynthetics

A geosynthetic is a two-dimensional product composed of polymeric material that is utilized in combination with other geotechnical engineering constituents as an integrated part of a system. The main reasons for using geosynthetic materials in soils are separation, purification, reinforcement, drainage, and control along with advantages like improving the performance of soil, reducing initial cost, providing longer service time and low-cost maintenance (D4439 - 20: Standard Terminology For Geosynthetics, 2020; Koerner, 2012).

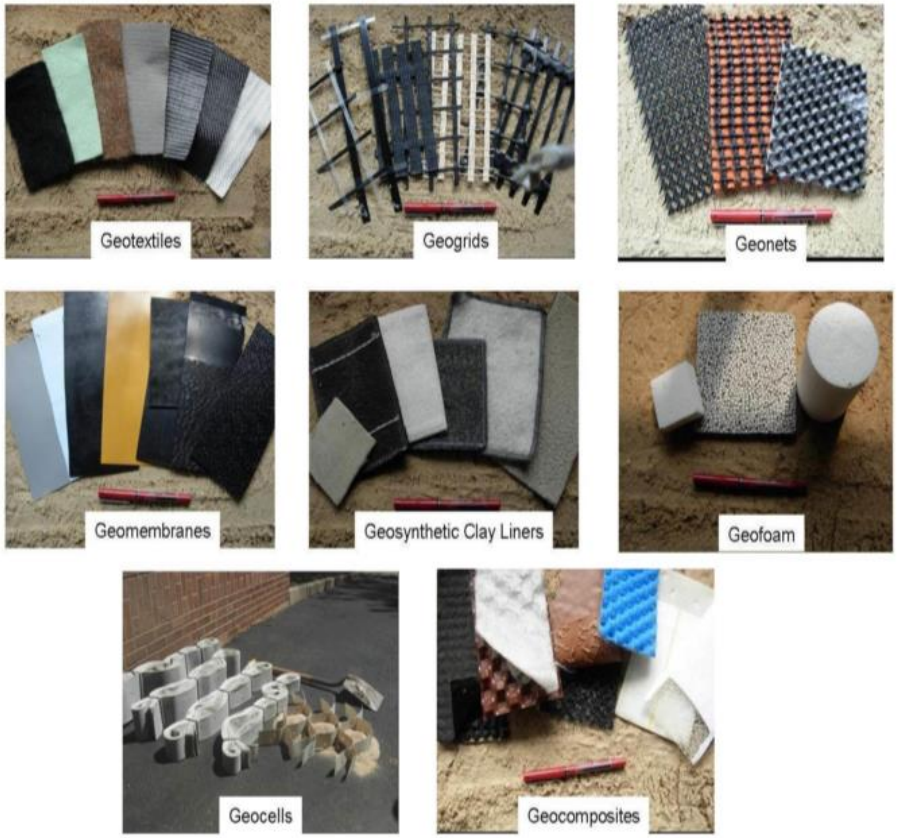

Figure 4.1. Overview Of Geosynthetic Categories (Koerner, 2012).

There are eight types of geosynthetics as shown in Figure 4.1, used according to the aim of soil improvement. Geotextiles are porous fabrics consisting of synthetic fibres and they are primarily used for drainage, purification, reinforcement, and separation. Geogrids are geosynthetics made up of a uniform grid of integrally connected components with openings large enough to allow interlocking with other materials and they are mainly used for reinforcement. Geonets are geosynthetics composed of parallel sets of integrally connected ribs covering similar sets at varied angles enabling planar drainage of gases or liquids. Geomembranes are impervious polymeric sheets that are typically utilized for the covers and linings of liquid or solid-storage facilities. Their application in geotechnical and transportation fields is expanding, as is their application in environmental fields. Geosynthetic clay liners (GCLs) are rolls of pre-fabricated tinny layers of bentonite clay squeezed in between two geotextiles or attached to a geomembrane. Geofoam is a polymeric expansion process product that is typically in the shape of big, yet light, blocks that provide lightweight fill in a variety of applications. Geocells shown in Figures 4.1 and 4.2 are

produced in the form of a network of connected strips that when opened, form a network of open cells. Geocomposites are composed of a combination of geosynthetic elements in a factory-fabricated unit, and they accomplish all of the functions previously described for geosynthetics (D4439 - 20: Standard Terminology For Geosynthetics, 2020; D8269-21: Standard Guide For The Use Of Geocells In Geotechnical And Roadway Projects 1, 2021; Koerner, 2012).

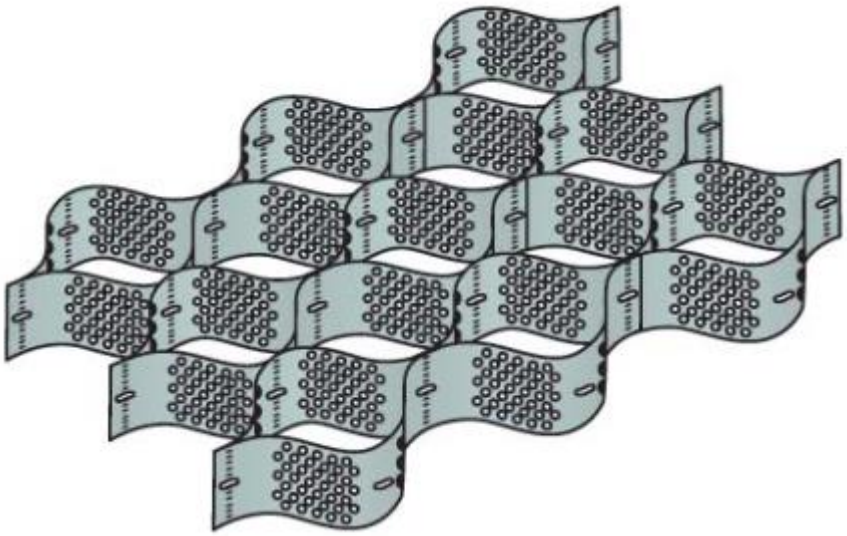

Figure 4.2. 3D View Of Geocells (D8269-21: Standard Guide For The Use Of Geocells In Geotechnical And Roadway Projects 1, 2021).

4.3. Geogrid-Reinforced Soil Foundations

The fundamental resolution of reinforcing a soil mass is to strengthen its steadiness, rise its bearing capacity, and lessen deformation and displacement. As explained in the earlier sections, insufficient soil properties play a huge part in the failure of the retaining walls. Modification of backfill soil using geosynthetics has been used and is being altered for years. Such improvements have proven that the geosynthetic reinforcement approach is effective and applicable to minimize the effects of earthquake-induced liquefaction, dynamic forces, and settlement at the backside of the wall.

Omar et al. (1993) investigated the influence of geogrid reinforcement on the ultimate bearing capacity of the soil. In this study, several variables such as the width of the reinforcement, the depth of the first layer of the reinforcement, and the number of reinforcement layers (***N***) are compared for square and strip footings. Figure 4.3 shows the schematic view of the test cases. The results show that

1. For square foundations and strip foundations, the effective depth of reinforcement is approximately ***1.4B*** and ***2B***, respectively, for the development of maximum bearing capacity where ***B*** is the width of the foundation.
2. For strip foundations and square foundations, respectively, the maximum width of reinforcing layers needed to mobilize the ultimate bearing-capacity ratio is ***8B*** and ***4.5B***.
3. To benefit from reinforcement, the first layer of reinforcement should not be placed deeper than approximately ***B*** (Omar et al., 1993).

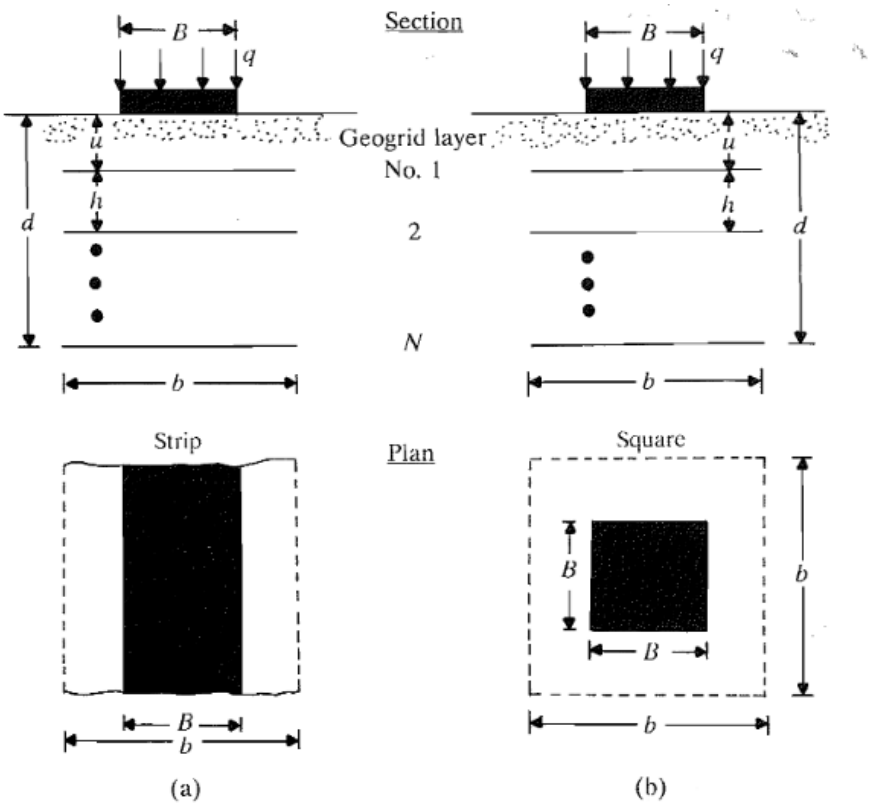

Figure 4.3. Square And Strip Foundations Supported By Sand Reinforced With Layers Of Geogrid. ***q***, load per unit area (Omar et al., 1993).

An alike study was conducted by Shin et al. (1993) for strip footings on clayey soil as shown in Figure 4.4. Several laboratory tests were completed to determine the critical values of reinforcement geometry. The findings of the study are:

1. The depth of reinforcement that contributes to the enhancement in the bearing capacity ratio of the foundation is approximately 1.8 times the width of the foundation when measured from the bottom.
2. For the greatest advantage, it is best to place the first layer of geogrid about 0.4 times the width of the foundation below the bottom of the foundation.
3. The width of the geogrid layers that contributes most to the increase in the ultimate bearing capacity is typically between 4.5 and 5 times the width of the foundation (Shin et al., 1993).

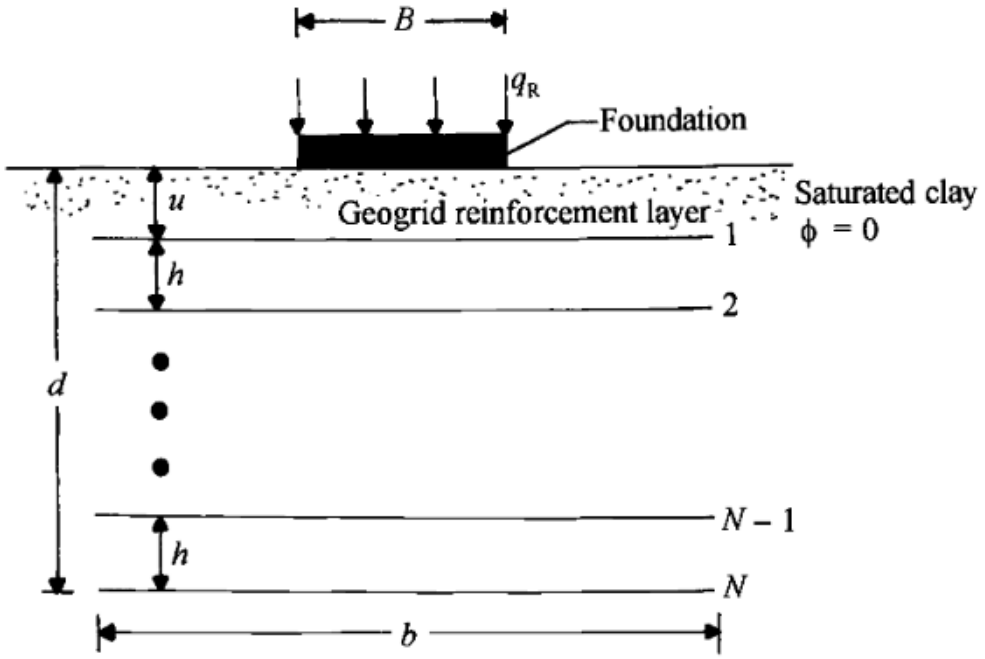

Figure 4.4. Strip Foundation On Geogrid-Reinforced Clay (Shin et al., 1993).

Das et al. (1993) conducts a series of laboratory tests to investigate the effect of geogrid reinforcement on the sand and the saturated clay. A comparison of the results is used to determine the optimum geometry of reinforcement. Based on the results, the magnitude of $\boldsymbol{BCR_{max}}$ achieved during the tests is 4.25-4.5 for sand and about 1.5 for clay when the geogrid reinforcement is placed with optimum values of ***d/B***, ***b/B***, and ***u/B*** while ***h/B=1/3*** where ***d*** is the depth of the reinforcement zone, ***b*** is the length of the reinforcement, ***u*** is the depth of the first reinforcement layer, and ***h*** is the distance between each reinforcement layer. Table 4.1 summarizes the testing cases and varying parameters while Figure 4.5 presents the results of the study in terms of ***BCR*** values concerning the ***d/B*** series. The other findings of the study are:

1. Geogrid reinforcement on clay does not provide any improvement in terms of settlement of strip foundation at ultimate load.

2. The optimum value of the total depth of reinforcement for ultimate bearing capacity is about ***2B*** and ***1.75B*** in sand and clay respectively.
3. The depth of the first reinforcement layer should not exceed ***0.4B*** to achieve the maximum benefit.
4. Maximum bearing capacity ratio (***BCR_{max}***) is obtained when the optimum width values of ***8B*** and ***5B*** are used in sand and clay respectively.
5. Geogrid reinforcement is more effective in the sand than clay in terms of maximum bearing capacity under the same reinforcement parameters (Das et al., 1994).

Table 4.1. Details of Laboratory-Model Test (Das et al., 1994).

Series	Variable parameter	Constant parameter	Remarks
A/S	–	–	Tests on unreinforced sand
A/C	–	–	Tests on unreinforced clay
B/S	N (i.e. d/B)	$u/B=h/B=1/3$, $b/B=10$	Tests on reinforced sand to determine $(d/B)_0$
B/C	N (i.e. d/B)	$u/B=0.4$, $h/B=1/3$, $b/B=4$	Tests on reinforced clay to determine $(d/B)_0$
C/S	b/B	$u/B=h/B=1/3$, $N=6$	Tests on reinforced sand to determine $(b/B)_0$
C/C	b/B	$u/B=0.4$, $h/B=1/3$, $N=4$	Tests on reinforced clay to determine $(b/B)_0$
D/S	u/B	$h/B=1/3$, $b/B=8$, $N=6$	Tests on reinforced sand to determine $(u/B)_0$ and $(u/B)_1$
D/C	u/B	$h/B=1/3$, $b/B=8$, $N=4$	Tests on reinforced clay to determine $(u/B)_0$ and $(u/B)_1$

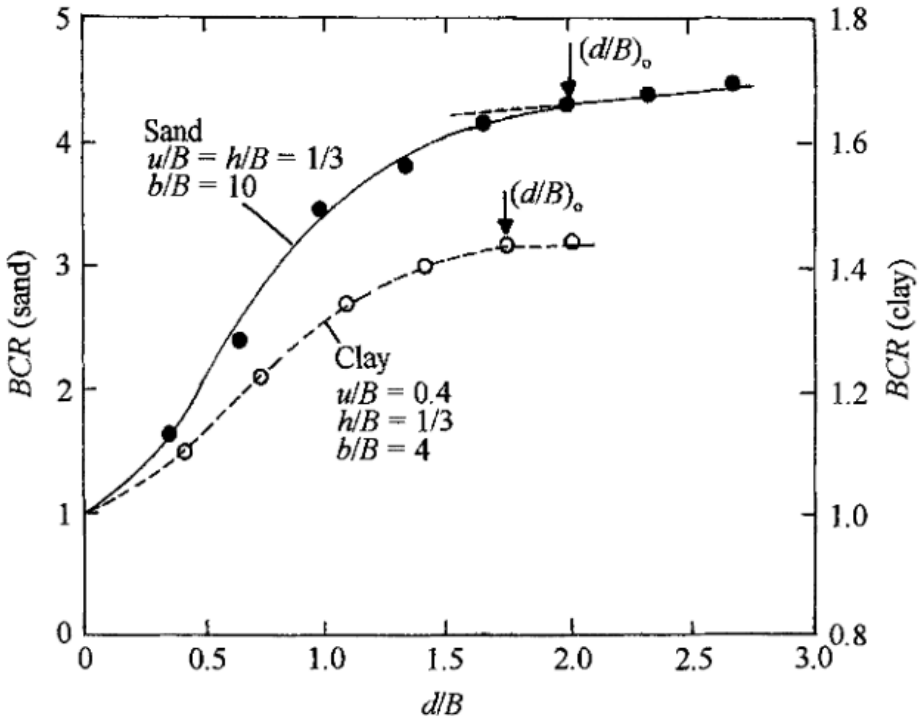

Figure 4.5. Changing Of BCR with d/B (Das et al., 1994).

Das and Omar (1994) completed laboratory tests using strip footing models with various foundation widths to inspect the impacts of the width of the foundation and the relative density of the soil on the bearing capacity of geogrid-reinforced soil. The values of relative densities (D_r) vary from 55% to 75%. The results show that for a given value of D_r, the ***BCR*** decreases as ***B*** increases; and for a given value of ***B***, the ***BCR*** increase as D_r decreases as seen in Figures 4.6 and 4.7. Lastly, the ***BCR*** reaches a limit value as the width of the footing reaches 140 mm for all relative densities (Das & Omar, 1994).

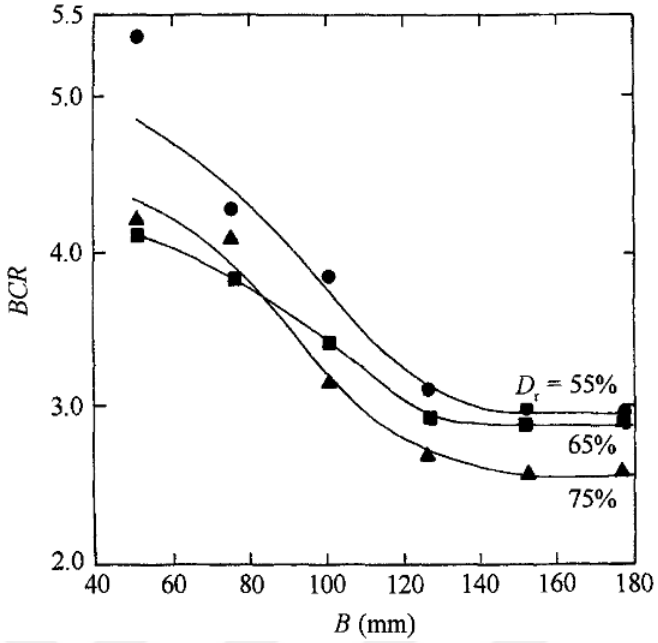

Figure 4.6. Variation Of Bearing Capacity Ratio With Foundation Width B (Das & Omar, 1994).

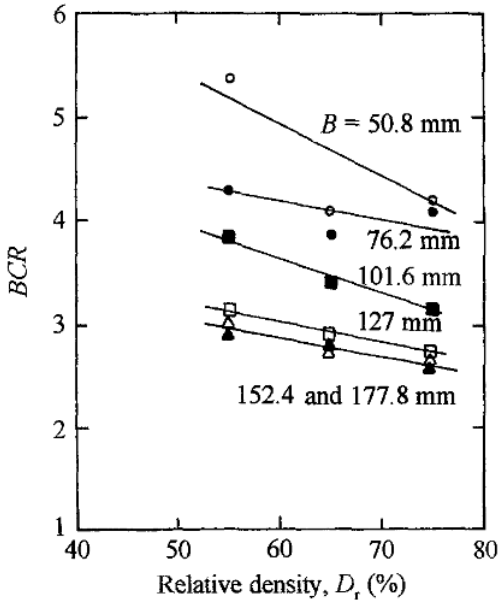

Figure 4.7. Variation Of Bearing Capacity Ratio With Relative Density (Das & Omar, 1994).

Shin and Das (2000) studied the effects of the depth of foundation on strip footings placed on geogrid-reinforced sand as shown in Figure 4.8. In the model tests, the depth of foundation ($\boldsymbol{D_f}$) varies from ***0*** to ***0.75B***. According to the test results given in Figure 4.9, the bearing capacity ratio increases with an increasing value of $\boldsymbol{D_f}$, the depth of the foundation (Shin & Das, 2000).

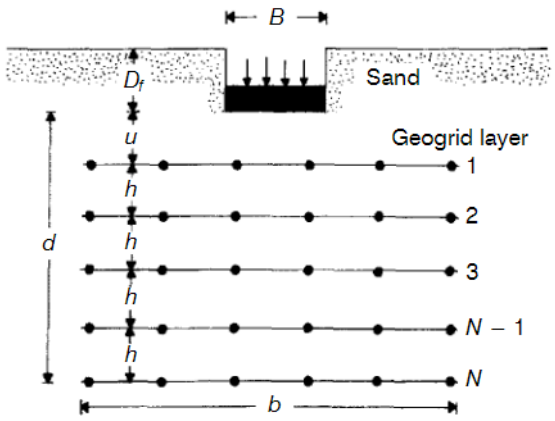

Figure 4.8. Strip Foundation On Sand Reinforced With Geogrid (Shin & Das, 2000).

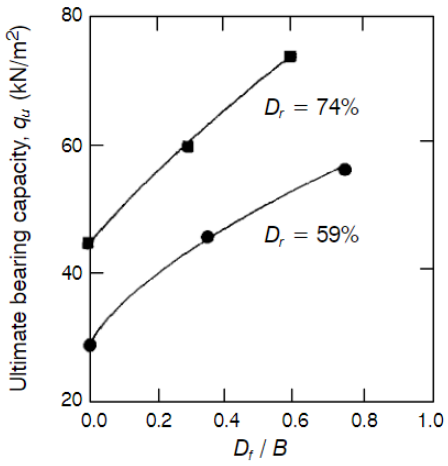

Figure 4.9. Ultimate Bearing Capacity Versus D_f/B (Shin & Das, 2000).

Santhakumar et al. (2001) conclude small-scale laboratory tests using a square plate to understand the dynamic behaviour of geogrid-reinforced soil. Dynamic loads of varying frequencies with a limited displacement of 2 mm are used. The findings of the study which are also given in Table 4.2 can be summarized as:

1. Dynamic bearing capacity of the soil rises with the increasing number of reinforcement layers by 200%, 250%, and 230% at frequencies of 0.2 Hz, 0.6 Hz, and 1.0 Hz respectively.
2. The optimal value of depth of the first layer (***u***) is determined as ***0.25B*** (Santhakumar et al., 2001).

Table 4.2. Dynamic Bearing Capacity Ratio (Santhakumar et al., 2001).

Sr.No.	N	u/B	Δz/B	h/B	f(Hz)	DBCR
1	1	0.25	-	3	0.2	1.1
2	1	0.35	-	3	0.2	1.1
3	4	0.25	0.25	3	0.2	3.0
4	4	0.35	0.35	3	0.2	2.5
5	1	0.25	-	3	0.6	1.7
6	2	0.25	0.25	3	0.6	2.4
7	4	0.25	0.25	3	0.6	3.5
8	1	0.25	-	3	1.0	1.8
9	1	0.35	-	3	1.0	1.7
10	4	0.25	0.25	3	1.0	3.3

Patra et al. (2005) concluded laboratory tests shown in Table 4.3 on sand reinforced with geogrid to understand the effectivity of embedment depth for strip footings on reinforced soil. A uniaxial geogrid with a maximum tensile strength of 60 kN/m is used as reinforcement with the parameters of $\boldsymbol{u/B}$=0.35, $\boldsymbol{h/B}$=0.25, and $\boldsymbol{b/B}$=5. The results are compared by a proposed theory. The findings of the study are given in Figures 4.10 to 4.12. The results show that ultimate bearing capacity increases as do the embedment ratio ($\boldsymbol{D_f/B}$) and the proposed theory provides conservative predictions compared to the laboratory tests (Patra et al., 2005).

Table 4.3. Details Of Model Tests (Patra et al., 2005).

Test series	N	u/B	h/B	b/B	d_f/B
A	0	—	—	—	0–1.0 (unreinforced sand)
B	2, 3, 4	0.35	0.25	5	0
C	4	0.35	0.25	5	0, 0.25, 0.5, 0.75, 1.0

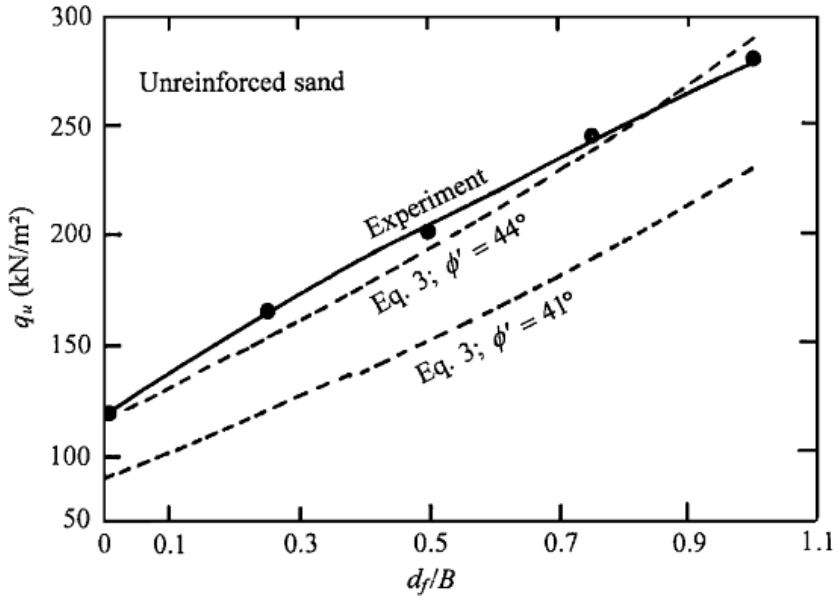

Figure 4.10. Ultimate Bearing Capacity Versus d_f/B (Series A) (Patra et al., 2005).

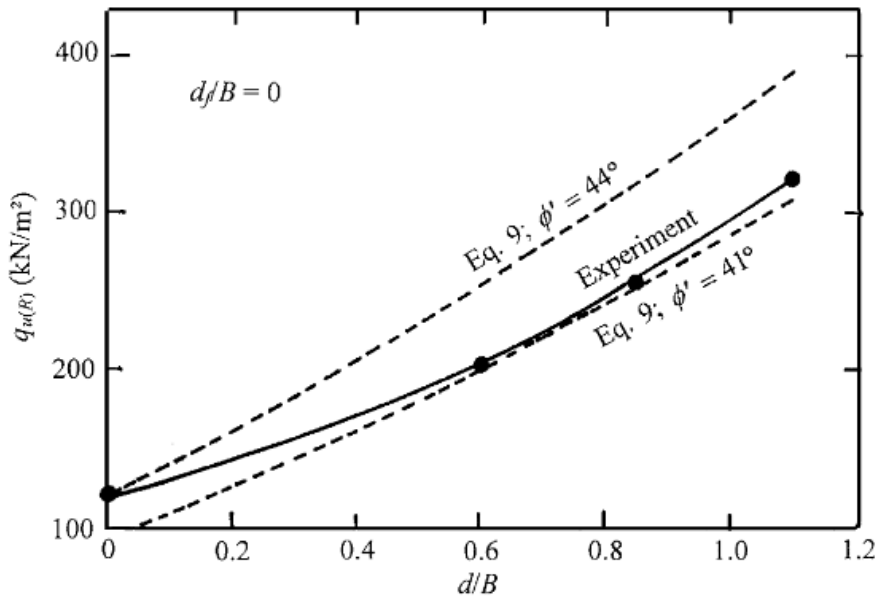

Figure 4.11. Reinforced Ultimate Bearing Capacity Versus d/B For Surface Foundation (Series B) (Patra et al., 2005).

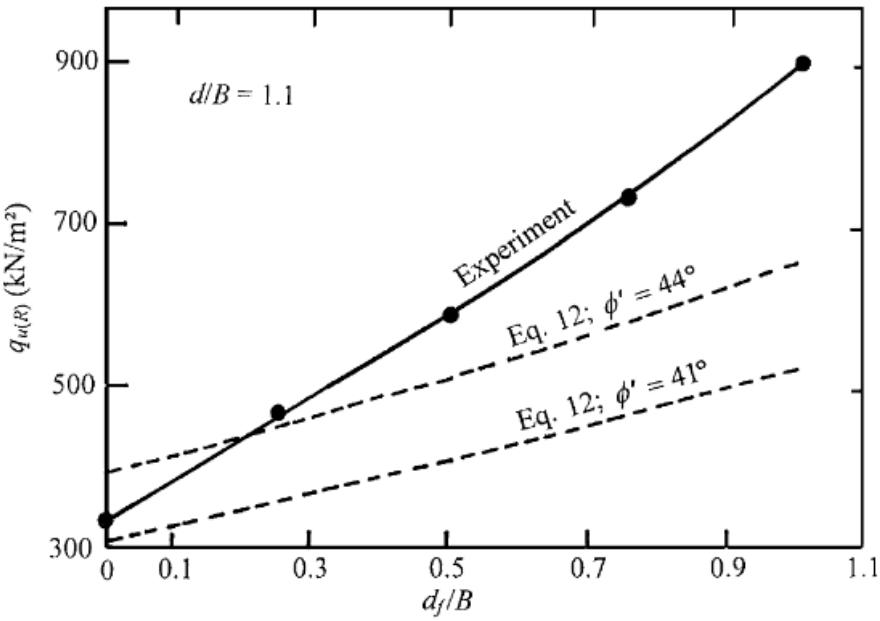

Figure 4.12. Reinforced Ultimate Bearing Capacity Versus d_f/B For d/B=1.1 For Surface Foundation (Series C) (Patra et al., 2005).

Patra et al. (2006) conducted some laboratory model tests for strip footings on geogrid-reinforced soil as shown in Figure 4.13. Geometrical reinforcement parameters used for model tests are $\boldsymbol{u/B}$=0.35, $\boldsymbol{h/B}$=0.25, and $\boldsymbol{b/B}$=5. The variables in the study are depth of foundation (embedment ratio, $\boldsymbol{D_f/B}$) and location of load (eccentricity ratio, $\boldsymbol{e/B}$). The findings show that the bearing capacity of the ratio of eccentrically loaded foundations to centrally loaded foundations depends on a reduction factor which can be explained as a function of the eccentricity ratio and embedment ratio (Patra et al., 2006).

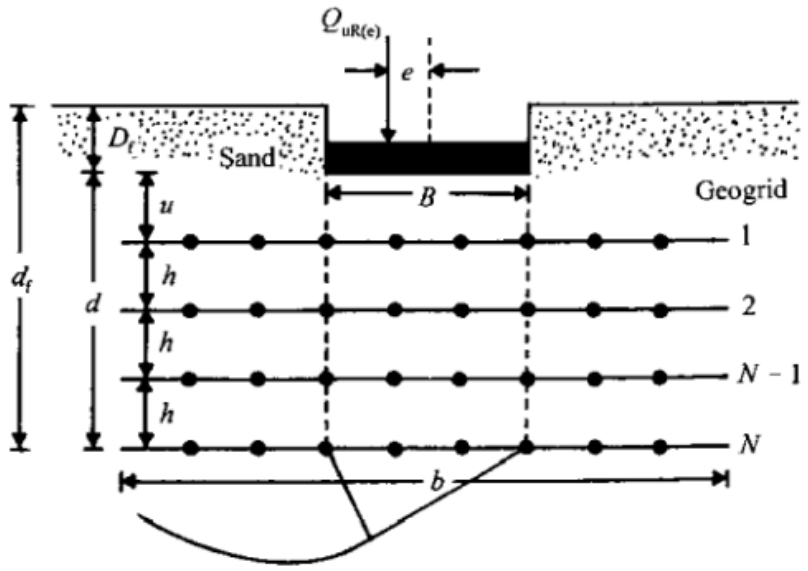

Figure 4.13. Assumed Failure Mode Under An Eccentrically Loaded Strip Foundation On Geogrid-Reinforced Sand (Patra et al., 2006).

Sharma et al. (2009) review the existing analytical solutions and experimental studies in the literature to bring up an analytical solution that can represent the effect of reinforcement as well as several other design parameters in the bearing capacity of the reinforced soil foundations. The outcomes of the study were compared with previous analytical solutions, laboratory tests, and large-scale tests existing in the literature to verify the success of the proposed approach. It was noticed that the calculated values of the ultimate bearing capacities were in good agreement with the literature as seen in Figure 4.14. Even more, the proposed solution overcomes some problems existing in the former studies (Sharma et al., 2009).

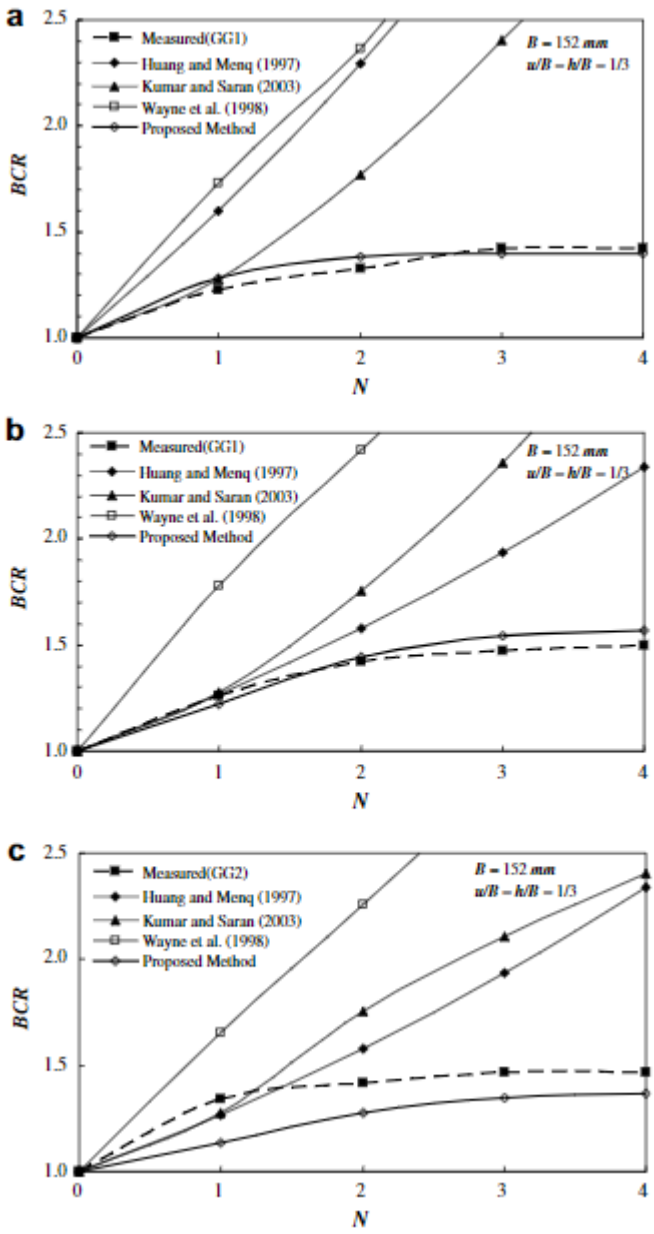

Figure 4.14. Comparison Of BCR With Number Of Reinforcement Layers (N) For Geogrid Reinforced Sand For The Selected Studies (Sharma et al., 2009).

Sawwaf (2009) conducted some laboratory tests along with a numerical study to examine the impact of the number of reinforcement layers ***(N)***, reinforcement length ***(L)***, reinforcement eccentricity ***(e_G)***, the relative density of sand ***(D_r)***, and load eccentricity ***(e_L)*** for eccentrically loaded strip footings resting on reinforced soil foundations as shown in

Figure 4.15. The results of both the numerical study and the laboratory tests given in Figures 4.16 and 4.17 show that:

1. the bearing capacity of the soil rises with increasing numbers of reinforcement layers concerning the effectiveness of reinforcement depth,
2. the ***BCR*** increases with increasing reinforcement length till ***L/B=4,***
3. the ***BCR*** decreases with increasing reinforcement eccentricity (e_G),
4. the ***BCR*** decreases with increasing load eccentricity (e_L),
5. there is a strong correlation between experimental and numerical data even though the ***BCR*** computed using finite element analysis appears to be higher than that calculated using model results due to scale effects (Sawwaf, 2009).

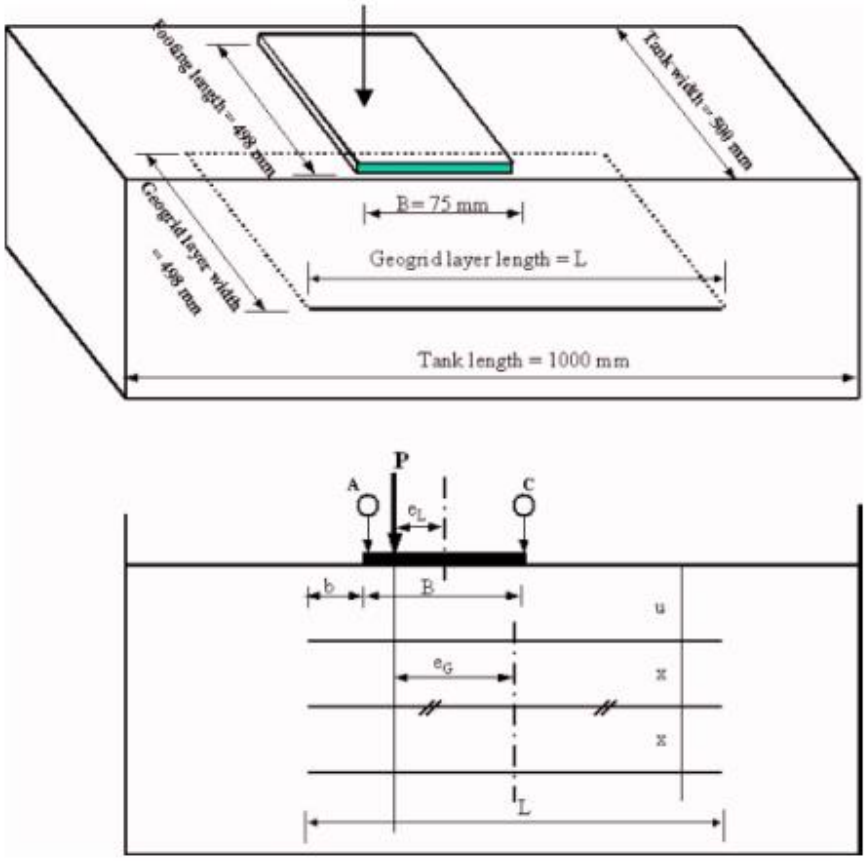

Figure 4.15. Geometric Parameters In The Laboratory Model Tests (Sawwaf, 2009).

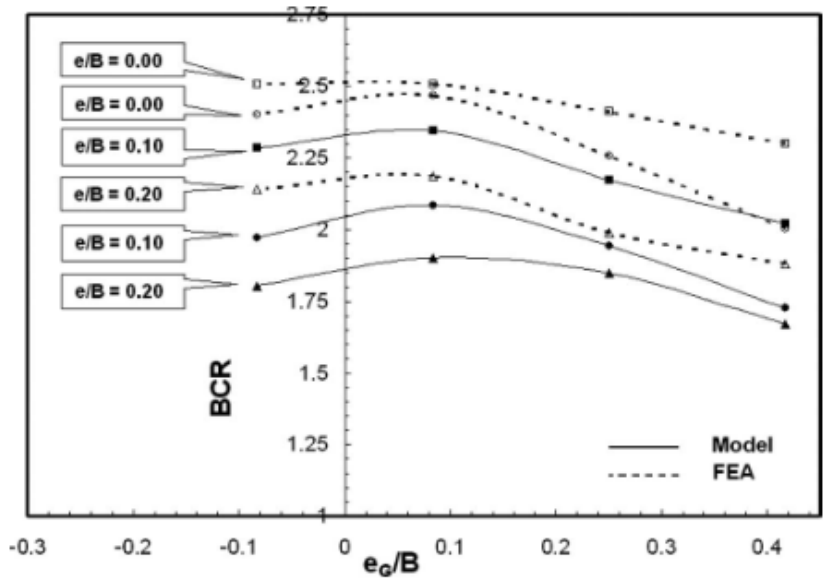

Figure 4.16. Variation Of BCR With e_G/B Ratio (Sawwaf, 2009).

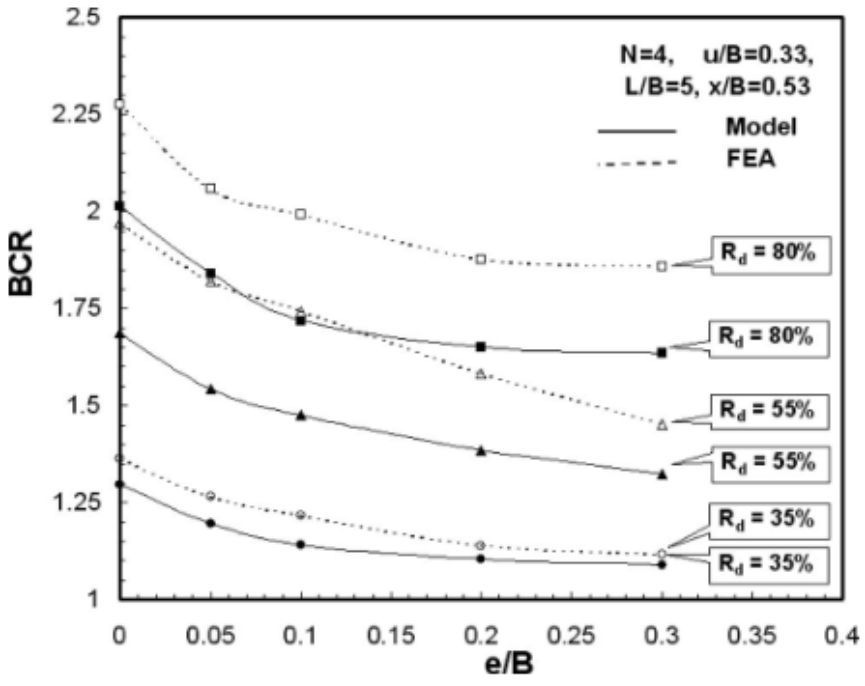

Figure 4.17. Variation Of BCR With e/B Ratio (Sawwaf, 2009).

Nasr and Azzam (2017) completed a series of laboratory model tests and finite-element analyses as shown in Figure 4.18 and Table 4.4 to examine the impact of footing width (***B***), type of reinforcement, load eccentricity (***e/B***), and relative density of sand (D_r) on the ultimate bearing capacity and failure mechanisms of eccentrically loaded strip footings on reinforced sand. The study states that increasing load eccentricity increases the enhancement of the bearing capacity of geogrid-reinforced sand. Also, it is found that improvement of sand with geotextile and geogrid provides about 38% and 67% increase in the ultimate bearing capacities, respectively when load eccentricity (***e/B***) is about 0.1 (Nasr & Azzam, 2017).

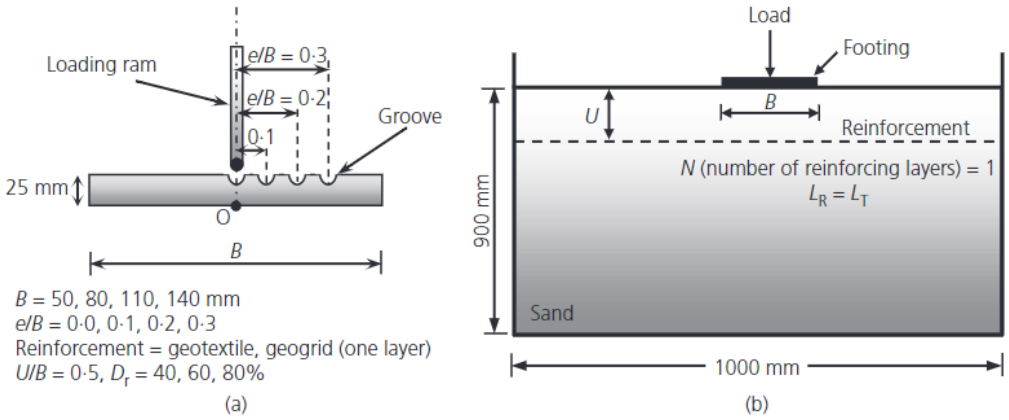

Figure 4.18. A Diagram Showing (a) A Model Strip Footing And (b) The Layout Of The Test Setup. (Not To Scale) (Nasr & Azzam, 2017).

Table 4.4. Test Results Of Model Footings On Sand Reinforced With Geogrid (Series II) (Nasr & Azzam, 2017).

		Physical model results			
		B: mm			
e/B		50	80	110	140
0·0	q_{uc}: kPa	86	96	119	139
	q_{ue}/q_{uc}	1·0	1·0	1·0	1·0
	R_K	0·0	0·0	0·0	0·0
	N_γ (back calculated)	201·0	140·4	126·5	117·0
0·1	q_{uc}: kPa	75	84	108	131
	q_{ue}/q_{uc}	0·87	0·88	0·91	0·94
	R_K	0·13	0·12	0·09	0·06
	N_γ (back calculated)	219·3	153·5	143·5	136·8
0·2	q_{uc}: kPa	54	65	81	96
	q_{ue}/q_{uc}	0·63	0·68	0·68	0·69
	R_K	0·37	0·32	0·32	0·31
	N_γ (back calculated)	210·5	158·4	143·5	133·7
0·3	q_{uc}: kPa	34	44	50	62
	q_{ue}/q_{uc}	0·40	0·46	0·42	0·45
	R_K	0·60	0·54	0·58	0·55
	N_γ (back calculated)	198·8	160·8	132·9	129·5

Hasan et al. (2020) investigate the effect of geogrid reinforcement of foundation soils under strip footing for different soil types with varying numbers and widths of reinforcement layers. The results of the numerical study are compared with the results of analytical approaches as well. The findings show that the geogrid-reinforcement can alter the bearing capacity and decrease settlement of the foundation but varying soil properties and footing size should also be considered to benefit from the improvement (Hasan et al., 2020).

5. EXPERIMENTAL STUDY

5.1. General

In this experimental study, a prototype of a cantilever retaining wall is scaled down for scaled model laboratory tests to be conducted on the shaking table. The experimental study purposes to investigate the seismic performance of the cantilever retaining walls built on geogrid-reinforced soil foundations. Several cases with varying parameters of the number of reinforcement layers and length of reinforcement are tested throughout the study to determine the effect of these parameters on the seismic performance of the retaining wall. During the shaking table tests, a 1/15 scaled cantilever retaining wall model was used.

5.2. Materials and Methods

5.2.1. Shaking Table

In this study, the shaking table used is located at the Boğaziçi University Kandilli Observatory and Earthquake Research Institute, Department of Earthquake Engineering, Shaking Table Laboratory. The table is uniaxial and hydraulic and is capable of applying horizontal vibration using a servo-hydraulic actuator. It has dimensions of 3 meters by 3 meters and can shake a maximum payload of 10 tons with 2g of acceleration. The table is designed for seismic applications and has a hydraulic actuator that allows for a stroke of +/- 12 cm, resulting in a total stroke of 24 cm. It is controlled by a digital outer loop control system and a newly modified computer-based software system.

5.2.2. Laminar Box

The geotechnical model cannot be mounted directly on the shaking table due to the need for confinement, so the soil must be placed in a container. There are two types of soil containers used in geotechnical experiments in the literature: rigid-sided and flexible-sided containers. Artificial rigid boundaries in the rigid-sided containers can create stress and strain similarity issues, as well as problems with the generation and reflection of P-waves. These problems are significant when it comes to accurately reflecting soil behaviour in geotechnical experiments. In contrast to rigid-sided soil containers, flexible-sided soil containers allow the soil to deform freely, just as it would in the natural ground when subjected to seismic excitations. In this study, a laminar box which is a flexible-sided soil container is used to observe the response and the performance of the soil under dynamic loadings accurately (Sekman, 2016).

The main idea behind a laminar box is to make it as flexible as possible so that the soil inside can move and behave naturally, without being restricted by the boundaries of the container. This is achieved by reducing the friction between the layers of the box to a minimum so that the soil inside can deform freely and respond to external forces in the same way that it would in its natural environment. In other words, the design of the laminar box is intended to allow the soil to dictate the behaviour of the entire system, rather than being influenced by the stiffness of the container itself (Sekman, 2016).

The laminar box shown in Figures 5.1 and 5.2 used in this research was designed and constructed with the support of the Boğaziçi University Research Fund (Project No. BU-BAP8084). Its dimensions are 1.5 meters long and 1.3 meters wide, with a depth of 1 meter. The dimensions of the box were chosen to be within the maximum loading capacity of the shaking table, and the rectangular shape was chosen to avoid any potential issues with torsion during one-directional shaking. Overall, the design of the laminar box was carefully considered to ensure its compatibility with the shaking table and its ability to accurately simulate soil behaviour during earthquakes.



Figure 5.1. Side View Of Laminar Box On Shaking Table.



Figure 5.2. Laminar Box On Shaking Table.

5.2.3. Measuring Instruments and Instrumentation

Various types of accelerometers and optical laser displacement measuring instruments are used during laboratory tests. Details of instrumentation devices and their placement in the testing setup are given in Table 5.1 and Figure 5.3. The optical laser displacement measuring instruments are Leuze Electronic ODSL B/V4-400-S12 and ODSL 96B M/V6.XL-1200-S12.

Table 5.1. Details Of Instrumentation

Instrument:	***Type:***	***Location:***
A1	Accelerometer	Shaking Table
A2	Accelerometer	Laminar Box
A3, A4, A5, A6, A7, and A8	Accelerometer	Retaining Wall
A9, A10, and A11	Accelerometer	Soil Foundation
A12, A13, A14, A15, and A16	Accelerometer	Backfill
D17	Optical Laser Displacement	Shaking Table
D18, D19, D20, and D21	Optical Laser Displacement	Retaining Wall
D22, D23, and D24	Optical Laser Displacement	Laminar Box
A25 and A26	Accelerometer	Laminar Box
A27	Accelerometer	Soil Foundation

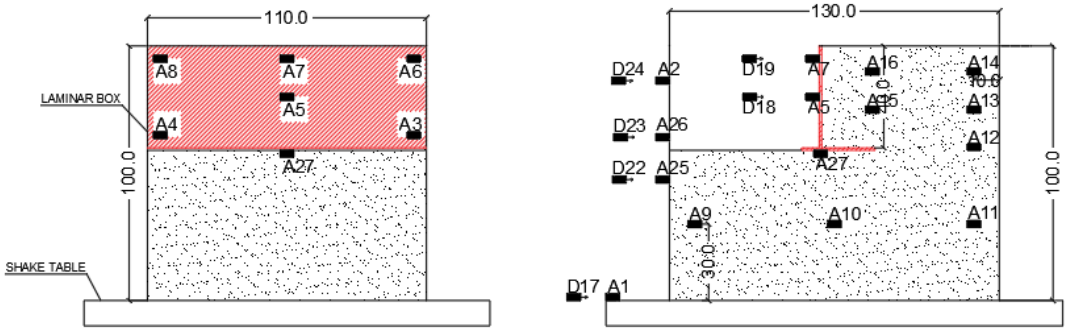

Figure 5.3. Instrumentation Of Test Model.

5.2.4. Soil Material

The soil substance used in the experimentations was Silivri Sand which is named after one of the districts of Istanbul. Silivri Sand was chosen due to its properties. It is defined as poorly graded sand (***SP***) with a constant of curvature of C_c = 2.29 and the constant of uniformity of C_u = 1.1. The inner friction angle is φ = 41.48°. Its specific gravity was estimated as G_s=2.67 and bulk unit weight (γ_{bulk}) as 16.5 kN/m^3. The maximum and minimum void ratios of the sand (e_{max} and e_{min}) were found as 0.73 and 0.37, respectively.

5.2.5. Geogrid

Biaxial geogrid materials produced and supplied by Istanbul Teknik are used for the model tests. Material properties of the used biaxial geogrid shown in Figure 5.4 are given in Table 5.2. ForTex series products are geogrids with high strength and durability. They are made by knitting reinforced polyester fibres and coating them with polymer material.

Table 5.2. Material Properties Of ForTex GG 40/40 P By Istanbul Teknik.

Material Property:	**Value:**	**Unit:**
Maximum Tensile Strength (Machine Direction)	40	kN/m
Maximum Tensile Strength (Cross-Machine Direction)	40	kN/m

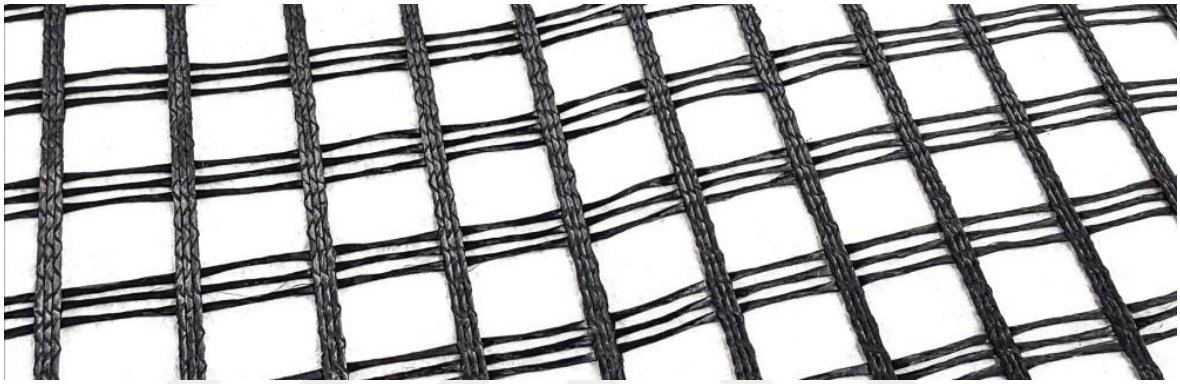

Figure 5.4. ForTex GG 40/40 P By Istanbul Teknik.

5.2.6. Retaining Wall Model

The prototype retaining wall is a concrete cantilever retaining wall. Dimensions of the prototype are a height of 6 meters, a foundation width of 3.75 meters, and a thickness of 0.35 meters. Based on Wood (2004), values of Young's modulus are taken as 20 GPa and 70 GPa for concrete in the prototype and aluminium in the model, respectively. Hence the dimensions of the prototype and the values of modulus of elasticities are known, considering a scale of 1/15, scaled dimensions of the model wall of aluminium can be decided by

$$\boldsymbol{t_m = t_p \left(\frac{E_p}{E_m} \frac{1}{n^{7/2}} \right)^{1/3}} \tag{5.1}$$

where $\boldsymbol{t}$ represents thickness, $\boldsymbol{E}$ represents modulus of elasticity, and $\boldsymbol{n}$ is the scaling value. The dimensions of the model are found as 40 centimetres in height, 25 centimetres in foundation width, and 1 centimetre in thickness by the equation (Wood, 2004).

The retaining wall model used in the study is designed and constructed with the support of Destech Müşavirlik Mühendislik ve Proje A.Ş.

Table 5.3. Scaling Factors For Geotechnical Studies (Wood, 2004).

	scale factors		
quantity	**general**	$1g$ **(laboratory)**	ng **(centrifuge)**
length	n_ℓ	$1/n$	$1/n$
mass density	n_ρ	1	1
acceleration	n_g	1	n
stiffness	n_G	$1/n^\alpha$	1
stress	$n_\rho n_g n_\ell$	$1/n$	1
force	$n_\rho n_g n_\ell^3$	$1/n^3$	$1/n^2$
force/unit length	$n_\rho n_g n_\ell^2$	$1/n^2$	$1/n$
strain	$n_\rho n_g n_\ell / n_G$	$1/n^{1-\alpha}$	1
displacement	$n_\rho n_g {n_\ell}^2 / n_G$	$1/n^{2-\alpha}$	$1/n$
pore fluid viscosity	n_μ	1 or* $n^{1-\alpha/2}$	1 or* n
pore fluid density	$n_{\rho f}$	1	1
permeability (Darcy's Law)	$n_{\rho f} n_g / n_\mu$	1 or* $1/n^{1-\alpha/2}$	n or* 1
hydraulic gradient	$n_\rho / n_{\rho f}$	1	1
time (diffusion)	$n_\mu n_\ell^2 / n_G$	$1/n^{2-\alpha}$ or* $1/n^{1-\alpha/2}$	$1/n^2$ or* $1/n$
time (creep)	1	1	1
time (dynamic)	$n_\ell \left(n_\rho / n_G\right)^{1/2}$	$1/n^{1-\alpha/2}$	$1/n$
velocity	$n_g n_\ell \left(n_\rho / n_G\right)^{1/2}$	$1/n^{1-\alpha/2}$	1
frequency	$\left(n_G / n_\rho\right)^{1/2} / n_\ell$	$n^{1-\alpha/2}$	n
shear wave velocity	$\left(n_G / n_\rho\right)^{1/2}$	$1/n^{\alpha/2}$	1

*scaling of pore fluid viscosity introduced in order to force identity of scale factors for diffusion time and dynamic time

5.2.7. Seismic Motions

Four different severe earthquake motions are selected for the shaking table tests. These earthquake motions are the 1940 Imperial Valley – El Centro Station, the 1999 Kocaeli – Iznik and Izmit Stations, and the 2014 North Aegean Sea – Gokceada Station. The uniaxial shaking table in the laboratory was used to only study the horizontal component of

earthquakes. The earthquakes were selected based on their frequency content and how well they could be reproduced on the shaking table. Also, the earthquake motions are scaled in the time domain per scaled model for accuracy. Table 5.4 shows the detailed data of the selected input motions while Figures 5.5 to 5.8 present the scaled acceleration, velocity, and displacement histories of them in the time domain.

Table 5.4. Earthquake Motions Used In The Experiments

Earthquake Name	Date	Station Name	Magnitude	PGA (g)
Imperial Valley - 02	19.08.1940	El Centro Array #9	6.95	0.32
Kocaeli, Turkey	17.08.1999	Izmit	7.51	0.22
Kocaeli, Turkey	17.08.1999	Iznik	7.51	0.12
North Aegean Sea	24.05.2014	Gokceada	6.9	0.14

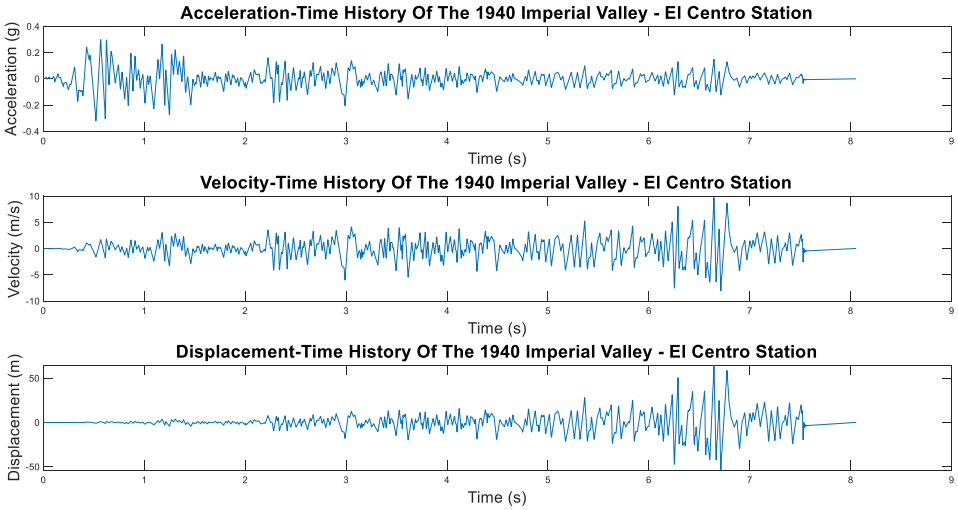

Figure 5.5. Scaled Motion Of The 1940 Imperial Valley Earthquake – El Centro Station.

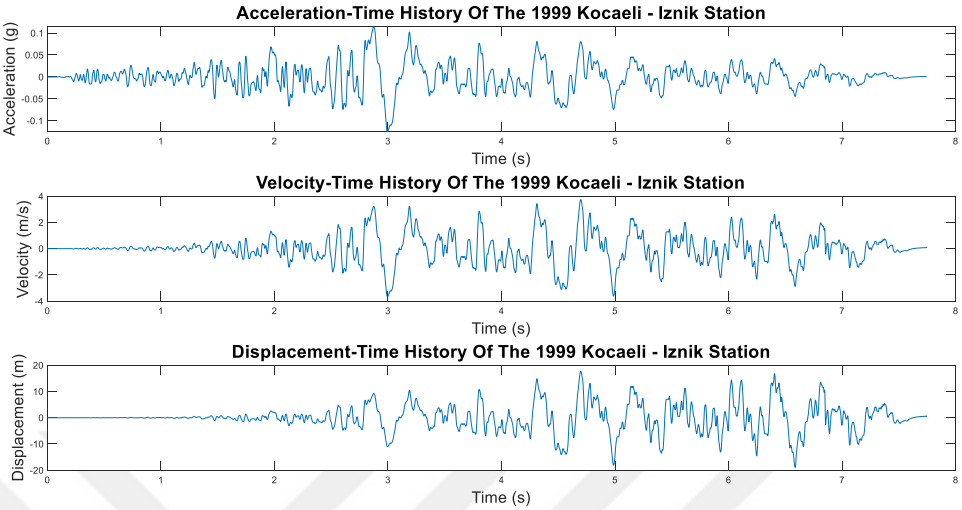

Figure 5.6. Scaled Motion Of The 1999 Kocaeli Earthquake – Iznik Station.

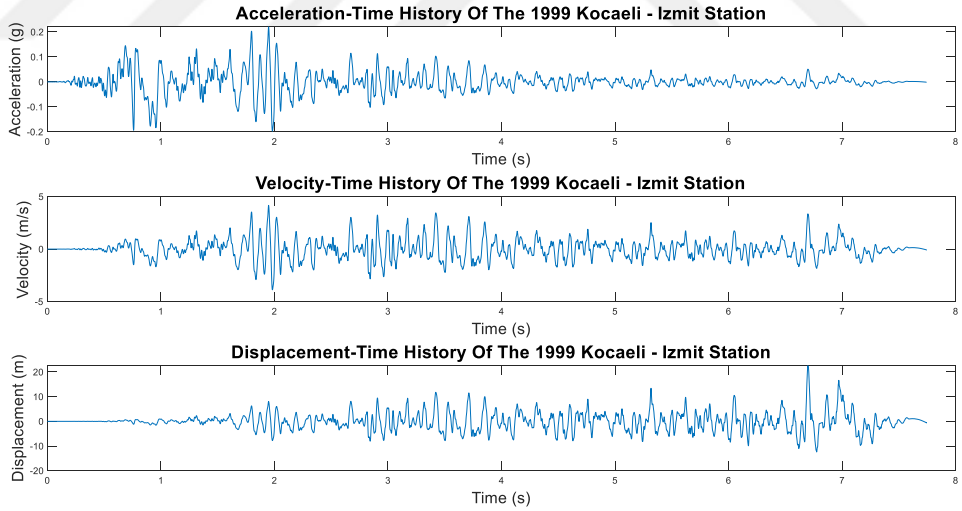

Figure 5.7. Scaled Motion Of The 1999 Kocaeli Earthquake – Izmit Station.

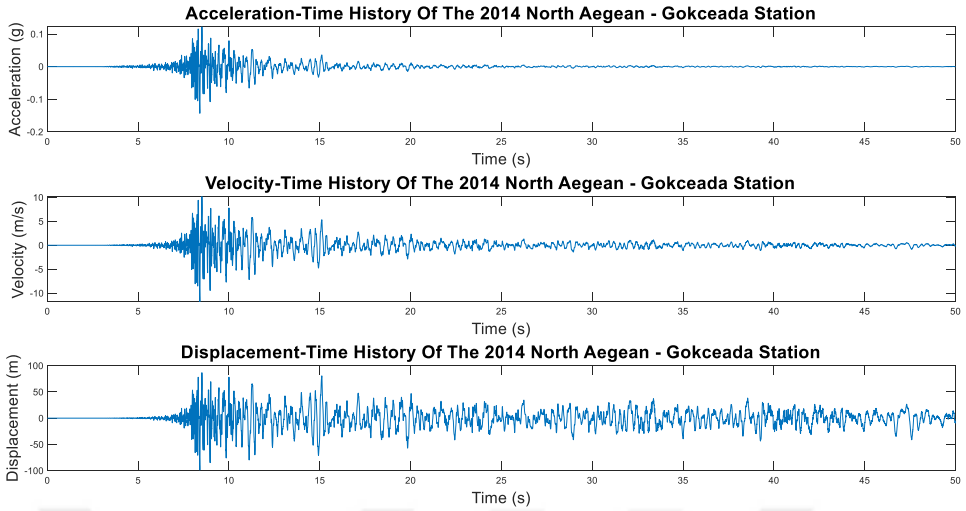

Figure 5.8. Scaled Motion Of The 2014 North Aegean Sea Earthquake – Gokceada Station.

5.3. Shaking Table Experiments

Shaking table experiments shown in Table 5.7 were completed at the Boğaziçi University Kandilli Observatory and Earthquake Research Institute, Department of Earthquake Engineering Shaking Table Laboratory. In the laboratory, a laminar box designed and constructed with the support of BU - BAP8084 is mounted on the shaking table and then, the performance of the built system is tested. Later, the scaled test models are built following the scaling factors shown in Table 5.5 by using the materials explained earlier. Nine test cases are constructed in the laboratory during the study. These cases were subjected to 4 shaking motions which were presented before. Varying parameters in these cases are the length of reinforcement (***L***) and the number of reinforcement layers (***N***).

Table 5.5. Scaling Factors (Iai, 1989).

Parameter	1:15 Scale ($\lambda = 1/15$)	Model / Prototype
Length	λ	1/15
Time	$\lambda^{1/2}$	$(1/15)^{1/2}$
Mass	λ^2	$(1/15)^2$
Displacement	λ	1/15
Acceleration	1	1/1
Stress	1	1/1
Strain	1	1/1
Force	λ^2	$(1/15)^2$

Table 5.6. Dimensions Of Model And Prototype Retaining Walls.

Dimensions of the Retaining Wall	Scale	Model	Prototype
Stem Height	1/15	40 cm	600 cm
Foundation Width	1/15	25 cm	375 cm
Thickness	1/15	1 cm	35 cm

Table 5.7. Experimental Program (The Case Numbers of the Models)

Test Model	Number of Reinforcement Layers (N)	Depth of Reinforcement (u)	Distance Between Reinforcement Layers (h)	Reinforcement Length (L)
Case 01	0	0	0	0
Case 02	1	0.2B	0.2B	2B
Case 03	2	0.2B	0.2B	2B
Case 04	3	0.2B	0.2B	2B
Case 05	4	0.2B	0.3B	2B
Case 06	1	0.2B	0.2B	4B

Table 5.7. Experimental Program (The Case Numbers of the Models). (cont.)

Test Model	Number of Reinforcement Layers (N)	Depth of Reinforcement (u)	Distance Between Reinforcement Layers (h)	Reinforcement Length (L)
Case 07	2	0.2B	0.2B	4B
Case 08	3	0.2B	0.2B	4B
Case 09	4	0.2B	0.2B	4B

5.3.1. Case 01

The aim of Case 01 is to understand the behaviour of the retaining wall model resting on an unreinforced soil foundation under the selected seismic motions. The data obtained from Case 01 was used to determine the efficiency of the improvement method based on parameters such as the length of the reinforcement and the number of reinforcement layers under different earthquake motions. Figure 5.9 shows the model geometry of Case 01 while Figures 5.10 to 5.12 show the setup of Case 01.

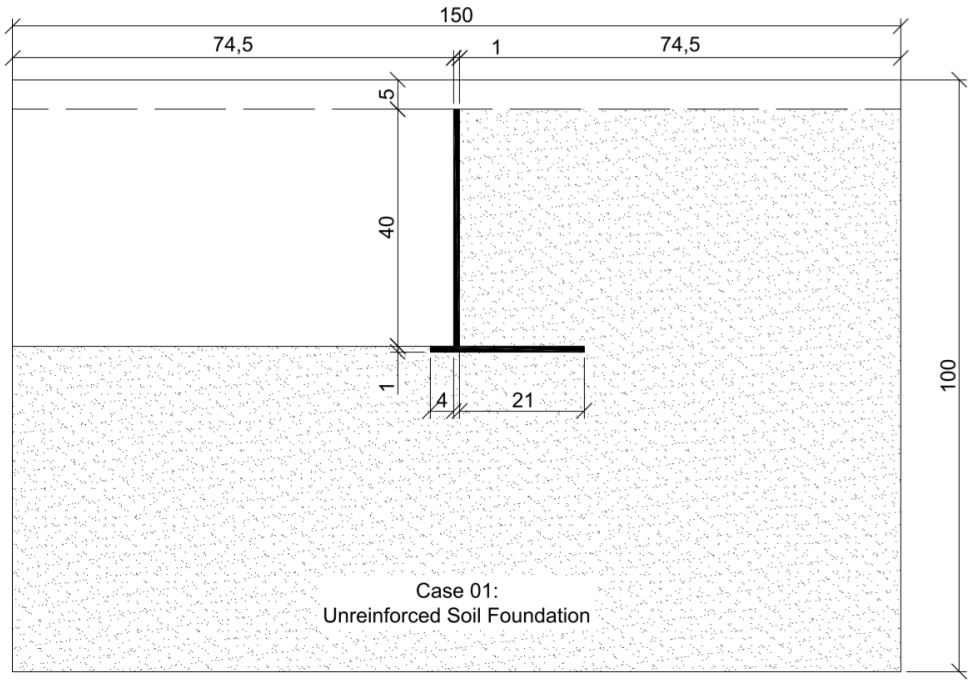

Figure 5.9. Model Geometry of Case 01.



Figure 5.10. Constructed Experimental Setup of Case 01.



Figure 5.11. Constructed Experimental Setup of Case 01.



Figure 5.12. Constructed Experimental Setup of Case 01.

5.3.2. Case 02

In Case 02, one layer of geogrid material having the length of ***2B*** is placed in the soil foundation as reinforcement. The distance between the reinforcement and the foundation of the retaining wall is ***0.2B***. Figure 5.13 shows the model geometry of Case 02. Figures 5.14 to 5.16 show the preparation of the testing model and its completed form.

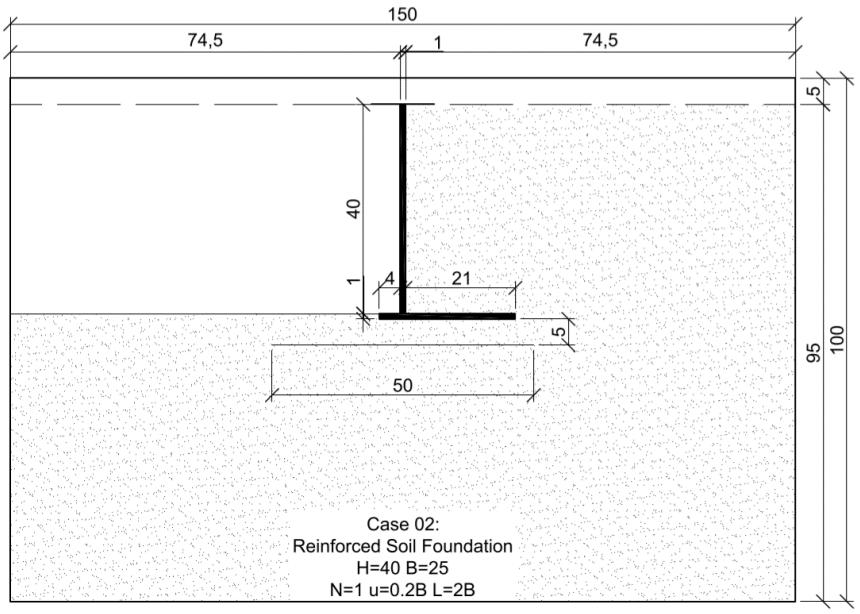

Figure 5.13. Model Geometry of Case 02.

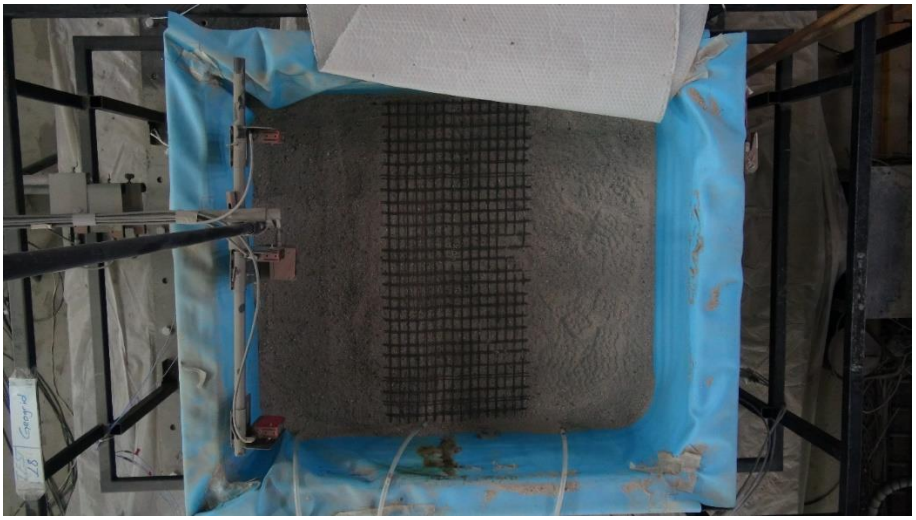

Figure 5.14. Placing Of Geogrid Material for Case 02.



Figure 5.15. Placing of Retaining Wall Model.

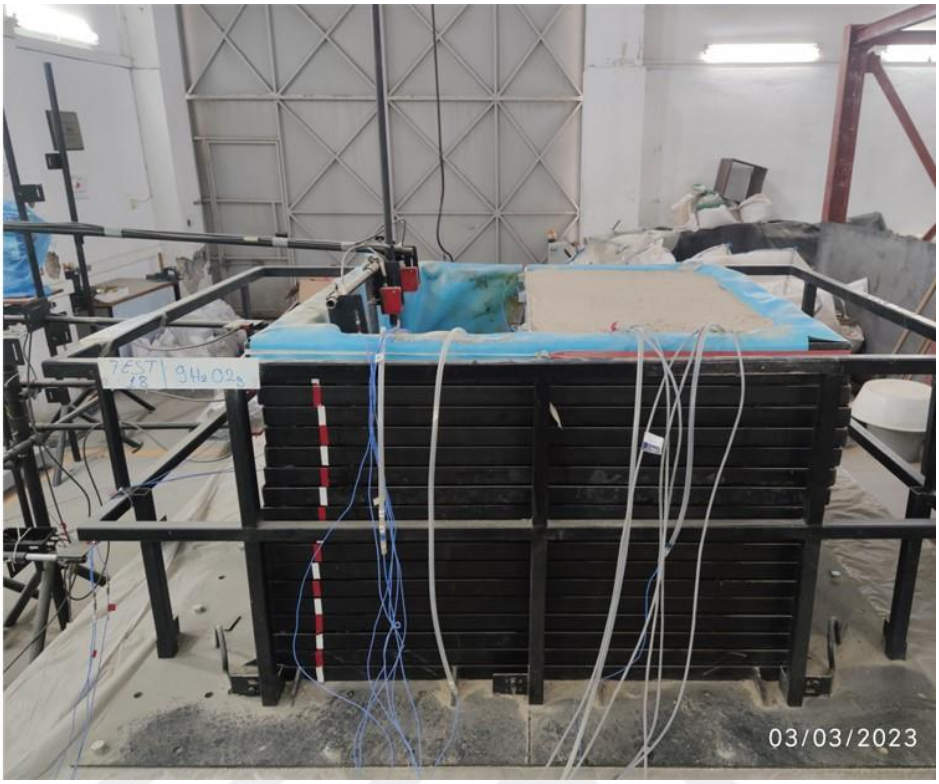

Figure 5.16. Constructed Experimental Setup of Case 02.

5.3.3. Case 03

In Case 03, two layers of geogrid materials having the length of ***2B*** are placed in the soil foundation as reinforcement. The distance between the upper reinforcement layer and the foundation of the retaining wall is ***0.2B*** and the distance between each reinforcement layer is ***0.2B***. Figure 5.17 shows the model geometry of Case 03. Figures 5.18 to 5.21 show the preparation of the testing model and its completed form.

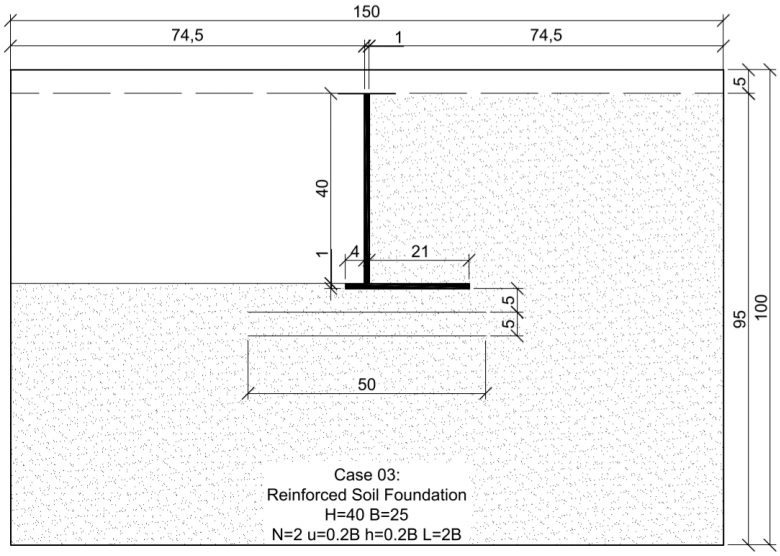

Figure 5.17. Model Geometry Of Case 03.

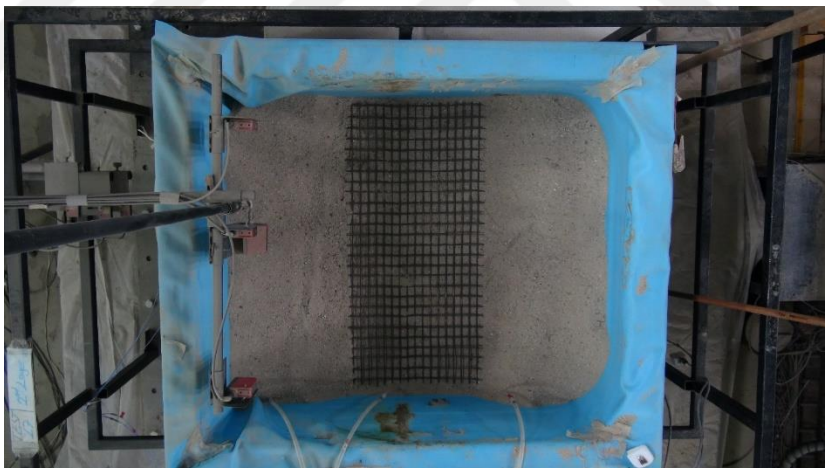

Figure 5.18. The Placing Of The Second Layer.

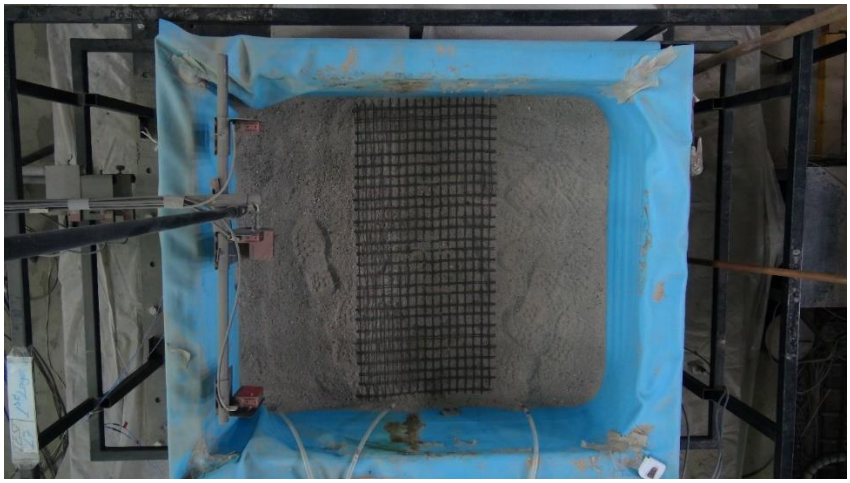

Figure 5.19. The Placing Of The First Layer.



Figure 5.20. Placing of Retaining Wall Model and Backfill For Case 03.



Figure 5.21. Completed Experimental Setup of Case 03.

5.3.4. Case 04

In Case 04, three layers of geogrid materials having the length of ***2B*** are placed in the soil foundation as reinforcement. The distance between the upper reinforcement and the foundation of the retaining wall is ***0.2B*** and the distance between each reinforcement layer is ***0.2B***. Figure 5.22 shows the model geometry of Case 04. Figures 5.23 to 5.26 show the preparation of the testing model and its completed form.

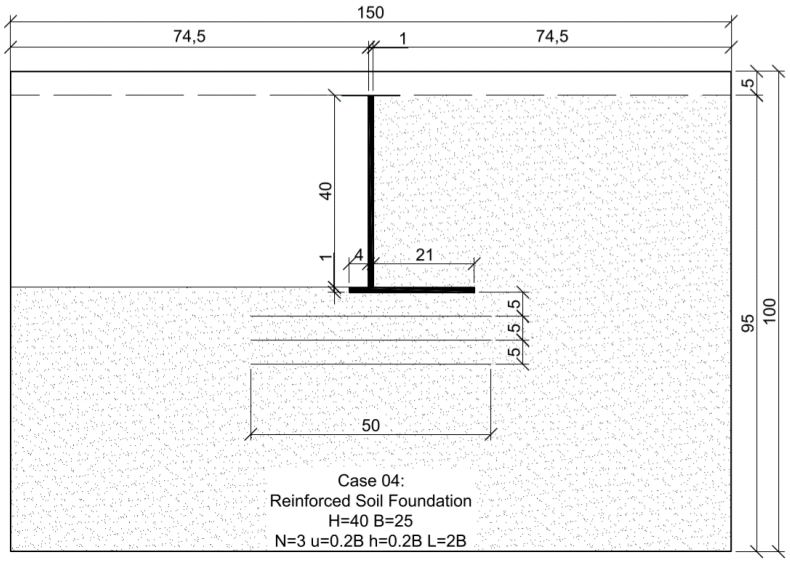

Figure 5.22. Model Geometry of Case 04.



Figure 5.23. Placing Third Layer Of Reinforcement Of Case 04.

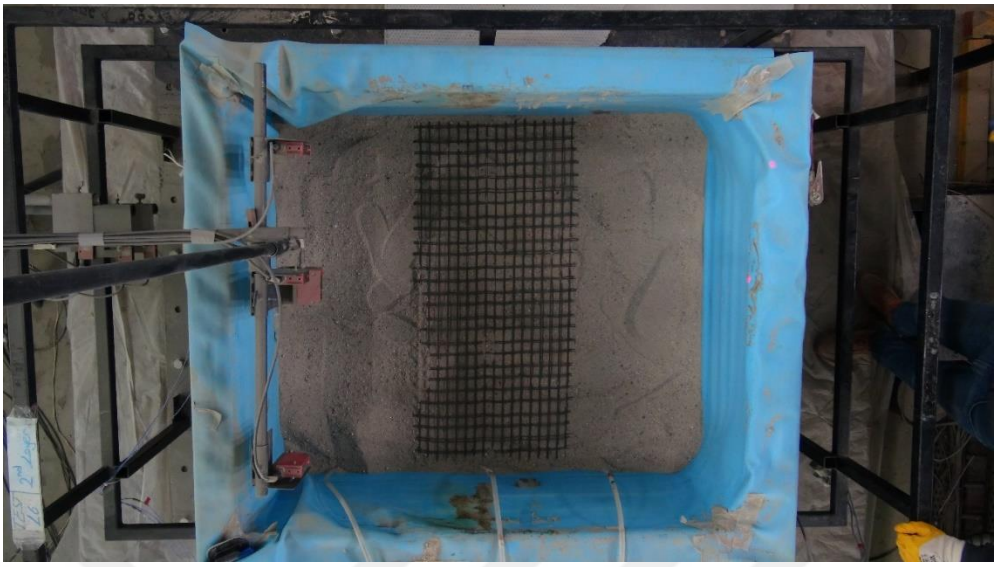

Figure 5.24. Placing Second Reinforcement Layer of Case 04.

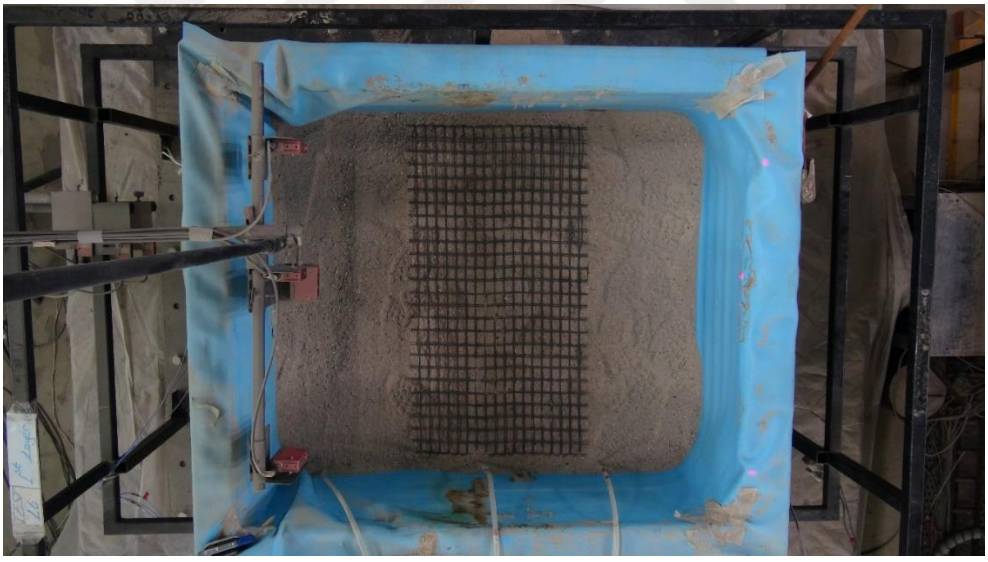

Figure 5.25. Placing First Layer Reinforcement of Case 04.



Figure 5.26. Completed Experimental Setup for Case 04.

5.3.5. Case 05

In Case 05, four layers of geogrid materials having the length of ***2B*** are placed in the soil foundation as reinforcement. The distance between the upper reinforcement and the foundation of the retaining wall is ***0.2B*** and the distance between each reinforcement layer is ***0.2B***. Figure 5.27 shows the model geometry of Case 05. Figures 5.28 to 5.33 show the preparation of the testing model and its completed form.

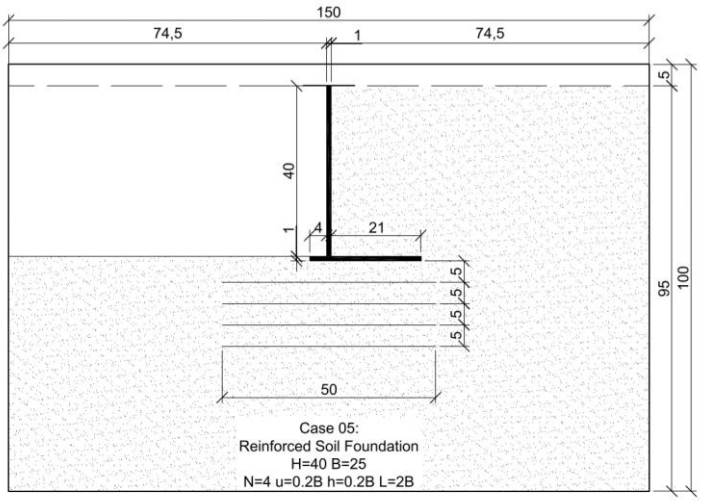

Figure 5.27. Model Geometry of Case 05.

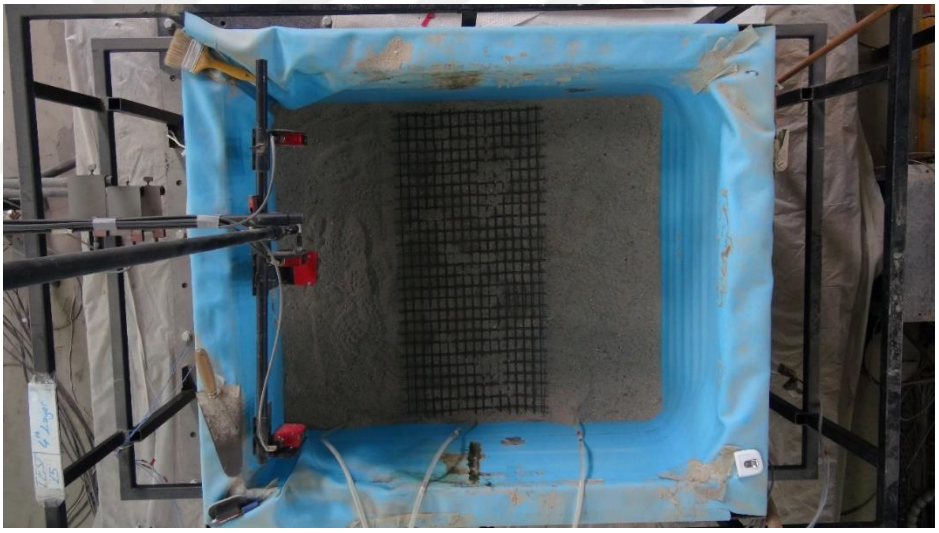

Figure 5.28. Placing Fourth Layer Of Reinforcement Of Case 05.

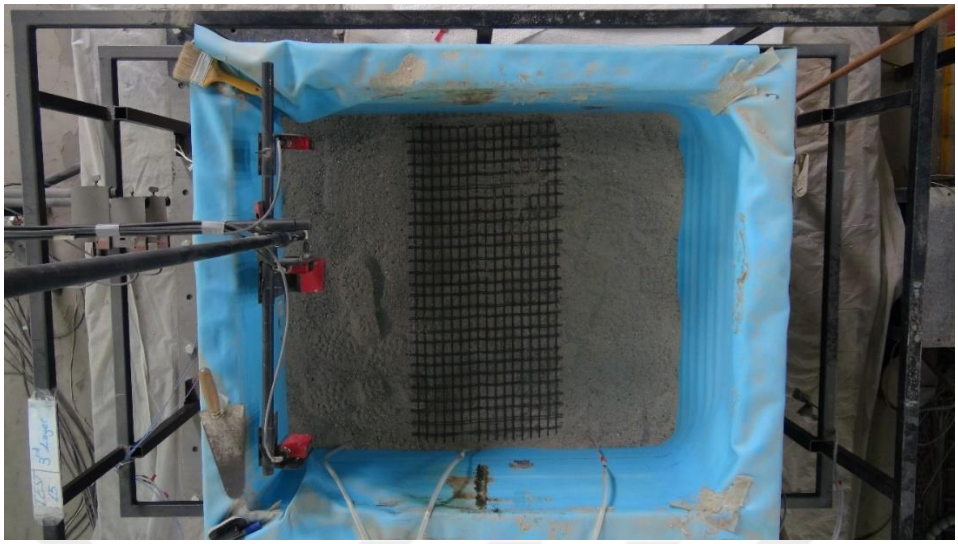

Figure 5.29. Placing Third Reinforcement Layer of Case 05.

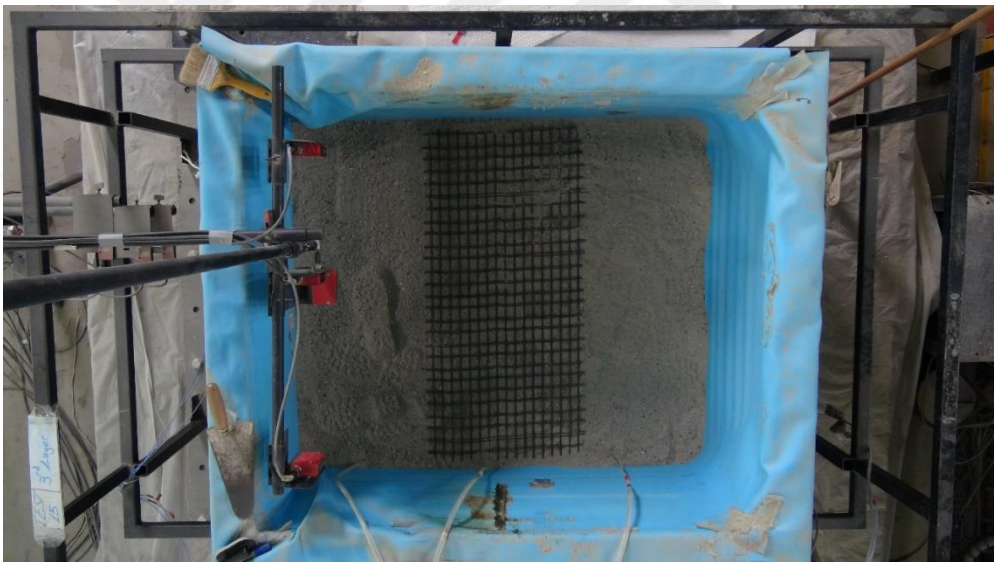

Figure 5.30. Placing Second Reinforcement Layer of Case 05.

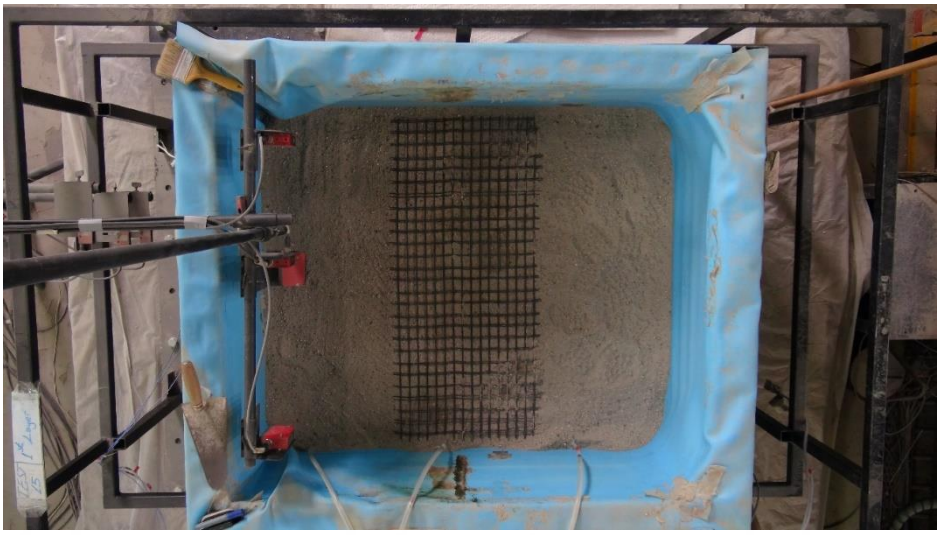

Figure 5.31. Placing First Layer Of Reinforcement Of Case 05.

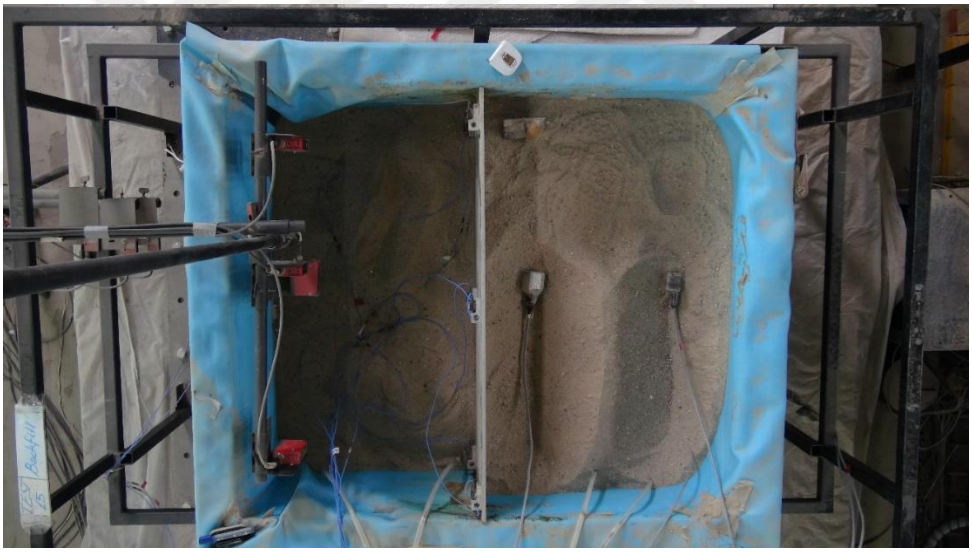

Figure 5.32. Placing Retaining Wall Model and Backfill for Case 05.



Figure 5.33. Completed Experimental Setup for Case 05.

5.3.6. Case 06

In Case 06, one layer of geogrid material having the length of ***4B*** is placed in the soil foundation as reinforcement. The distance between the upper reinforcement and the foundation of the retaining wall is ***0.2B***. Figure 5.34 shows the model geometry of Case 06. Figures 5.35 to 5.37 show the preparation of the testing model and its completed form.

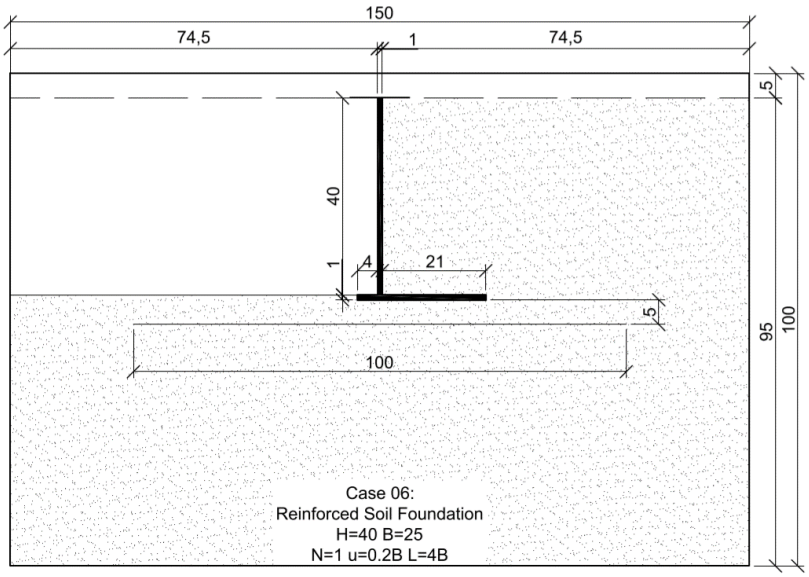

Figure 5.34. Model Geometry of Case 06.

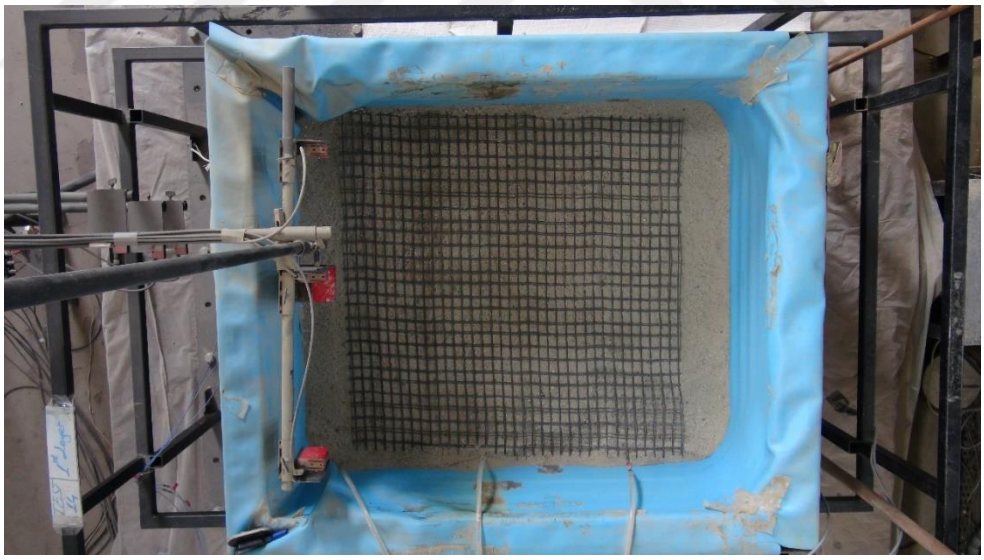

Figure 5.35. Placing Reinforcement Layer of Case 06.

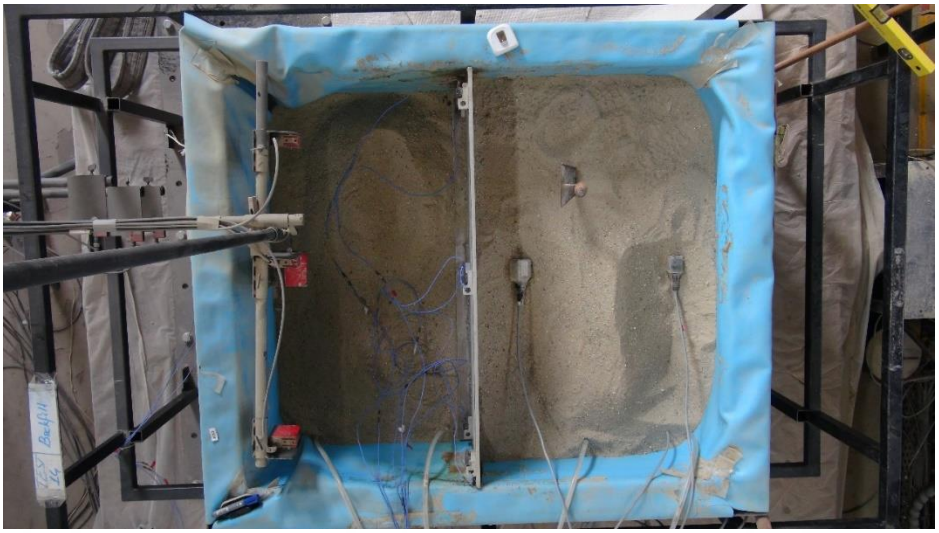

Figure 5.36. Placing of Retaining Wall Model and Backfill for Case 06.



Figure 5.37. Completed Experimental Setup for Case 06.

5.3.7. Case 07

In Case 07, two layers of geogrid materials having the length of ***4B*** are placed in the soil foundation as reinforcement. The distance between the upper reinforcement and the foundation of the retaining wall is ***0.2B***. The distance between each reinforcement layer is

0.2B. Figure 5.38 shows the model geometry of Case 07. Figures 5.39 to 5.42 show the preparation of the testing model and its completed form.

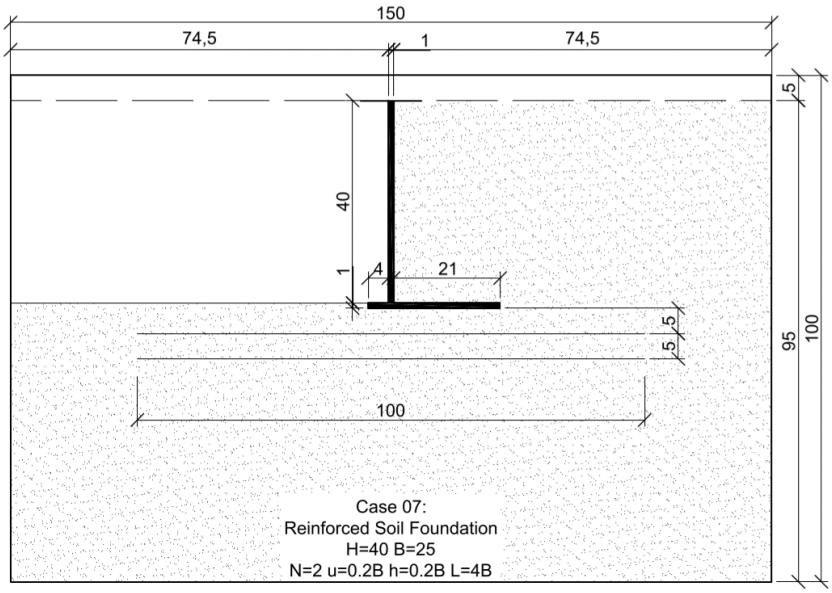

Figure 5.38. Model Geometry of Case 07.

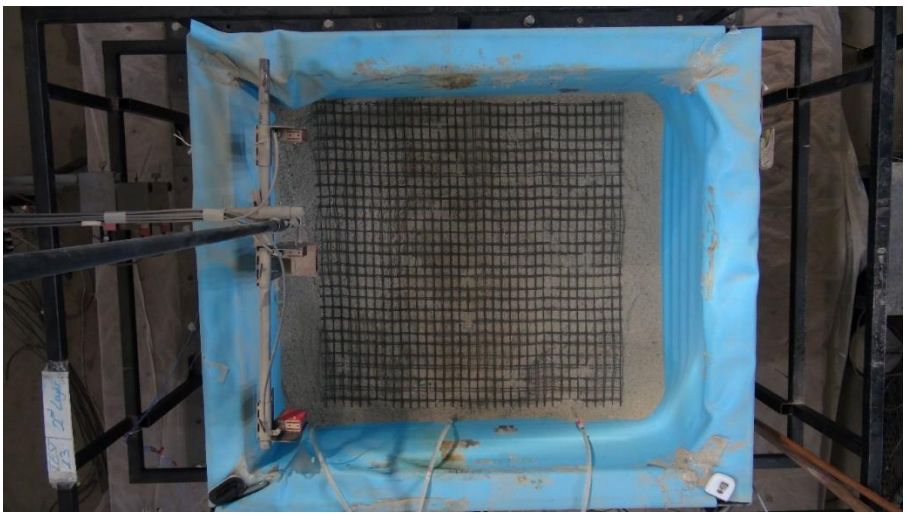

Figure 5.39. Placing Second Reinforcement Layer of Case 07.

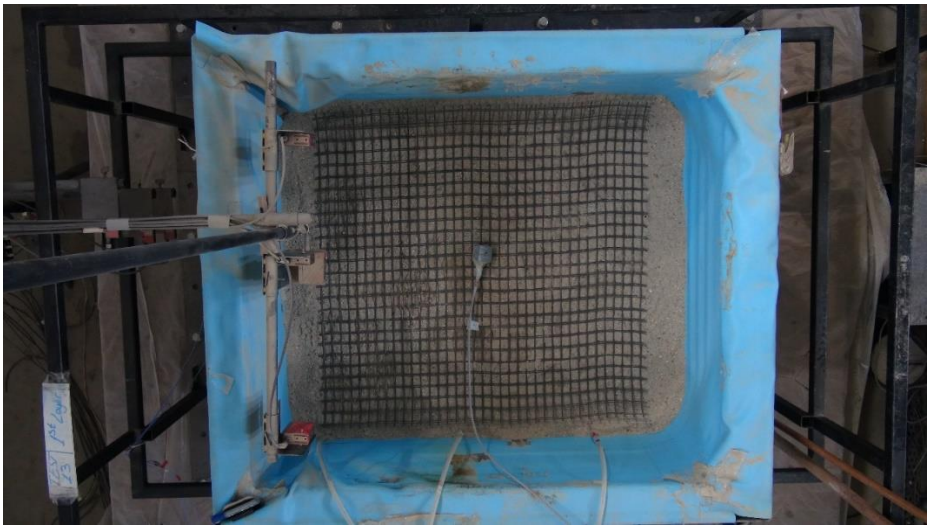

Figure 5.40. Placing First Reinforcement Layer and Accelerometer A27 For Case 07.



Figure 5.41. Placing Model Retaining Wall and Backfill For Case 07.



Figure 5.42. Completed Experimental Setup for Case 07.

5.3.8. Case 08

In Case 08, three layers of geogrid materials having the length of ***4B*** are placed in the soil foundation as reinforcement. The distance between the upper reinforcement and the foundation of the retaining wall is ***0.2B***. The distance between each reinforcement layer is ***0.2B***. Figure 5.43 shows the model geometry of Case 08. Figures 5.44 to 5.48 show the preparation of the testing model and its completed form.

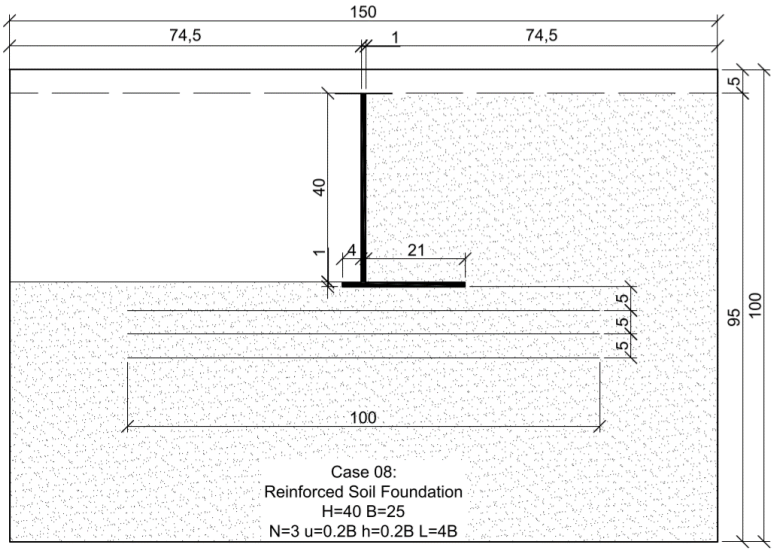

Figure 5.43. Model Geometry of Case 08.

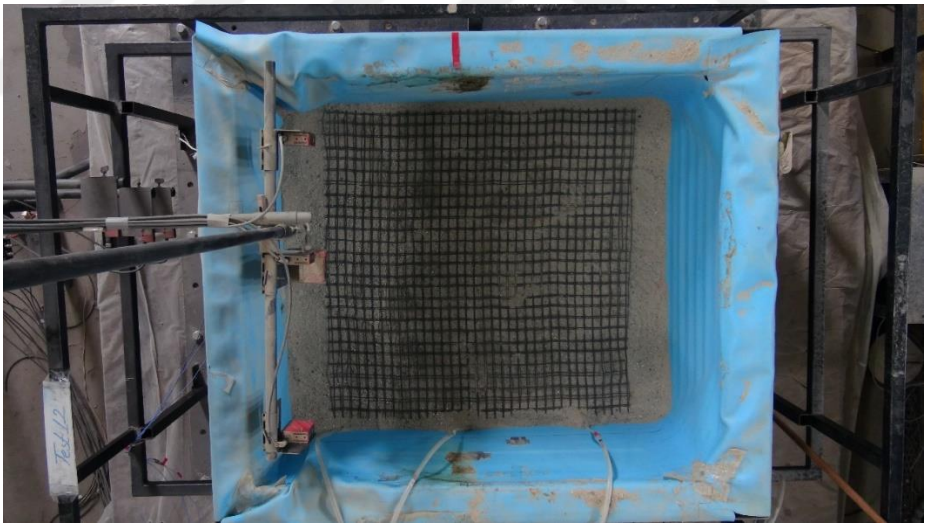

Figure 5.44. Placing Third Reinforcement Layer For Case 08.

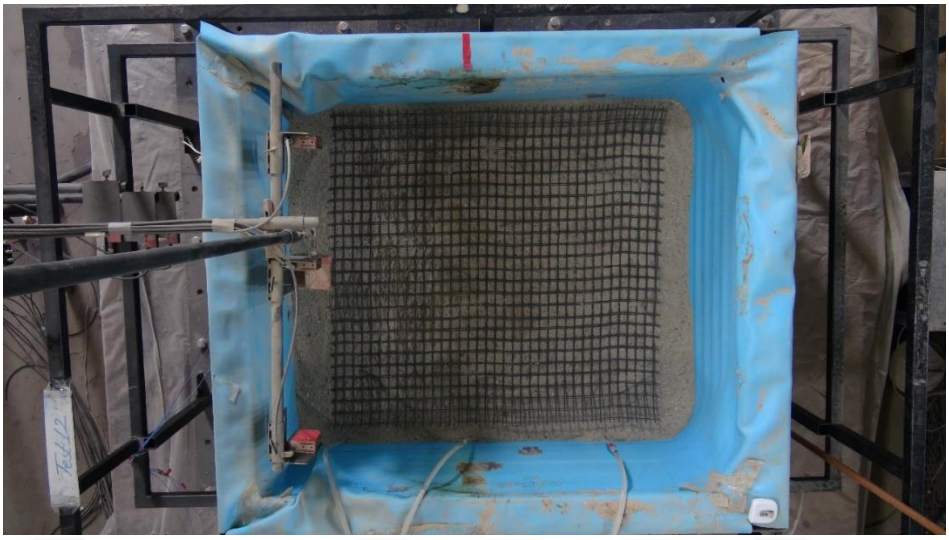

Figure 5.45. Placing Second Reinforcement Layer For Case 08.

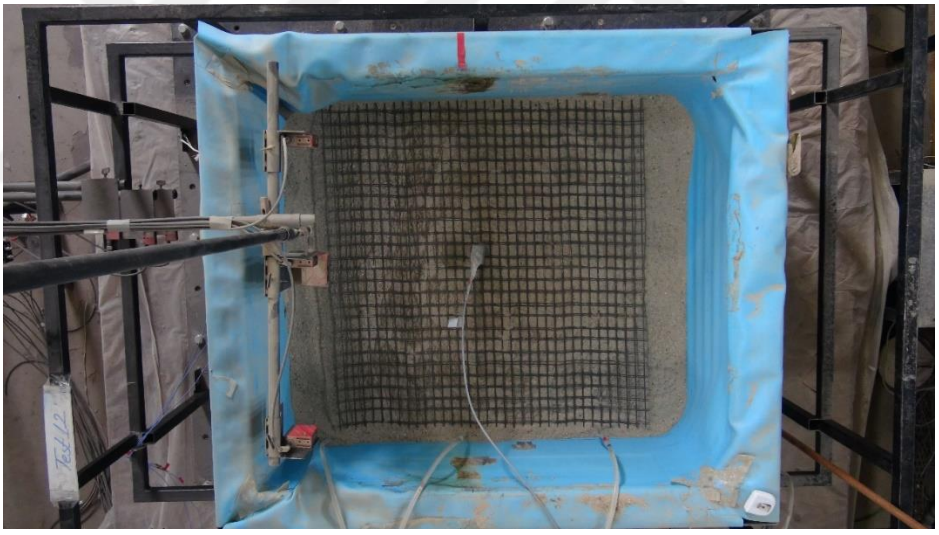

Figure 5.46. Placing First Reinforcement Layer and Accelerometer A27 For Case 08.



Figure 5.47. Placing Retaining Wall Model and Backfill For Case 08.



Figure 5.48. Completed Experimental Setup for Case 08.

5.3.9. Case 09

In Case 09, four layers of geogrid materials having the length of ***4B*** are placed in the soil foundation as reinforcement. The distance between the upper reinforcement and the foundation of the retaining wall is ***0.2B***. The distance between each reinforcement layer is

0.2B. Figure 5.49 shows the model geometry of Case 09. Figures 5.50 to 5.54 show the preparation of the testing model and its completed form.

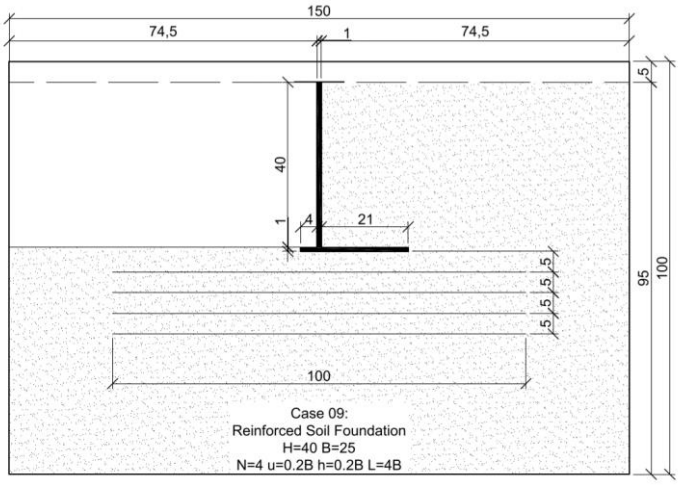

Figure 5.49. Model Geometry of Case 09.

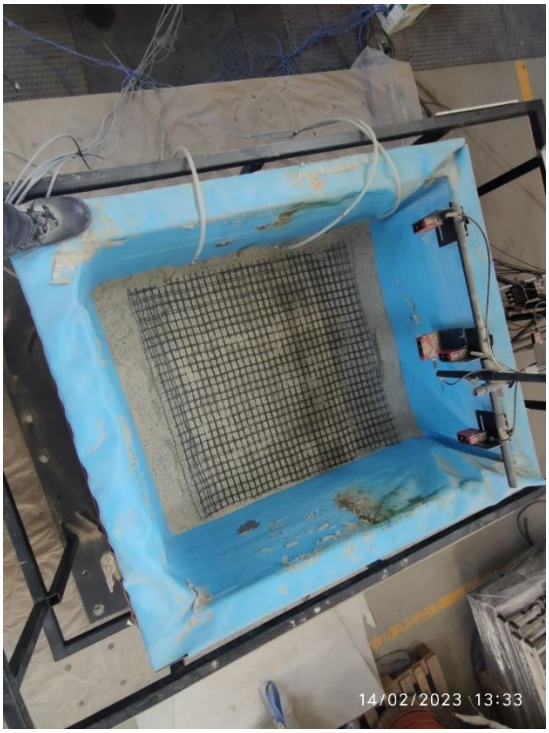

Figure 5.50. Placing Fourth Reinforcement Layer for Case 09.



Figure 5.51. Placing Third Reinforcement Layer for Case 09.



Figure 5.52. Placing Second Reinforcement Layer For Case 09.



Figure 5.53. Placing First Reinforcement Layer and Accelerometer A27 For Case 09.



Figure 5.54. Completed Experimental Setup for Case 09.

5.4. Results Of Shaking Table Experiments

Experiments of all cases summarized in Chapter 5.3 are completed in Boğaziçi University Kandilli Observatory and Earthquake Research Institute, Department of Earthquake Engineering, Shaking Table Laboratory. The seismic response of the cases is analysed through the data recorded. Following chapters present the detailed results of the completed tests based on acceleration and displacement data recorded from sensors A07, A10, A16, and D19. The location of these sensors can be seen in Figure 5.3. Sensor A07 is an accelerometer located on top of the retaining wall model. Sensor D19 which measures displacement is also located on top of the retaining wall model. Sensor A10 is an accelerometer located below the foundation of the retaining wall model in the soil. Sensor A16 is an accelerometer located in the backfill at a depth of one-third of the height of the model wall.

5.4.1. Performance Of The Retaining Wall Model Under The 1940 Imperial Valley Earthquake Motion – El Centro Station

Acceleration and displacement values under the effect of the earthquake motion of the 1940 Imperial Valley – El Centro Station were gathered from experimental setups with sensors A05, A07, D18, and D19 located on the retaining wall model; A10 and A27 located in the foundation soil; A15 and A16 located in the backfill are presented in Table 5.8. Table 5.8a presents the maximum acceleration and displacement values obtained by these sensors for the cases with a reinforcement length of 2B while Table 5.8b presents the related information for the cases with a reinforcement length of 4B. Amongst them, the results of A07, D19, A10, and A16 are explained below.

Table 5.8. Peak Acceleration And Displacement Values For (a) Cases With A Reinforcement Length Of 2B And (b) Cases With A Reinforcement Length Of 4B Under The 1940 Imperial Valley Earthquake Motion – El Centro Station.

(a)

Peak Accelerations and Displacements						
Location:	**Instrument:**	**Case 01:**	**Case 02:**	**Case 03:**	**Case 04:**	**Case 05:**
On Wall	**A05 (g):**	0.44	0.45	0.42	0.44	0.41
	A07 (g):	0.70	0.56	0.57	0.56	0.57
	D18 (cm):	1.74	1.85	1.73	1.83	1.75
	D19 (cm):	1.80	1.83	1.80	1.89	1.82
In Soil	**A10 (g):**	0.36	0.39	0.36	0.37	0.34
	A27 (g):	0.37	0.43	0.37	0.39	0.36
	A15 (g):	0.41	0.43	0.41	0.42	0.39
	A16 (g):	0.45	0.45	0.43	0.43	0.42

(b)

Peak Accelerations and Displacements						
Location:	**Instrument:**	**Case 01:**	**Case 06:**	**Case 07:**	**Case 08:**	**Case 09:**
On Wall	**A05 (g):**	0.44	0.43	0.44	0.43	0.45
	A07 (g):	0.70	0.60	0.59	0.58	0.59
	D18 (cm):	1.74	1.73	1.71	1.72	1.66
	D19 (cm):	1.80	1.86	1.83	1.74	1.76
In Soil	**A10 (g):**	0.36	0.38	0.38	0.36	0.34
	A27 (g):	0.37	0.40	0.39	0.38	0.38
	A15 (g):	0.41	0.42	0.42	0.41	0.43
	A16 (g):	0.45	0.44	0.48	0.45	0.47

5.4.1.1. Acceleration On Top Of The Retaining Wall Model Under The 1940 Imperial Valley Earthquake Motion – El Centro Station. Figures 5.55 to 5.58 show the measured acceleration and Fourier amplitude Spectra of Cases 02 to 05 (the cases with the reinforcement length of 2B) compared to the unreinforced case, Case 01. Peak accelerations

obtained on top of the retaining wall model during experiments of Cases 01 to 05 are 0.70 g, 0.56 g, 0.57 g, 0.56 g, and 0.57 g as seen in Table 5.8a. Based on this, evaluated improvement percentages of these cases in acceleration are 20.0 %, 18.7 %, 19.8 %, and 19.4 %, respectively. Another outcome of the geogrid reinforcement is the decrease of spectral accelerations in short periods.

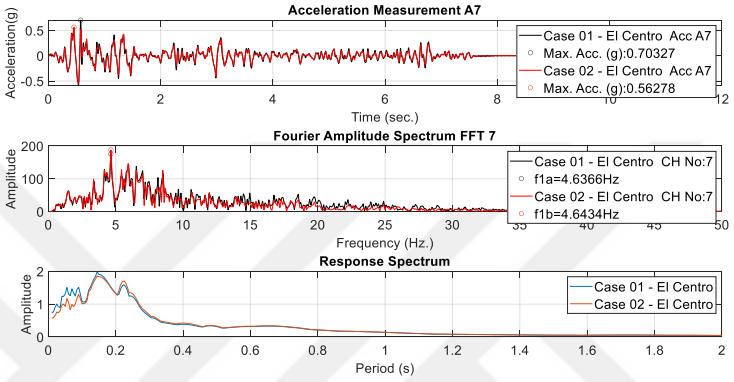

Figure 5.55. Comparison Of Acceleration, Fourier Amplitude, And Spectral Acceleration Values On Top Of The Retaining Wall Model Of Case 01 With Case 02 Under The 1940 Imperial Valley Earthquake Motion – El Centro Station.

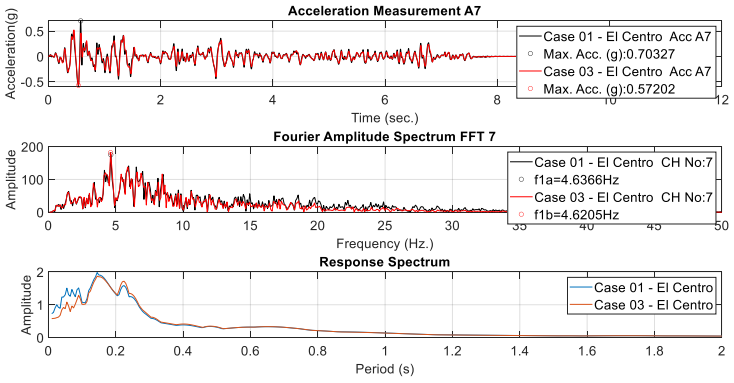

Figure 5.56. Comparison Of Acceleration, Fourier Amplitude, With Spectral Acceleration Values On Top Of The Retaining Wall Model Of Case 01 With Case 03 Under The 1940 Imperial Valley Earthquake Motion – El Centro Station.

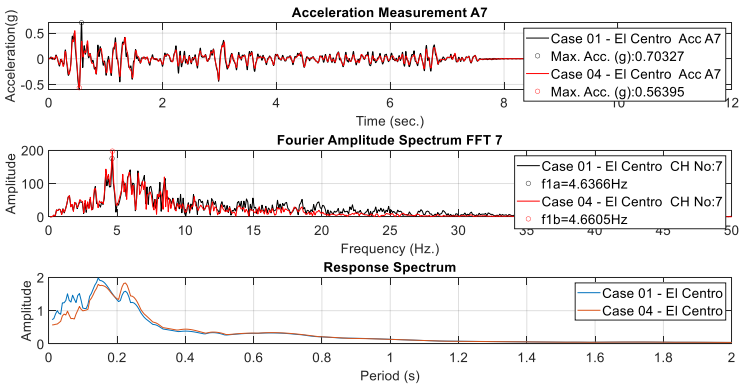

Figure 5.57 Comparison Of Acceleration, Fourier Amplitude, And Spectral Acceleration Values On Top Of The Retaining Wall Model Of Case 01 With Case 04 Under The 1940 Imperial Valley Earthquake Motion – El Centro Station.

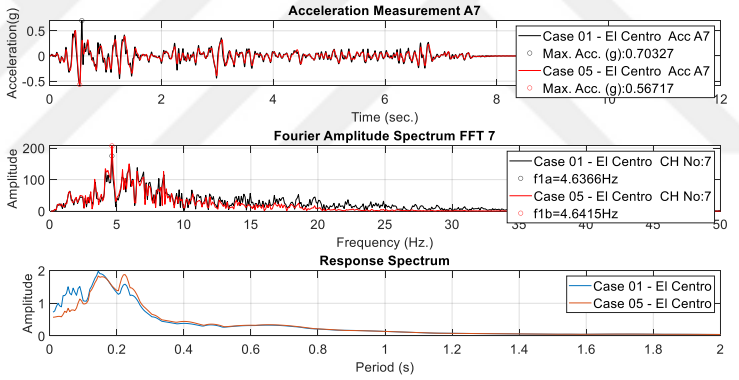

Figure 5.58. Comparison Of Acceleration, Fourier Amplitude, And Spectral Acceleration Values On Top Of The Retaining Wall Model Of Case 01 With Case 05 Under The 1940 Imperial Valley Earthquake Motion – El Centro Station.

Figures 5.59 to 5.62 show acceleration measures and the Fourier amplitudes of Cases 06 to 09 (cases with the reinforcement length of 4B) compared to the unreinforced case, Case 01. Peak accelerations obtained on top of the retaining wall model during experiments of Cases 01 and 06 to 09 are 0.70 g, 0.60 g, 0.59 g, 0.58 g, and 0.59 g accordingly as seen in Table 5.8b. Improvement percentages of acceleration values are 14.5 %, 16.1 %, 16.9 %, and 16.3 % respectively. Spectral acceleration values in short periods are decreased by the use of geogrid reinforcement as seen in Figures 5.59 to 5.62.

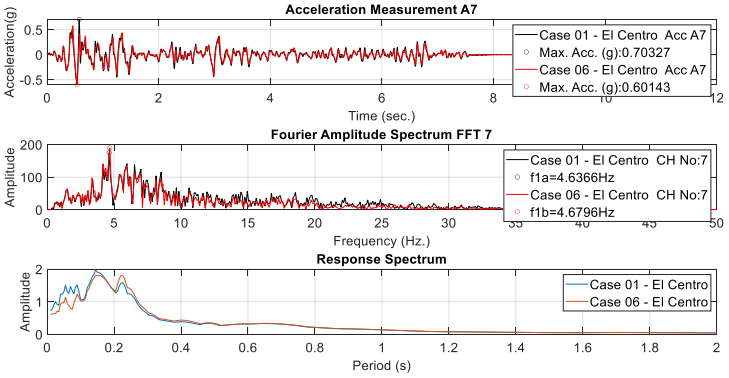

Figure 5.59. Comparison Of Acceleration, Fourier Amplitude, And Spectral Acceleration Values On Top Of The Retaining Wall Model Of Case 01 With Case 06 Under The 1940 Imperial Valley Earthquake Motion – El Centro Station.

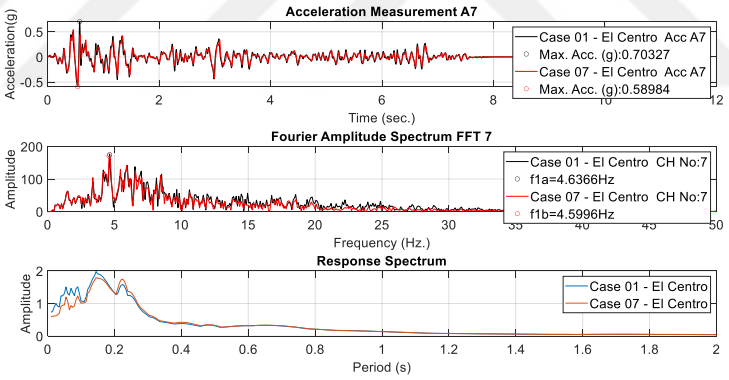

Figure 5.60. Comparison Of Acceleration, Fourier Amplitude, And Spectral Acceleration Values On Top Of The Retaining Wall Model Of Case 01 With Case 07 Under The 1940 Imperial Valley Earthquake Motion – El Centro Station.

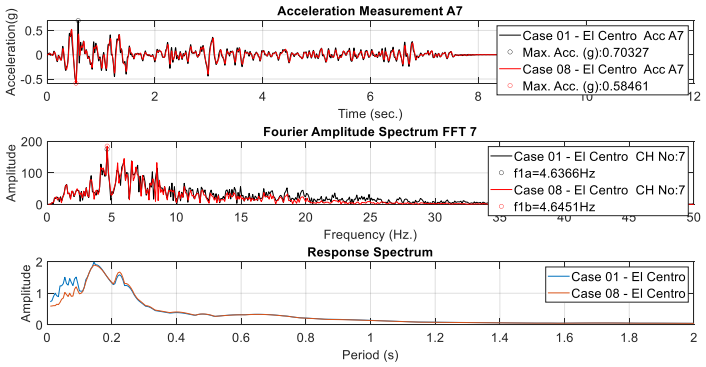

Figure 5.61. Comparison Of Acceleration, Fourier Amplitude, And Spectral Acceleration Values On Top Of The Retaining Wall Model Of Case 01 With Case 08 Under The 1940 Imperial Valley Earthquake Motion – El Centro Station.

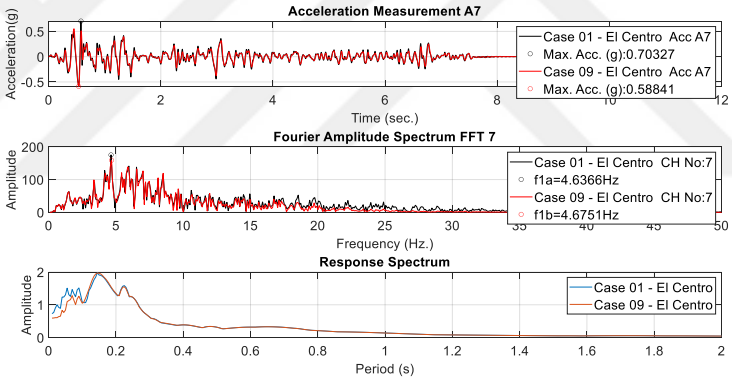

Figure 5.62. Comparison Of Acceleration, Fourier Amplitude, And Spectral Acceleration Values On Top Of The Retaining Wall Model Of Case 01 With Case 09 Under The 1940 Imperial Valley Earthquake Motion – El Centro Station.

5.4.1.2. Displacement On Top Of The Retaining Wall Model Under The 1940 Imperial Valley Earthquake Motion – El Centro Station. Figures 5.63 to 5.66 show displacement measures and the Fourier amplitudes of Cases 02 to 05 (the cases with the reinforcement length of 2B) in comparison with the unreinforced case, Case 01. Maximum displacement experienced on top of the retaining wall model is 1.80 cm, 1.83 cm, 1.89 cm, and 1.82 cm for Cases 01 to 05 as seen in Table 5.8a. The difference in the maximum displacement values

is -1.5 %, -0.3 %, -4.9 %, and -1.4 %. Unlike spectral accelerations, spectral displacement values are increased in reinforced cases as seen in Figures 5.63 to 5.66.

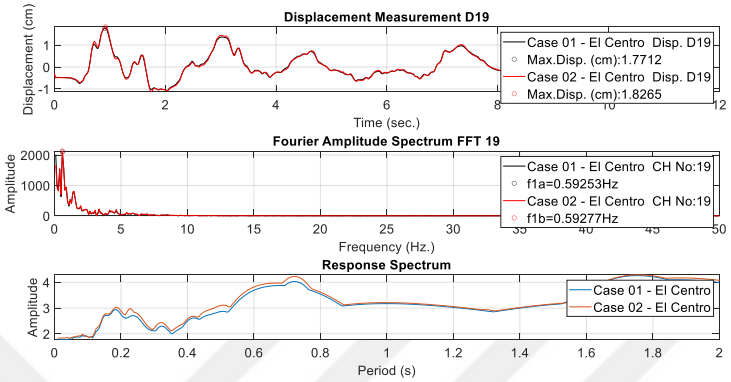

Figure 5.63. Comparison Of Displacement, Fourier Amplitude, And Spectral Displacement Values On Top Of The Retaining Wall Model Of Case 01 With Case 02 For Sensor D19 Under The 1940 Imperial Valley Earthquake Motion – El Centro Station.

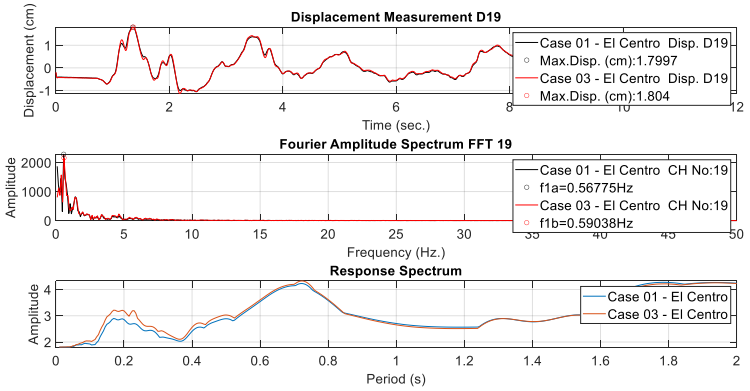

Figure 5.64. Comparison Of Displacement, Fourier Amplitude, And Spectral Displacement Values On Top Of The Retaining Wall Model Of Case 01 With Case 03 For Sensor D19 Under The 1940 Imperial Valley Earthquake Motion – El Centro Station.

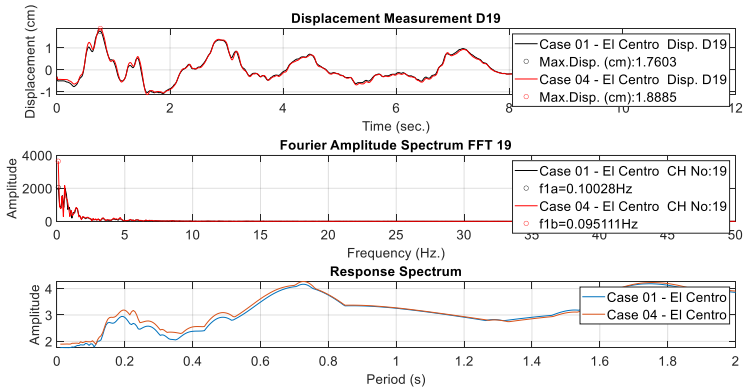

Figure 5.65. Comparison Of Displacement, Fourier Amplitude, And Spectral Displacement Values On Top Of The Retaining Wall Model Of Case 01 With Case 04 For Sensor D19 Under The 1940 Imperial Valley Earthquake Motion – El Centro Station.

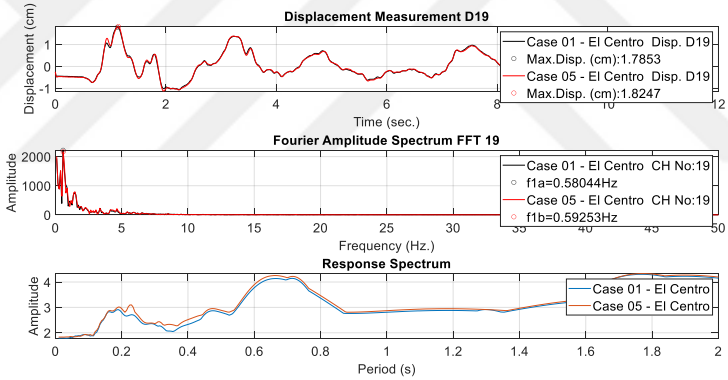

Figure 5.66. Comparison Of Displacement, Fourier Amplitude, And Spectral Displacement Values On Top Of The Retaining Wall Model Of Case 01 With Case 05 For Sensor D19 Under The 1940 Imperial Valley Earthquake Motion – El Centro Station.

Figures 5.67 to 5.70 present displacement measures and the Fourier amplitudes of Cases 06 to 09 (the cases with the reinforcement length of 4B) in comparison with the unreinforced case, Case 01. The maximum displacement values are 1.86 cm, 1.83 cm, 1.74 cm, and 1.76 cm for Cases 06 to 09 as seen in Table 5.8b. The difference in the maximum displacement values is -3.6 %, -1.7 %, 3.1 %, and 2.0 % in Cases 06 to 09. Similarly to Cases 02 to 05, spectral displacement values are increased for Cases 06 to 09 as seen in Figures 5.67 to 5.70.

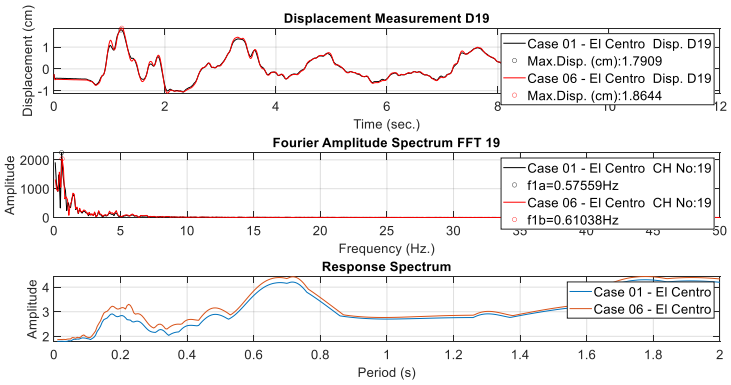

Figure 5.67. Comparison Of Displacement, Fourier Amplitude, And Spectral Displacement Values On Top Of The Retaining Wall Model Of Case 01 With Case 06 For Sensor D19 Under The 1940 Imperial Valley Earthquake Motion – El Centro Station.

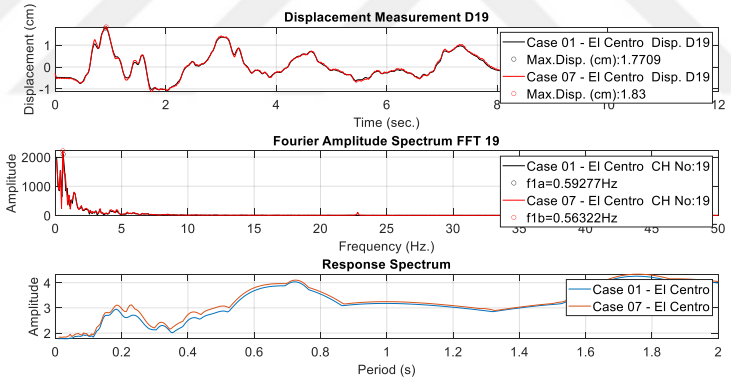

Figure 5.68. Comparison Of Displacement, Fourier Amplitude, And Spectral Displacement Values On Top Of The Retaining Wall Model Of Case 01 With Case 07 For Sensor D19 Under The 1940 Imperial Valley Earthquake Motion – El Centro Station.

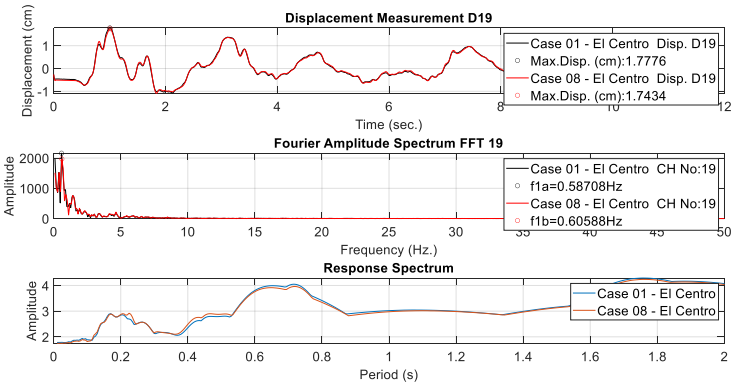

Figure 5.69. Comparison Of Displacement, Fourier Amplitude, And Spectral Displacement Values On Top Of The Retaining Wall Model Of Case 01 With Case 08 For Sensor D19 Under The 1940 Imperial Valley Earthquake Motion – El Centro Station.

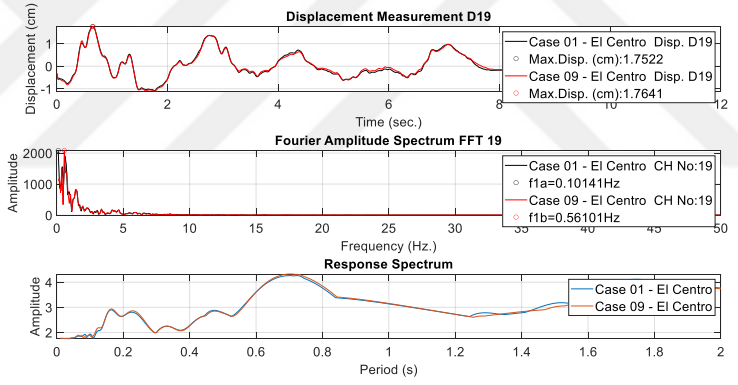

Figure 5.70. Comparison Of Displacement, Fourier Amplitude, And Spectral Displacement Values On Top Of The Retaining Wall Model Of Case 01 With Case 09 For Sensor D19 Under The 1940 Imperial Valley Earthquake Motion – El Centro Station.

5.4.1.3. Acceleration Below The Reinforced Soil Foundation Under The 1940 Imperial Valley Earthquake Motion – El Centro Station. Figures 5.71 to 5.74 show acceleration measures and the Fourier amplitudes of Cases 02 to 05 (cases with the reinforcement length of 2B) compared to the unreinforced case, Case 01. Peak accelerations measured below the reinforcement zone during experiments of Cases 01 to 05 are 0.36 g, 0.39 g, 0.36 g, 0.37 g, and 0.34 g as seen in Table 5.8a. The difference in the maximum accelerations is -9.2 %, 1.5

%, -1.4 %, and 5.4 %. The reduction of spectral acceleration values in short periods is seen in Figures 5.71 to 5.74

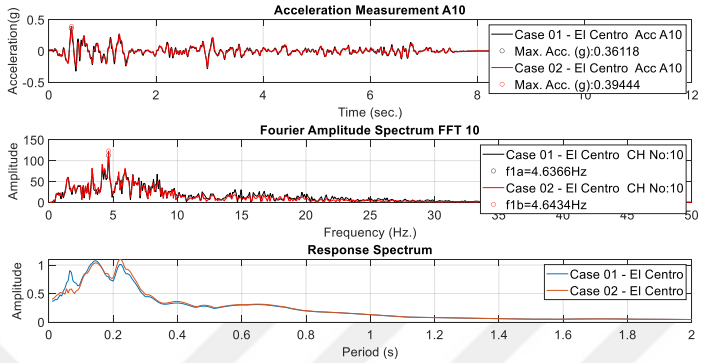

Figure 5.71. Comparison Of Acceleration, Fourier Amplitude, And Spectral Acceleration Values Below The Reinforced Soil Foundation Of The Retaining Wall Model Of Case 01 With Case 02 For Accelerometer A10 Under The 1940 Imperial Valley Earthquake Motion – El Centro Station.

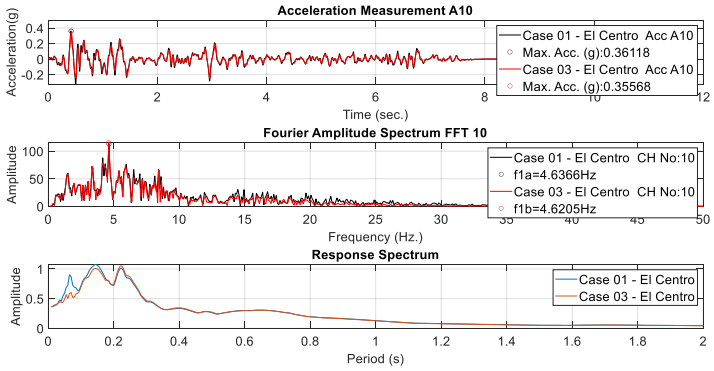

Figure 5.72. Comparison Of Acceleration, Fourier Amplitude, And Spectral Acceleration Values Below The Reinforced Soil Foundation Of The Retaining Wall Model Of Case 01 With Case 03 For Accelerometer A10 Under The 1940 Imperial Valley Earthquake Motion – El Centro Station.

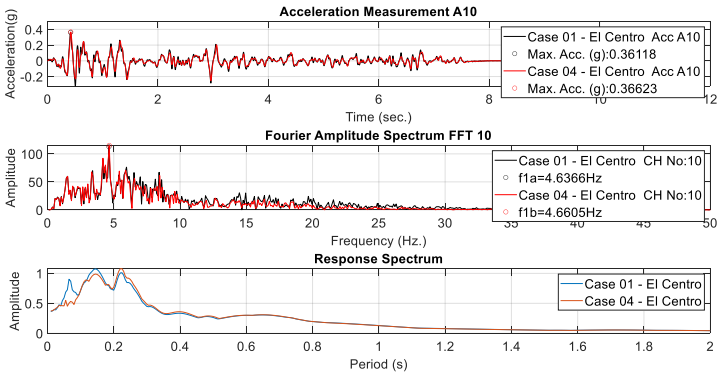

Figure 5.73. Comparison Of Acceleration, Fourier Amplitude, And Spectral Acceleration Values Below The Reinforced Soil Foundation Of The Retaining Wall Model Of Case 01 With Case 04 For Accelerometer A10 Under The 1940 Imperial Valley Earthquake Motion – El Centro Station.

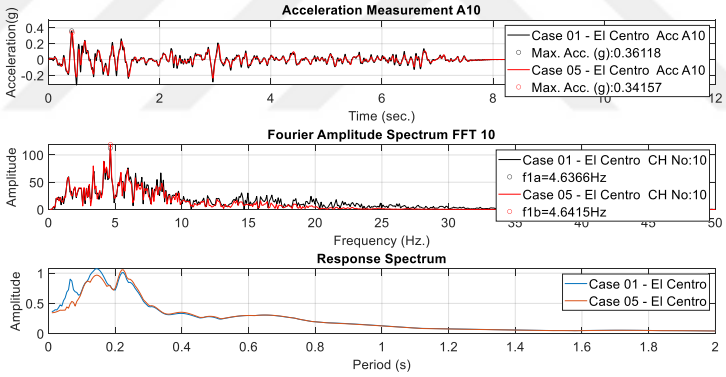

Figure 5.74. Comparison Of Acceleration, Fourier Amplitude, And Spectral Acceleration Values Below The Reinforced Soil Foundation Of The Retaining Wall Model Of Case 01 With Case 05 For Accelerometer A10 Under The 1940 Imperial Valley Earthquake Motion – El Centro Station.

Figures 5.75 to 5.78 show the Fourier amplitudes and acceleration measures of Cases 06 to 09 (cases with the reinforcement length of 4B) compared to the unreinforced case, Case 01. Peak accelerations measured below the reinforcement zone during experiments of Cases 06 to 09 are 0.38 g, 0.38 g, 0.36 g, and 0.34 g as seen in Table 5.8b. The difference in the maximum acceleration values is -6.0 %, -5.1 %, -0.4 %, and 5.6 %.

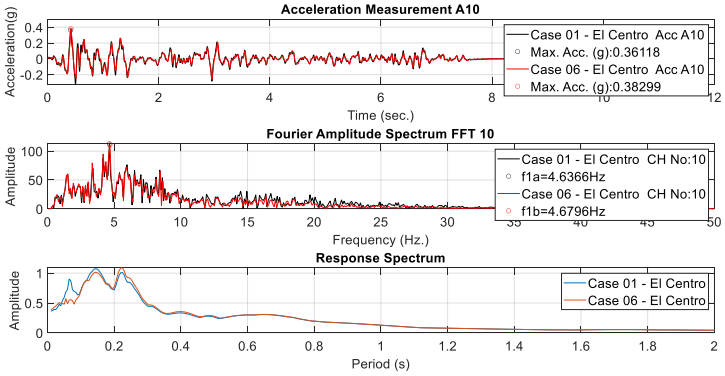

Figure 5.75. Comparison Of Acceleration, Fourier Amplitude, And Spectral Acceleration Values Below The Reinforced Soil Foundation Of The Retaining Wall Model Of Case 01 With Case 06 For Accelerometer A10 Under The 1940 Imperial Valley Earthquake Motion – El Centro Station.

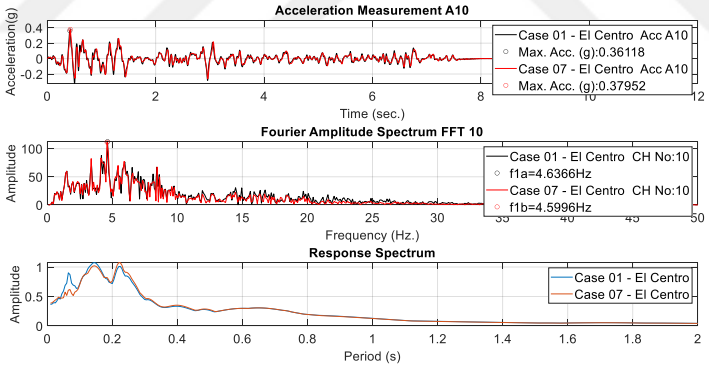

Figure 5.76. Comparison Of Acceleration, Fourier Amplitude, And Spectral Acceleration Values Below The Reinforced Soil Foundation Of The Retaining Wall Model Of Case 01 With Case 07 For Accelerometer A10 Under The 1940 Imperial Valley Earthquake Motion – El Centro Station.

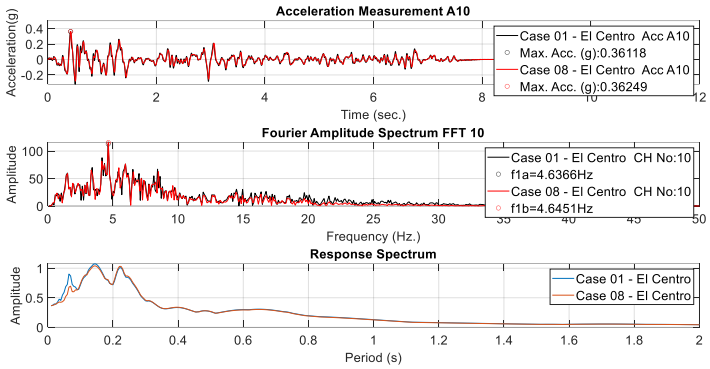

Figure 5.77. Comparison Of Acceleration, Fourier Amplitude, And Spectral Acceleration Values Below The Reinforced Soil Foundation Of The Retaining Wall Model Of Case 01 With Case 08 For Accelerometer A10 Under The 1940 Imperial Valley Earthquake Motion – El Centro Station.

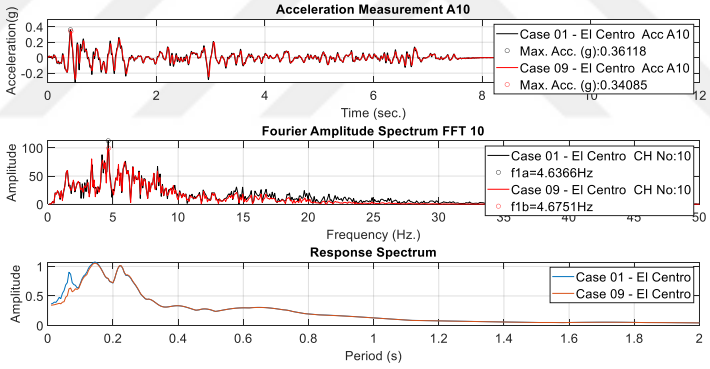

Figure 5.78. Comparison Of Acceleration, Fourier Amplitude, And Spectral Acceleration Values Below The Reinforced Soil Foundation Of The Retaining Wall Model Of Case 01 With Case 09 For Accelerometer A10 Under The 1940 Imperial Valley Earthquake Motion – El Centro Station.

5.4.1.4. Acceleration In The Backfill Of The Retaining Wall Model Under The 1940 Imperial Valley Earthquake Motion – El Centro Station. Figures 5.79 to 5.82 show the Fourier amplitudes and acceleration measures of Cases 02 to 05 (cases with the reinforcement length of 2B) compared to the unreinforced case, Case 01. Peak accelerations measured behind the retaining wall model during experiments of Cases 01 to 05 are 0.45 g,

0.45 g, 0.43 g, 0.43 g, and 0.42 g as seen in Table 5.8a. The difference in the maximum accelerations is 0.3 %, 3.6 %, 4.1 %, and 5.6 %. The reduction of the peak ground acceleration in the backfill increases with the increasing number of reinforcement layers. The reduction in spectral accelerations is also seen in Figures 5.79 to 5.82.

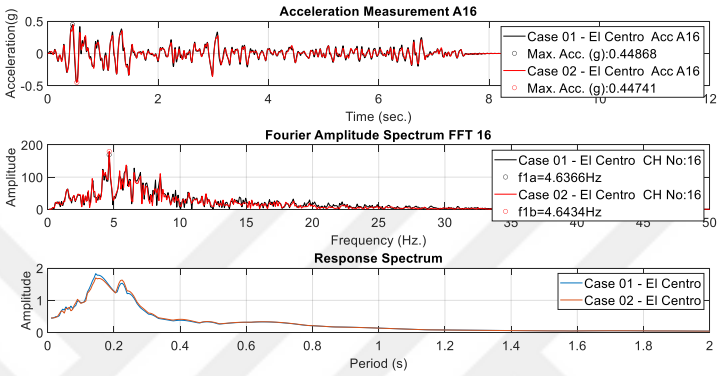

Figure 5.79. Comparison Of Acceleration, Fourier Amplitude, And Spectral Acceleration Values In The Backfill Of The Retaining Wall Model Of Case 01 With Case 02 For Accelerometer A16 Under The 1940 Imperial Valley Earthquake Motion – El Centro Station.

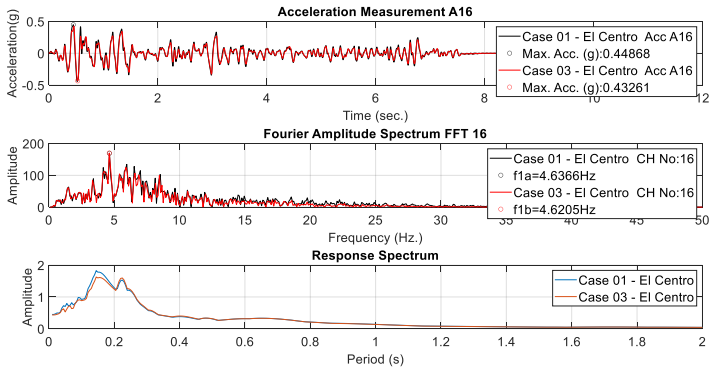

Figure 5.80. Comparison Of Acceleration, Fourier Amplitude, And Spectral Acceleration Values In The Backfill Of The Retaining Wall Model Of Case 01 With Case 03 For Accelerometer A16 Under The 1940 Imperial Valley Earthquake Motion – El Centro Station.

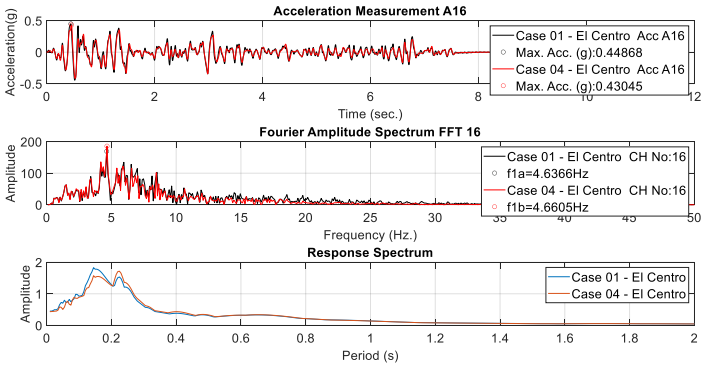

Figure 5.81. Comparison Of Acceleration, Fourier Amplitude, And Spectral Acceleration Values In The Backfill Of The Retaining Wall Model Of Case 01 With Case 04 For Accelerometer A16 Under The 1940 Imperial Valley Earthquake Motion – El Centro Station.

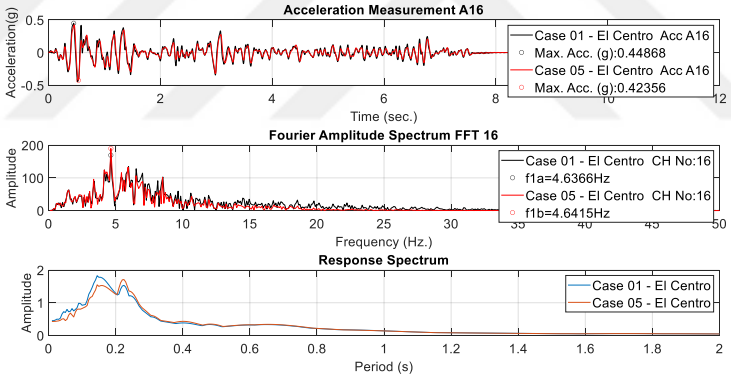

Figure 5.82. Comparison Of Acceleration, Fourier Amplitude, And Spectral Acceleration Values In The Backfill Of The Retaining Wall Model Of Case 01 With Case 05 For Accelerometer A16 Under The 1940 Imperial Valley Earthquake Motion – El Centro Station.

Figures 5.83 to 5.86 show the Fourier amplitudes and acceleration measures of Cases 06 to 09 (cases with the reinforcement length of 4B) compared to the unreinforced case, Case 01. Peak accelerations measured in the backfill of the retaining wall model during experiments of Cases 06 to 09 are 0.44 g, 0.48 g, 0.45 g, and 0.47 g as seen in Table 5.8b. The difference in the maximum accelerations is 2.6 %, -8.0 %, -0.7, and -4.7, respectively.

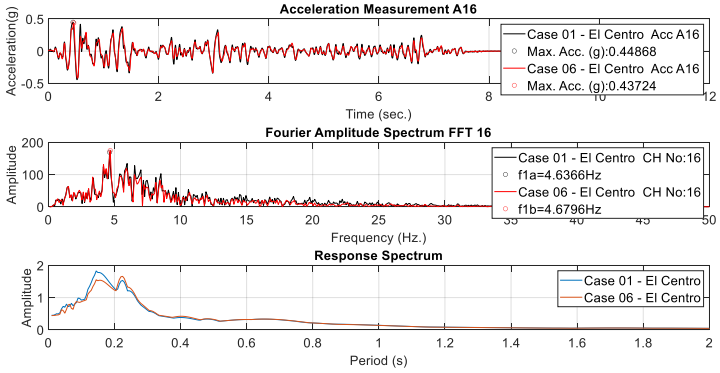

Figure 5.83. Comparison Of Acceleration, Fourier Amplitude, And Spectral Acceleration Values In The Backfill Of The Retaining Wall Model Of Case 01 With Case 06 For Accelerometer A16 Under The 1940 Imperial Valley Earthquake Motion – El Centro Station.

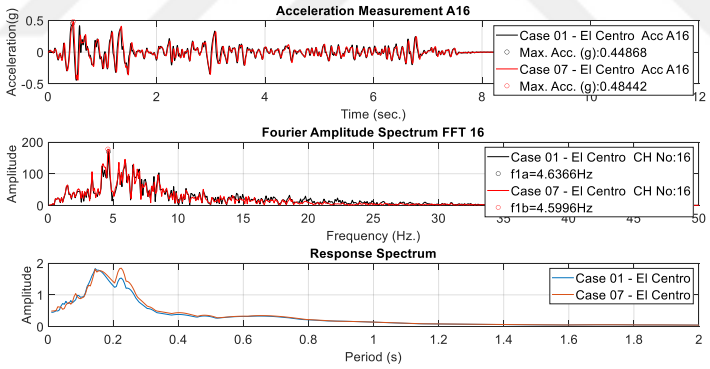

Figure 5.84. Comparison Of Acceleration, Fourier Amplitude, And Spectral Acceleration Values In The Backfill Of The Retaining Wall Model Of Case 01 With Case 07 For Accelerometer A16 Under The 1940 Imperial Valley Earthquake Motion – El Centro Station.

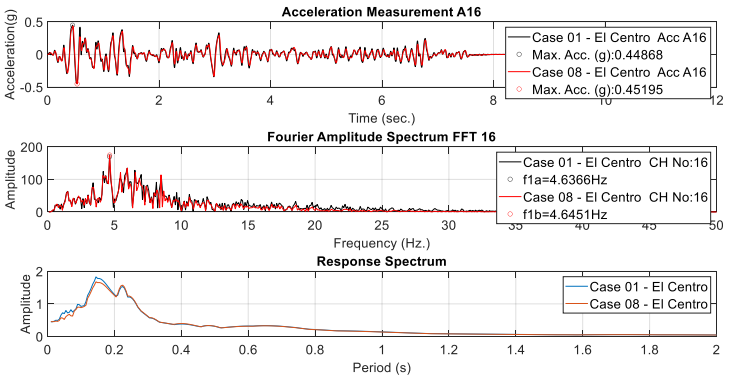

Figure 5.85. Comparison Of Acceleration, Fourier Amplitude, And Spectral Acceleration Values In The Backfill Of The Retaining Wall Model Of Case 01 With Case 08 For Accelerometer A16 Under The 1940 Imperial Valley Earthquake Motion – El Centro Station.

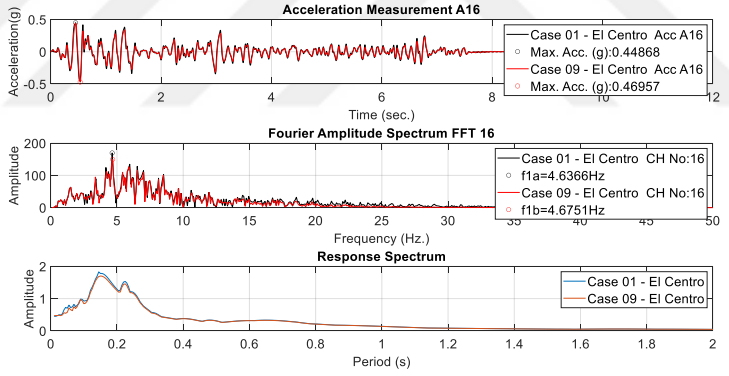

Figure 5.86. Comparison Of Acceleration, Fourier Amplitude, And Spectral Acceleration Values In The Backfill Of The Retaining Wall Model Of Case 01 With Case 08 For Accelerometer A16 Under The 1940 Imperial Valley Earthquake Motion – El Centro Station.

5.4.2. Performance Of The Retaining Wall Model Under The 1999 Kocaeli Earthquake Motion - Iznik Station

Acceleration and displacement values under the effect of the earthquake motion of the 1999 Kocaeli – Iznik Station were obtained from experimental setups with sensors A05, A07, D18, and D19 located on the retaining wall model; A10 and A27 located in the foundation soil; A15 and A16 located in the backfill are presented in Table 5.9. Table 5.9a presents the maximum acceleration and displacement values obtained by these sensors for the cases with a reinforcement length of 2B while Table 5.9b presents the related information for the cases with a reinforcement length of 4B. Amongst them, the results of A07, D19, A10, and A16 are explained below.

Table 5.9. Peak Acceleration And Displacement Values For (a) Cases With A Reinforcement Length Of 2B And (b) Cases With A Reinforcement Length Of 4B Under The 1999 Kocaeli Earthquake Motion - Iznik Station

(a)

Peak Accelerations and Displacements						
Location:	**Instrument:**	**Case 01:**	**Case 02:**	**Case 03:**	**Case 04:**	**Case 05:**
On Wall	**A05 (g):**	0.12	0.13	0.12	0.12	0.12
	A07 (g):	0.15	0.15	0.14	0.13	0.14
	D18 (cm):	0.97	1.20	1.11	1.11	1.13
	D19 (cm):	1.11	1.21	1.17	1.18	1.18
In Soil	**A10 (g):**	0.11	0.11	0.11	0.11	0.11
	A27 (g):	0.11	0.12	0.11	0.11	0.12
	A15 (g):	0.12	0.12	0.12	0.12	0.12
	A16 (g):	0.13	0.13	0.13	0.12	0.13

Table 5.9. Peak Acceleration And Displacement Values For (a) Cases With A Reinforcement Length Of 2B And (b) Cases With A Reinforcement Length Of 4B Under The 1999 Kocaeli Earthquake Motion - Iznik Station. (cont.)

(b)

Peak Accelerations and Displacements						
Location:	**Instrument:**	**Case 01:**	**Case 06:**	**Case 07:**	**Case 08:**	**Case 09:**
On Wall	**A05 (g):**	0.12	0.13	0.12	0.12	0.12
	A07 (g):	0.15	0.14	0.14	0.13	0.13
	D18 (cm):	0.97	1.16	1.08	1.12	0.98
	D19 (cm):	1.11	1.23	1.16	1.11	1.03
In Soil	**A10 (g):**	0.11	0.11	0.11	0.10	0.10
	A27 (g):	0.11	0.12	0.12	0.11	0.10
	A15 (g):	0.12	0.12	0.12	0.12	0.11
	A16 (g):	0.13	0.13	0.13	0.12	0.12

5.4.2.1. Acceleration On Top Of The Retaining Wall Model Under The 1999 Kocaeli Earthquake Motion - Iznik Station. Figures 5.87 to 5.90 show acceleration measures and the Fourier amplitudes on top of the retaining wall model under the effect of the earthquake motion of the 1999 Kocaeli – Iznik Station for Cases 02 to 05 (cases with the reinforcement length of 2B). The peak accelerations obtained are 0.15 g, 0.15 g, 0.14 g, 0.13 g, and 0.14 g for Cases 01 to 05 as per Table 5.9a. The difference in the peak accelerations is 5.4 %, 8.3 %, 12.6 %, and 8.8 % with the increasing number of reinforcement layers. The decrease in spectral acceleration is observed in a longer range of periods as seen in Figures 5.87 to 5.90.

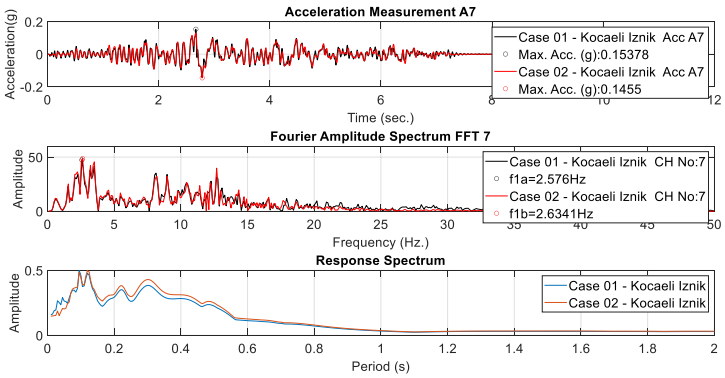

Figure 5.87. Comparison Of Acceleration, Fourier Amplitude, And Spectral Acceleration Values On Top Of The Retaining Wall Model Of Case 01 With Case 02 For Accelerometer A07 Under The 1999 Kocaeli Earthquake Motion - Iznik Station.

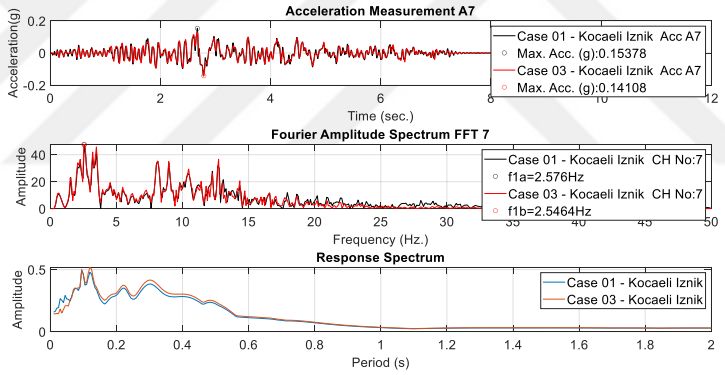

Figure 5.88. Comparison Of Acceleration, Fourier Amplitude, And Spectral Acceleration Values On Top Of The Retaining Wall Model Of Case 01 With Case 03 For Accelerometer A07 Under The 1999 Kocaeli Earthquake Motion - Iznik Station.

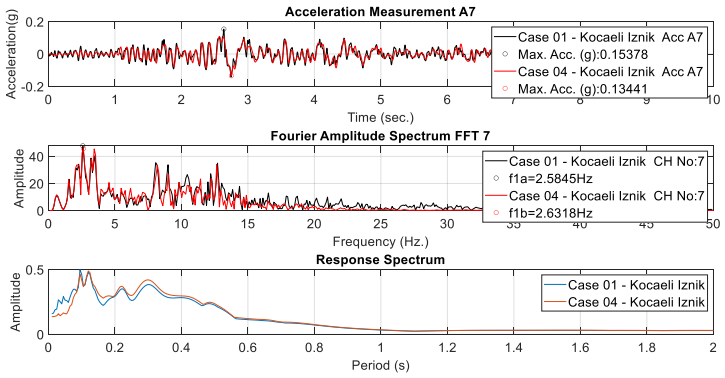

Figure 5.89. Comparison Of Acceleration, Fourier Amplitude, And Spectral Acceleration Values On Top Of The Retaining Wall Model Of Case 01 With Case 04 For Accelerometer A07 Under The 1999 Kocaeli Earthquake Motion - Iznik Station.

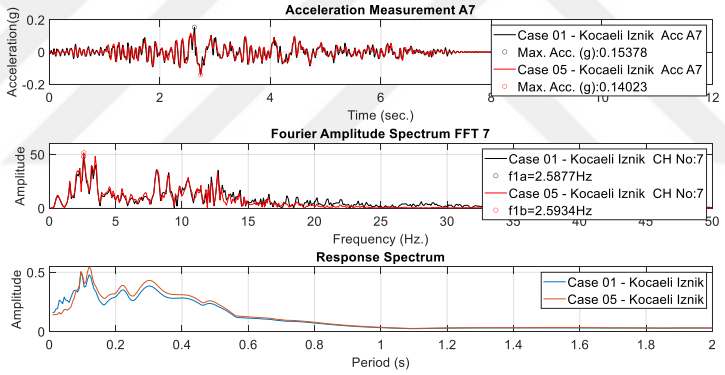

Figure 5.90. Comparison Of Acceleration, Fourier Amplitude, And Spectral Acceleration Values On Top Of The Retaining Wall Model Of Case 01 With Case 05 For Accelerometer A07 Under The 1999 Kocaeli Earthquake Motion - Iznik Station.

Figures 5.91 to 5.94 show acceleration measures and the Fourier amplitudes on top of the retaining wall model under the effect of the earthquake motion of the 1999 Kocaeli – Iznik Station. The peak accelerations obtained are 0.14 g, 0.14 g, 0.13 g, and 0.13 g for Cases 06 to 09 (cases with the reinforcement length of 4B). The difference in the peak accelerations is 6.3 %, 10.1 %, 13.4 %, and 14.2 %. The reduction in peak accelerations and the decrease in spectral accelerations in a longer range of periods are seen in Figures 5.91 to 5.94.

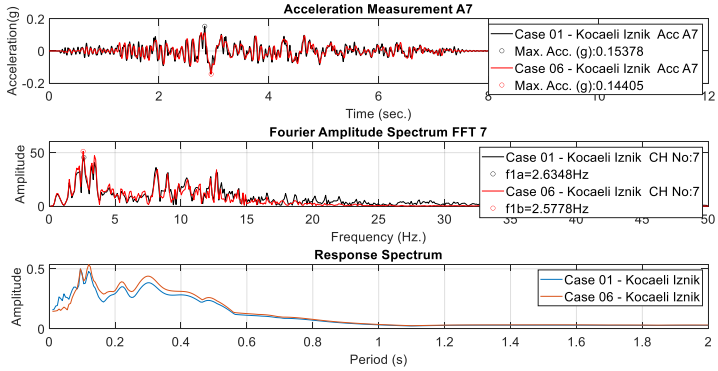

Figure 5.91. Comparison Of Acceleration, Fourier Amplitude, and Spectral Acceleration Values On Top Of The Retaining Wall Model Of Case 01 With Case 06 For Accelerometer A07 Under The 1999 Kocaeli Earthquake Motion - Iznik Station.

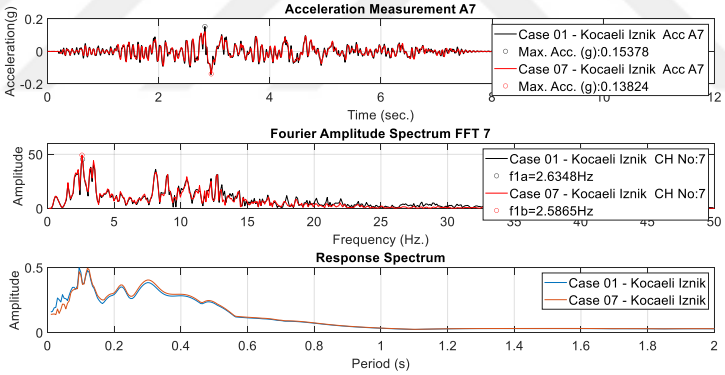

Figure 5.92. Comparison Of Acceleration, Fourier Amplitude, And Spectral Acceleration Values On Top Of The Retaining Wall Model Of Case 01 With Case 07 For Accelerometer A07 Under The 1999 Kocaeli Earthquake Motion - Iznik Station.

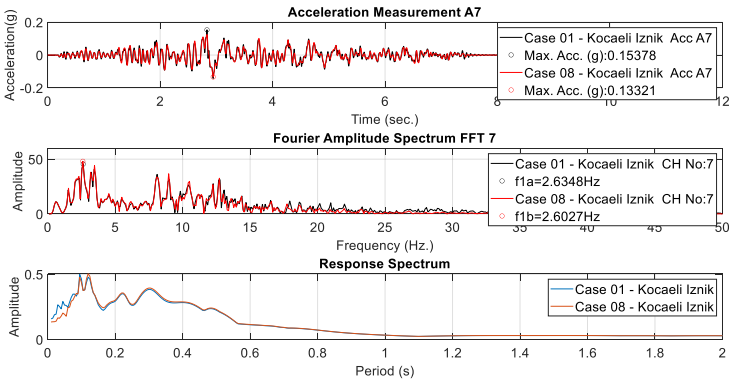

Figure 5.93. Comparison Of Acceleration, Fourier Amplitude, And Spectral Acceleration Values On Top Of The Retaining Wall Model Of Case 01 With Case 08 For Accelerometer A07 Under The 1999 Kocaeli Earthquake Motion - Iznik Station.

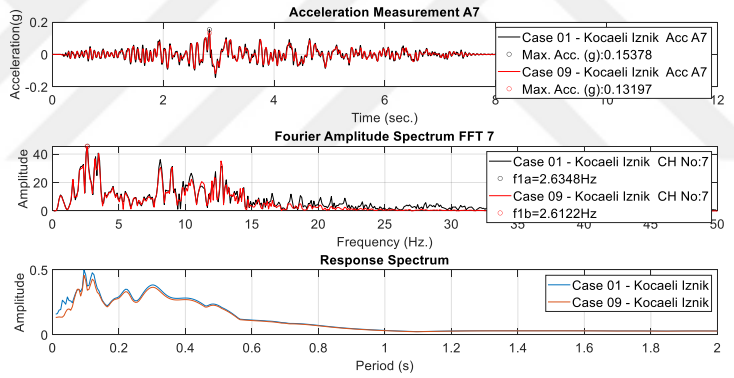

Figure 5.94. Comparison Of Acceleration, Fourier Amplitude, And Spectral Acceleration Values On Top Of The Retaining Wall Model Of Case 01 With Case 09 For Accelerometer A07 Under The 1999 Kocaeli Earthquake Motion - Iznik Station.

5.4.2.2. Displacement On Top Of The Retaining Wall Model Under The 1999 Kocaeli Earthquake Motion - Iznik Station. Figures 5.95 to 5.98 present the maximum displacements and Fourier amplitudes on top of the retaining wall model during the earthquake motion of the 1999 Kocaeli – Iznik Station. The values are 1.11 cm, 1.21 cm, 1.17 cm, 1.18 cm, and 1.18 cm for Cases 01 to 05 (cases with the reinforcement length of 2B), respectively. The change in peak displacements is -8.6 %, -5.7 %, -6.0 %, and -6.5 % for Cases 02 to 05 based on the unreinforced case, Case 01.

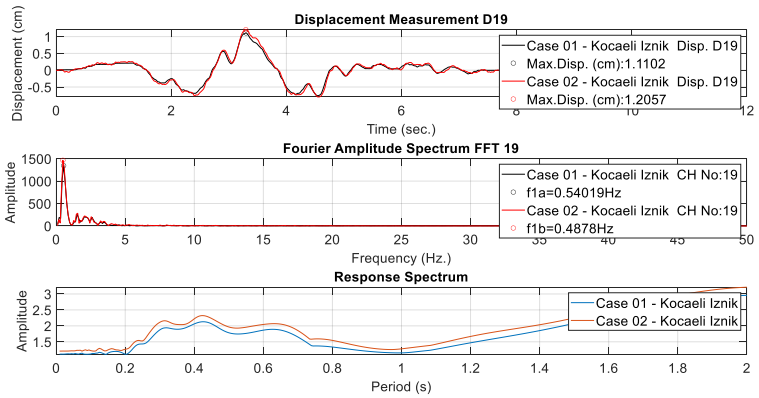

Figure 5.95. Comparison Of Displacement, Fourier Amplitude, And Spectral Displacement Values On Top Of The Retaining Wall Model Of Case 01 With Case 02 For Sensor D19 Under The 1999 Kocaeli Earthquake Motion - Iznik Station.

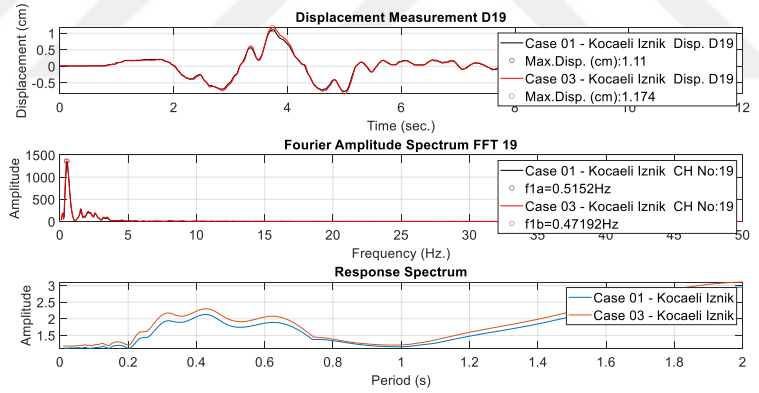

Figure 5.96. Comparison Of Displacement, Fourier Amplitude, And Spectral Displacement Values On Top Of The Retaining Wall Model Of Case 01 With Case 03 For Sensor D19 Under The 1999 Kocaeli Earthquake Motion - Iznik Station.

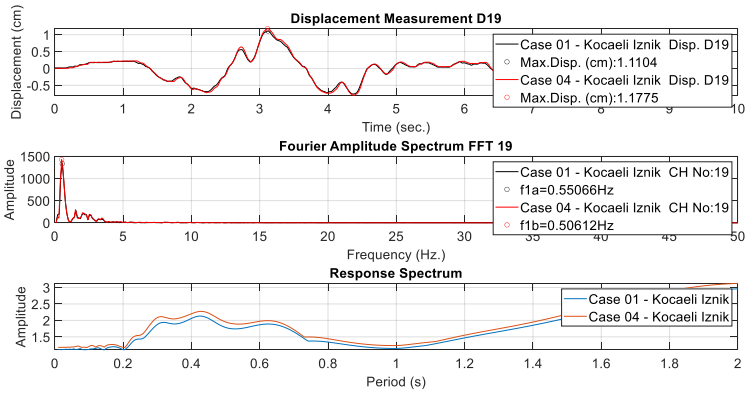

Figure 5.97. Comparison Of Displacement, Fourier Amplitude, And Spectral Displacement Values On Top Of The Retaining Wall Model Of Case 01 With Case 04 For Sensor D19 Under The 1999 Kocaeli Earthquake Motion - Iznik Station.

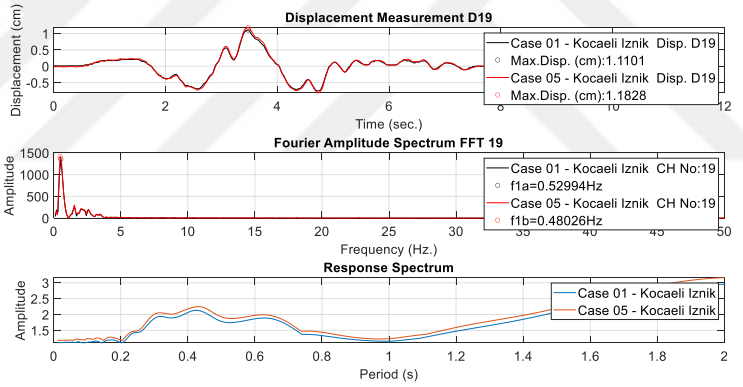

Figure 5.98. Comparison Of Displacement, Fourier Amplitude, And Spectral Displacement Values On Top Of The Retaining Wall Model Of Case 01 With Case 05 For Sensor D19 Under The 1999 Kocaeli Earthquake Motion - Iznik Station.

Figures 5.99 to 5.102 present the maximum displacements and Fourier amplitudes on top of the retaining wall model during the earthquake motion of the 1999 Kocaeli – Iznik Station. The values are 1.23 cm, 1.16 cm, 1.11 cm, and 1.03 cm for Cases 06 to 09 (cases with the reinforcement length of 4B), respectively. The change in peak displacements is -11.1 %, -4.5 %, -0.2 %, and 7.0 % for Cases 06 to 09 based on the unreinforced case, Case 01.

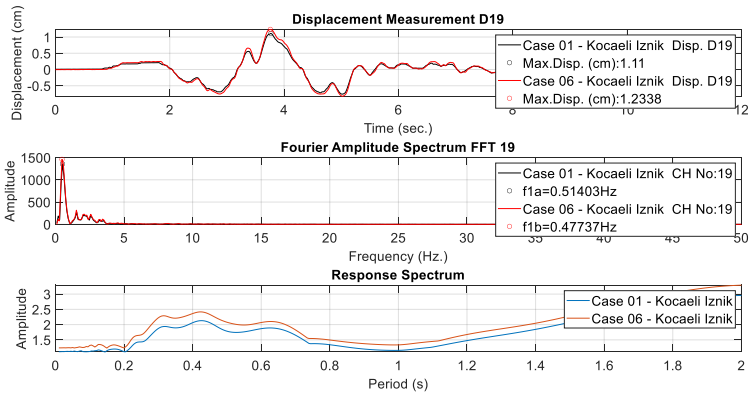

Figure 5.99. Comparison Of Displacement, Fourier Amplitude, And Spectral Displacement Values On Top Of The Retaining Wall Model Of Case 01 With Case 06 For Sensor D19 Under The 1999 Kocaeli Earthquake Motion - Iznik Station.

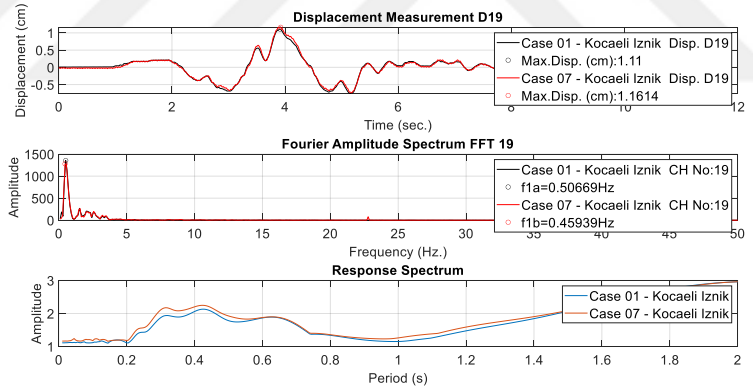

Figure 5.100. Comparison Of Displacement, Fourier Amplitude, And Spectral Displacement Values On Top Of The Retaining Wall Model Of Case 01 With Case 07 For Sensor D19 Under The 1999 Kocaeli Earthquake Motion - Iznik Station.

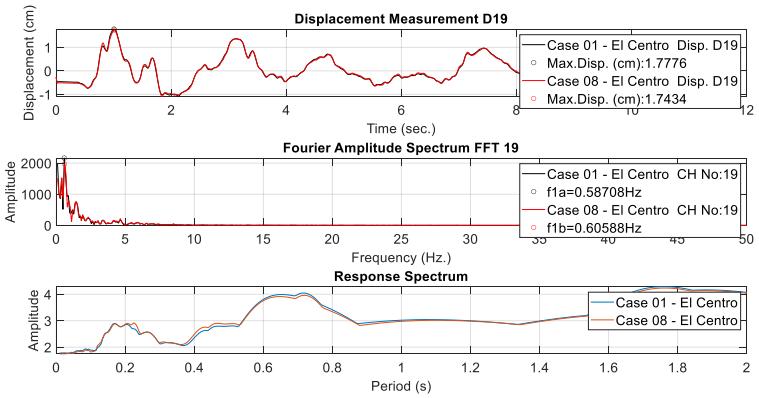

Figure 5.101. Comparison Of Displacement, Fourier Amplitude, And Spectral Displacement Values On Top Of The Retaining Wall Model Of Case 01 With Case 08 For Sensor D19 Under The 1999 Kocaeli Earthquake Motion - Iznik Station.

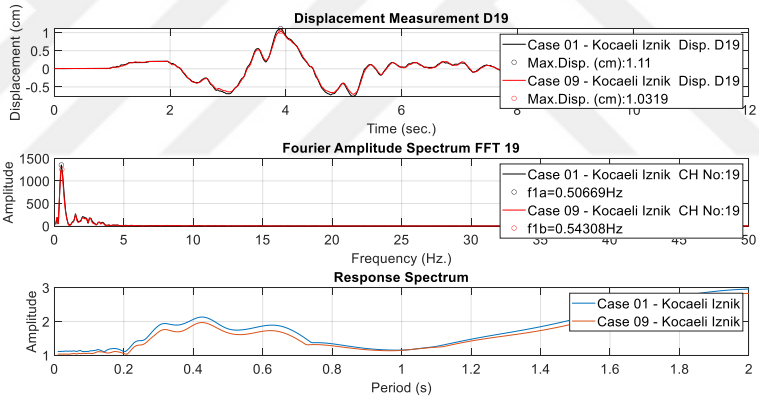

Figure 5.102. Comparison Of Displacement, Fourier Amplitude, And Spectral Displacement Values On Top Of The Retaining Wall Model Of Case 01 With Case 09 For Sensor D19 Under The 1999 Kocaeli Earthquake Motion - Iznik Station.

5.4.2.3. Acceleration Below The Reinforcement Zone Under The 1999 Kocaeli Earthquake Motion - Iznik Station. Figures 5.103 to 5.106 show the Fourier amplitudes and acceleration measures below the reinforcement zone under the effect of the earthquake motion of the 1999 Kocaeli – Iznik Station. The peak accelerations obtained are 0.11 g, 0.11 g, 0.11 g, 0.11 g, and 0.11 g for Cases 01 to 05 (cases with the reinforcement length of 2B) as seen in Table 5.9a. The difference in peak accelerations is -4.4 %, -0.5 %, -0.2 %, and -3.0 %.

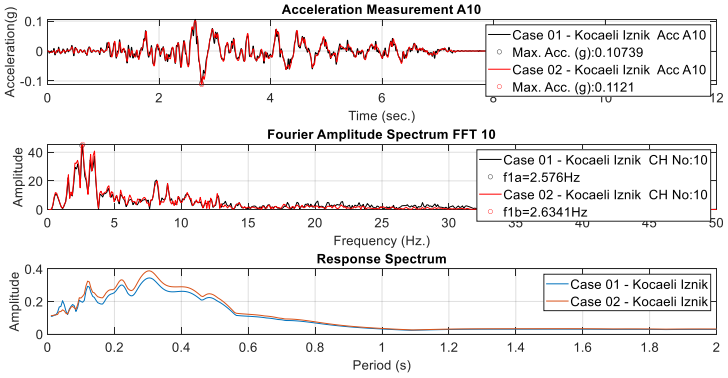

Figure 5.103. Comparison Of Acceleration, Fourier Amplitude, And Spectral Acceleration Values Below The Reinforced Soil Foundation Of The Retaining Wall Model Of Case 01 With Case 02 For Accelerometer A10 Under The 1999 Kocaeli Earthquake Motion - Iznik Station.

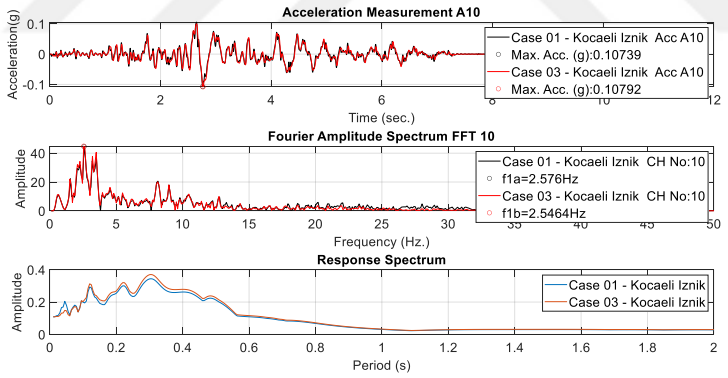

Figure 5.104. Comparison Of Acceleration, Fourier Amplitude, And Spectral Acceleration Values Below The Reinforced Soil Foundation Of The Retaining Wall Model Of Case 01 With Case 03 For Accelerometer A10 Under The 1999 Kocaeli Earthquake Motion - Iznik Station.

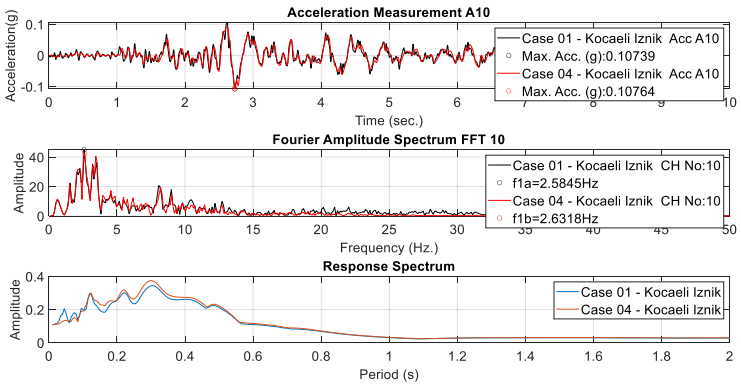

Figure 5.105. Comparison Of Acceleration, Fourier Amplitude, And Spectral Acceleration Values Below The Reinforced Soil Foundation Of The Retaining Wall Model Of Case 01 With Case 04 For Accelerometer A10 Under The 1999 Kocaeli Earthquake Motion - Iznik Station.

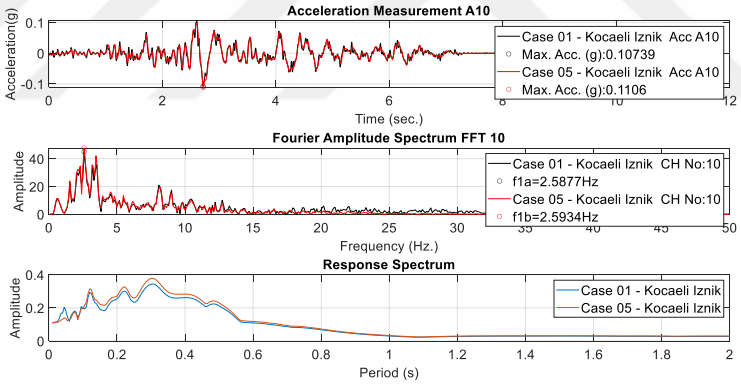

Figure 5.106. Comparison Of Acceleration, Fourier Amplitude, And Spectral Acceleration Values Below The Reinforced Soil Foundation Of The Retaining Wall Model Of Case 01 With Case 05 For Accelerometer A10 Under The 1999 Kocaeli Earthquake Motion - Iznik Station.

Figures 5.107 to 5.110 show the Fourier amplitude and acceleration measures below the reinforcement zone under the effect of the earthquake motion of the 1999 Kocaeli – Iznik Station. The peak accelerations obtained are 0.11 g, 0.11 g, 0.10 g, and 0.10 g for Cases 06

to 09 (cases with the reinforcement length of 4B) as seen in Table 5.9b. The difference in maximum accelerations is -4.6 %, -2.1 %, 3.4 %, and 9.7 %.

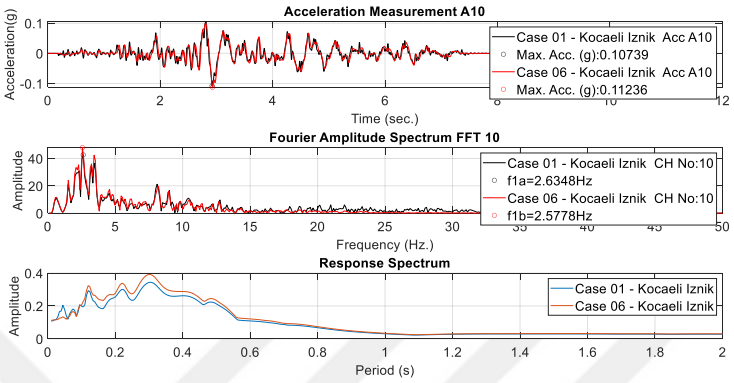

Figure 5.107. Comparison Of Acceleration, Fourier Amplitude, And Spectral Acceleration Values Below The Reinforced Soil Foundation Of The Retaining Wall Model Of Case 01 With Case 06 For Accelerometer A10 Under The 1999 Kocaeli Earthquake Motion - Iznik Station.

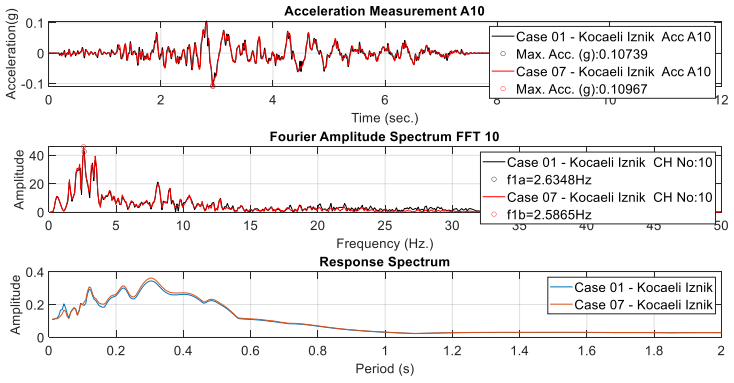

Figure 5.108. Comparison Of Acceleration, Fourier Amplitude, And Spectral Acceleration Values Below The Reinforced Soil Foundation Of The Retaining Wall Model Of Case 01 With Case 07 For Accelerometer A10 Under The 1999 Kocaeli Earthquake Motion - Iznik Station.

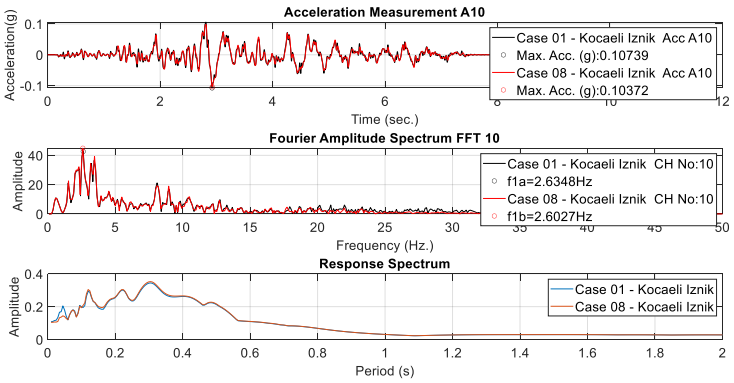

Figure 5.109. Comparison Of Acceleration, Fourier Amplitude, And Spectral Acceleration Values Below The Reinforced Soil Foundation Of The Retaining Wall Model Of Case 01 With Case 08 For Accelerometer A10 Under The 1999 Kocaeli Earthquake Motion - Iznik Station.

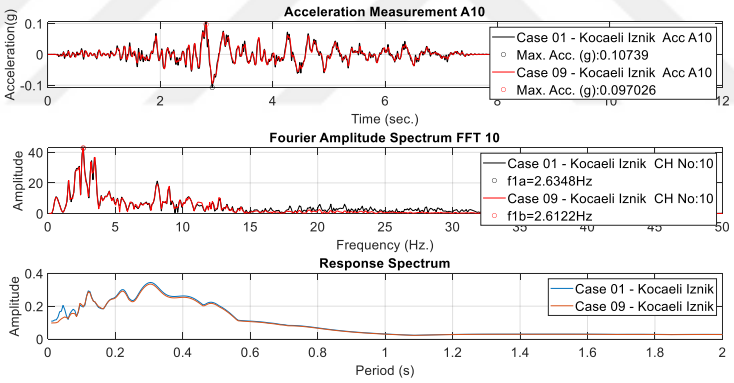

Figure 5.110. Comparison Of Acceleration, Fourier Amplitude, And Spectral Acceleration Values Below The Reinforced Soil Foundation Of The Retaining Wall Model Of Case 01 With Case 09 For Accelerometer A10 Under The 1999 Kocaeli Earthquake Motion - Iznik Station.

5.4.2.4. Acceleration In The Backfill Of The Retaining Wall Model Under The 1999 Kocaeli Earthquake Motion - Iznik Station. Figures 5.111 to 5.114 show acceleration measures and the Fourier amplitudes in the backfill of the retaining wall model under the effect of the earthquake motion of the 1999 Kocaeli – Iznik Station. The peak accelerations obtained are

0.13 g, 0.13 g, 0.13 g, 0.12 g, and 0.13 g for Cases 01 to 05 according to Table 5.9a. The change in peak accelerations is -0.7 %, 3.7 %, 6.6 %, and 3.1 %.

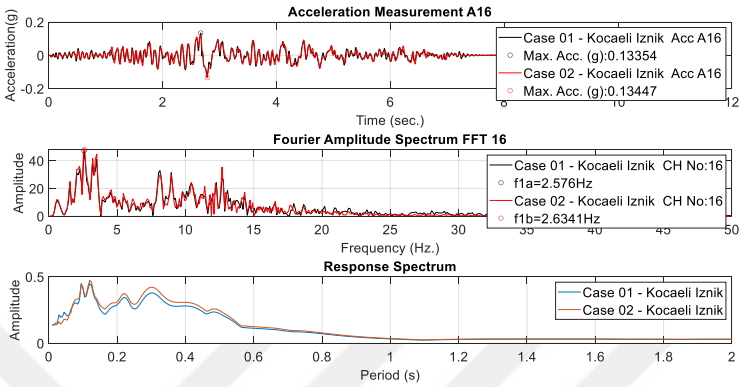

Figure 5.111. Comparison Of Acceleration, Fourier Amplitude, And Spectral Acceleration Values In The Backfill Of The Retaining Wall Model Of Case 01 With Case 02 For Accelerometer A16 Under The 1999 Kocaeli Earthquake Motion - Iznik Station.

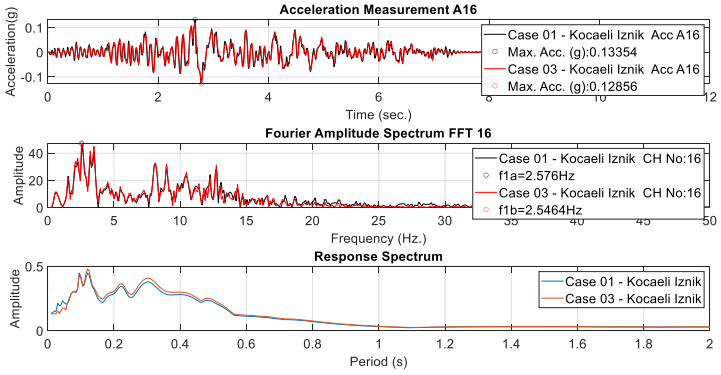

Figure 5.112. Comparison Of Acceleration, Fourier Amplitude, And Spectral Acceleration Values In The Backfill Of The Retaining Wall Model Of Case 01 With Case 03 For Accelerometer A16 Under The 1999 Kocaeli Earthquake Motion - Iznik Station.

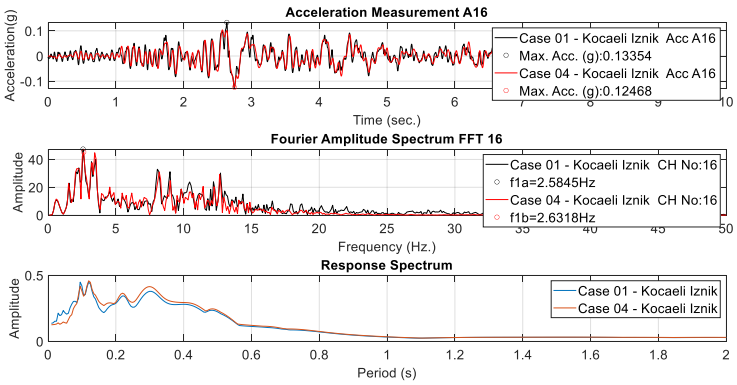

Figure 5.113. Comparison Of Acceleration, Fourier Amplitude, And Spectral Acceleration Values In The Backfill Of The Retaining Wall Model Of Case 01 With Case 04 For Accelerometer A16 Under The 1999 Kocaeli Earthquake Motion - Iznik Station.

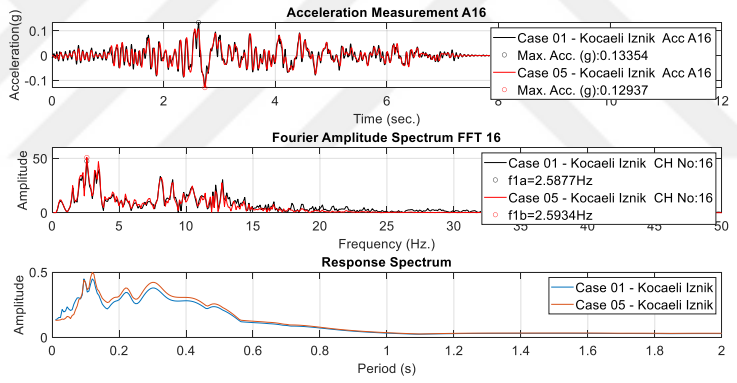

Figure 5.114. Comparison Of Acceleration, Fourier Amplitude, And Spectral Acceleration Values In The Backfill Of The Retaining Wall Model Of Case 01 With Case 05 For Accelerometer A16 Under The 1999 Kocaeli Earthquake Motion - Iznik Station.

Figures 5.115 to 5.118 show acceleration measures and the Fourier amplitudes in the backfill of the retaining wall model under the effect of the earthquake motion of the 1999 Kocaeli - Iznik. The peak accelerations obtained are 0.13 g, 0.13 g, 0.12 g, and 0.12 g for Cases 06 to 09 as per Table 5.9b. The difference in the maximum accelerations is 1.4 %, 0.2 %, 7.1 %, and 7.5 %.

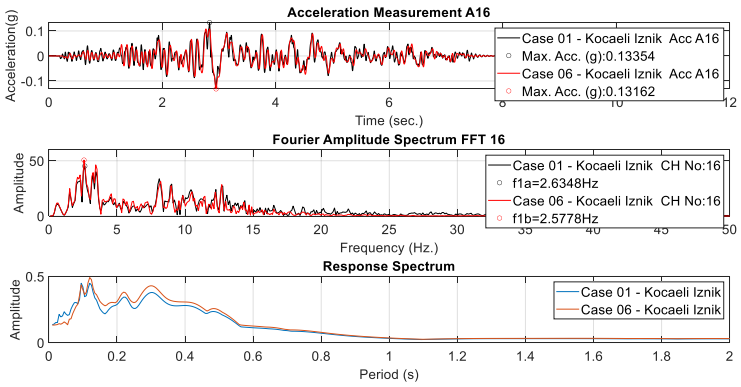

Figure 5.115. Comparison Of Acceleration, Fourier Amplitude, And Spectral Acceleration Values In The Backfill Of The Retaining Wall Model Of Case 01 With Case 06 For Accelerometer A16 Under The 1999 Kocaeli Earthquake Motion - Iznik Station.

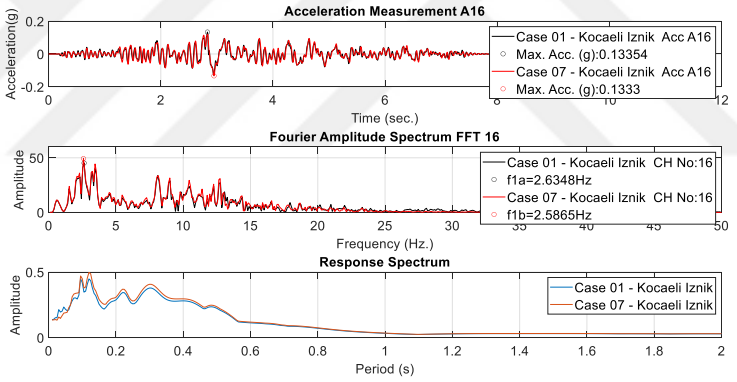

Figure 5.116. Comparison Of Acceleration, Fourier Amplitude, And Spectral Acceleration Values In The Backfill Of The Retaining Wall Model Of Case 01 With Case 07 For Accelerometer A16 Under The 1999 Kocaeli Earthquake Motion - Iznik Station.

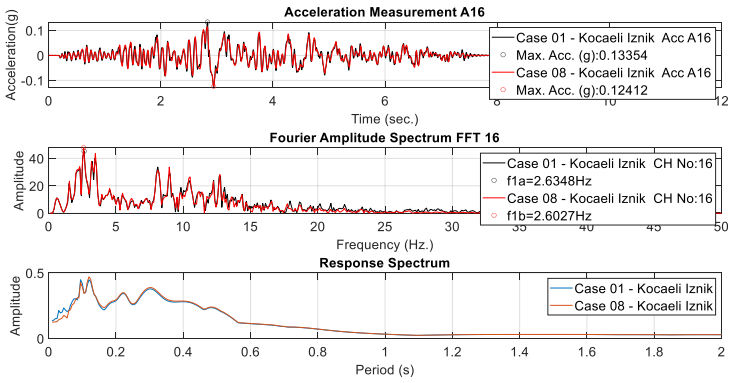

Figure 5.117. Comparison Of Acceleration, Fourier Amplitude, And Spectral Acceleration Values In The Backfill Of The Retaining Wall Model Of Case 01 With Case 08 For Accelerometer A16 Under The 1999 Kocaeli Earthquake Motion - Iznik Station.

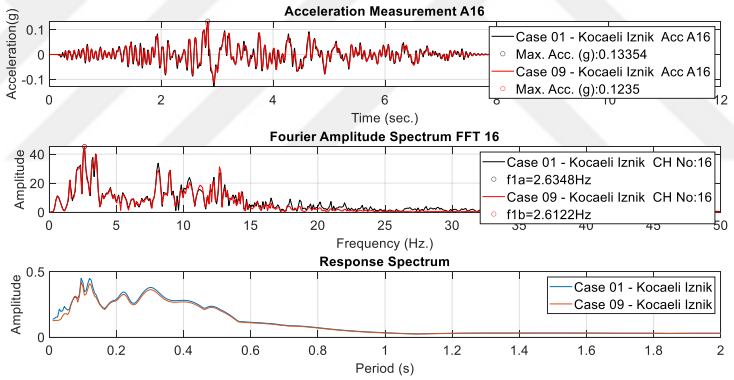

Figure 5.118. Comparison Of Acceleration, Fourier Amplitude, and Spectral Acceleration Values In The Backfill Of The Retaining Wall Model Of Case 01 With Case 09 For Accelerometer A16 Under The 1999 Kocaeli Earthquake Motion - Iznik Station.

5.4.3. Performance Of The Retaining Wall Model Under The 1999 Kocaeli Earthquake Motion - Izmit Station

Acceleration and displacement values under the effect of the earthquake motion of the 1999 Kocaeli – Izmit Station were gathered from experimental setups with sensors A05, A07, D18, and D19 located on the retaining wall model; A10 and A27 located in the

foundation soil; A15 and A16 located in the backfill are presented in Table 5.10. Table 5.10a presents the maximum acceleration and displacement values obtained by these sensors for the cases with a reinforcement length of 2B while Table 5.10b presents the related information for the cases with a reinforcement length of 4B. Amongst them, the results of A07, D19, A10, and A16 are explained below.

Table 5.10. Peak Acceleration And Displacement Values For (a) Cases With A Reinforcement Length Of 2B And (b) Cases With A Reinforcement Length Of 4B Under The 1999 Kocaeli Earthquake Motion - Izmit Station.

(a)

Peak Accelerations and Displacements						
Location:	**Instrument:**	**Case 01:**	**Case 02:**	**Case 03:**	**Case 04:**	**Case 05:**
On Wall	**A05 (g):**	0.26	0.26	0.27	0.26	0.27
	A07 (g):	0.32	0.30	0.30	0.29	0.30
	D18 (cm):	1.69	1.75	1.77	1.68	1.65
	D19 (cm):	1.71	1.75	1.93	1.78	1.78
In Soil	**A10 (g):**	0.23	0.23	0.24	0.23	0.22
	A27 (g):	0.25	0.24	0.26	0.25	0.24
	A15 (g):	0.25	0.25	0.27	0.26	0.25
	A16 (g):	0.27	0.28	0.28	0.27	0.27

(b)

Peak Accelerations and Displacements						
Location:	**Instrument:**	**Case 01:**	**Case 06:**	**Case 07:**	**Case 08:**	**Case 09:**
On Wall	**A05 (g):**	0.26	0.27	0.27	0.27	0.25
	A07 (g):	0.32	0.30	0.30	0.31	0.29
	D18 (cm):	1.69	1.71	1.74	1.80	1.73
	D19 (cm):	1.71	1.77	1.82	1.81	1.72

Table 5.10. Peak Acceleration And Displacement Values For (a) Cases With A Reinforcement Length Of 2B And (b) Cases With A Reinforcement Length Of 4B Under The 1999 Kocaeli Earthquake Motion - Izmit Station. ((b) cont.)

Peak Accelerations and Displacements						
Location:	**Instrument:**	**Case 01:**	**Case 06:**	**Case 07:**	**Case 08:**	**Case 09:**
In Soil	**A10 (g):**	0.23	0.23	0.23	0.23	0.22
	A27 (g):	0.25	0.24	0.25	0.25	0.23
	A15 (g):	0.25	0.25	0.26	0.27	0.24
	A16 (g):	0.27	0.27	0.28	0.29	0.26

5.4.3.1. Acceleration On Top Of The Retaining Wall Model Under The 1999 Kocaeli Earthquake Motion - Izmit Station. Figures 5.119 to 5.122 show acceleration measures and the Fourier amplitudes on top of the retaining wall model under the effect of the earthquake motion of the 1999 Kocaeli – Izmit Station. The peak accelerations obtained are 0.32 g, 0.30 g, 0.30 g, 0.29 g, and 0.30 g for Cases 01 to 05 as seen in Table 5.10a. The change in the maximum accelerations is 6.0 %, 6.2 %, 10.0 %, and 6.3 % accordingly. The reduction in peak acceleration and spectral acceleration values can be seen in Figures 5.119 to 5.122.

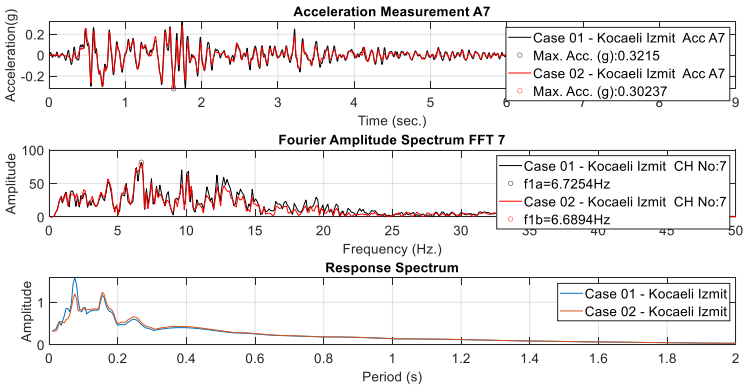

Figure 5.119. Comparison Of Acceleration, Fourier Amplitude, And Spectral Acceleration Values On Top Of The Retaining Wall Model Of Case 01 With Case 02 For Accelerometer A07 Under The 1999 Kocaeli Earthquake Motion - Izmit Station.

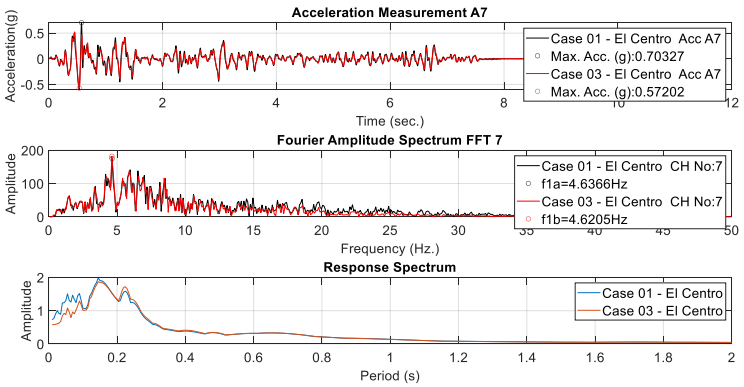

Figure 5.120. Comparison Of Acceleration, Fourier Amplitude, And Spectral Acceleration Values On Top Of The Retaining Wall Model Of Case 01 With Case 03 For Accelerometer A07 Under The 1999 Kocaeli Earthquake Motion - Izmit Station.

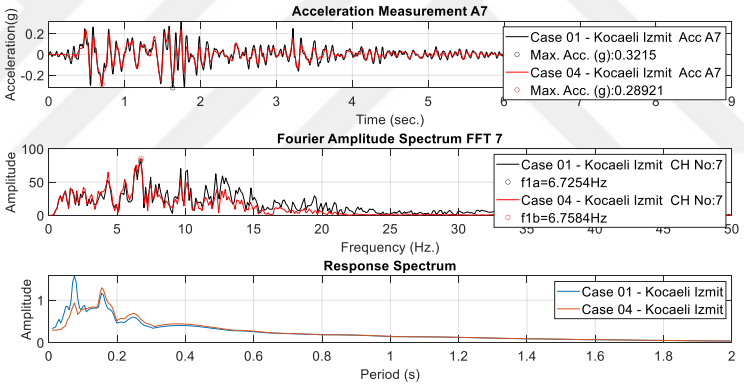

Figure 5.121. Comparison Of Acceleration, Fourier Amplitude, And Spectral Acceleration Values On Top Of The Retaining Wall Model Of Case 01 With Case 04 For Accelerometer A07 Under The 1999 Kocaeli Earthquake Motion - Izmit Station.

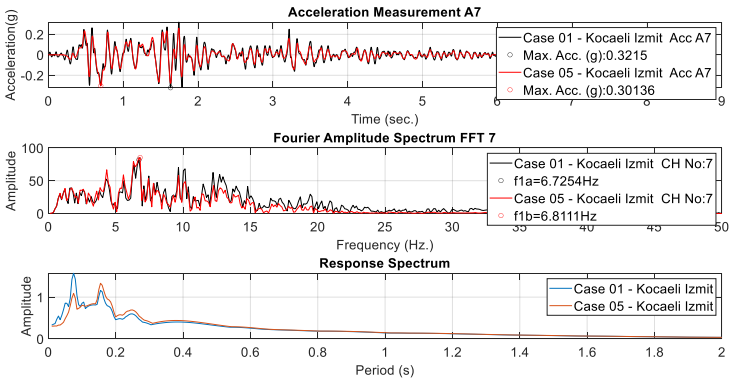

Figure 5.122. Comparison Of Acceleration, Fourier Amplitude, And Spectral Acceleration Values On Top Of The Retaining Wall Model Of Case 01 With Case 05 For Accelerometer A07 Under The 1999 Kocaeli Earthquake Motion - Izmit Station.

Figures 5.123 to 5.126 show acceleration measures and the Fourier amplitudes on top of the retaining wall model under the effect of the earthquake motion of the 1999 Kocaeli – Izmit Station. The peak accelerations obtained are 0.30 g, 0.30 g, 0.31 g, and 0.29 g for Cases 06 to 09 according to Table 5.10b. The difference in the maximum accelerations is 6.6 %, 5.8 %, 4.9 %, and 11.0 % respectively.

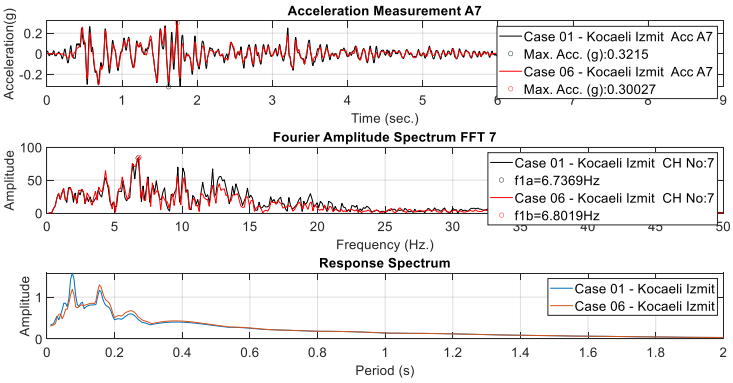

Figure 5.123. Comparison Of Acceleration, Fourier Amplitude, And Spectral Acceleration Values On Top Of The Retaining Wall Model Of Case 01 With Case 06 For Accelerometer A07 Under The 1999 Kocaeli Earthquake Motion - Izmit Station.

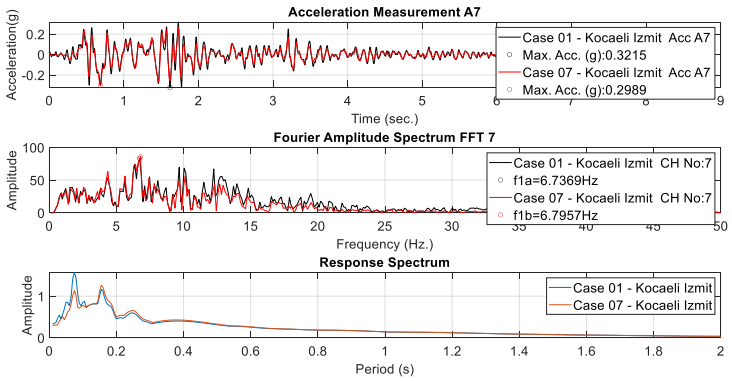

Figure 5.124. Comparison Of Acceleration, Fourier Amplitude, And Spectral Acceleration Values On Top Of The Retaining Wall Model Of Case 01 With Case 07 For Accelerometer A07 Under The 1999 Kocaeli Earthquake Motion - Izmit Station.

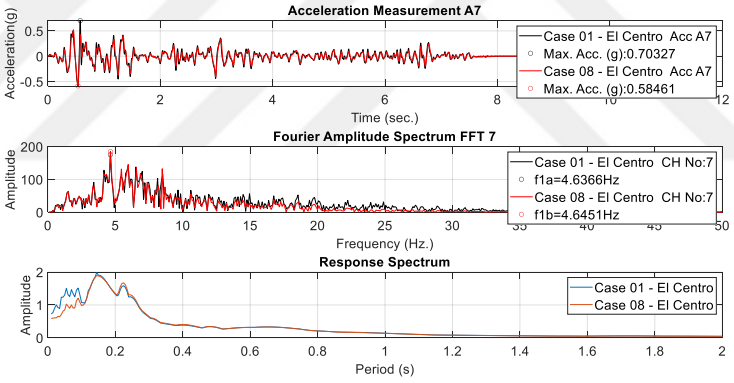

Figure 5.125. Comparison Of Acceleration, Fourier Amplitude, And Spectral Acceleration Values On Top Of The Retaining Wall Model Of Case 01 With Case 08 For Accelerometer A07 Under The 1999 Kocaeli Earthquake Motion - Izmit Station.

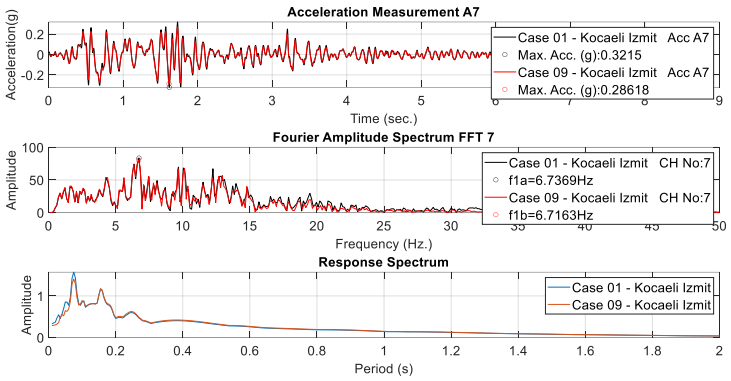

Figure 5.126. Comparison Of Acceleration, Fourier Amplitude, And Spectral Acceleration Values On Top Of The Retaining Wall Model Of Case 01 And Case 09 For Accelerometer A07 Under The 1999 Kocaeli Earthquake Motion - Izmit Station.

5.4.3.2. Displacement On Top Of The Retaining Wall Model Under The 1999 Kocaeli Earthquake Motion - Izmit Station. Figures 5.127 to 5.130 present the maximum displacements on top of the retaining wall model during the earthquake motion of the 1999 Kocaeli – Izmit Station. The values are 1.71 cm, 1.75 cm, 1.93 cm, 1.78 cm, and 1.78 cm for Cases 01 to 05 according to Table 5.10a. The change in peak displacements is -2.6 %, -13.1 %, -4.0 %, and -4.0 % for Cases 02 to 05 (cases with the reinforcement length of 2B) based on the unreinforced case, Case 01.

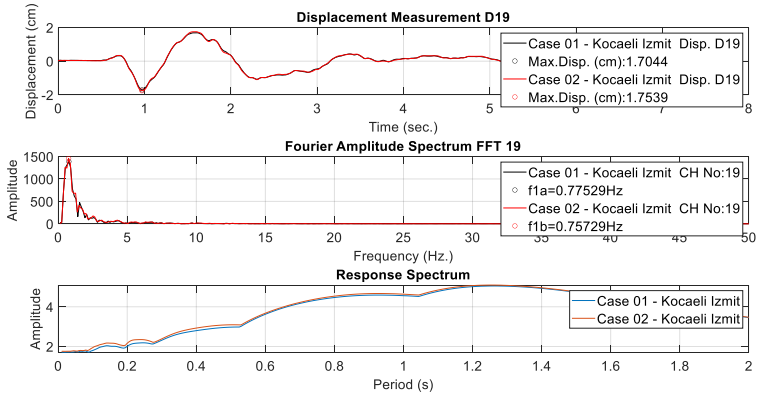

Figure 5.127. Comparison Of Displacement, Fourier Amplitude, And Spectral Displacement Values On Top Of The Retaining Wall Model Of Case 01 With Case 02 For Sensor D19 Under The 1999 Kocaeli Earthquake Motion - Izmit Station.

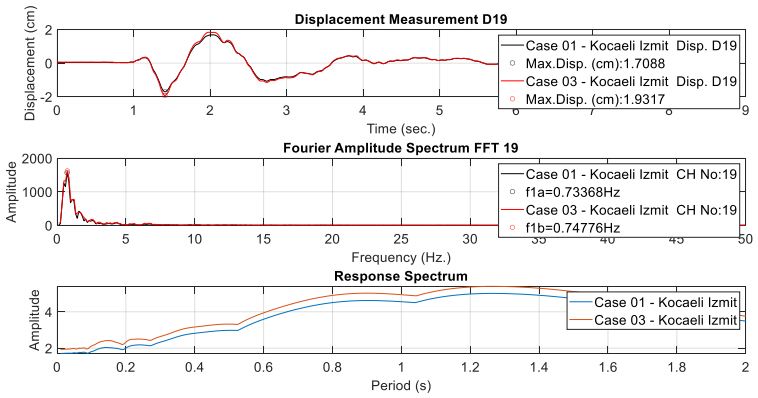

Figure 5.128. Comparison Of Displacement, Fourier Amplitude, And Spectral Displacement Values On Top Of The Retaining Wall Model Of Case 01 With Case 03 For Sensor D19 Under The 1999 Kocaeli Earthquake Motion - Izmit Station.

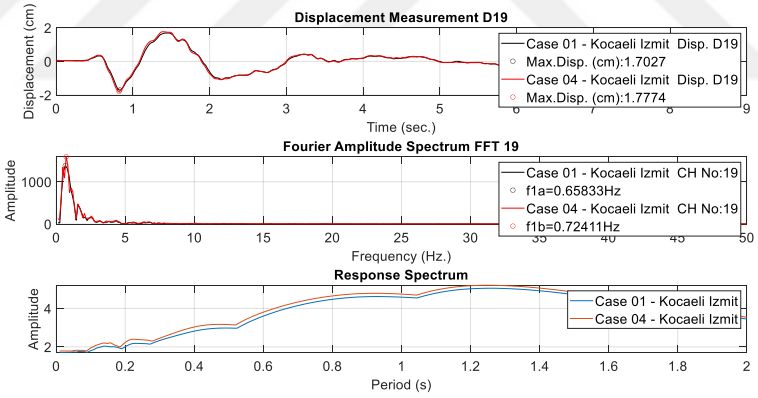

Figure 5.129. Comparison Of Displacement, Fourier Amplitude, And Spectral Displacement Values On Top Of The Retaining Wall Model Of Case 01 With Case 04 For Sensor D19 Under The 1999 Kocaeli Earthquake Motion - Izmit Station.

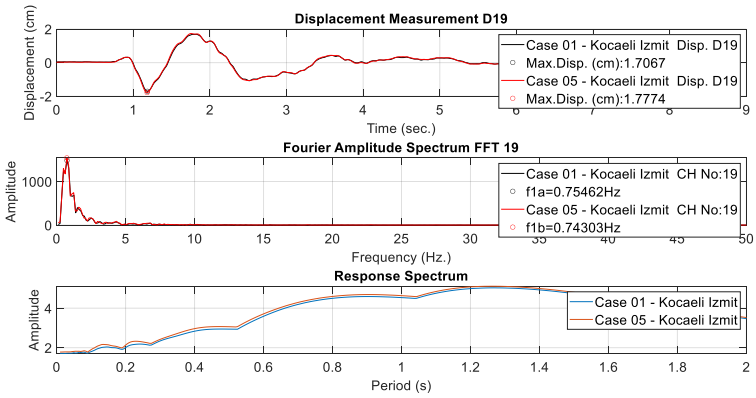

Figure 5.130. Comparison Of Displacement, Fourier Amplitude, And Spectral Displacement Values On Top Of The Retaining Wall Model Of Case 01 With Case 05 For Sensor D19 Under The 1999 Kocaeli Earthquake Motion - Izmit Station.

Figures 5.131 to 5.134 present the maximum displacements on top of the retaining wall model under the earthquake motion of the 1999 Kocaeli - Izmit Station. The values are 1.77 cm, 1.82 cm, 1.81 cm, and 1.72 cm for Cases 06 to 09 according to Table 5.10b. The change in peak displacements is -3.3%, -6.6 %, -5.6 %, and -0.8 % for Cases 06 to 09 (cases with the reinforcement length of 4B) based on the unreinforced case, Case 01.

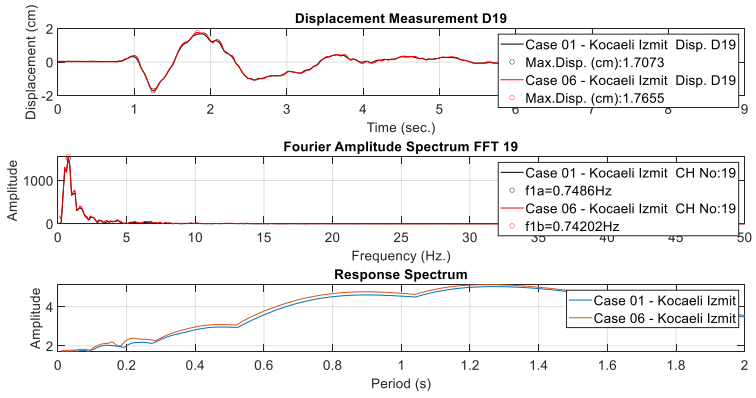

Figure 5.131. Comparison Of Displacement, Fourier Amplitude, And Spectral Displacement Values On Top Of The Retaining Wall Model Of Case 01 With Case 06 For Sensor D19 Under The 1999 Kocaeli Earthquake Motion - Izmit Station.

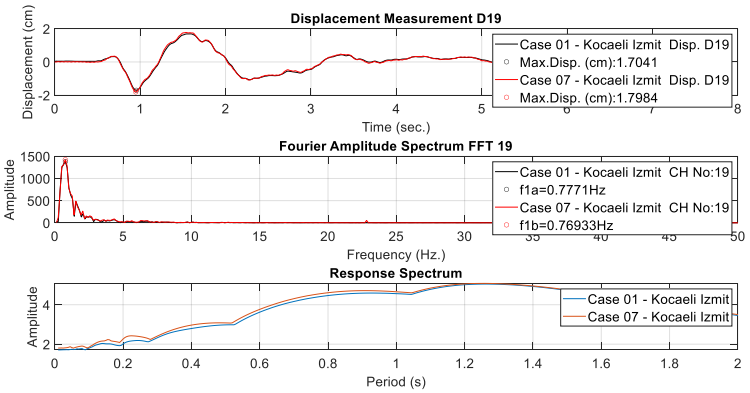

Figure 5.132. Comparison Of Displacement, Fourier Amplitude, And Spectral Displacement Values On Top Of The Retaining Wall Model Of Case 01 With Case 07 For Sensor D19 Under The 1999 Kocaeli Earthquake Motion - Izmit Station.

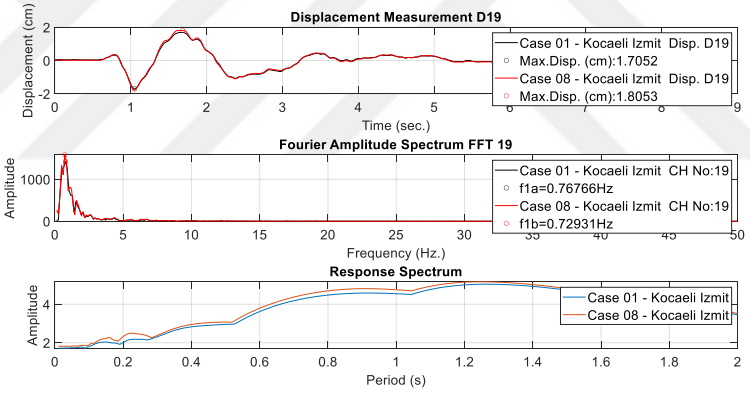

Figure 5.133. Comparison Of Displacement, Fourier Amplitude, And Spectral Displacement Values On Top Of The Retaining Wall Model Of Case 01 With Case 08 For Sensor D19 Under The 1999 Kocaeli Earthquake Motion - Izmit Station.

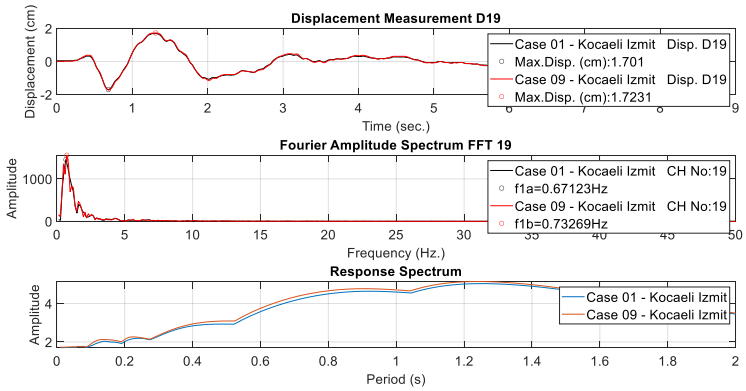

Figure 5.134. Comparison Of Displacement, Fourier Amplitude, And Spectral Displacement Values On Top Of The Retaining Wall Model Of Case 01 With Case 09 For Sensor D19 Under The 1999 Kocaeli Earthquake Motion - Izmit Station.

5.4.3.3. Acceleration Below The Reinforcement Zone Under The 1999 Kocaeli Earthquake Motion - Izmit Station. Figures 5.135 to 5.138 show acceleration measures and the Fourier amplitudes below the reinforcement zone under the effect of the earthquake motion of the 1999 Kocaeli – Izmit Station. The peak accelerations obtained are 0.23 g, 0.23 g, 0.24 g, 0.23 g, and 0.22 g for Cases 01 to 05 according to Table 5.10a. The change in peak accelerations is -2.6 %, -3.4 %, -1.8 %, and 3.0 % respectively.

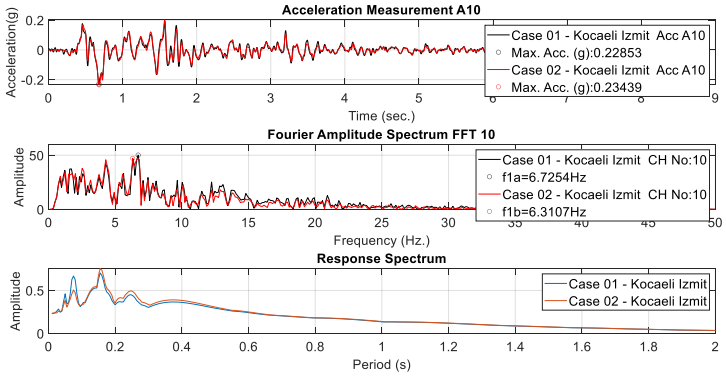

Figure 5.135. Comparison Of Acceleration, Fourier Amplitude, And Spectral Acceleration Values Below The Reinforced Soil Foundation Of The Retaining Wall Model Of Case 01 With Case 02 For Accelerometer A10 Under The 1999 Kocaeli Earthquake Motion - Izmit Station.

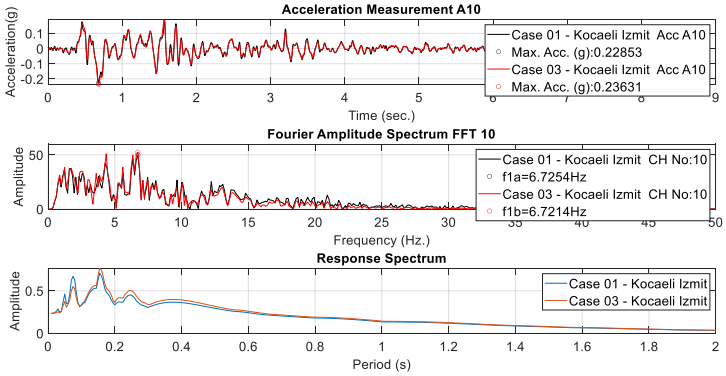

Figure 5.136. Comparison Of Acceleration, Fourier Amplitude, And Spectral Acceleration Values Below The Reinforced Soil Foundation Of The Retaining Wall Model Of Case 01 With Case 03 For Accelerometer A10 Under The 1999 Kocaeli Earthquake Motion - Izmit Station.

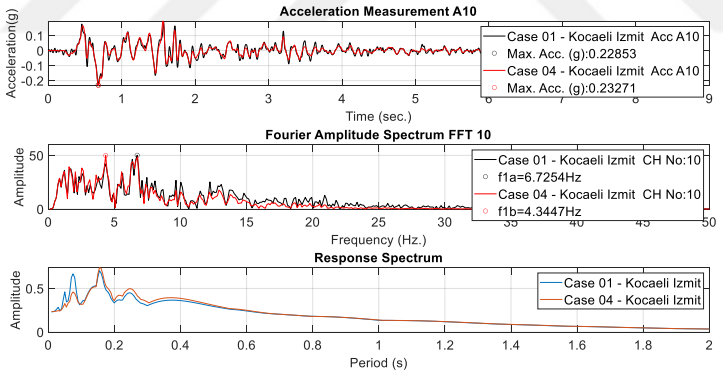

Figure 5.137. Comparison Of Acceleration, Fourier Amplitude, And Spectral Acceleration Values Below The Reinforced Soil Foundation Of The Retaining Wall Model Of Case 01 With Case 04 For Accelerometer A10 Under The 1999 Kocaeli Earthquake Motion - Izmit Station.

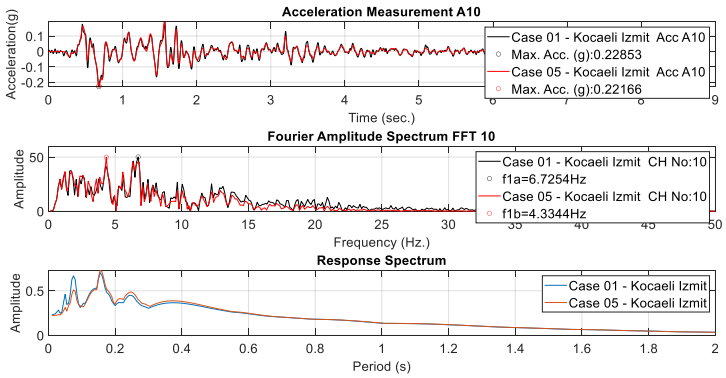

Figure 5.138. Comparison Of Acceleration, Fourier Amplitude, And Spectral Acceleration Values Below The Reinforced Soil Foundation Of The Retaining Wall Model Of Case 01 With Case 05 For Accelerometer A10 Under The 1999 Kocaeli Earthquake Motion - Izmit Station.

Figures 5.139 to 5.142 show acceleration measures and the Fourier amplitudes below the reinforcement zone under the effect of the earthquake motion of the 1999 Kocaeli – Izmit Station. The peak accelerations obtained are 0.23 g, 0.23 g, 0.23 g, and 0.22 g for Cases 06 to 09 as seen in Table 5.10b. The change in peak accelerations is 0.1 %, -1.5 %, -1.1 %, and 3.6 %.

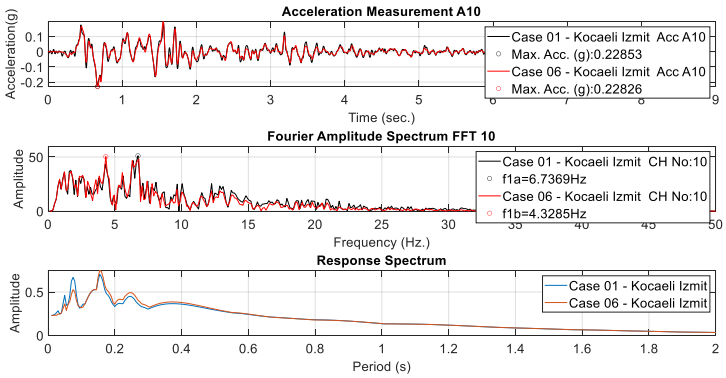

Figure 5.139. Comparison Of Acceleration, Fourier Amplitude, And Spectral Acceleration Values Below The Reinforced Soil Foundation Of The Retaining Wall Model Of Case 01 With Case 06 For Accelerometer A10 Under The 1999 Kocaeli Earthquake Motion - Izmit Station.

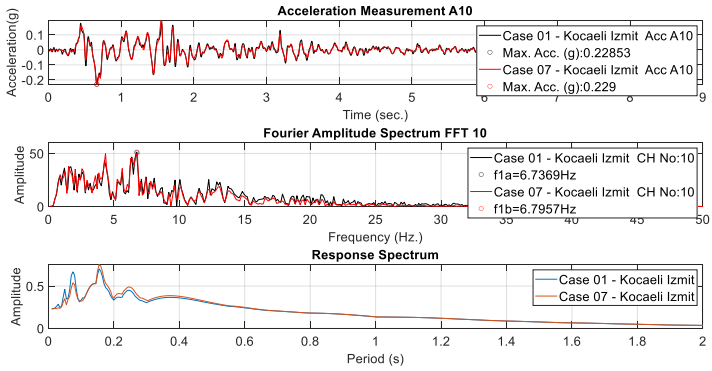

Figure 5.140. Comparison Of Acceleration, Fourier Amplitude, And Spectral Acceleration Values Below The Reinforced Soil Foundation Of The Retaining Wall Model Of Case 01 With Case 07 For Accelerometer A10 Under The 1999 Kocaeli Earthquake Motion - Izmit Station.

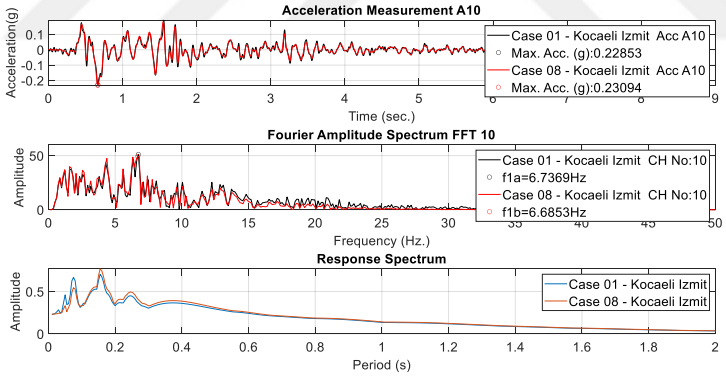

Figure 5.141. Comparison Of Acceleration, Fourier Amplitude, And Spectral Acceleration Values Below The Reinforced Soil Foundation Of The Retaining Wall Model Of Case 01 With Case 08 For Accelerometer A10 Under The 1999 Kocaeli Earthquake Motion - Izmit Station.

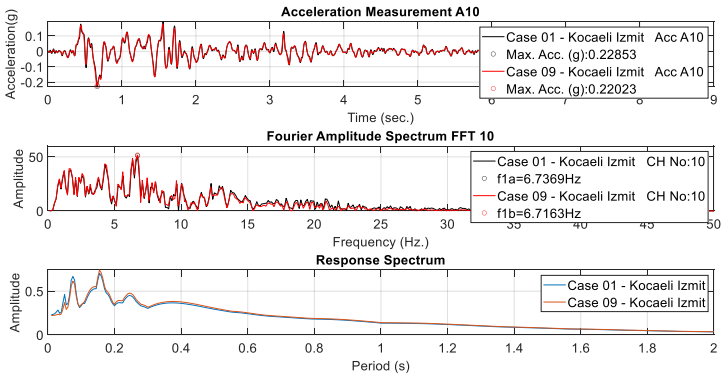

Figure 5.142. Comparison Of Acceleration, Fourier Amplitude, And Spectral Acceleration Values Below The Reinforced Soil Foundation Of The Retaining Wall Model Of Case 01 With Case 09 For Accelerometer A10 Under The 1999 Kocaeli Earthquake Motion - Izmit Station.

5.4.3.4. Acceleration In The Backfill Of The Retaining Wall Model Under The 1999 Kocaeli Earthquake Motion - Izmit Station. Figures 5.143 to 5.146 show acceleration measures and the Fourier amplitudes in the backfill of the retaining wall model under the effect of the earthquake motion of the 1999 Kocaeli – Izmit Station. The peak accelerations obtained are 0.27 g, 0.28 g, 0.28 g, 0.27 g, and 0.27 g for Cases 01 to 05 as seen in Table 5.10a. The difference in the maximum accelerations is -2.4 %, -3.4 %, 0.1 %, and -1.3 %.

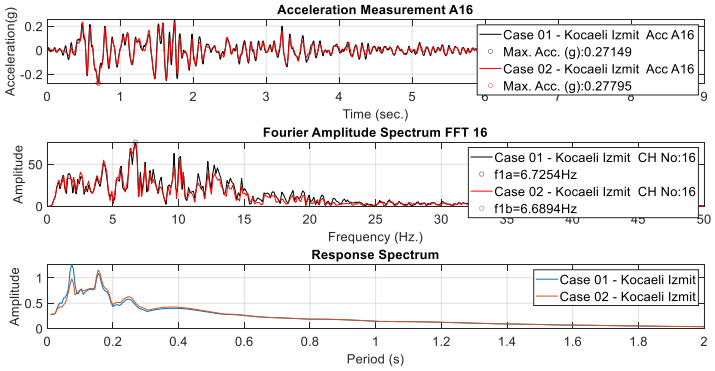

Figure 5.143. Comparison Of Acceleration, Fourier Amplitude, And Spectral Acceleration Values In The Backfill Of The Retaining Wall Model Of Case 01 With Case 02 For Accelerometer A16 Under The 1999 Kocaeli Earthquake Motion - Izmit Station.

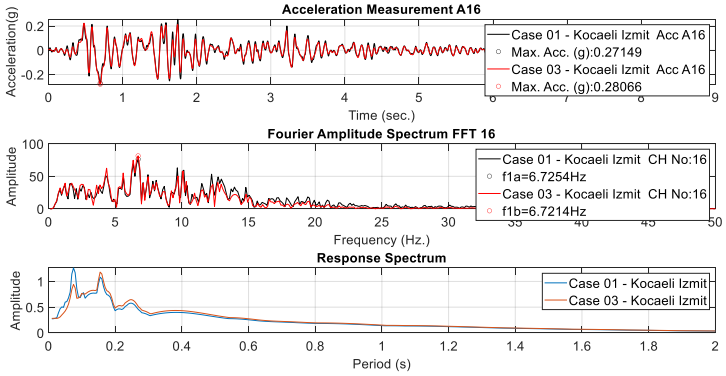

Figure 5.144. Comparison Of Acceleration, Fourier Amplitude, And Spectral Acceleration Values In The Backfill Of The Retaining Wall Model Of Case 01 With Case 03 For Accelerometer A16 Under The 1999 Kocaeli Earthquake Motion - Izmit Station.

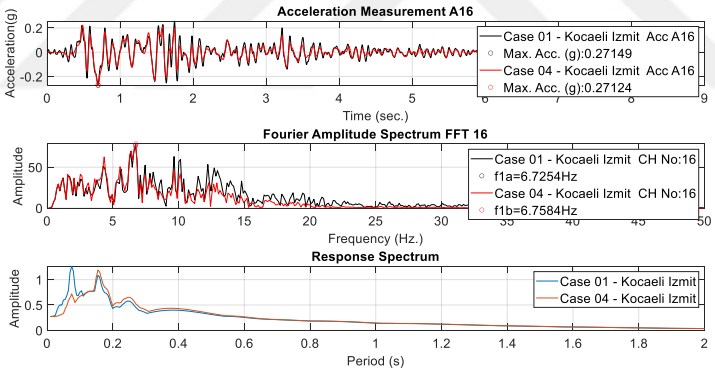

Figure 5.145. Comparison Of Acceleration, Fourier Amplitude, And Spectral Acceleration Values In The Backfill Of The Retaining Wall Model Of Case 01 With Case 04 For Accelerometer A16 Under The 1999 Kocaeli Earthquake Motion - Izmit Station.

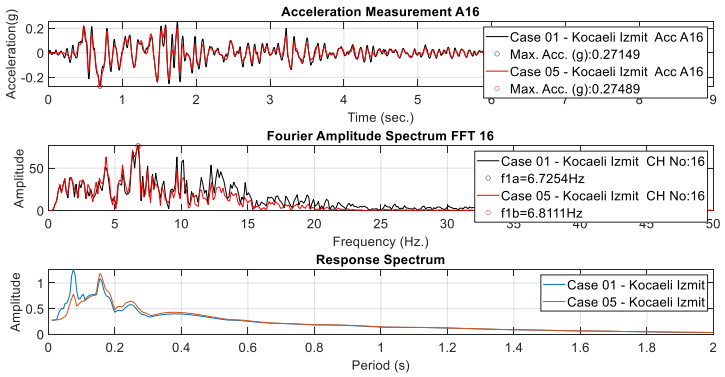

Figure 5.146. Comparison Of Acceleration, Fourier Amplitude, And Spectral Acceleration Values In The Backfill Of The Retaining Wall Model Of Case 01 With Case 05 For Accelerometer A16 Under The 1999 Kocaeli Earthquake Motion - Izmit Station.

Figures 5.147 to 5.150 show acceleration measures and the Fourier amplitudes in the backfill of the retaining wall model under the effect of the earthquake motion of the 1999 Kocaeli – Izmit Station. The peak accelerations obtained are 0.27 g, 0.28 g, 0.29 g, and 0.26 g for Cases 06 to 09 according to Table 5.10b. The change in maximum accelerations is -0.5 %, -4.3 %, -5.5 %, and 6.0 %.

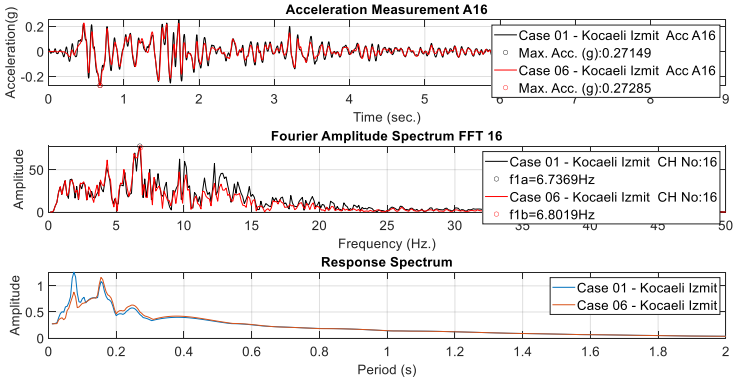

Figure 5.147 Comparison Of Acceleration, Fourier Amplitude, And Spectral Acceleration Values In The Backfill Of The Retaining Wall Model Of Case 01 With Case 06 For Accelerometer A16 Under The 1999 Kocaeli Earthquake Motion - Izmit Station.

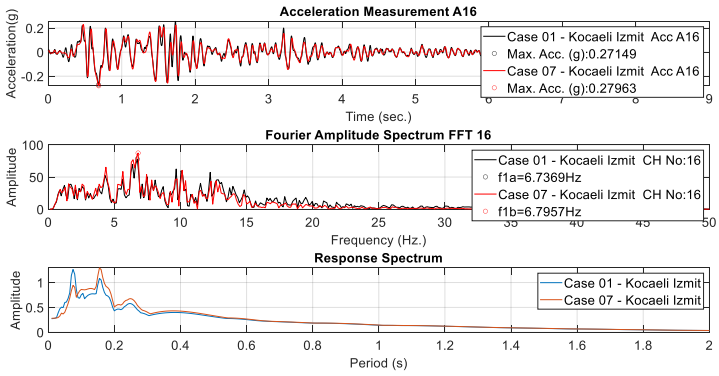

Figure 5.148. Comparison Of Acceleration, Fourier Amplitude, And Spectral Acceleration Values In The Backfill Of The Retaining Wall Model Of Case 01 With Case 07 For Accelerometer A16 Under The 1999 Kocaeli Earthquake Motion - Izmit Station.

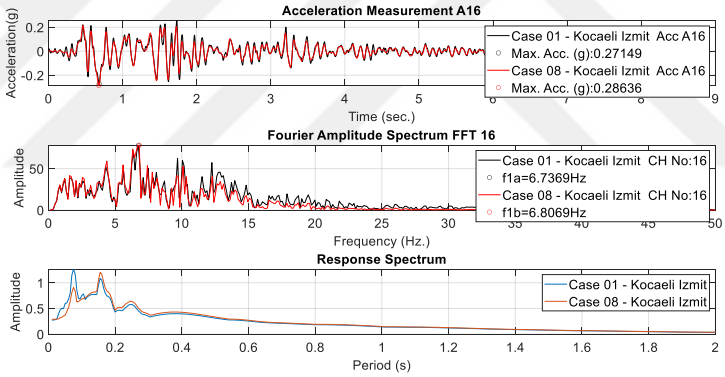

Figure 5.149. Comparison Of Acceleration, Fourier Amplitude, And Spectral Acceleration Values In The Backfill Of The Retaining Wall Model Of Case 01 With Case 08 For Accelerometer A16 Under The 1999 Kocaeli Earthquake Motion - Izmit Station.

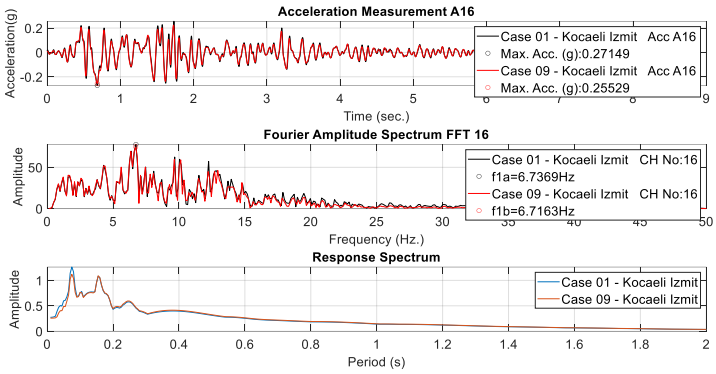

Figure 5.150. Comparison Of Acceleration, Fourier Amplitude, And Spectral Acceleration Values In The Backfill Of The Retaining Wall Model Of Case 01 With Case 09 For Accelerometer A16 Under The 1999 Kocaeli Earthquake Motion - Izmit Station.

5.4.4. Performance Of The Retaining Wall Model Under The 2014 North Aegean Sea Earthquake Motion - Gokceada Station

Acceleration and displacement values under the effect of the earthquake motion of the 2014 North Aegean Sea – Gokceada Station were obtained from experimental setups with sensors A05, A07, D18, and D19 located on the retaining wall model; A10 and A27 located in the foundation soil; A15 and A16 located in the backfill are presented in Table 5.11. Table 5.11a presents the maximum acceleration and displacement values obtained by these sensors for the cases with a reinforcement length of 2B while Table 5.11b presents the related information for the cases with a reinforcement length of 4B. Amongst them, the results of A07, D19, A10, and A16 are explained below.

Table 5.11. Peak Acceleration And Displacement Values For (a) Cases With A Reinforcement Length Of 2B And (b) Cases With A Reinforcement Length Of 4B Under The 2014 North Aegean Sea Earthquake Motion - Gokceada Station

(a)

Peak Accelerations and Displacements						
Location:	**Instrument:**	**Case 01:**	**Case 02:**	**Case 03:**	**Case 04:**	**Case 05:**
On Wall	**A05 (g):**	0.22	0.19	0.20	0.20	0.20
	A07 (g):	0.29	0.26	0.27	0.25	0.26
	D18 (cm):	0.60	0.64	0.60	0.62	0.65
	D19 (cm):	0.70	0.67	0.69	0.70	0.71
In Soil	**A10 (g):**	0.15	0.14	0.13	0.13	0.13
	A27 (g):	0.18	0.16	0.16	0.16	0.15
	A15 (g):	0.21	0.18	0.19	0.18	0.18
	A16 (g):	0.25	0.23	0.22	0.22	0.22

(b)

Peak Accelerations and Displacements						
Location:	**Instrument:**	**Case 01:**	**Case 06:**	**Case 07:**	**Case 08:**	**Case 09:**
On Wall	**A05 (g):**	0.22	0.21	0.21	0.21	0.21
	A07 (g):	0.29	0.27	0.27	0.26	0.25
	D18 (cm):	0.60	0.68	0.65	0.63	0.60
	D19 (cm):	0.70	0.73	0.69	0.61	0.67
In Soil	**A10 (g):**	0.15	0.14	0.14	0.14	0.15
	A27 (g):	0.18	0.16	0.16	0.16	0.18
	A15 (g):	0.21	0.19	0.19	0.20	0.20
	A16 (g):	0.25	0.22	0.25	0.23	0.22

5.4.4.1. Acceleration On Top Of The Retaining Wall Model Under The 2014 North Aegean Sea Earthquake Motion - Gokceada Station. Figures 5.151 to 5.154 show acceleration measures and the Fourier amplitudes on top of the retaining wall model under the effect of

the earthquake motion of the 2014 North Aegean Sea – Gokceada Station. The peak accelerations obtained are 0.29 g, 0.26 g, 0.27 g, 0.25 g, and 0.26 g for Cases 01 to 05 according to Table 5.11a. The improvement percentage for these peak accelerations are 11.0 %, 8.4 %, 12.1 %, and 11.3 % accordingly.

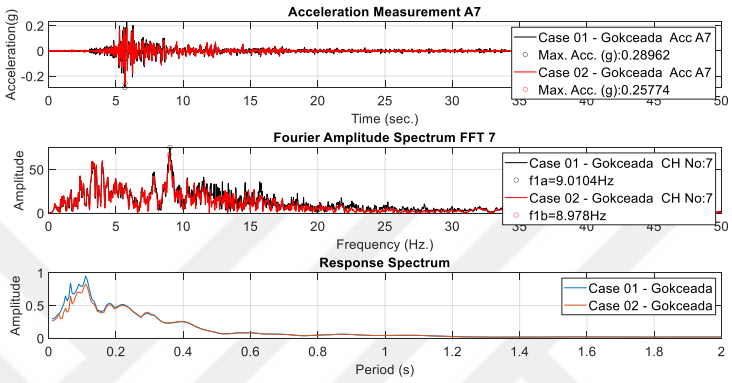

Figure 5.151. Comparison Of Acceleration, Fourier Amplitude, And Spectral Acceleration Values On Top Of The Retaining Wall Model Of Case 01 With Case 02 For Accelerometer A07 Under The 2014 North Aegean Sea Earthquake Motion - Gokceada Station.

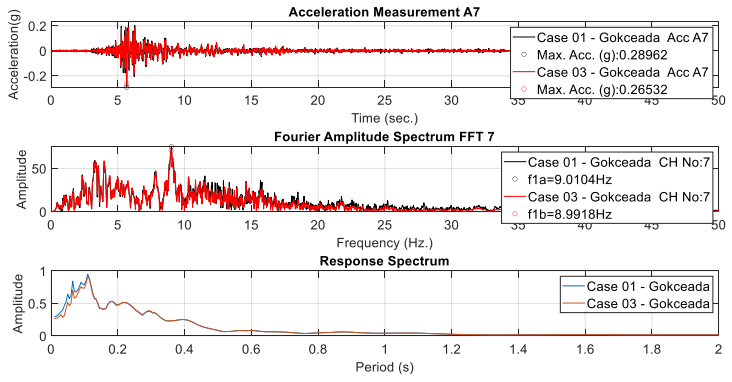

Figure 5.152. Comparison Of Acceleration, Fourier Amplitude, And Spectral Acceleration Values On Top Of The Retaining Wall Model Of Case 01 With Case 03 For Accelerometer A07 Under The 2014 North Aegean Sea Earthquake Motion - Gokceada Station.

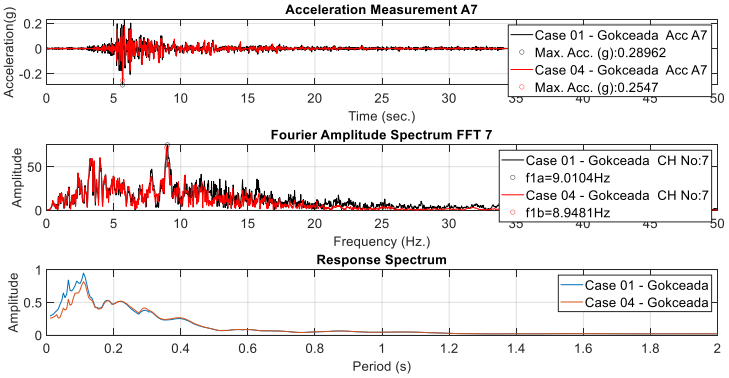

Figure 5.153. Comparison Of Acceleration, Fourier Amplitude, And Spectral Acceleration Values On Top Of The Retaining Wall Model Of Case 01 With Case 04 For Accelerometer A07 Under The 2014 North Aegean Sea Earthquake Motion - Gokceada Station.

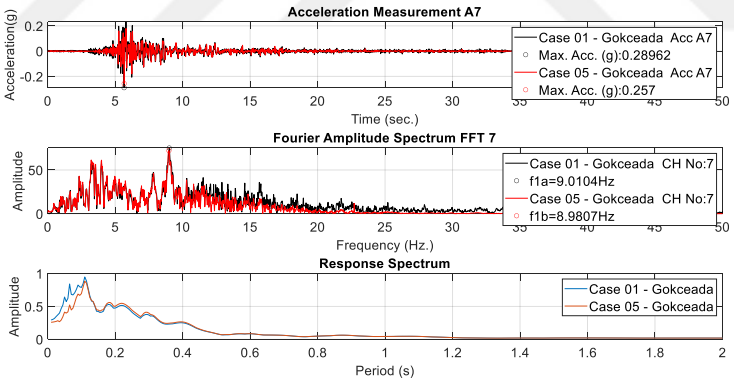

Figure 5.154. Comparison Of Acceleration, Fourier Amplitude, And Spectral Acceleration Values On Top Of The Retaining Wall Model Of Case 01 With Case 05 For Accelerometer A07 Under The 2014 North Aegean Sea Earthquake Motion - Gokceada Station.

Figures 5.155 to 5.158 show acceleration measures and the Fourier amplitudes on top of the retaining wall model under the effect of the earthquake motion of the 2014 North Aegean Sea – Gokceada Station. The peak accelerations obtained are 0.27 g, 0.27 g, 0.26 g,

and 0.25 g for Cases 06 to 09 as seen in Table 5.11b. The improvement ratios of these acceleration values are 6.5 %, 8.4 %, 9.9 %, and 14.9 %.

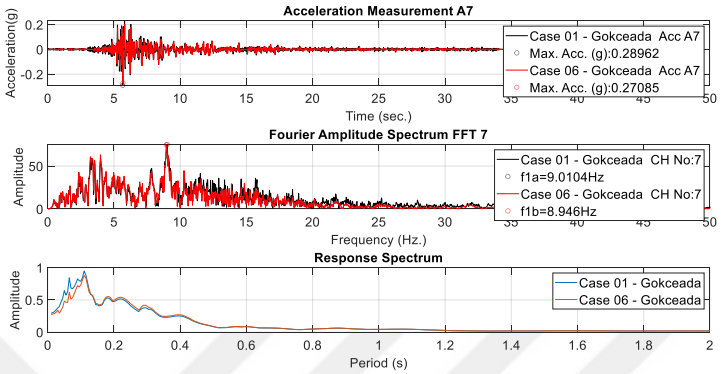

Figure 5.155. Comparison Of Acceleration, Fourier Amplitude, And Spectral Acceleration Values On Top Of The Retaining Wall Model Of Case 01 With Case 06 For Accelerometer A07 Under The 2014 North Aegean Sea Earthquake Motion - Gokceada Station.

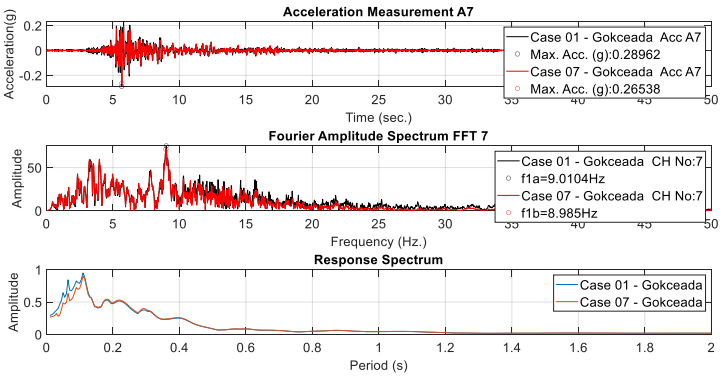

Figure 5.156. Comparison Of Acceleration, Fourier Amplitude, And Spectral Acceleration Values On Top Of The Retaining Wall Model Of Case 01 With Case 07 For Accelerometer A07 Under The 2014 North Aegean Sea Earthquake Motion - Gokceada Station.

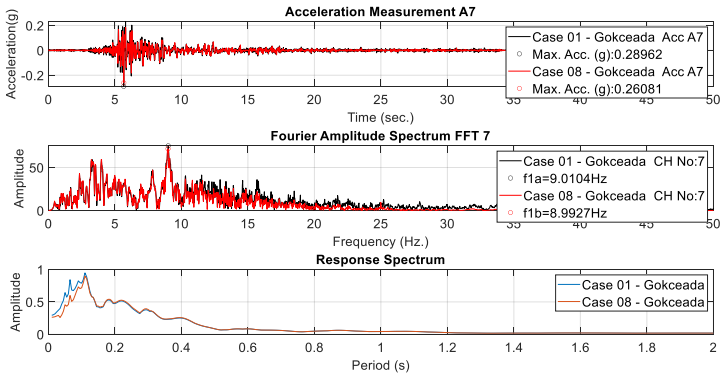

Figure 5.157. Comparison Of Acceleration, Fourier Amplitude, And Spectral Acceleration Values On Top Of The Retaining Wall Model Of Case 01 With Case 08 For Accelerometer A07 Under The 2014 North Aegean Sea Earthquake Motion - Gokceada Station.

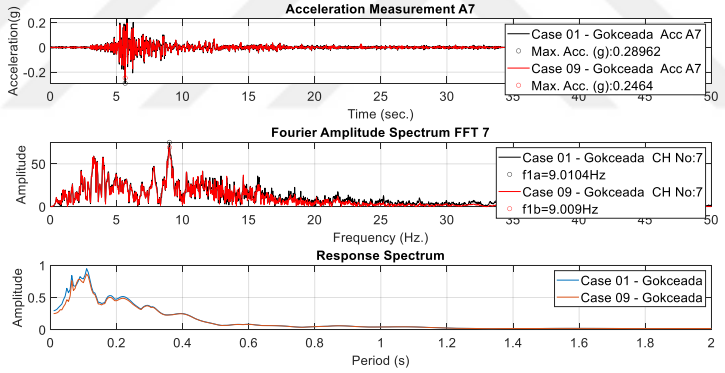

Figure 5.158. Comparison Of Acceleration, Fourier Amplitude, And Spectral Acceleration Values On Top Of The Retaining Wall Model Of Case 01 With Case 09 For Accelerometer A07 Under The 2014 North Aegean Sea Earthquake Motion - Gokceada Station.

5.4.4.2. Displacement On Top Of The Retaining Wall Model Under The 2014 North Aegean Sea Earthquake Motion - Gokceada Station. Figures 5.159 to 5.162 present the maximum displacements on top of the retaining wall model during the earthquake motion of the 2014 North Aegean Sea – Gokceada Station. The values are 0.70 cm, 0.67 cm, 0.69 cm, 0.70 cm, and 0.71 cm for Cases 01 to 05, respectively. The change in peak displacements is 4.0 %,

0.7 %, -0.7 %, and -0.8 % for Cases 02 to 05 based on the unreinforced case, Case 01 according to Table 5.11a.

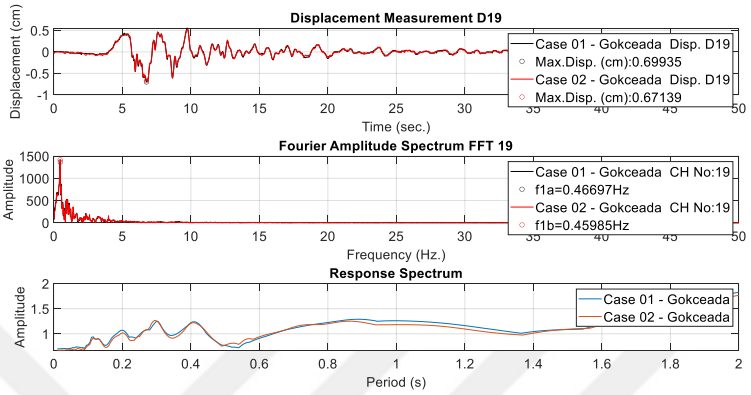

Figure 5.159. Comparison Of Displacement, Fourier Amplitude, And Spectral Displacement Values On Top Of The Retaining Wall Model Of Case 01 With Case 02 For Sensor D19 Under The 2014 North Aegean Sea Earthquake Motion - Gokceada Station.

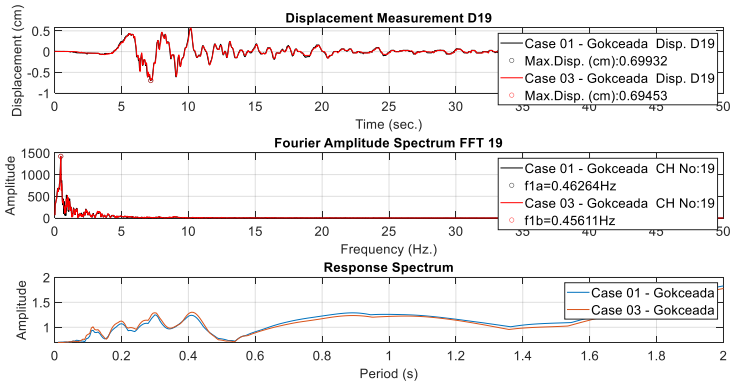

Figure 5.160. Comparison Of Displacement, Fourier Amplitude, And Spectral Displacement Values On Top Of The Retaining Wall Model Of Case 01 With Case 03 For Sensor D19 Under The 2014 North Aegean Sea Earthquake Motion - Gokceada Station.

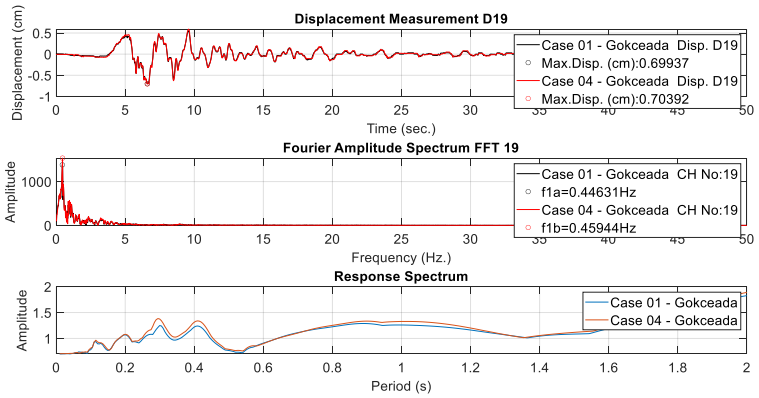

Figure 5.161. Comparison Of Displacement, Fourier Amplitude, And Spectral Displacement Values On Top Of The Retaining Wall Model Of Case 01 With Case 04 For Sensor D19 Under The 2014 North Aegean Sea Earthquake Motion - Gokceada Station.

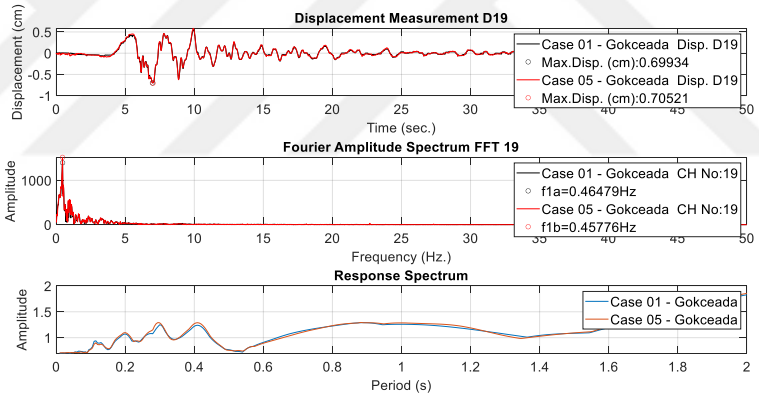

Figure 5.162. Comparison Of Displacement, Fourier Amplitude, And Spectral Displacement Values On Top Of The Retaining Wall Model Of Case 01 With Case 05 For Sensor D19 Under The 2014 North Aegean Sea Earthquake Motion - Gokceada Station.

Figures 5.163 to 5.166 present the maximum displacements on top of the retaining wall model under the earthquake motion of the 2014 North Aegean Sea – Gokceada Station. The values are 0.73 cm, 0.69 cm, 0.61 cm, and 0.67 cm for Cases 06 to 09, respectively. The change in peak displacements is -3.8 %, 2.0 %, 12.3 %, and 4.2 % for Cases 06 to 09 based on the unreinforced case, Case 01 according to Table 5.11b.

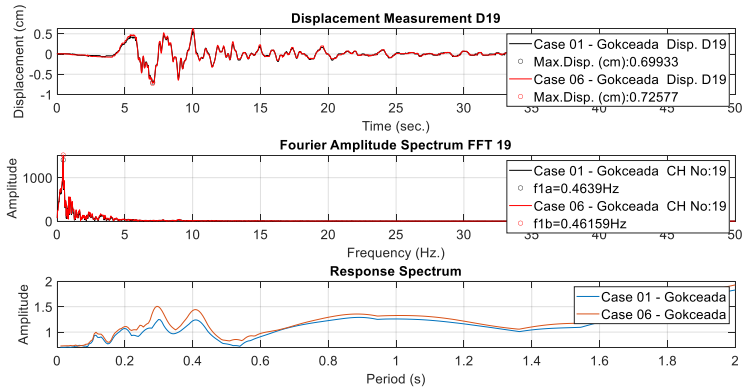

Figure 5.163. Comparison Of Displacement, Fourier Amplitude, And Spectral Displacement Values On Top Of The Retaining Wall Model Of Case 01 With Case 06 For Sensor D19 Under The 2014 North Aegean Sea Earthquake Motion - Gokceada Station.

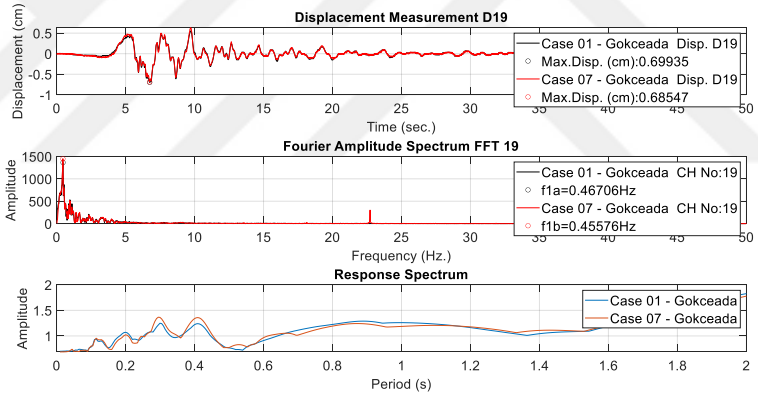

Figure 5.164. Comparison Of Displacement, Fourier Amplitude, And Spectral Displacement Values On Top Of The Retaining Wall Model Of Case 01 With Case 07 For Sensor D19 Under The 2014 North Aegean Sea Earthquake Motion - Gokceada Station.

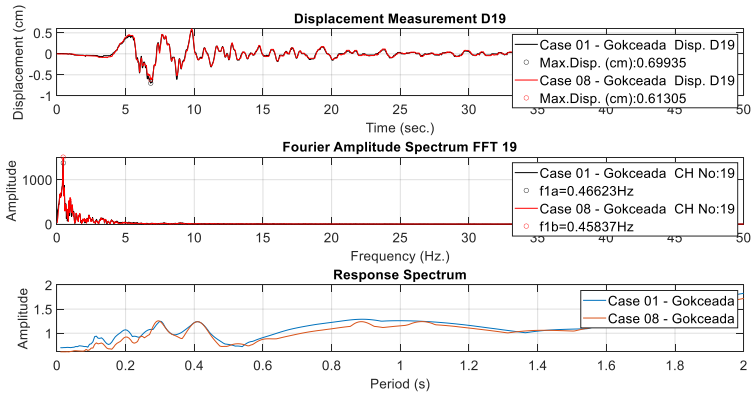

Figure 5.165. Comparison Of Displacement, Fourier Amplitude, And Spectral Displacement Values On Top Of The Retaining Wall Model Of Case 01 With Case 08 For Sensor D19 Under The 2014 North Aegean Sea Earthquake Motion - Gokceada Station.

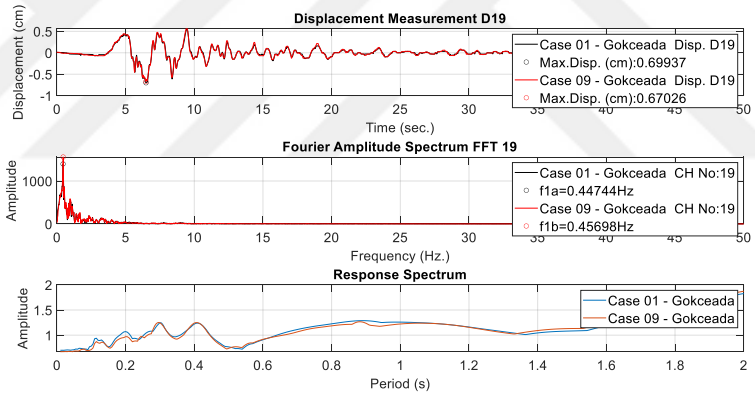

Figure 5.166. Comparison Of Displacement, Fourier Amplitude, And Spectral Displacement Values On Top Of The Retaining Wall Model Of Case 01 With Case 09 For Sensor D19 Under The 2014 North Aegean Sea Earthquake Motion - Gokceada Station.

5.4.4.3. Acceleration Below The Reinforcement Zone Under The 2014 North Aegean Sea Earthquake Motion - Gokceada Station. Figures 5.167 to 5.170 show acceleration measures and the Fourier amplitudes below the reinforcement zone under the effect of the earthquake motion of the 2014 North Aegean Sea – Gokceada Station. The peak accelerations obtained are 0.15 g, 0.14 g, 0.13 g, 0.13 g, and 0.13 g for Cases 01 to 05 as seen in Table 5.11a. The change in peak acceleration values is 5.5 %, 8.7 %, 10.4 %, and 12.7, respectively.

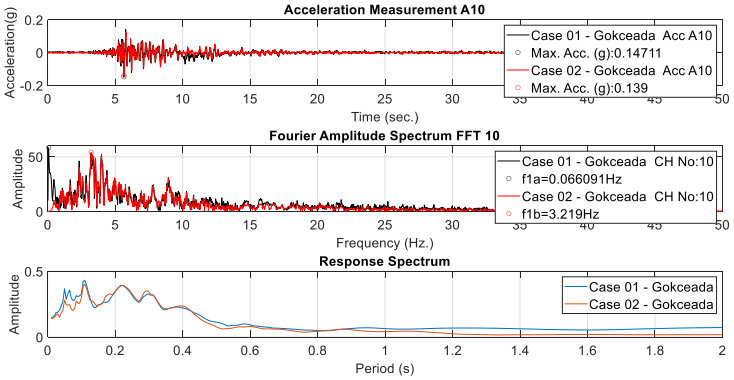

Figure 5.167. Comparison Of Acceleration, Fourier Amplitude, And Spectral Acceleration Values Below The Reinforced Soil Foundation Of The Retaining Wall Model Of Case 01 With Case 02 For Accelerometer A10 Under The 2014 North Aegean Sea Earthquake Motion - Gokceada Station.

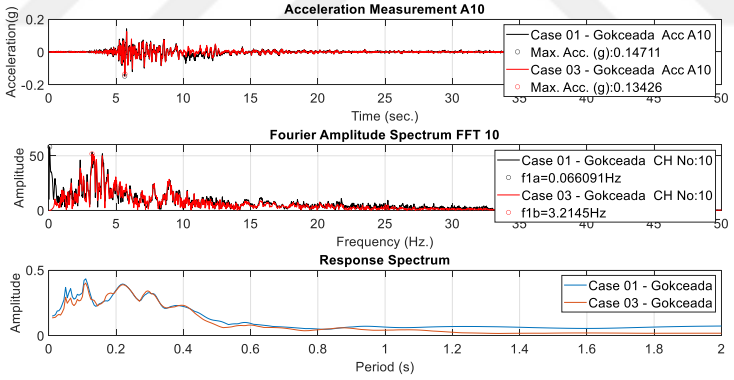

Figure 5.168. Comparison Of Acceleration, Fourier Amplitude, And Spectral Acceleration Values Below The Reinforced Soil Foundation Of The Retaining Wall Model Of Case 01 With Case 03 For Accelerometer A10 Under The 2014 North Aegean Sea Earthquake Motion - Gokceada Station.

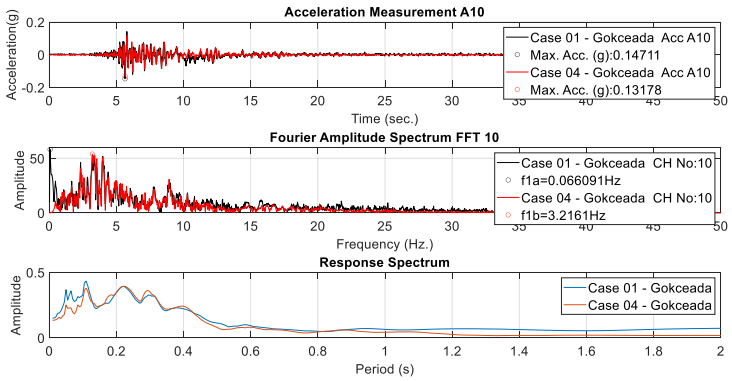

Figure 5.169. Comparison Of Acceleration, Fourier Amplitude, And Spectral Acceleration Values Below The Reinforced Soil Foundation Of The Retaining Wall Model Of Case 01 With Case 04 For Accelerometer A10 Under The 2014 North Aegean Sea Earthquake Motion - Gokceada Station.

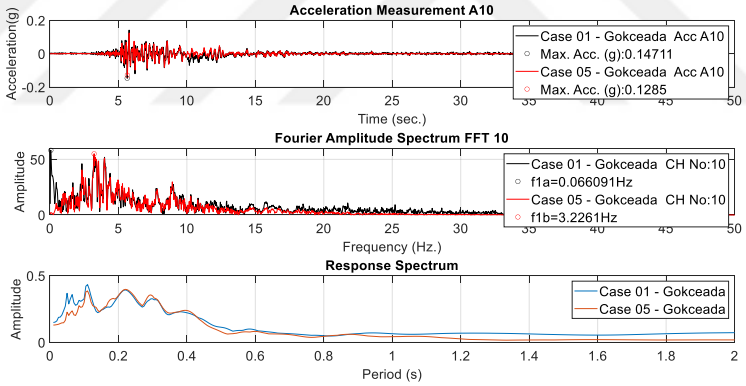

Figure 5.170. Comparison Of Acceleration, Fourier Amplitude, And Spectral Acceleration Values Below The Reinforced Soil Foundation Of The Retaining Wall Model Of Case 01 With Case 05 For Accelerometer A10 Under The 2014 North Aegean Sea Earthquake Motion - Gokceada Station.

Figures 5.171 to 5.174 show acceleration measures and the Fourier amplitudes below the reinforcement zone under the effect of the earthquake motion of the 2014 North Aegean Sea – Gokceada Station. The peak accelerations obtained are 0.14 g, 0.14 g, 0.14 g, and 0.15 g for Cases 06 to 09 as seen in Table 5.11b. The difference in peak accelerations is 6.6 %, 5.4 %, 8.2 %, and -2.8 %.

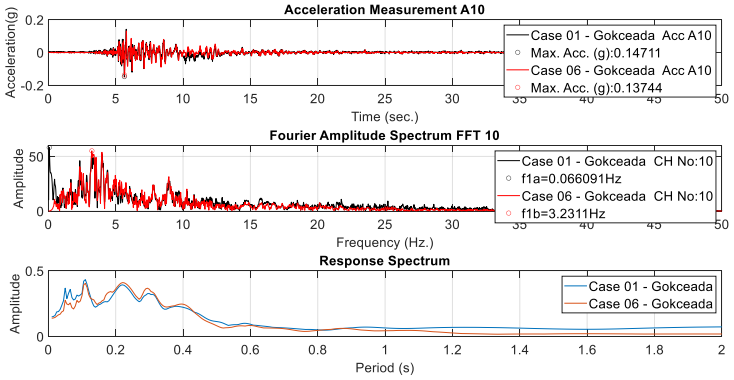

Figure 5.171. Comparison Of Acceleration, Fourier Amplitude, And Spectral Acceleration Values Below The Reinforced Soil Foundation Of The Retaining Wall Model Of Case 01 With Case 06 For Accelerometer A10 Under The 2014 North Aegean Sea Earthquake Motion - Gokceada Station.

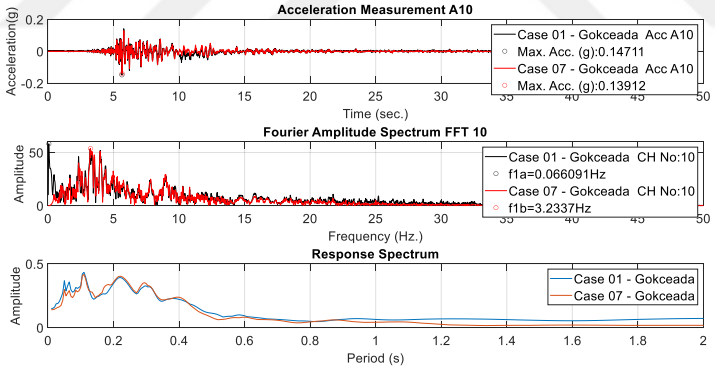

Figure 5.172. Comparison Of Acceleration, Fourier Amplitude, And Spectral Acceleration Values Below The Reinforced Soil Foundation Of The Retaining Wall Model Of Case 01 With Case 07 For Accelerometer A10 Under The 2014 North Aegean Sea Earthquake Motion - Gokceada Station.

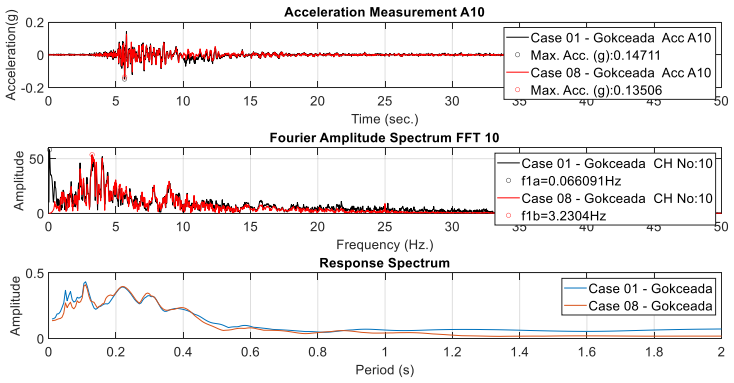

Figure 5.173. Comparison Of Acceleration, Fourier Amplitude, And Spectral Acceleration Values Below The Reinforced Soil Foundation Of The Retaining Wall Model Of Case 01 With Case 08 For Accelerometer A10 Under The 2014 North Aegean Sea Earthquake Motion - Gokceada Station.

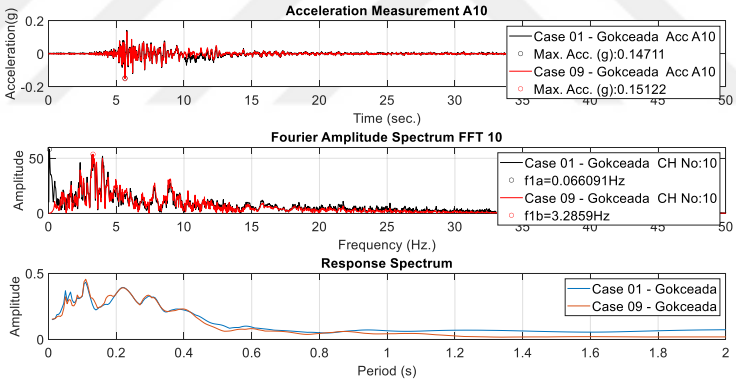

Figure 5.174. Comparison Of Acceleration, Fourier Amplitude, And Spectral Acceleration Values Below The Reinforced Soil Foundation Of The Retaining Wall Model Of Case 01 With Case 09 For Accelerometer A10 Under The 2014 North Aegean Sea Earthquake Motion - Gokceada Station.

5.4.4.4. Acceleration In The Backfill Of The Retaining Wall Model Under The 2014 North Aegean Sea Earthquake Motion - Gokceada Station. Figures 5.175 to 5.178 show acceleration measures and the Fourier amplitude in the backfill of the retaining wall model under the effect of the earthquake motion of the 2014 North Aegean Sea – Gokceada Station. The peak accelerations obtained are 0.25 g, 0.23 g, 0.22 g, 0.22 g, and 0.22 g for Cases 01

to 05 as seen in Table 5.11a. The difference in peak accelerations is 8.4 %, 9.6 %, 11.2 %, and 12.2 % respectively.

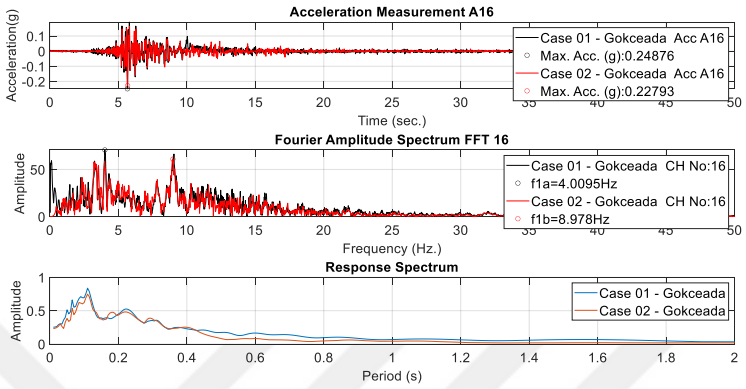

Figure 5.175. Comparison Of Acceleration, Fourier Amplitude, And Spectral Acceleration Values In The Backfil Of The Retaining Wall Model Of Case 01 With Case 02 For Accelerometer A16 Under The 2014 North Aegean Sea Earthquake Motion - Gokceada Station.

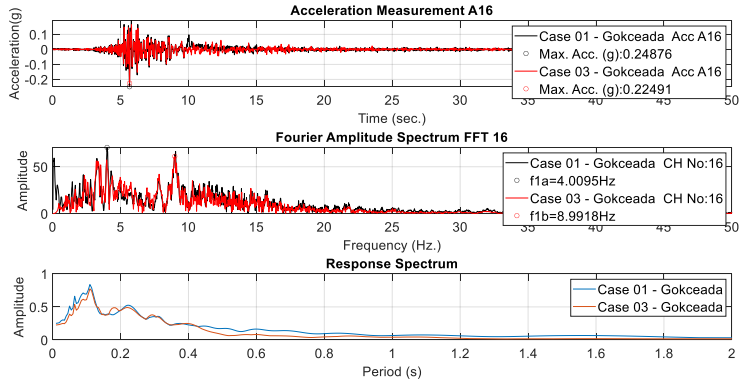

Figure 5.176. Comparison Of Acceleration, Fourier Amplitude, And Spectral Acceleration Values In The Backfil Of The Retaining Wall Model Of Case 01 With Case 03 For Accelerometer A16 Under The 2014 North Aegean Sea Earthquake Motion - Gokceada Station.

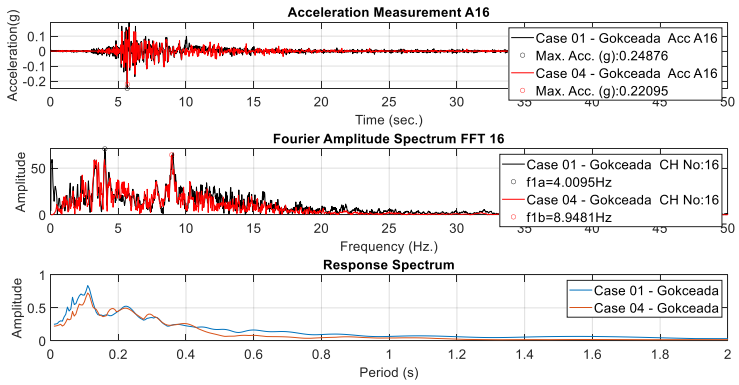

Figure 5.177. Comparison Of Acceleration, Fourier Amplitude, And Spectral Acceleration Values In The Backfil Of The Retaining Wall Model Of Case 01 With Case 04 For Accelerometer A16 Under The 2014 North Aegean Sea Earthquake Motion - Gokceada Station.

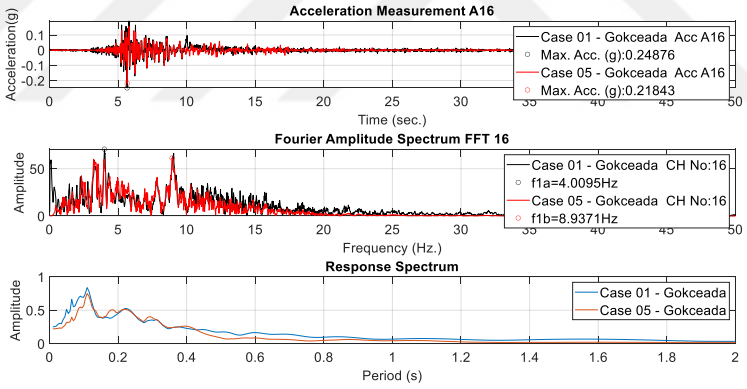

Figure 5.178. Comparison Of Acceleration, Fourier Amplitude, And Spectral Acceleration Values In The Backfil Of The Retaining Wall Model Of Case 01 With Case 05 For Accelerometer A16 Under The 2014 North Aegean Sea Earthquake Motion - Gokceada Station.

Figures 5.179 to 5.182 show acceleration measures and the Fourier amplitudes in the backfill of the retaining wall model under the effect of the earthquake motion of the 2014 North Aegean Sea – Gokceada Station. The peak accelerations obtained are 0.22 g, 0.25 g,

0.23 g, and 0.22 g for Cases 06 to 09 as seen in Table 5.11b. The improvement percentages of these acceleration values are 9.8 %, -1.5 %, 8.3 %, and 12.3 %.

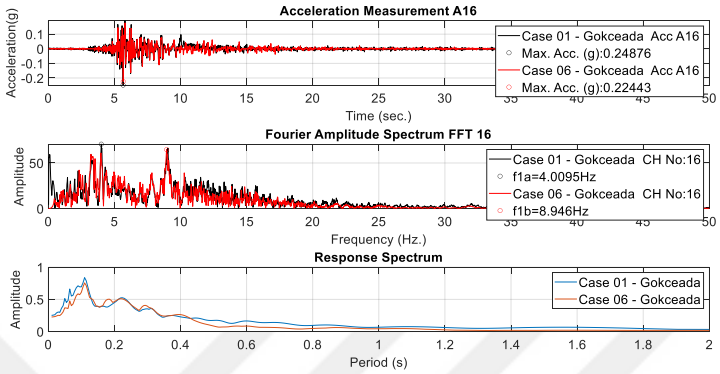

Figure 5.179. Comparison Of Acceleration, Fourier Amplitude, And Spectral Acceleration Values In The Backfil Of The Retaining Wall Model Of Case 01 With Case 06 For Accelerometer A16 Under The 2014 North Aegean Sea Earthquake Motion - Gokceada Station.

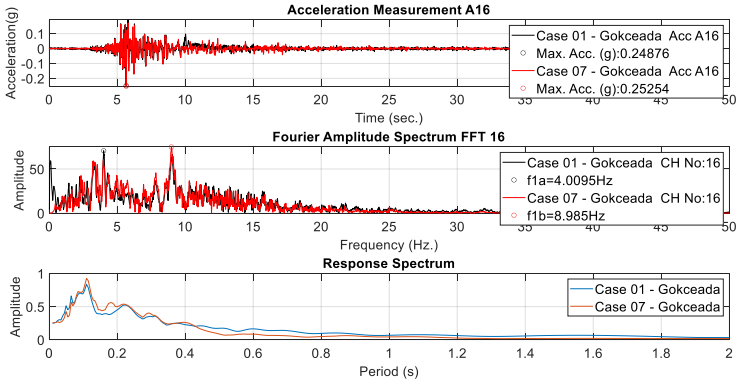

Figure 5.180. Comparison Of Acceleration, Fourier Amplitude, And Spectral Acceleration Values In The Backfil Of The Retaining Wall Model Of Case 01 With Case 07 For Accelerometer A16 Under The 2014 North Aegean Sea Earthquake Motion - Gokceada Station.

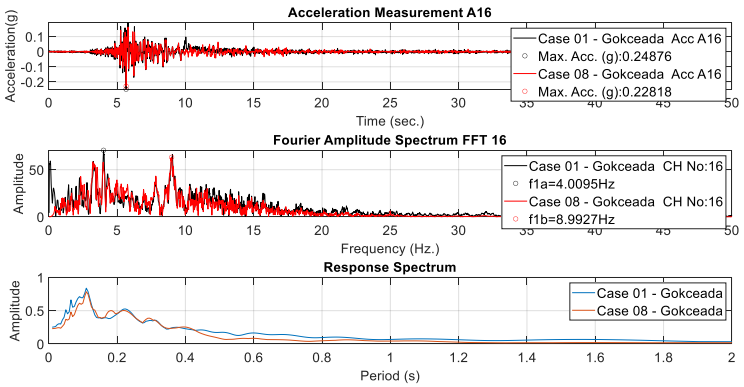

Figure 5.181. Comparison Of Acceleration, Fourier Amplitude, And Spectral Acceleration Values In The Backfil Of The Retaining Wall Model Of Case 01 With Case 08 For Accelerometer A16 Under The 2014 North Aegean Sea Earthquake Motion - Gokceada Station.

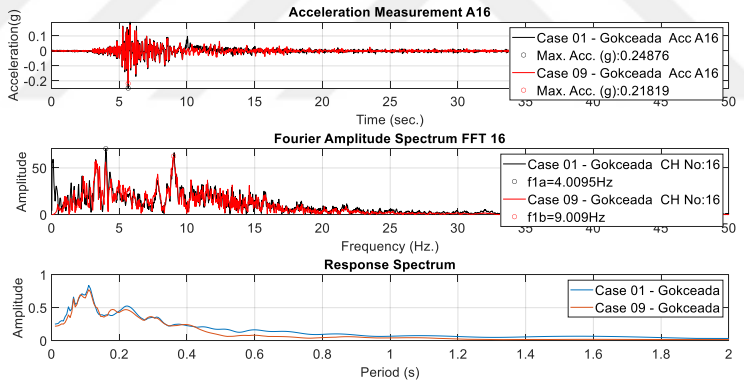

Figure 5.182. Comparison Of Acceleration, Fourier Amplitude, And Spectral Acceleration Values In The Backfil Of The Retaining Wall Model Of Case 01 With Case 09 For Accelerometer A16 Under The 2014 North Aegean Sea Earthquake Motion - Gokceada Station.

6. DISCUSSION

In this study, the effectiveness of geogrid-reinforced soil foundations on the seismic performance of the retaining walls was investigated by shaking table experiments. The study analysed the effects of various factors, including the number and length of geogrid reinforcement layers, as well as ground motion characteristics, on the seismic performance of the retaining wall. The main goal was to determine the factors affecting the effectiveness of geogrid reinforcement beneath the retaining wall.

To estimate the efficiency of the geogrid reinforcement, the percentage change in peak acceleration and displacement values on top of the retaining wall of the reinforced cases compared to unreinforced cases as performance criteria. The results of the study can provide valuable insights into the behaviour of geogrid-reinforced soil under dynamic loads to inform the design and construction of retaining wall systems for improving seismic performance.

6.1. Effects Of The Geogrid-Reinforcement On Top Of The Retaining Wall Model Under The 1940 Imperial Valley Earthquake Motion – El Centro Station

Detailed results of the experimental study explained in Chapter 5.4.1 are evaluated to understand the effectiveness of the geogrid reinforcement. The sensors, A07 and D19, provide the acceleration and displacement values on top of the retaining wall model. Figure 6.1 displays acceleration measures and the Fourier amplitudes of all cases under the effect of the earthquake motion of the 1940 Imperial Valley – El Centro Station. The reduction of peak acceleration values and spectral acceleration values in short periods is seen on top of the retaining wall model. The improvement percentage of acceleration values are 20.0 %, 18.7 %, 19.8 %, and 19.4 % for Cases 02 to 05 and 14.5 %, 16.1 %, 16.9 %, and 16.3 % due

to the unreinforced case, Case 01. Figure 6.2 displays displacement measures and the Fourier amplitudes of all cases on top of the retaining wall model. The difference in maximum displacements is -1.5 %, -0.3 %, -4.9 %, and -1.4 % for Cases 02 to 05 and -3.6 %, -1.7 %, 3.1 %, and 2.0 % for Cases 06 to 09. It is seen that the maximum displacement on top of the wall is not reduced by the inclusion of the geogrid reinforcement, unlike the peak acceleration.

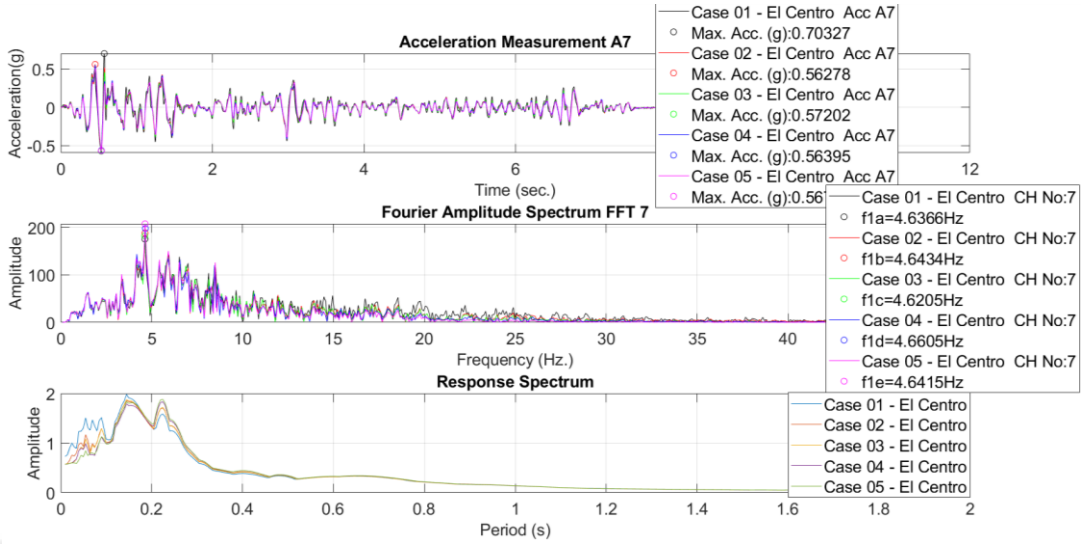

(a)

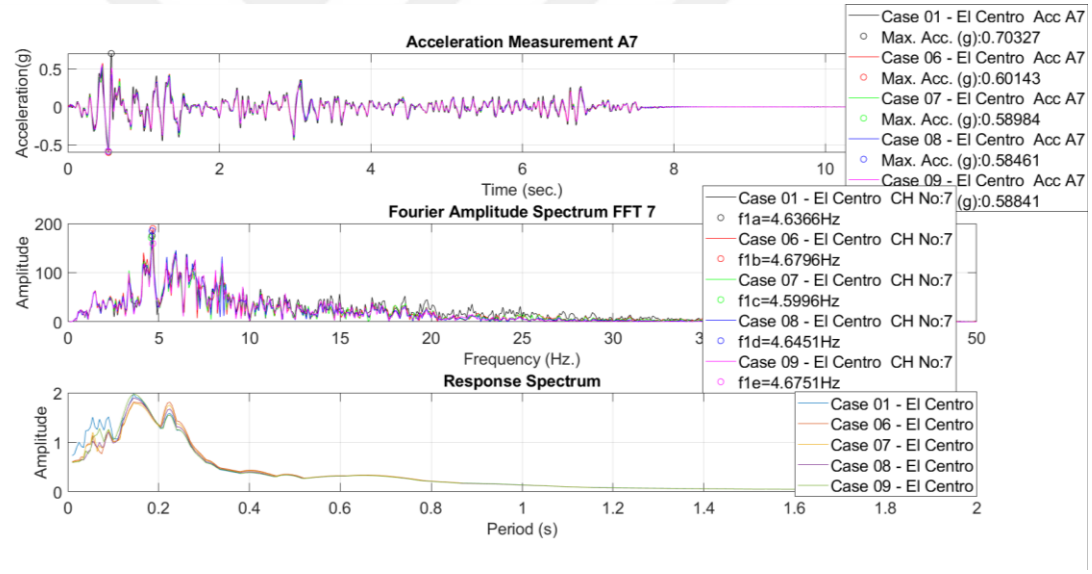

(b)

Figure 6.1. Comparison Of Acceleration, Fourier Amplitude, And Spectral Acceleration Values On Top Of The Retaining Wall Model For (a) Cases 02 To 05 And (b) Cases 06 To 09 Under The 1940 Imperial Valley Earthquake Motion - El Centro Station.

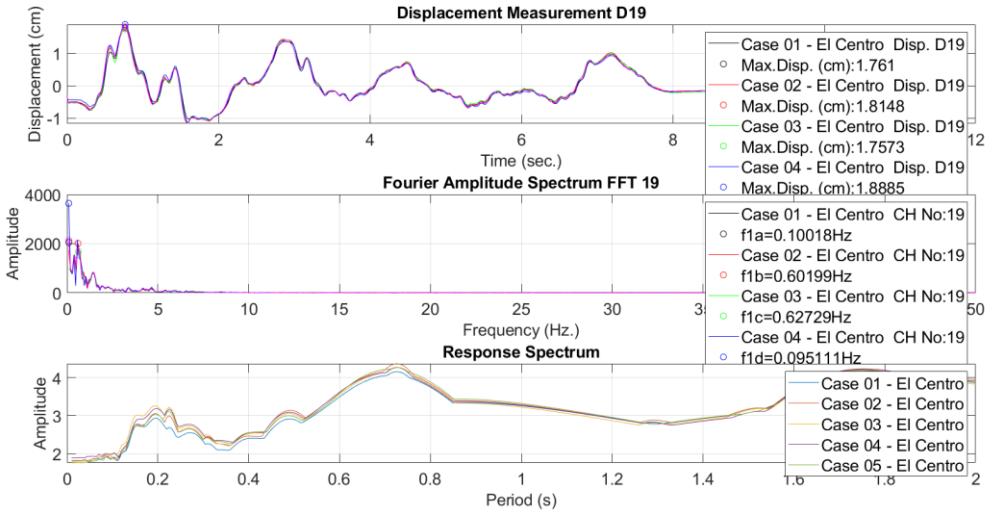

(a)

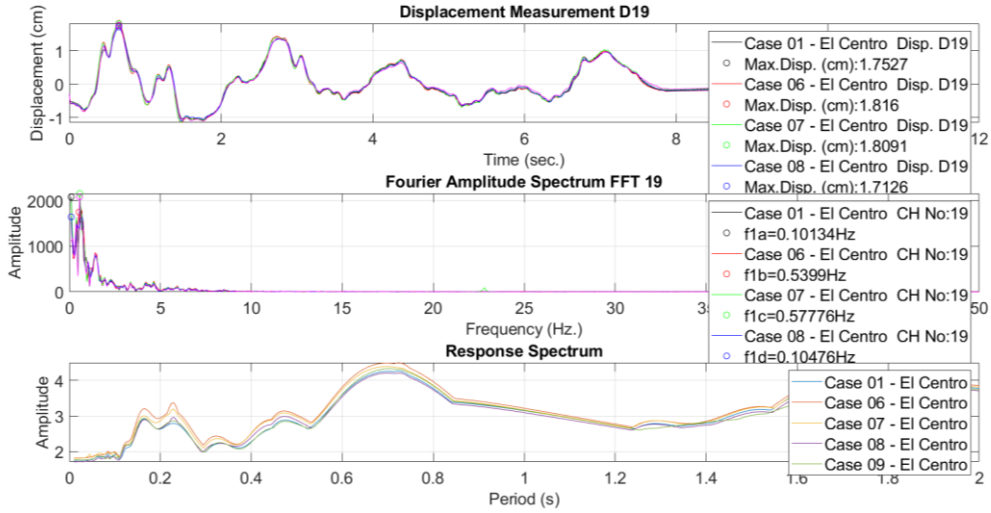

(b)

Figure 6.2. Comparison Of Displacement, Fourier Amplitude, And Spectral Displacement Values On Top Of The Retaining Wall Model For (a) Cases 02 To 05 And (b) Cases 06 To 09 Under The 1940 Imperial Valley Earthquake Motion - El Centro Station.

6.1.1. Effects Of The Number Of Reinforcement Layers Under The 1940 Imperial Valley Earthquake Motion - El Centro Station

Figure 6.3 indicates that the cases with a reinforcement length of 2B reached the optimal improvement ratio when ***N=1*** (Case 02) and did not experience any more improvement with the increasing number of geogrid reinforcement layers. Cases with reinforcement length of 4B show similar behaviour with an important difference. The improvement percentage increases slowly but consistently with an increasing number of geogrid reinforcement layers until ***N=3***. The comparison of the improvement percentages given in Figures 6.3a and 6.3b shows that the optimal effect of the reinforcement is seen immediately with the inclusion of the reinforcement and neither increasing the number of reinforcement layers nor increasing the reinforcement length alters the effect of the reinforcement.

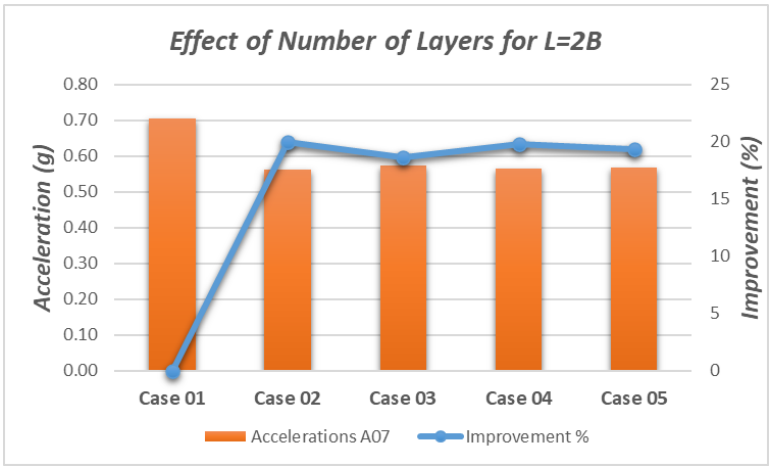

(a)

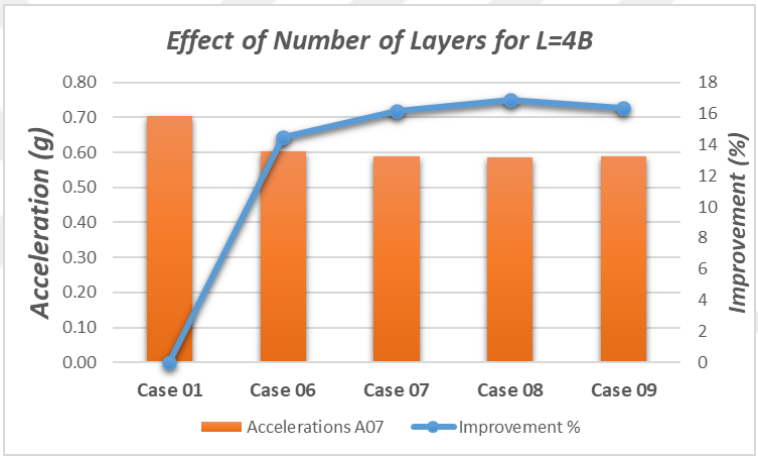

(b)

Figure 6.3. Improvement Percentages And Peak Accelerations On Top Of The Retaining Wall Model Of (a) Cases 02 To 05 And (b) Cases 06 To 09 For Accelerometer A07 Under The 1940 Imperial Valley Earthquake Motion - El Centro Station.

6.1.2. Effects Of The Reinforcement Length Under The 1940 Imperial Valley Earthquake Motion - El Centro Station

Figure 6.4 presents the comparisons of the improvement percentages and peak accelerations for the cases with the same number of reinforcement layers. The variable in these comparisons is the reinforcement length of the cases. In the literature, the reinforcement length is considered an effective factor for the efficiency of the geogrid

reinforcement. However, the experiments using the earthquake motion of the 1940 Imperial Valley – El Centro Station fail to point to an increase in improvement ratio with increasing reinforcement length. The improvement percentages of cases with different reinforcement lengths vary by about 5 % as seen in Figures 6.4a to d.

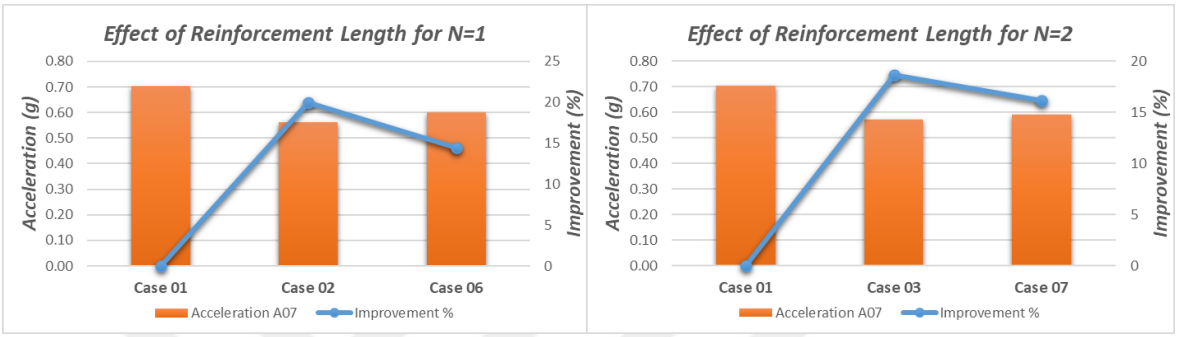

(a)

(b)

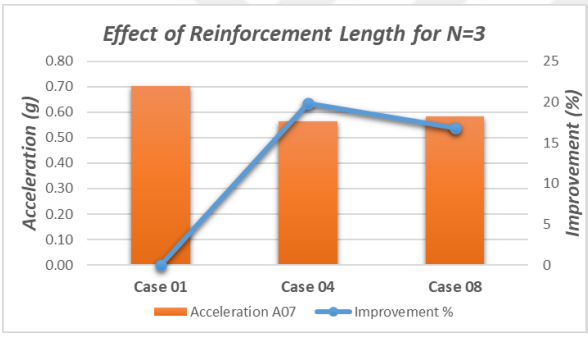

(c)

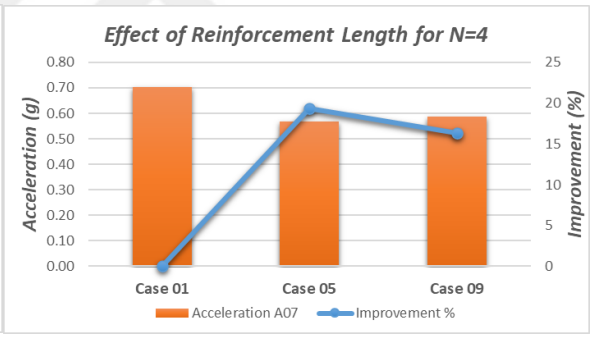

(d)

Figure 6.4. Comparisons Of Improvement Percentages And Peak Accelerations On Top Of The Retaining Wall Model Of (a) Case 02 And Case 06, (b) Case 03 And Case 07, (c) Case 04 And Case 08, And (d) Case 05 And Case 09 To Understand The Effect Of Reinforcement Length Under The 1940 Imperial Valley Earthquake Motion - El Centro Station.

6.2. Effects Of The Geogrid-Reinforcement On Top Of The Retaining Wall Model Under The 1999 Kocaeli Earthquake Motion – Iznik Station

Detailed results of the experimental study explained in Chapter 5.4.2 are evaluated to understand the effectiveness of the reinforcement. Figure 6.5 shows the Fourier amplitudes and acceleration measures of all cases under the earthquake motion of the 1999 Kocaeli – Iznik Station. A decrease in peak acceleration values and spectral acceleration values in short periods is seen on top of the retaining wall model. The improvement percentage of acceleration values are 5.4 %, 8.3 %, 12.6 %, and 8.8 % for Cases 02 to 05 and 6.3 %, 10.1 %, 13.4 %, and 14.2 % based on the unreinforced case, Case 01. Figure 6.6 displays displacement measures and the Fourier amplitudes of all cases on top of the retaining wall model. The difference in maximum displacements is -8.6 %, -5.7 %, -6.0 %, and -6.5 % for Cases 02 to 05 and -11.1 %, -4.5 %, -0.2 %, and 7.0 % for Cases 06 to 09. It is seen that the maximum dislocation on top of the wall is not reduced by the reinforcement during Cases 02 to 05. However, a decreasing trend is seen for Cases 06 to 09.

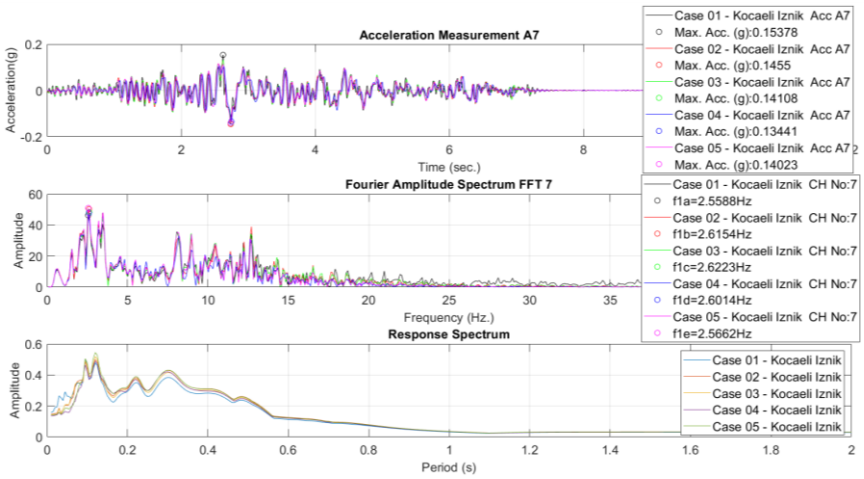

(a)

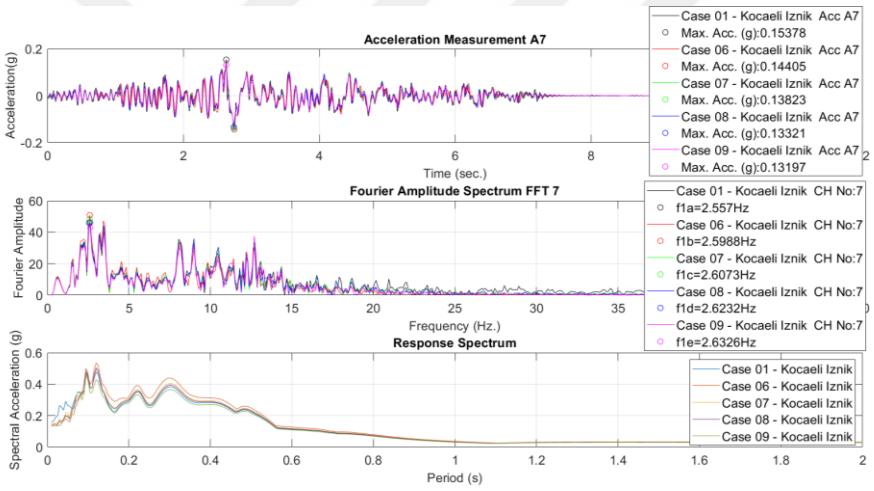

(b)

Figure 6.5. Comparison Of Acceleration, Fourier Amplitude, And Spectral Acceleration Values On Top Of The Retaining Wall Model For (a) Cases 02 To 05 And (b) Cases 06 To 09 Under The 1999 Kocaeli Earthquake Motion – Iznik Station.

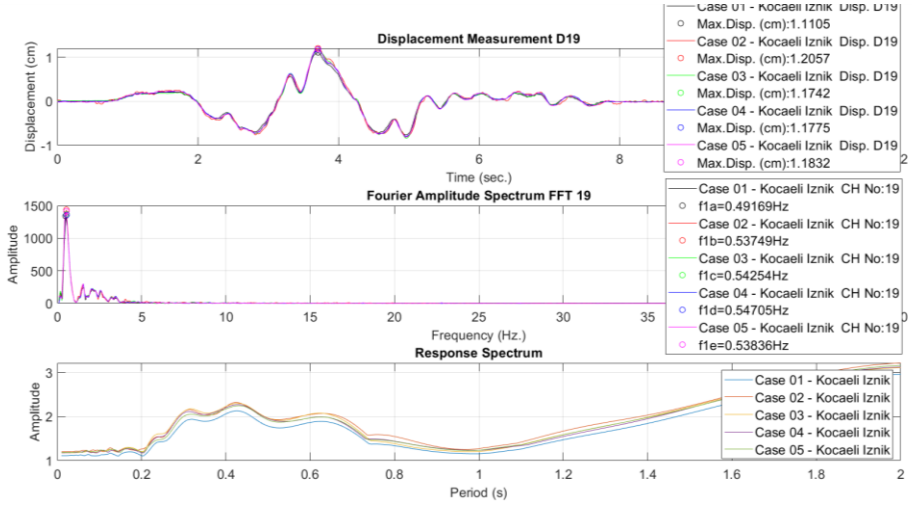

(a)

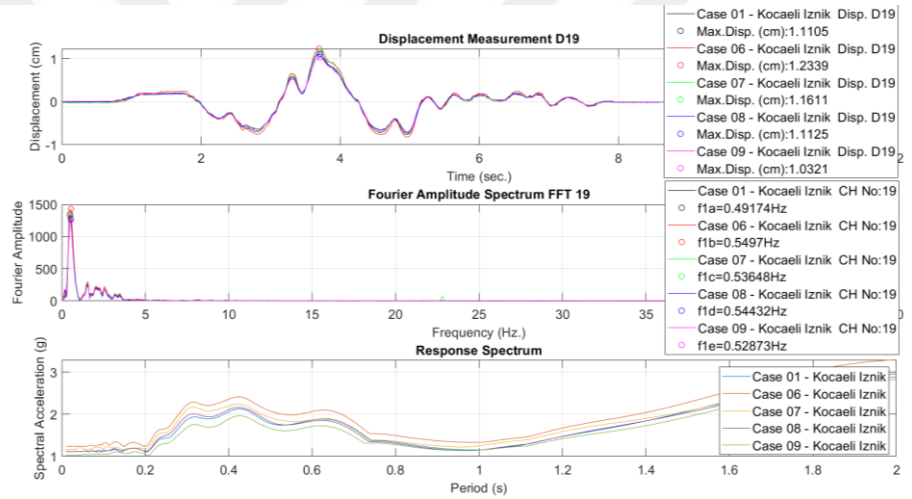

(b)

Figure 6.6. Comparison Of Displacement, Fourier Amplitude, And Spectral Displacement Values On Top Of The Retaining Wall Model For (a) Cases 02 To 05 And (b) Cases 06 To 09 Under The 1999 Kocaeli Earthquake Motion – Iznik Station.

6.2.1. Effects Of The Number Of Reinforcement Layers Under The 1999 Kocaeli Earthquake Motion – Iznik Station

Figure 6.7a shows the improvement percentages and the maximum accelerations obtained on top of the retaining wall model under the earthquake motion of the 1999 Kocaeli – Iznik Station for the cases with the reinforcement length of 2B and Figure 6.7b presents the same information for the cases with the reinforcement length of 4B. In Figure 6.7a, it is seen that the effect of the reinforcement increases consistently with the increasing number of reinforcement layers until ***N=3***. When the reinforcement length is increased to 4B, it is seen that the effect of the reinforcement keeps increasing after ***N=3*** according to Figure 6.7b.

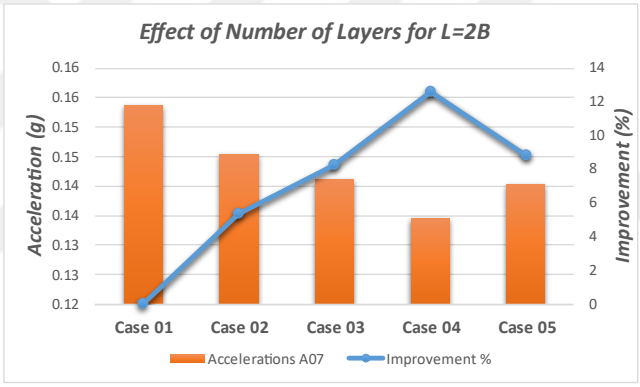

(a)

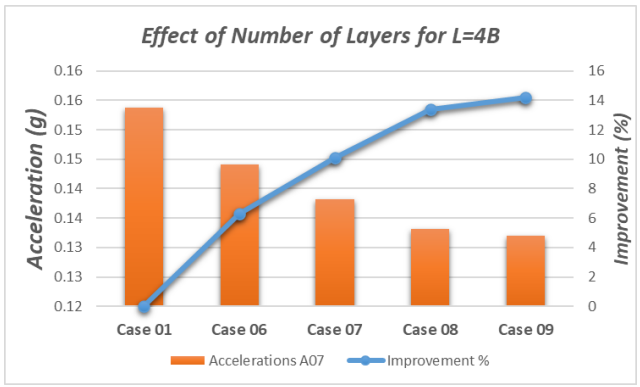

(b)

Figure 6.7. Improvement Percentages And Peak Accelerations On Top Of The Retaining Wall Model Of (a) Cases 02 To 05 And (b) Cases 06 To 09 Under The 1999 Kocaeli Earthquake Motion – Iznik Station.

6.2.2. Effects Of The Reinforcement Length Under The 1999 Kocaeli Earthquake Motion – Iznik Station

Figure 6.8 presents the comparisons of the improvement percentages and peak accelerations for the cases with the same number of reinforcement layers. The variable in these comparisons is the reinforcement length of the cases. Unlike the results of tests under the earthquake motion of the 1940 Imperial Valley - El Centro Station, the effect of increasing reinforcement length is seen in the results of the tests under the earthquake motion of the 1999 Kocaeli – Iznik Station. Figure 6.8 displays the consistent effect of the increasing reinforcement length on the improvement ratio.

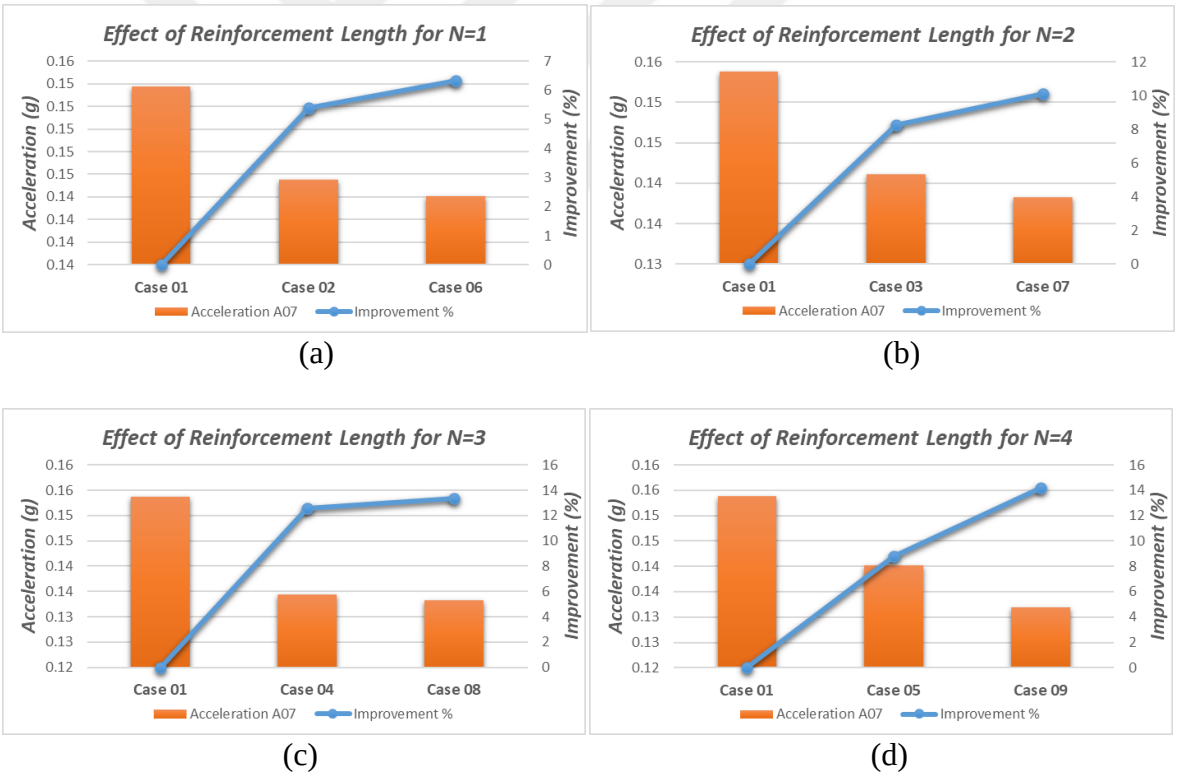

Figure 6.8. Comparisons Of Improvement Percentages And Peak Accelerations On Top Of The Retaining Wall Model For (a) Case 02 And Case 06, (b) Case 03 And Case 07, (c) Case 04 And Case 08, And (d) Case 05 And Case 09 To Understand The Effect Of Reinforcement Length Under The 1999 Kocaeli Earthquake Motion – Iznik Station.

6.3. Effects Of The Geogrid-Reinforcement On Top Of The Retaining Wall Model Under The 1999 Kocaeli Earthquake Motion - Izmit Station

Detailed results of the experimental study explained in Chapter 5.4.3 are evaluated to understand the effectiveness of the reinforcement. Figure 6.9 shows acceleration measures and the Fourier amplitudes of all cases under the earthquake motion of the 1999 Kocaeli – Izmit Station for the top of the retaining wall model. A decrease in peak acceleration values and spectral acceleration values in short periods is seen on top of the retaining wall model. The improvement percentage of acceleration values are 6.0 %, 6.2 %, 10.0 %, and 6.8 % for Cases 02 to 05 and 6.6 %, 5.1 %, 4.9 %, and 11.0 % based on the unreinforced case, Case 01. Figure 6.10 displays the Fourier amplitudes and displacement measures of all cases on top of the retaining wall model. The difference in maximum displacements is -2.6 %, -13.1 %, -4.0 %, and -4.0 % for Cases 02 to 05 and -3.3 %, -6.6 %, -5.6%, and -0.8 % for Cases 06 to 09.

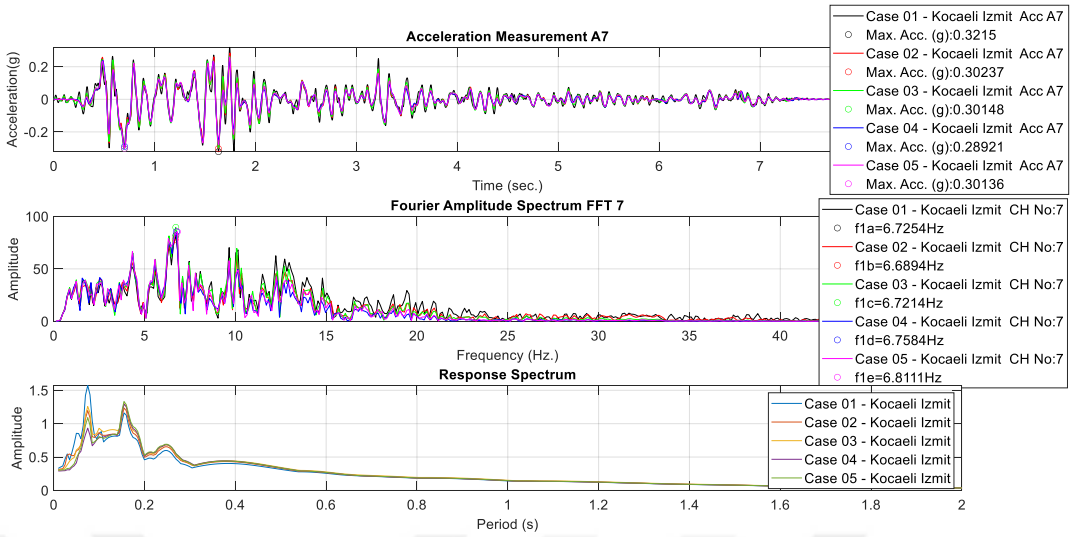

(a)

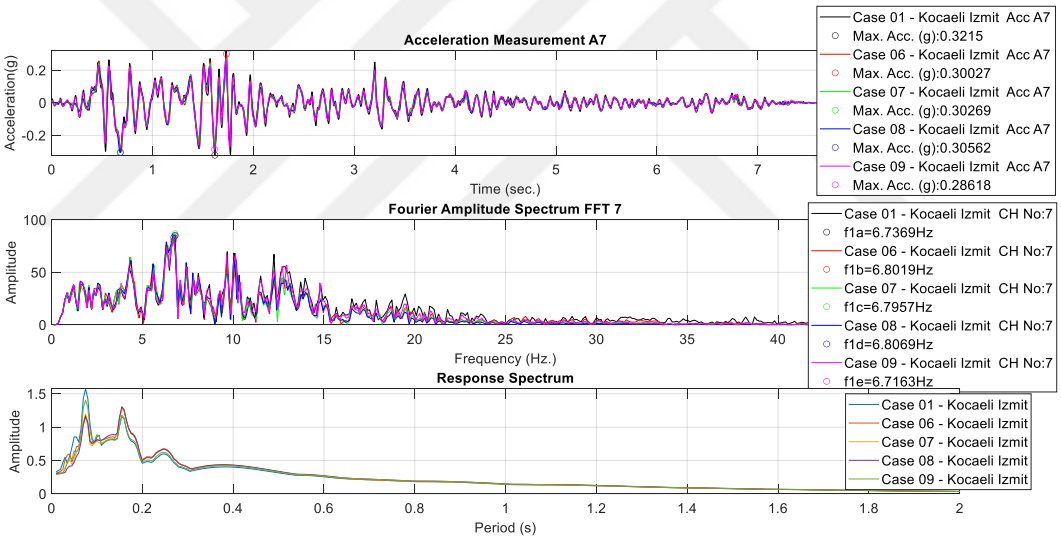

(b)

Figure 6.9. Comparison Of Acceleration, Fourier Amplitude, And Spectral Acceleration Values On Top Of The Retaining Wall Model For (a) Cases 02 To 05 And (b) Cases 06 To 09 Under The 1999 Kocaeli Earthquake Motion – Izmit Station.

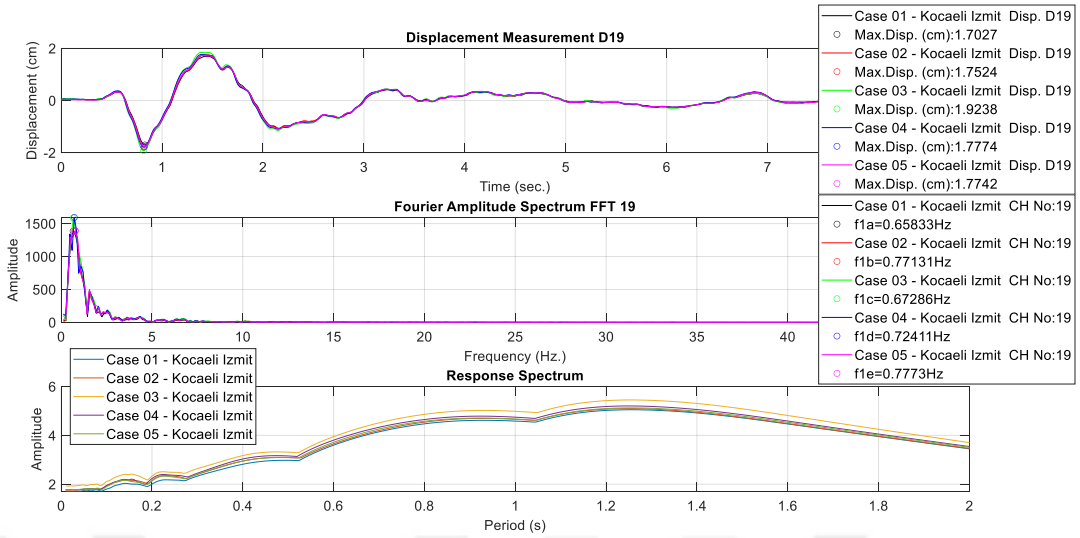

(a)

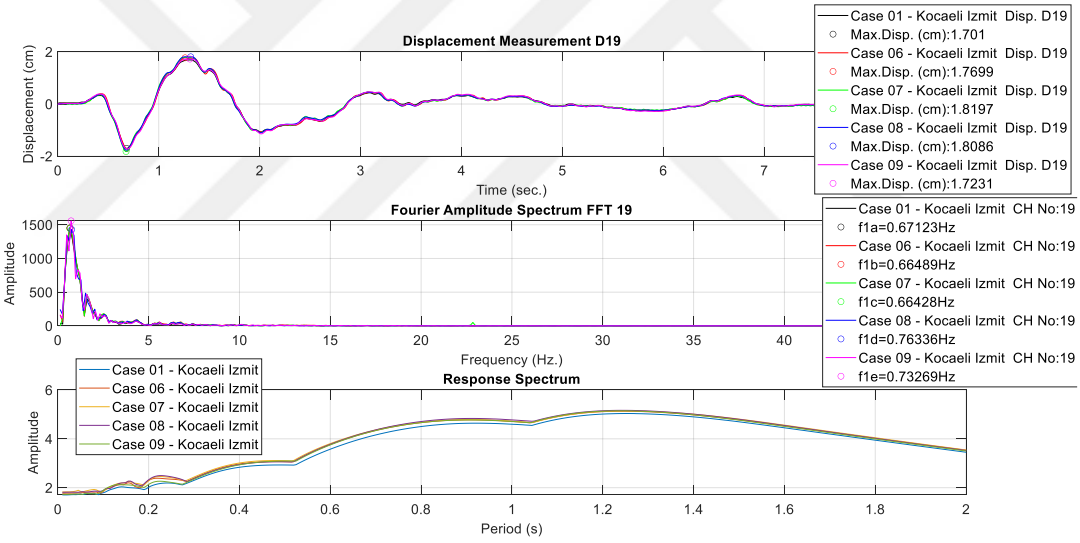

(b)

Figure 6.10. Comparison Of Displacement, Fourier Amplitude, And Spectral Displacement Values On Top Of The Retaining Wall Model For (a) Cases 02 To 05 And (b) Cases 06 To 09 Under The 1999 Kocaeli Earthquake Motion – Izmit Station.

6.3.1. Effects Of The Number Of Reinforcement Layers Under The 1999 Kocaeli Earthquake Motion – Izmit Station

Figure 6.11a shows that the effect of the reinforcement reaches its maximum when ***N=3*** with a consistent response to the increasing number of reinforcement layers. After that point, a decrease in the improvement percentage is seen when ***N=4***. In Figure 6.11b, it is seen that increasing the number of the reinforcement layers does not cause a great effect until ***N=4*** in which case, the improvement percentage is almost triple the improvement percentage of ***N=3***.

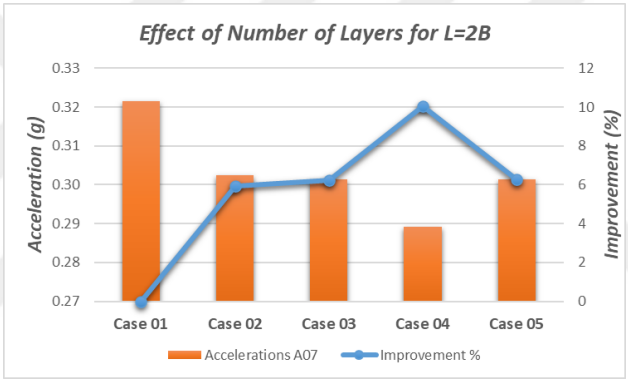

(a)

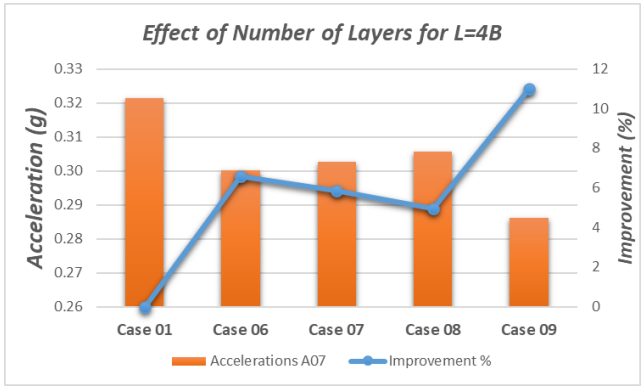

(b)

Figure 6.11. Improvement Percentages And Peak Accelerations On Top Of The Retaining Wall Model Of (a) Cases 02 To 05 And (b) Cases 06 To 09 Under The 1999 Kocaeli Earthquake Motion – Izmit Station.

6.3.2. Effects Of The Reinforcement Length Under The 1999 Kocaeli Earthquake Motion – Izmit Station

Figure 6.12 presents the comparisons of the improvement percentages and peak accelerations for the cases with the same number of reinforcement layers. The variable in these comparisons is the reinforcement length of the cases. While Figures 6.12a and d display the effect of the increasing reinforcement length on the improvement ratios clearly, Figure 6.12c displays a contrary result. This is led by the initial increase of the peak acceleration value on top of the retaining wall model in Case 08.

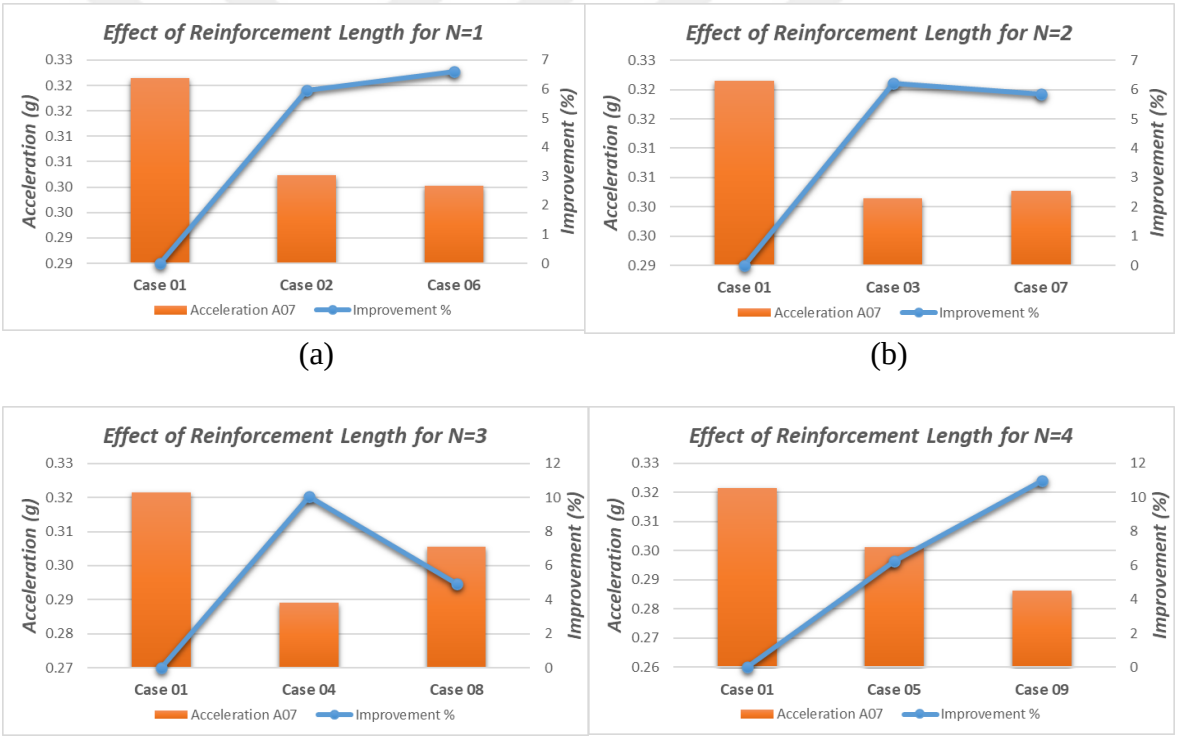

Figure 6.12. Comparisons Of Improvement Percentages And Peak Accelerations On Top Of The Retaining Wall Model For (a) Case 02 And Case 06, (b) Case 03 And Case 07, (c) Case 04 And Case 08, And (d) Case 05 And Case 09 To Understand The Effect Of Reinforcement Length Under The 1999 Kocaeli Earthquake Motion – Izmit Station.

6.4. Effects Of The Geogrid-Reinforcement On Top Of The Retaining Wall Model Under The 2014 North Aegean Sea Earthquake Motion – Gokceada Station

Detailed results of the experimental study explained in Chapter 5.4.4 are evaluated to understand the effectiveness of the reinforcement. Figure 6.13 presents the Fourier amplitudes and acceleration measures of all cases under the earthquake motion of the 2014 North Aegean Sea - Gokceada Station for the top of the retaining wall model. A decrease in peak acceleration values and spectral acceleration values in short periods is seen on top of the retaining wall model. The improvement percentage of acceleration values are 11.0 %, 8.4 %, 12.1 %, and 11.3 % for Cases 02 to 05 and 6.5 %, 8.4 %, 9.9 %, and 14.9 % based on the unreinforced case, Case 01. Figure 6.14 displays the Fourier amplitudes and displacement measurements of all cases on top of the retaining wall model. The difference in maximum displacements is 4.0 %, 0.7%, -0.7 %, and -0.8 % for Cases 02 to 05 and -3.8 %, 2.0 %, 12.3 %, and 4.2 % for Cases 06 to 09.

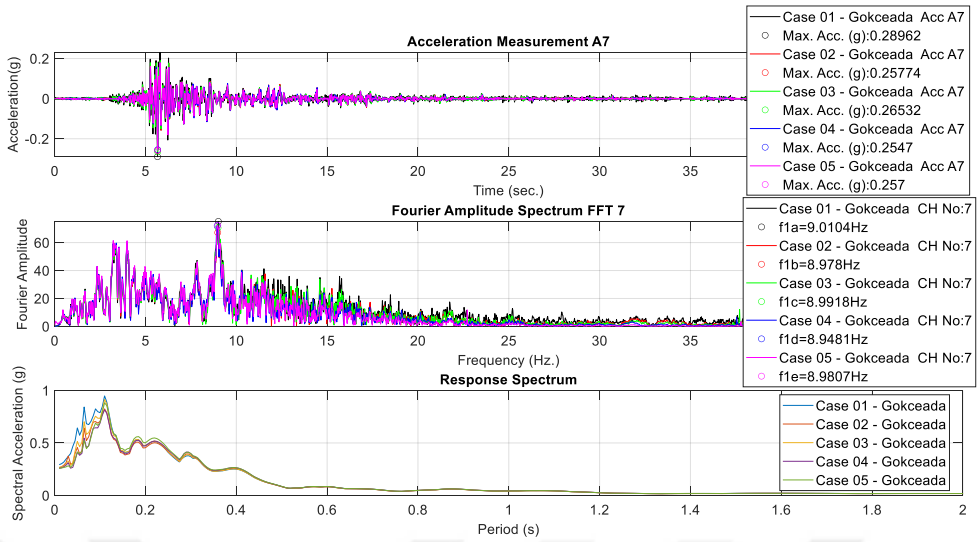

(a)

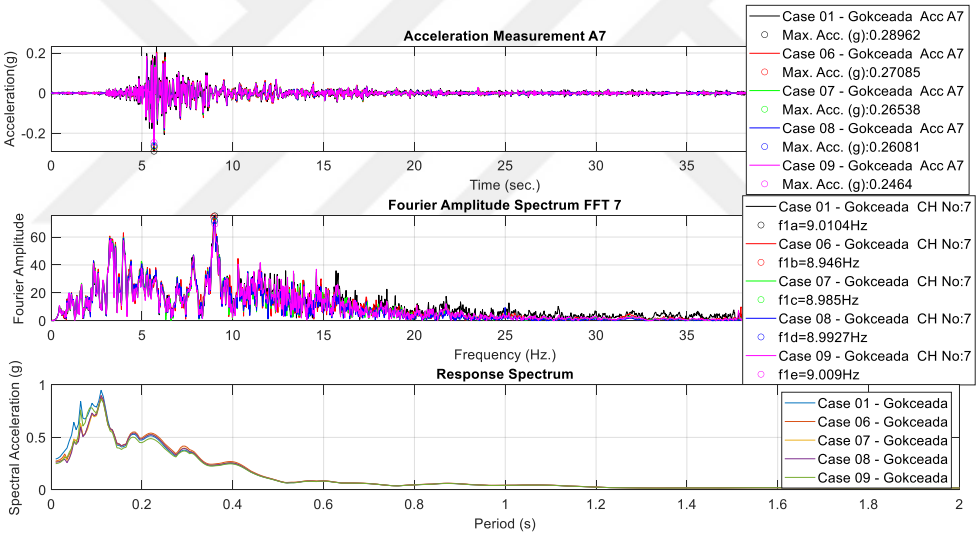

(b)

Figure 6.13. Comparison Of Acceleration, Fourier Amplitude, And Spectral Acceleration Values On Top Of The Retaining Wall Model For (a) Cases 02 To 05 And (b) Cases 06 To 09 Under The 2014 North Aegean Sea Earthquake Motion – Gokceada Station

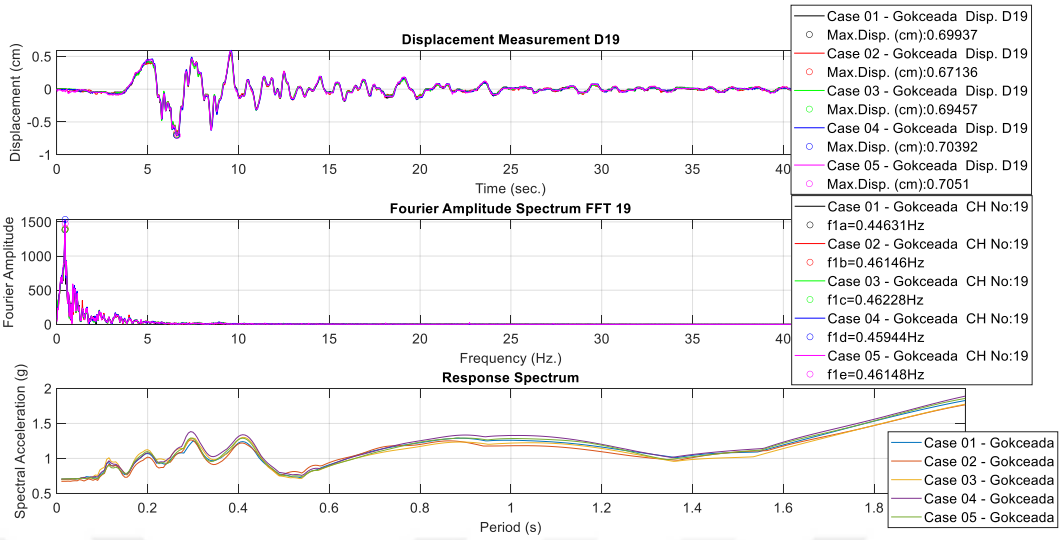

(a)

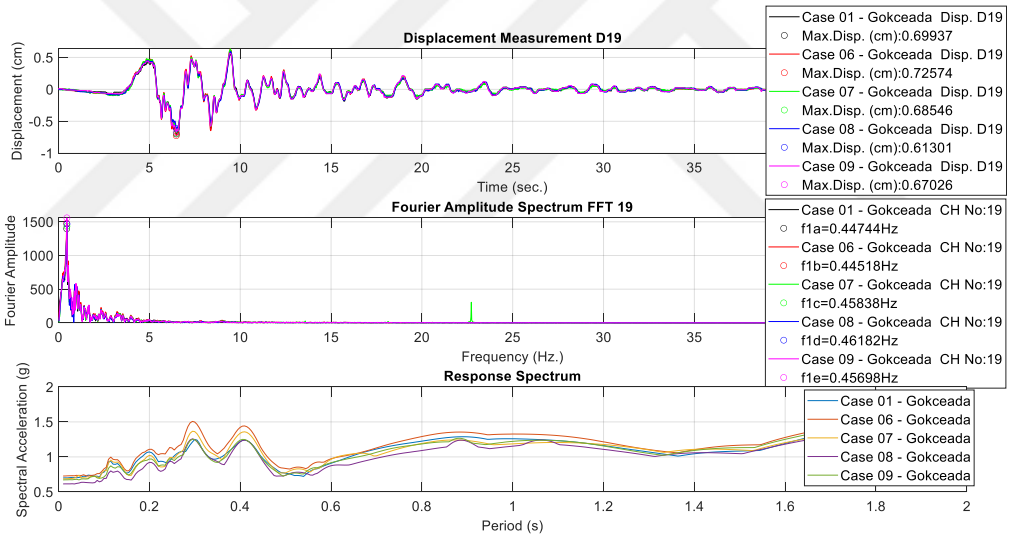

(b)

Figure 6.14. Comparison Of Displacement, Fourier Amplitude, And Spectral Displacement Values On Top Of The Retaining Wall Model For (a) Cases 02 To 05 And (b) Cases 06 To 09 Under The 2014 North Aegean Sea Earthquake Motion – Gokceada Station

6.4.1. Effects Of The Number Of Reinforcement Layers Under The 2014 North Aegean Sea Earthquake Motion – Gokceada Station

Figure 6.15 shows the comparison of improvement ratios based on the number of reinforcement layers. The initial increase of the peak acceleration on top of the retaining wall model in Case 03 disturbs the consistent effect of the reinforcement but it is seen that the later cases (Case 04 and 05) do not reflect the same response as seen in Figure 6.15a. Figure 6.15b displays the increasing improvement percentages as the number of reinforcement layers increases for the cases with the reinforcement length of 4B.

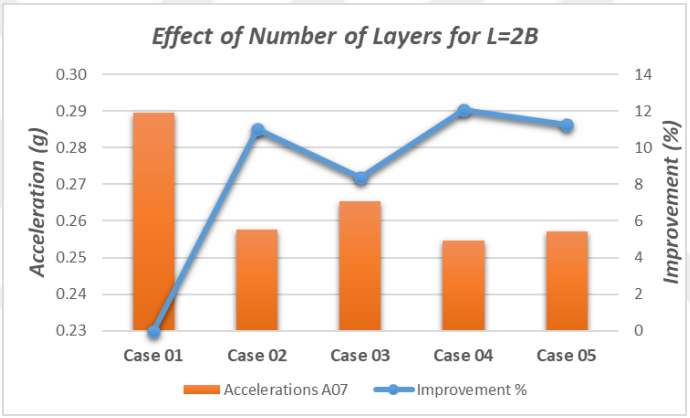

(a)

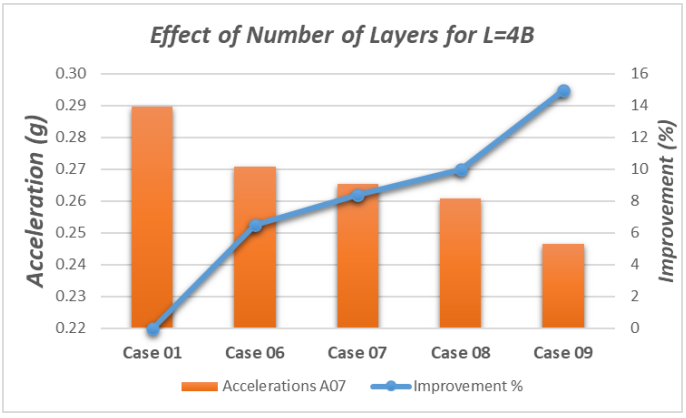

(b)

Figure 6.15. Improvement Percentages And Peak Accelerations On Top Of The Retaining Wall Model Of (a) Cases 02 To 05 And (b) Cases 06 To 09 Under The 2014 North Aegean Sea Earthquake Motion – Gokceada Station

6.4.2. Effects Of The Reinforcement Length Under The 2014 North Aegean Sea Earthquake Motion – Gokceada Station

Figure 6.16 presents the comparisons of the improvement percentages and peak accelerations for the cases with the same number of reinforcement layers. The variable in these comparisons is the reinforcement length of the cases. Figures 6.16a, and c shows that increasing the reinforcement length does not alter the effect of the reinforcement, however; the improvement percentages shown in Figure 6.16d are increased by increasing the reinforcement length.

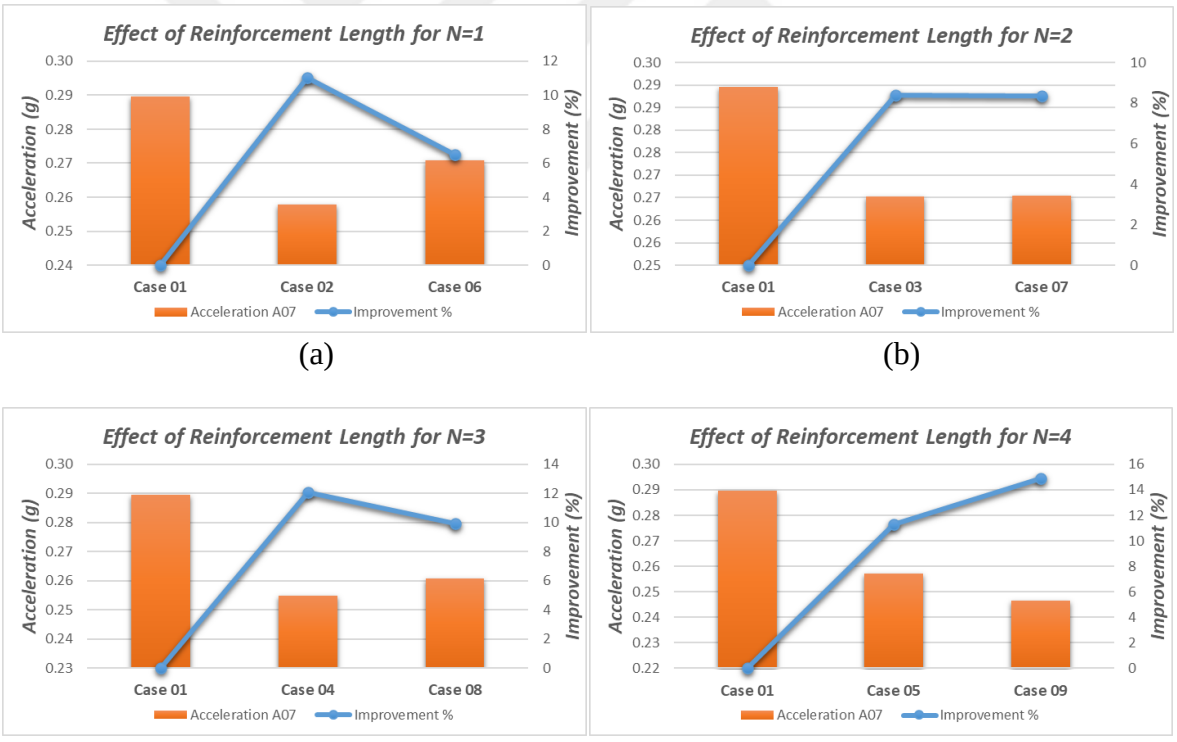

Figure 6.16. Comparisons Of Improvement Percentages And Peak Accelerations On Top Of The Retaining Wall Model For (a) Case 02 And Case 06, (b) Case 03 And Case 07, (c) Case 04 And Case 08, And (d) Case 05 And Case 09 To Understand The Effect Of Reinforcement Length Under The 2014 North Aegean Sea Earthquake Motion – Gokceada Station

7. CONCLUSIONS

The thesis aims to determine the effects of constructing a reinforced soil foundation for a retaining wall on the seismic performance of the retaining wall. To judge the effectiveness of the improvement method, the impact of various factors should be verified. In this study, the length of the geogrid and the number of geogrid layers are the factors being considered. The length of the reinforcement is dependent on the width of the foundation of the retaining wall.

The improvement method of applying a geogrid-reinforced soil foundation beneath a retaining wall is expected to increase the seismic performance of the retaining wall. The main idea behind the expectation is that the inclusion of geogrid reinforcement will enhance the strength of the soil foundation due to the interlocking mechanism of geogrid material with sand.

The results of the experimental study show that there are three main parameters affecting the efficiency of the reinforcement of the foundation soil under the retaining wall model. These parameters are the reinforcement length, the number of reinforcement layers, and the ground motion character.

Comparison of the peak accelerations recorded on top of the unreinforced retaining wall model helps us to understand how the ground motion characteristics affect the efficiency of the reinforcement. The 1999 Kocaeli Earthquake – Iznik Station results in 0.15 g, the 2014 North Aegean Sea Earthquake – Gokceada Station results in 0.29 g, the 1999 Kocaeli Earthquake – Izmit Station results in 0.32 g, and the 1940 Imperial Valley Earthquake – El Centro Station results in 0.70 g on top of the unreinforced retaining wall model. The reduction of the peak accelerations measured on top of the retaining wall model varies between 14.5 % and 20.0 % for the 1940 Imperial Valley Earthquake - El Centro Station, between 5.4 % and 14.2 % for the 1999 Kocaeli Earthquake – Iznik Station, between

4.9 % and 11.0 % for the 1999 Kocaeli Earthquake – Izmit Station, and between 6.5 % and 14.9 % for the 2014 North Aegean Sea Earthquake – Gokceada Station. Evaluating the improvement percentages on top of the retaining wall model states that the efficiency of the reinforcement increases as the peak acceleration caused by the ground motion increase since the greatest reduction percentages are obtained against the 1940 Imperial Valley Earthquake - El Centro Station and the lowest reduction percentages are obtained against the 1999 Kocaeli Earthquake – Iznik Station.

Another parameter affecting the efficiency of the reinforcement is the number of reinforcement layers. The evaluated reduction percentages in Chapter 6 show that increasing the number of reinforcement layers alters the efficiency of the reinforcement except for the 1940 Imperial Valley Earthquake - El Centro Station. The improvement percentages against the 1940 Imperial Valley Earthquake - El Centro Station are the highest values observed but increasing the number of the reinforcement layers does not alter the efficiency in this case.

The last parameter affecting the efficiency of the reinforcement is the reinforcement length. Similar to the effect of the number of reinforcement layers, increasing the reinforcement length alters the improvement percentages of the reinforcement for the 1999 Kocaeli Earthquake – Iznik and Izmit Stations, and the 2014 North Aegean Sea Earthquake – Gokceada Station. The impact of the reinforcement length does not seem to be great but its effect is consistent, especially in the case of the 1999 Kocaeli Earthquake – Izmit Station.

In conclusion, the results of the experimental study show that the efficiency of the geogrid-reinforced foundation soil beneath the retaining wall is quite effective against the earthquake motion of the 1940 Imperial Valley - El Centro Station, and the level of its efficiency is related to the parameters such as the reinforcement length, the number of reinforcement layers, and the characteristic of ground motion considered in this thesis.

8. REFERENCES

1. AbdelSalam, S. S., & Azzam, S. A. (2016). Reduction of Lateral Pressures on Retaining Walls Using Geofoam Inclusion. *Geosynthetics International*, *23*(6), 395–407.

2. D4439 - 20: Standard Terminology for Geosynthetics, (2020).

3. D8269-21: Standard Guide for the Use of Geocells in Geotechnical and Roadway Projects 1, (2021).

4. Başbuğ, E., Cengiz, C., & Güler, E. (2021). 1-g Shaking Table Tests to Determine the Behavior of Geosynthetic Reinforced Soil Walls Under Seismic Loads. *Transportation Geotechnics*, *30*.

5. Bathurst, R. J., Zarnani, S., & Gaskin, A. (2007). Shaking Table Testing of Geofoam Seismic Buffers. *Soil Dynamics and Earthquake Engineering*, *27*(4), 324–332.

6. Cai, X., Li, S., Xu, H., Jing, L., Huang, X., & Zhu, C. (2021). Shaking Table Study on the Seismic Performance of Geogrid Reinforced Soil Retaining Walls. *Advances in Civil Engineering*, *2021*.

7. Das, B. M., & Omar, M. T. (1994). The Effects of Foundation Width on Model Tests for the Bearing Capacity of Sand with Geogrid Reinforcement. *Geotechnical and Geological Engineering*, *12*, 133–141.

8. Das, B. M., & Ramana, G. V. (2011). *Principles of Soil Dynamics, 2nd Edition (International Edition)*.

9. Das, B. M., Shin, E. C., & Omar, M. T. (1994). The Bearing Capacity of Surface Strip Foundations on Geogrid-Reinforced Sand and Clay - A Comparative Study. *Geotechnical and Geological Engineering*, *12*(1), 1–14.

10. Day, R. W. (2012). *Geotechnical Earthquake Engineering Handbook: With the 2012 International Building Code, 2nd Edition.*

11. Edinçliler, A., & Toksoy, Y. S. (2011). Effects of Dimensions of Tire Waste Cushion on Seismic Performance of Retaining Wall. *Eurasian Journal of Civil Engineering and Architecture*, *2*(2).

12. Edinçliler, A., & Toksoy, Y. S. (2017, January 9). Effect of Ground Motion Characteristics on the Seismic Performance of Retaining Walls with Tire Waste Cushion. *16th World Conference on Earthquake Engineering, 16WCEE 2017, Santiago Chile*.

13. Edinçliler, A., & Toksoy, Y. S. (2019). The Effect of EPS Geofoam Thickness on the Seismic Performance of Quay Walls. In *5th International Conference on Geofoam Blocks in Construction Applications* (pp. 339–350). Springer International Publishing.

14. El-Emam, M. M., & Bathurst, R. J. (2007). Influence of Reinforcement Parameters on the Seismic Response of Reduced-Scale Reinforced Soil Retaining Walls. *Geotextiles and Geomembranes*, *25*(1), 33–49.

15. Gade, V. K., & Dasaka, S. M. (2022). Short- and Long-Term Behavior of EPS Geofoam in Reduction of Lateral Earth Pressure on Rigid Retaining Wall Subjected to Surcharge Loading. *Geotextiles and Geomembranes*, *50*(5), 868–880.

16. Guler, E., Cicek, E., Demirkan, M. M., & Hamderi, M. (2012). Numerical Analysis of Reinforced Soil Walls with Granular and Cohesive Backfills Under Cyclic Loads. *Bulletin of Earthquake Engineering*, *10*(3), 793–811.

17. Hasan, N. I., Mohd Taib, A., Muhammad, N. S., Yazid, M. R. M., Mutalib, A. A., & Hasbollah, D. Z. A. (2020). Effectiveness of Strip Footing with Geogrid Reinforcement for Different Types of Soils in Mosul, Iraq. *PLoS ONE*, *15*(12 December).

18. Hausmann, M. R. (1989). *Engineering Principles of Ground Modification*. McGraw-Hill.

19. Iai, S. (1989). Similitude for Shaking Table Tests on Soil-Structure-Fluid Model in 1g Gravitational Field. *Soils And Foundations*, *29*(1), 105–118.

20. Kilic, I. E., Cengiz, C., Edincliler, A., & Guler, E. (2021). Seismic Behavior of Geosynthetic-Reinforced Retaining Walls Backfilled with Cohesive Soil. *Geotextiles and Geomembranes*, *49*(5), 1256–1269.

21. Koerner, R. M. (2012). *Designing with Geosynthetics*. Pearson Prentice Hall.

22. Kramer, S. L. (1996). *Geotechnical Earthquake Engineering* (1st Ed.). Prentice Hall.

23. Matsuo, O., Tsutsumi, T., Yokoyama, K., & Saito, Y. (1998). Shaking Table Tests and Analyses of Geosynthetic-Reinforced Soil Retaining Walls. *Geosynthetics International*, *5*(2), 97–126.

24. Murthy, V. N. S. (2002). *Geotechnical Engineering*. CRC Press.

25. Nasr, A. M. A., & Azzam, W. R. (2017). Behaviour of Eccentrically Loaded Strip Footings Resting on Sand. *International Journal of Physical Modelling in Geotechnics*, *17*(3), 177–194.

26. Omar, M. T., Das, B. M., Puri, V. K., & Yen, S. C. (1993). Ultimate Bearing Capacity of Shallow Foundations on Sand with Geogrid Reinforcement. *Canadian Geotechnical Journal*, *30*(3), 545–549.

27. Patra, C. R., Das, B. M., & Atalar, C. (2005). Bearing Capacity of Embedded Strip Foundation on Geogrid-Reinforced Sand. *Geotextiles and Geomembranes*, *23*(5), 454–462.

28. Patra, C. R., Das, B. M., Bhoi, M., & Shin, E. C. (2006). Eccentrically Loaded Strip Foundation on Geogrid-Reinforced Sand. *Geotextiles and Geomembranes*, *24*(4), 254–259.

29. Santhakumar, A. R., Verma, A. K., & Appa Rao, T. V. S. R. (2001). Dynamic Behavior of Geogrid-Reinforced Soil. *International Conference on Recent Advances in Geotechnical Earthquake Engineering and Soil Dynamics*.

30. Sawwaf, M. El. (2009). Experimental and Numerical Study of Eccentrically Loaded Strip Footings Resting on Reinforced Sand. *Journal of Geotechnical and Geoenvironmental Engineering*, *135*(10), 1509–1518.

31. Sekman, M. (2016). *Experimental Study on Mitigation of Earthquake Hazards Using Geosynthetics* [Master of Science]. Boğaziçi University.

32. Sharma, R., Chen, Q., Abu-Farsakh, M., & Yoon, S. (2009). Analytical Modeling of Geogrid Reinforced Soil Foundation. *Geotextiles and Geomembranes*, *27*(1), 63–72.

33. Shin, E. C., & Das, B. M. (2000). Experimental Study of Bearing Capacity of A Strip Foundation on Geogrid-Reinforced Sand. *Geosynthetics International*, *7*(1), 59–71.

34. Shin, E. C., Das, B. M., Puri, V. K., Yen, S.-C., & Cook, E. E. (1993). Bearing Capacity of Strip Foundation on Geogrid-Reinforced Clay. *Geotechnical Testing Journal, GTJODJ*, *16*(4), 534–541.

35. Shrestha, S., Ravichandran, N., Raveendra, M., & Attenhofer, J. A. (2016). Design and Analysis of Retaining Wall Backfilled with Shredded Tire and Subjected to Earthquake Shaking. *Soil Dynamics and Earthquake Engineering*, *90*, 227–239.

36. Tsang, H. H. (2009). Geotechnical Seismic Isolation. In T. Miura & Y. Ikeda (Eds.), *Earthquake Engineering: New Research* (pp. 55–87).

37. Wang, L., Chen, G., & Chen, S. (2015). Experimental Study on Seismic Response of Geogrid Reinforced Rigid Retaining Walls with Saturated Backfill Sand. *Geotextiles and Geomembranes*, *43*(1), 35–45.

38. Wood, D. M. (2004). *Geotechnical Modelling* (2.2).

39. Yang, G., Liu, H., Lv, P., & Zhang, B. (2012). Geogrid-Reinforced Lime-Treated Cohesive Soil Retaining Wall: Case Study and Implications. *Geotextiles and Geomembranes*, *35*, 112–118.